Fundamental Studies on the Deposition and Characterisation of Novel Diamond-like Materials

Jacob Filik, September 2006

A dissertation submitted to the University of Bristol in accordance with the requirements of the degree of Doctor of Philosophy in the Faculty of Science.

Word Count ~64000

Abstract

This thesis contains three separate studies of novel diamond-like materials; incorporation of sulphur into hydrogenated amorphous carbon, Raman spectroscopy of diamondoids and Raman spectroscopy of nanocrystalline diamond. In the first study, amorphous hydrogenated carbon-sulfur thin films (a-C:H:S) were deposited from CH_4/H_2S gas mixtures using plasma enhanced chemical vapour deposition. Various analytical techniques were used to study the composition, structure and optical properties of the films. The ratio of S to C deposited in the film was found to be proportional to the process gas S/C ratio, with a maximum S/C ratio of 2/5. In the second study, Raman spectroscopy was used to analyze a selection of diamondoids, from adamantane ($C_{10}H_{16}$) to heptamantane ($C_{30}H_{34}$). Spectra were assigned by calculating the vibrational frequencies and Raman intensities using density functional theory. Each molecule was found to produce a unique spectrum, allowing for easy differentiation between molecules. Using the peak assignments derived from the calculations we find that the low frequency region of the spectra, corresponding to CCC-bending/CC-stretching modes, is characteristic of the geometric shape of the diamondoid molecules. The final section is a theoretical study of the Raman spectra of nanodiamond. Hartree-Fock theory was used to calculate the vibrational frequencies and Raman intensities of (≤ 1 nm) hydrogen-terminated diamond clusters. The calculated spectra are discussed in terms of the signals commonly observed in the Raman spectra of nanocrystalline diamond samples. This study finds no evidence for Raman active vibrations of hydrogen terminated or matrix confined diamond nanocrystals at either $\sim$500 cm^{-1} or $\sim$1150 cm^{-1}. Further, it appears that the only signals produced by a nanodiamond crystal are the broadened zone-centre (1332 cm^{-1}) mode and low frequency ($<$100 cm^{-1}) deformations/Lamb-type vibrations. This suggests any other peaks observed in the Raman spectra of nanocrystalline diamond are due to non-diamond material in the sample, and should not be taken as definitive evidence of nanocrystalline diamond.

Acknowledgements

Thanks to;

My supervisor Dr. Paul May for the project, guidance and good times, Prof. Mike Ashfold for the excellent advice and so much more, Dr. Jeremy Harvey and Prof. Neil Allan whose input and suggestions I could not have done without, Dr. Jeremy Dahl and all at Molecular Diamond Technologies, for throwing some good experiments my way, Mr. Keith Rosser, for simply making things work and the EPSRC for funding.

Also, Sean Pearce, Ian Lane and Mark Williams, my scientific father and sons, Kevin Jack and Youssef Espidel for the NMR, Des Davis from the Microanalytical lab and the lovely people in the Mechanical and Electronics workshops.

Finally thanks to my parents for basically everything, Bríd, Ed, Jim, Fred, Fuge, the members of the University of Bristol Diamond and Laser groups and all my other homies.

Cheers then.

I declare that the work in this dissertation was carried out in accordance with the Regulations of the University of Bristol. The work is original, except where indicated by special reference in the text, and no part of the dissertation has been submitted for any other academic award. Any views expressed in the dissertation are those of the author.

SIGNED: ..... DATE:.....

Contents

1 Introduction **1**

1.1 Graphite 1

1.2 Diamond 2

1.2.1 Natural Production 3

1.2.2 Synthetic Production 3

1.3 Amorphous Carbon 8

1.3.1 The Growth Mechanisms for Amorphous Carbon 8

1.3.2 Doping of Amorphous Carbon 11

1.3.3 Carbon Nitride and Phosphorus Carbide 13

1.4 Diamondoid Hydrocarbons 13

1.4.1 The Discovery of the Lower Diamondoids 13

1.4.2 Systematic Nomenclature 14

1.4.3 Higher Diamondoids in oil 15

1.4.4 Diamondoids: Experiment and Theory 17

1.5 Aims of this Study 19

1.5.1 Incorporation of Sulfur into Amorphous Carbon 19

1.5.2 Raman Spectroscopy of Diamondoids 20

1.5.3 Raman Spectroscopy of Nano-Crystalline Diamond: An *Ab Initio* Approach 20

2 Experimental and Theoretical Techniques **27**

2.1 Raman Spectroscopy 27

2.1.1 The Theory of Raman Spectroscopy 27

2.1.2 Calculating Vibrational Frequencies and Raman Intensities . . . 35

2.1.3 Raman Spectroscopy of Diamondoids 45

2.1.4 Raman Spectroscopy as a Characterisation Tool for Carbon Based Materials 47

2.1.5 Description of the Raman Spectrometers 55

2.2 The Deposition Method 58

2.2.1 The RF Discharge Process . . . 59
2.2.2 Experimental Set-up . . . 60
2.3 X-Ray Photoelectron Spectroscopy . . . 62
2.3.1 Theory . . . 62
2.3.2 X-ray Photoelectron Spectroscopy in Surface Analysis . . . 63
2.3.3 X-Ray Photoelectron Spectroscopy of Amorphous Carbon . . . 64
2.4 Secondary Ion Mass Spectrometry . . . 66
2.4.1 Secondary Ion Mass Spectrometry of Amorphous Carbon . . . 68
2.5 UV/Visible Absorption Spectroscopy . . . 68
2.5.1 UV/Vis Absorption Spectroscopy of Amorphous Carbon . . . 69
2.6 Ellipsometry . . . 70
2.6.1 Theory of Ellipsometry . . . 70
2.6.2 Spectroscopic Ellipsometry of Amorphous Carbon . . . 75
2.6.3 Ellipsometry method . . . 77
2.7 Micro-Combustion Elemental Analysis . . . 77
2.8 Micro-Combustion Elemental Analysis of Amorphous Carbon . . . 78

3 Incorporation of Sulfur into Hydrogenated Amorphous Carbon 87
3.1 Introduction . . . 87
3.2 Deposition Conditions . . . 88
3.3 Compositional Analysis . . . 89
3.3.1 X-Ray Photoelectron Spectroscopy . . . 89
3.3.2 Secondary Ion Mass Spectrometry . . . 94
3.4 Structural Analysis . . . 95
3.4.1 Raman Spectroscopy . . . 95
3.5 Growth Rate and Optical Properties . . . 100
3.5.1 Growth Rate . . . 100
3.5.2 Optical Properties . . . 102
3.6 Deposition of a-C:S films from CS_2 . . . 106
3.6.1 Raman Spectroscopy . . . 106
3.7 Comparison of a-C:S:H, a-C:N:H and a-C:S:N:H films . . . 108
3.8 Deposition Conditions . . . 108
3.9 Structural Analysis . . . 110
3.9.1 Raman Spectroscopy . . . 110
3.10 Growth Rate and Optical Properties . . . 112
3.10.1 Growth Rate . . . 112
3.10.2 Optical Properties . . . 115
3.11 Compositional Analysis . . . 115
3.11.1 Micro-Combustion Elemental Analysis . . . 117

3.12 Summary and Conclusions 118

4 Raman Spectroscopy of Diamondoids 125
4.1 Introduction 125
4.2 Results 126
4.2.1 Different Excitation Energies 128
4.2.2 Theory 130
4.2.3 Adamantane, Diamantane, and Triamantane 131
4.2.4 [1(2)3] tetramantane, [1(2,3)4] pentamantane and 3-methyl-[1(2,3)4] pentamantane 133
4.2.5 [121] tetramantane and [1212] pentamantane 141
4.2.6 [123] tetramantane and [1234] pentamantane 144
4.2.7 [12(3)4] pentamantane, [12(1)3] pentamantane and [1213] pentamantane 146
4.2.8 [12312] hexamantane and [121321] heptamantane 148
4.2.9 Theoretical molecules 148
4.3 Conclusions 157

5 Raman Spectroscopy of Nano-Crystalline Diamond: An *Ab Initio* Approach 163
5.1 Introduction 163
5.2 Theoretical Methods 165
5.3 Selecting the Level of Theory 165
5.4 Results 168
5.4.1 The first-order diamond Raman peak - the crystal-molecule transition 168
5.4.2 The $\sim$500 cm^{-1} mode in the Raman spectrum of nanodiamond powders 172
5.4.3 Decoupling the hydrogen motion - nanodiamond thin films . . . 175
5.5 Conclusions 179

A Publication List 187

B Solid-State Nuclear Magnetic Resonance 189
B.1 Introduction 189
B.2 Experimental 189
B.3 Results 190
B.4 Conclusions 190

C Vibrational Frequencies and Raman Intensities of Adamantane 193

Chapter 1

Introduction

Within the last 50 years many important advances have been made in the field of diamond and related materials. The synthetic production of diamond [1], the discovery of buckminsterfullerene [2], carbon nanotubes [3] and large diamondoid hydrocarbons [4], as well as the development of diamond-like carbon thin films [5], are just a few examples of this continuously expanding research area.

This thesis concentrates specifically on three areas of carbon science; amorphous carbon, diamondoid hydrocarbons and nanocrystalline diamond. The following chapter is a brief introduction to the study of diamond and related materials, particularly focusing on the three topics mentioned above. The final section (section 1.5) is a more in depth discussion of the aims of this project with respect to these three areas.

Let us start by discussing two of the allotropes of carbon; graphite and diamond.

1.1 Graphite

Graphite is made up of graphene sheets bound together by weak van der Waals forces (Figure 1.1). The graphene sheets are made of sp^2 hybridised carbon bonded in a network of six-membered rings. The carbon-carbon bonds in the graphene network are stronger than those in diamond (Table 1.1); it is the weakness of the bonding of between the layers that gives graphite its softness and makes it a good lubricant. The properties of graphite are strongly anisotropic. The thermal and electrical conductivity values in the planes of the graphene sheets are much higher than those perpendicular to the layers (Table 1.1). The short, stiff bonds give graphite a higher thermal conductivity than diamond when measured across the graphene planes. However, the thermal conductivity perpendicular to the planes is very low by comparison because of the weak van der Waals bonding. Similarly, graphite shows metallic conduction in the plane of the graphene sheets but not perpendicular to them, it is a semimetal. The π orbitals in graphite are similar to those in a single benzene ring, except the delocalisation is

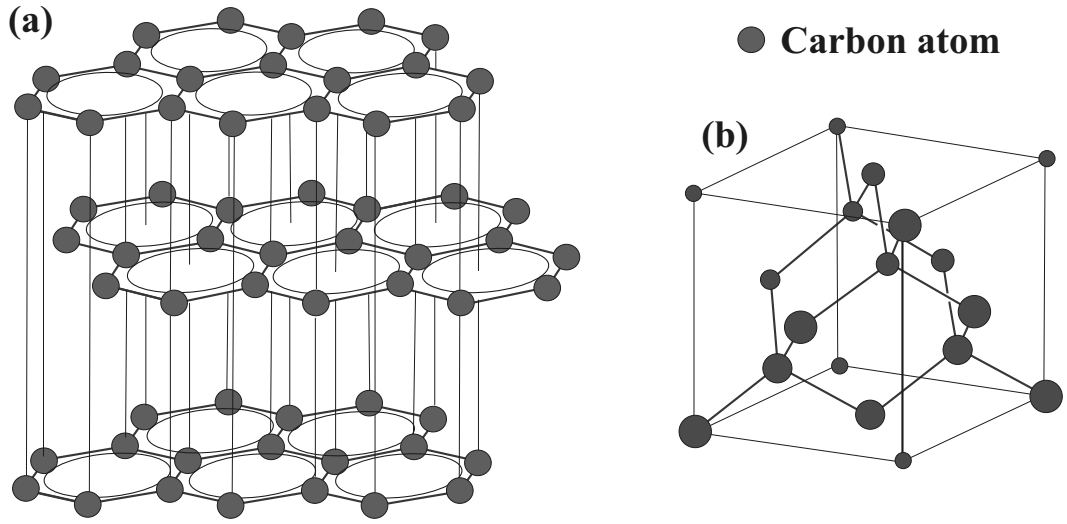

Figure 1.1: Structures of (a) Graphite and (b) Diamond.

Material	Bond Strength kJ mol^{-1}	Thermal Conductivity W/m.K	Electrical Resistivity Ω cm
Graphite			
In-plane	~ 524	< 4180	10^{-4}
Out-of-plane	~ 7	2	1
Diamond			
	~ 349	~ 2000	10^{14}

Table 1.1: Comparison of the bond strengths, thermal conductivities and electrical resistivites of diamond and graphite [6–9].

across the entire graphene sheet. It is the free movement of electrons in this delocalised orbital that allows an electrical current to flow. Electrons cannot easily move from one graphene sheet to another, so the electrical conductivity perpendicular to the graphite planes is very low.

1.2 Diamond

The physical and chemical properties of diamond are very different to those of graphite. The cause of these differences is the way the carbon atoms are arranged in each crystal. Unlike graphite, the carbon atoms in diamond are sp^3 hybridised and tetrahedrally bonded to other carbon atoms. It is the tetrahedral arrangement of strong C-C single bonds that gives diamond its extreme properties.

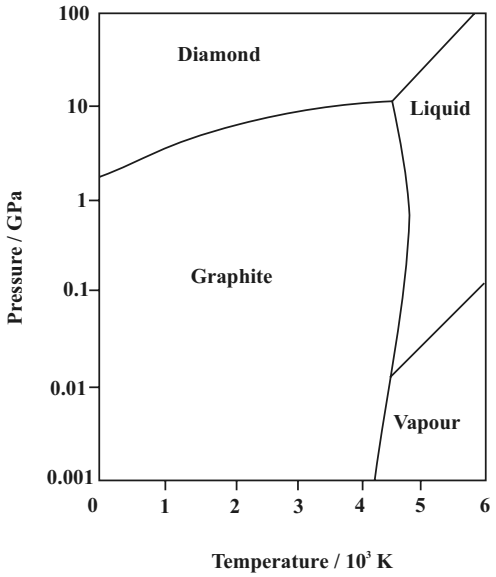

Figure 1.2: Simplified version of the carbon phase diagram traced from reference [10]

Despite being harder and denser than graphite, under ambient conditions, diamond is less stable by 2.9 kJ mol^{-1}. Fortunately, a large activation barrier prevents an appreciable rate for interconversion from diamond to graphite. Since diamond is only metastable at standard temperature and pressures, the production of diamond from other forms of carbon is difficult. Yet several tonnes of natural diamonds are mined annually, so how is this diamond formed?

1.2.1 Natural Production

At high pressures, diamond is the stable solid form of carbon (Figure 1.2). In nature, diamond is formed within the mantle, beneath the Earth's crust. At depths below 150 km, the pressure and temperature are such that diamond becomes the most thermodynamically stable form of carbon. Diamonds grow in the mantle over billions of years and are brought to the surface in rocks carried by magma.

1.2.2 Synthetic Production

Being prized for their aesthetic qualities, natural diamonds are generally used for decorative purposes rather than as a scientific/engineering material. Small or low quality diamonds do find their way into industrial applications however. The hardness of diamond makes it an excellent abrasive for grinding and polishing applications. Diamond powders cannot be used in a way that takes advantage of the excellent optical trans-

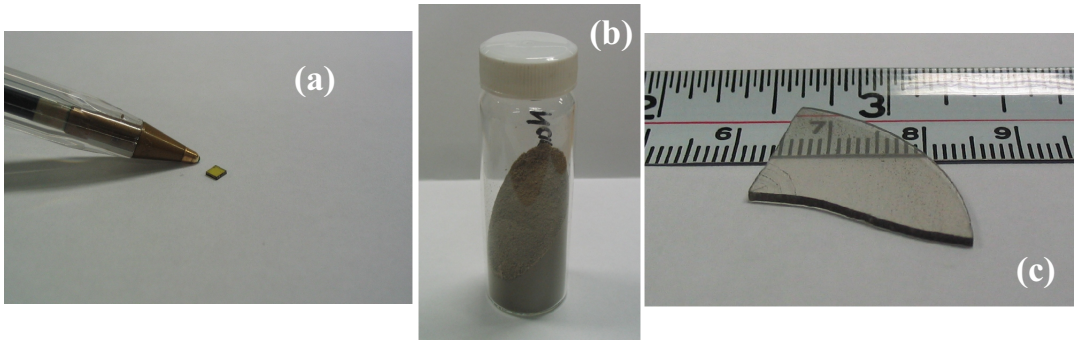

Figure 1.3: Photographs of (a) commercial HPHT diamond (ball point pen for scale), (b) commercial nanodiamond powder, (c) piece of a free-standing, micro-crystalline, CVD diamond window.

parency and thermal conductivity of diamond. A major problem in microelectronics is dissipating the heat generated during device operation. If diamond could be used as a substrate for microelectronic circuits, thermal management would be easier. Moreover, if electronic grade (containing extremely low levels of impurities and defects) diamond could be produced, and doped, it would be possible to create microelectronics out of diamond. The high carrier mobility [11], wide band gap and thermal stability of diamond means these devices would be able to operate faster, and under much more extreme conditions than silicon based devices. To produce such devices would require relatively large, high grade diamond samples, unlikely to be found in nature. In order to take full advantage of the extreme properties of diamond, samples must be synthetically grown, with their properties tailored specifically for each application.

High Pressure High Temperature Synthesis

The simplest method of synthetically growing diamond mimics the conditions used in nature. The first high pressure high temperature (HPHT) diamond synthesis was performed by Bundy *et al.* [1] at the General Electric Research Laboratory. They used pressures of 10 GPa and temperatures in excess of 2300 K to produce diamond crystals with an edge length of over 1 mm. Over the years the process has been refined, and it is now possible to produce different types of diamonds of several carats in mass [12]. The relatively large diamond crystals grown nowadays are produced by compressing carbon (and a catalyst) to 6 GPa at around 1400°C for several days (Figure 1.3(a)).

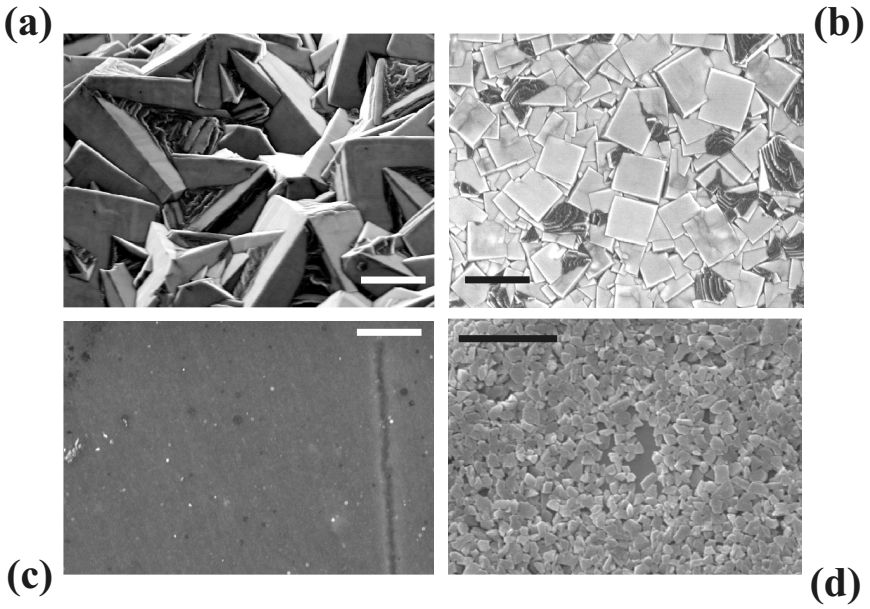

Figure 1.4: Scanning electron micrographs of (a) a microcrystalline CVD diamond sample showing the (111) facets (10 μm scale bar), (b) a microcrystalline CVD diamond sample showing the (100) facets (10 μm scale bar), (c) a nanocrystalline CVD diamond sample, showing the relatively smooth homogeneous surface (10 μm scale bar), (d) commercial 500 nm crystallite diamond powder (5 μm scale bar).

Explosion Synthesised Nanodiamond

Other methods of diamond synthesis that take advantage of the stability of diamond at high pressure are high explosive detonation or shock wave compression synthesis. These methods only produce nanodiamond powders (Figures 1.3(b) and 1.4(d)) but are considerably faster than traditional HTHP methods. After the detonation of a carbon-containing high explosive in an inert atmosphere, diamond crystallites can be found as constituent of the residual soot [13]. Shock synthesis is similar, but in this case an explosion is used to rapidly compress a carbon sample in a stainless steel container [14]. In both instances only nanocrystals of diamond are formed due to the incredibly short reaction time (<5 sec [15]).

Chemical Vapour Deposition

So, by mimicking nature, it is possible to produce isolated diamond crystals with diameters ranging from nanometres to millimetres. But this is not the only way to produce diamond synthetically.

The process of chemical vapour deposition (CVD) involves the growth of a solid material from reactions of chemicals in the gas phase. Feasible growth of diamond by CVD was first shown by Angus *et al.* in 1968 [16]. To deposit diamond by CVD, the precursor gas can be any common hydrocarbon but it must be diluted heavily in hydrogen (∼1%). Diamond can be grown from a mixture of C, H and O as long the the appropriate ratios of each element are used [17] (Figure 1.5).

Diamond does not just deposit onto a substrate from a mixture of carbon, hydrogen and oxygen. The gas must be activated in some way and the substrate must be hot (around 900°C). Activation of the precursor gas creates many hydrogen and carbon radical species. During the CVD process, the carbon species are continually deposited onto the surface of the hot substrate and then etched away by the atomic hydrogen. If the conditions are tuned correctly, the deposition rate of diamond exceeds its etch rate, while the opposite occurs for all non-diamond species. This leads to the formation of an essentially pure diamond film bound to the substrate [18].

Common substrates for CVD of diamond are silicon and molybdenum, as they can withstand the high temperatures required for the diamond growth process. Diamond has a lower thermal expansion coefficient than either of these materials, so shrinks less on cooling. This leads to a high compressive stress within the diamond film, causing fracture and sometimes complete delamination from the substrate (which can be used to produce free-standing diamond films, see Figure 1.3(c)). Before deposition, substrates are usually abraded with nano or micrometre sized diamond grit, to aid the nucleation of the diamond film.

Many different methods of gas activation are used to grow CVD diamond [18], from atmospheric-pressure combustion torches, to hot filaments and plasma discharges. Combustion torches grow diamond at a very fast rate (100-1000 μm h^{-1}) but growth is difficult to control, and often non-uniform. Hot filament activation can be used to grow uniform, good quality diamond films, but the filament is unreliable, deposition rates are slow (0.1-10 μm h^{-1}) and metal atoms can evaporate off the filament during deposition and contaminate the growing film. Microwave discharges are the most common method used to grow good quality CVD diamond films. Advantages of these discharges over other methods are; uniform deposition, no filaments or electrodes to contaminate the sample, use of oxygen containing gases (which would destroy a filament) and relatively high growth rates (∼70 μm h^{-1}) [19] are achievable by tailoring the discharge.

The diamond films grown onto Si and Mo substrates are microcrystalline, that is,

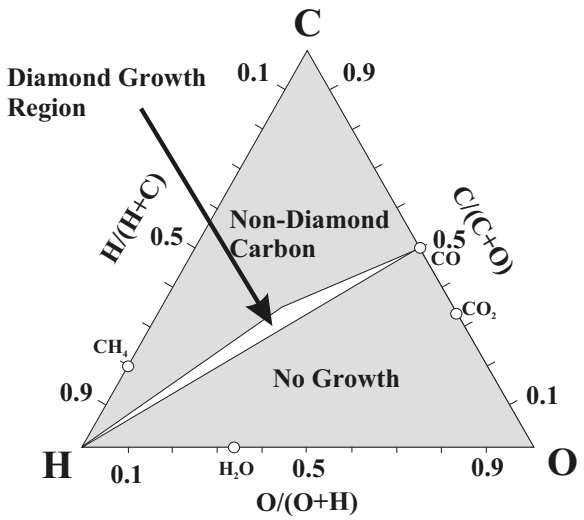

Figure 1.5: The Bachmann Diagram [17]. This diagram shows the relative proportions of C, H, and O required in the gas phase for CVD diamond growth to occur.

micron-sized diamond crystals bound together with non-diamond carbon. By changing the process gas mixture it is possible to vary the crystallite size from microns to nanometres [20].

It is possible to grow single crystals of diamond using CVD, but the substrate must be a single diamond crystal. This type of growth is called *homo-epitaxial*. The most popular substrates for homo-epitaxial growth are the diamonds grown by HPHT. Microwave CVD can be used to grow single crystal diamond films several millimetres thick onto HPHT diamond substrates [19].

Applications of Synthetic Diamond

The synthetic production of diamond has opened up the possibility of using this exotic material for scientific and engineering purposes, but what applications might benefit from its range of extreme properties?

The large size, high thermal conductivity, low thermal expansion, and low dielectric constant of HPHT diamonds makes them excellent as heat sinks. As stated above, they are also the substrate of choice for homo-epitaxial diamond CVD.

Shock or explosion synthesised nanodiamond is important for fine polishing, but other uses are being investigated. The low abrasiveness and antiwear properties of nanodiamond powders make them promising solid lubricants [21]. Solid lubricants are required when conditions, such as high vacuum, restrict the use of traditional liquid lubricants. One of the most interesting properties of diamond is the negative

electron affinity of the hydrogen-terminated surface [22,23]. A negative electron affinity implies diamond could be used as a cold cathode in electron emitting devices. Indeed, nanodiamond powders have been shown to produce stable electron emission, with low turn-on voltages (3.2 V/μm) and high current densities ($\sim$95 mA m^2 under the applied field of 5 V/μm) [24].

Microcrystalline CVD diamond films are the most versatile form of synthetic diamond. They can be used as protective coatings [25], for heat dissipation [26], and even as windows in fusion reactors [27]. Nanocrystalline CVD diamond (NCD) films are increasingly studied due to their smooth surface and relatively homogeneous structure (compared to microcrystalline diamond films). Combined with the other properties of microcrystalline diamond, this makes NCD excellent for constructing micro-electronic mechanical devices (MEMS) [28].

1.3 Amorphous Carbon

The high temperatures required for deposition limits the number of substrate materials that can be coated with CVD diamond. Low melting point materials, such as glass and plastics do not survive the 900°C required for diamond CVD. Also, for some applications, CVD diamond, and even nanodiamond, is too rough. In the cases where a hard, atomically flat coating is needed, on a low melting point material, *amorphous carbon* can be used.

The term, amorphous carbon (a-C) refers to any non-crystalline, disordered form of carbon. Amorphous carbons tend to contain both sp^3 and sp^2 hybridised carbon in various ratios. Films with higher sp^3 proportions are often called *diamond-like carbon* (DLC). Other common acronyms used for naming amorphous carbons are; ta-C (t for tetrahedral, very high sp^3 proportion a-C), a-C:H (hydrogen containing a-C) and ta-C:H (very high sp^3 proportion, hydrogen containing a-C). A comparison of some of the properties of the different kinds of amorphous carbons to diamond, graphite and polyethylene are shown in Table 1.2.

The fact that high quality a-C is mechanically hard, chemically inert and optically transparent gives it a variety of uses, from protective coatings on optical windows or hard drives, to MEMS devices [29–31].

1.3.1 The Growth Mechanisms for Amorphous Carbon

To produce hard a-C films, a large fraction of the carbon must be in the metastable sp^3 hybridisation. In CVD diamond growth, the sp^3 hybridised phase is produced by complex surface chemistry between the hot growing film and gas-phase hydrogen atoms [18]. High sp^3 proportion amorphous carbon films are grown at room temperature or

Material	sp^3 (atomic %)	H (atomic %)	Density (g cm^{-3})	Band Gap (eV)	Hardness (GPa)
Diamond	100	0	3.515	5.5	100
Graphite	0	0	2.267	0	
Glassy C	0	0	1.3-1.55	0.01	3
Evaporated C	0	0	1.9	0.4-0.7	3
Sputtered C	5	0	2.2	0.5	
ta-C	80-88	0	3.1	2.5	80
a-C:H (hard)	40	30-40	1.6-2.2	1.1-1.7	10-20
a-C:H (soft)	60	40-50	1.2-1.6	1.7-4	<10
ta-C:H	70	30	2.4	2-2.5	50
Polyethylene	100	67	0.92	6	0.01

Table 1.2: Comparison of some of the properties of various types of amorphous carbon to diamond, graphite and polyethylene [32].

below. How is the relatively unstable sp^3 phase produced in these materials?

Amorphous carbons of significant sp^3 proportion can be produced by various different techniques, from ion beam deposition, to laser ablation and Plasma-Enhanced CVD (PECVD) [32]. All of these methods have one thing in common; they all bombard the substrate with high energy species.

The growth mechanism of a-C is called *subplantation*. A detailed description of the development of the theory behind this mechanism is given in the review by Robertson [32]. What follows is a brief explanation as to how this mechanism stabilises sp^3 hybridised carbon.

It is generally accepted that the highest sp^3 proportion a-C films are grown from ions with an impact energy of 100 eV per carbon atom in the ion [33]. If the impact energy is above or below this energy, the a-C films become more graphitic in nature.

Consider carbon ions accelerated toward an amorphous carbon substrate. If the impact energy is too low the ion cannot penetrate the surface. Instead, it sticks to the surface, forming the low energy sp^2 hybridisation. If the ion energy is increased, the probability of the ion penetrating the surface increases. Penetration of the ion into the film increases the local density. Under the highly energetic conditions of the impact, the hybridisations of the carbon atoms can change with the local environment. The sp^3 hybridisation of carbon is more stable at higher densities, so impact of the ion produces more sp^3 hybridised carbon. As the ion energy is increased further still, only a fraction of the energy is required to penetrate the surface. The excess energy must be lost as heat within the a-C film. This *thermal spike* associated with a high energy impact allows the thermodynamically unstable high density (sp^3) regions to relax, favouring the more stable sp^2 hybridisation.

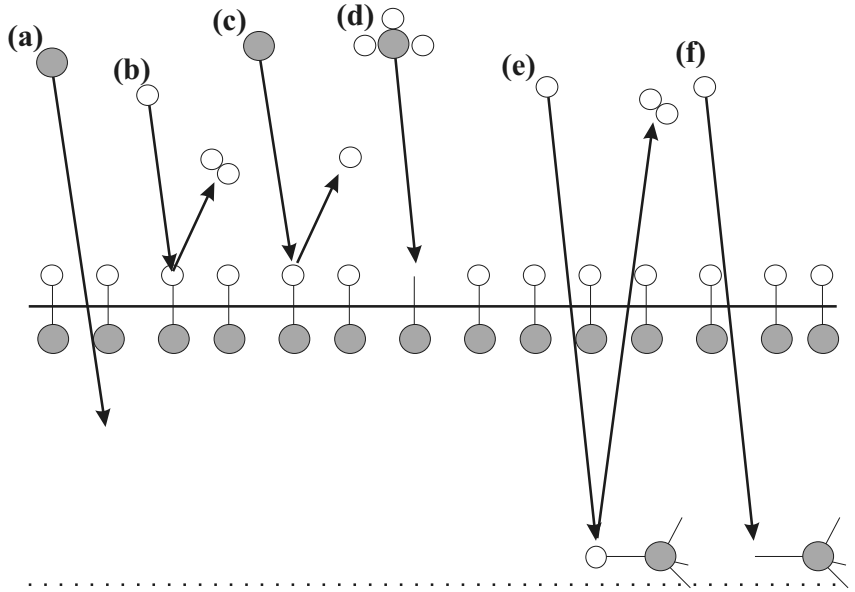

Figure 1.6: Illustration of the various process involved in the growth of hydrogenated amorphous carbon films (a) ion subplantation, (b) surface dangling bond from hydrogen abstraction, (c) surface sputtering to produce dangling bonds, (d) growth by radical addition to dangling bonds (e) bulk hydrogen abstraction and (f) bulk dangling bond passivation [32]. Dashed line shows H ion penetration depth for an arbitrary ion impact energy.

Growth of a-C:H

The above process describes how high sp^3 a-C films are produced by careful choice of the carbon ion impact energy. Generally, in PECVD, hydrocarbon process gases are used. The presence of hydrogen adds an extra layer of complexity (Figure 1.6).

Hydrogen is known to soften a-C films, remove stress and passivate dangling bonds [34]. If low ion impact energies are used when depositing hydrogenated amorphous carbon films (a-C:H), the ionic hydrocarbons polymerise on the surface. The hydrogen stabilises the sp^3 hybridised carbon forming a-C:H films with high sp^3 content. Almost all of the sp^3 hybridised carbon is bonded to one or more hydrogen atoms, and is therefore not diamond-like, so these films are very soft (polymeric a-C:H). Increasing the impact energy reduces the hydrogen content by increasing the sputtering of the light hydrogen atoms. Films produced under these conditions have the highest sp^3 C-C bonding, and are hence the most diamond-like. At even higher impact energy, the hydrogen content decreases, and the proportion of sp^2 hybridised carbon increases as in non-hydrogenated a-C films.

1.3.2 Doping of Amorphous Carbon

The ability to tune the band gap of a-C to between 4 eV (for polymeric a-C:H) and effectively 0 eV (graphitic a-C) makes it a promising material for electronic devices. To turn the highly insulating a-C films into semiconductors requires doping. To be electronically useful both p- and n-type doping is required (Figure 1.7).

p-type doping is generally achieved by replacing some atoms in the crystal with atoms of an element with one less valence electron. Diamond can be made into a p-type semiconductor by the addition of boron. The boron atom creates an empty level 0.37 eV above the valence band [35]. An electron from the valence band is excited into this empty state, creating a mobile *hole* in the valence band. It is mobile carriers like the hole in the valence band that allow electricity to flow through the material.

In n-type doping, some of the atoms in the crystal are replaced by atoms of an element with one extra valence electron. n-type doping of diamond is less straightforward than p-type doping. The donor levels produced by the addition of nitrogen are too far from the conduction band for electrons to be excited at room temperature ($\sim$2 eV below the conduction band [35]). Doping with phosphorus improves the situation [36] (0.55 eV below the conduction band), but is still not ideal. Arsenic and antimony are predicted to possess donor levels significantly shallower than phosphorus but these large atoms are likely to have a poor solubility in the diamond lattice [37].

Doping a-C is difficult for many reasons. Firstly the flexibility of the amorphous network allows dopant atoms to exert their chemically preferred valence [38]. Secondly, the addition of other elements tends to increase the proportion and clustering of sp^2 bonds [39]. This could be due to the lower density of the sp^2 regions reducing the lattice strain, therefore making the dopant easier to accommodate (for large atoms) or the dopant encouraging bonding in the the sp^2 configuration (as in the case for nitrogen). It can be difficult to show whether an increase in the conduction of the doped a-C sample is due to the dopant or the increase in sp^2 bonding. Finally, the density of defects in a-C films is too high for most electronic device applications [32] (10^{20} cm^{-3} in ta-C compared to 10^{16} cm^{-3} in a-Si:H).

Elements that have commonly been used to dope amorphous carbons are; boron [40] or iodine [41] for p-type, and nitrogen [42] or phosphorus [43] for n-type. Nitrogen doping works in a-C despite failing in diamond because the the narrower band gap of a-C makes the nitrogen donor levels closer to the conduction band.

Kleinsorge *et al.* [40] showed boron doping of ta-C films increased their conductivity by five orders of magnitude (10^{-6} to 0.1 $(\Omega\text{cm})^{-1}$), without changing the band gap. They also showed that a ta-C:B/n-type Si heterojunction can be used as a rectifier. Iodine doping of a-C:H also produces an increase in the conductivity of the films, but only by two orders of magnitude [41]. In this case the increase in conductivity coincided

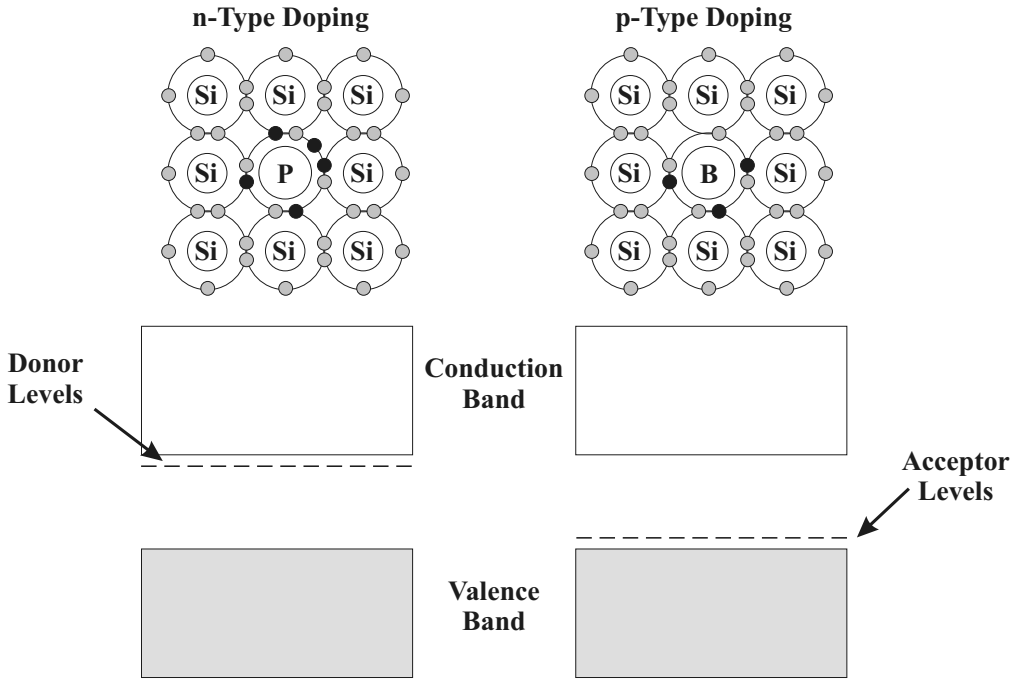

Figure 1.7: Illustration of n- and p-type doping in silicon. The grey circles represent the electrons of silicon, the black circles represent the dopant element's electrons. In n-type doping, the donor electrons are excited into the conduction band, producing a free electron, allowing electricity to flow. In p-type doping, the empty acceptor level accepts an electron from the valence band, producing a free hole, which allows electricity to flow.

with a decrease in the band gap (1.1 to 0.78 eV), and therefore may be due to changes in the sample structure.

Conway *et al.* [42] showed that undoped ta-C:H films showed p-type behaviour when made into ta-C:H/doped-Si heterojunctions. An addition of a low concentration of nitrogen reduced the conductivity of the film by compensating for the p-type dangling bond defects. Films deposited with higher levels of nitrogen doping showed n-type behaviour. Veerasamy *et al.* [43] studied the doping of ta-C films with phosphorus. They found a dramatic decrease in the resistivity of the films (from 10^7 to 5 Ω cm)) with the addition of a small amount of phosphorus ($\leq$1%). From electron energy loss measurements the managed to show that predominately tetrahedral bonding was maintained after doping.

1.3.3 Carbon Nitride and Phosphorus Carbide

Studies of the incorporation of dopants into a-C samples have shown that it is possible to introduce stoichiometric amounts of another element into the a-C film. Most research in this area is toward the deposition of a crystalline form of carbon and nitrogen, β-C_3N_4, predicted to have a high sound velocity and a bulk modulus in excess of that of diamond [44]. Another binary carbon compound that has been gathering interest is *phosphorus carbide* [45]. Studies of the radio-frequency PECVD deposition of a-C:H films doped with P have shown that very high levels of P (atomic P/C ratio $\leq$3) can be incorporated [46].

1.4 Diamondoid Hydrocarbons

The term "diamond hydrocarbon" is used to describe hydrocarbon molecules that are totally or largely superimposable on the diamond lattice [47]. The lower limit of this definition is set at adamantane ($C_{10}H_{16}$) to prevent the inclusion of cyclohexane and other simple alkanes. The diamond hydrocarbon (or diamondoid) classification can be further split into two groups: (I) Diamondoids that are only partly superimposable on the diamond lattice, and (II) Diamondoids which are completely superimposable on the diamond lattice. The latter of these are known as polymantanes. The most fundamental series of polymantanes is formed by the face-fusing of adamantane units; starting with adamantane, then fusing two together to form diamantane, then fusing another adamantane to form triamantane, and so on *ad infinitum*.

The history of the polymantanes falls loosely into two categories, natural isolation and synthetic production. This introduction shall briefly review the most important discoveries of each, in chronological order.

1.4.1 The Discovery of the Lower Diamondoids

Tricylco[3.3.1.1^{3,7}]decane (using the systematic von Baeyer nomenclature, see section 1.4.2) was first isolated in 1933 [48], from a sample of petroleum collected near the village of Hodonín in Moravia. The name *adamantane*, derived from the Greek for diamond (*adamas*), was proposed on the basis of the unusual physical properties and X-ray structural analysis.

The first synthesis of adamantane was completed in 1941 by Prelog and Seiwerth [49], and consisted of many steps and produced only a low yield. Although this synthesis was improved over time [50], it was not till 1957, when Schleyer [51] published a single page communication describing the two-step synthesis from a commercially available precursor, that substantial amounts of adamantane could be produced.

The next polymantane in the series is pentacyclo[7.3.1.1^{2,1}.0^{2,7}.0^{4,11}]tetradecane, and was originally called *congressane* before becoming known by the more systematic name of diamantane. Diamantane was first produced in 1965 by Cupas *et al.* [52], although it was isolated from petroleum a year later [53].

It is at this point that synthetic chemistry leapt ahead of the natural product isolation with the production of heptacyclo[7.7.1.1^{3,15}.0^{1,12}.0^{2,7}.0^{4,13}.0^{4,11}]octadecane (triamantane) in 1966 [54], but the synthesis of progressive polymantanes became increasingly difficult. It was another ten years before one of the four tetramantanes was prepared. In 1976 Burns *et al.* [55] successfully synthesised *anti*-tetramantane, so called because of its structural similarity to butane in its *anti* conformation.

Further information on the history of the diamondoid molecules can be found in reference [56].

1.4.2 Systematic Nomenclature

The systematic von Baeyer nomenclature is excellent for the naming of small cyclic systems. Consider the systematic name for adamantane, that is tricylco[3.3.1.1^{3,7}]decane. Decane refers to the ten carbons in the molecule and tricyclo indicates the number of rings. The numbers in the parenthesis refer to the number of carbons in the different rings (or more specifically the length of each bridge across the largest ring).

It is clear that use of the von Baeyer system of nomenclature for large polycyclic compounds is cumbersome, and to overcome this, trivial names are adopted to identify polymantane isomers. This is acceptable to differentiate between the four tetramantanes (*anti*-, *iso*-, M and P *skew*-) but becomes unfeasible when studying the 10 different pentamantanes or the hundreds of different octamantanes. Clearly something more methodical is called for.

Foreseeing the requirement of a systematic way to classify these molecules, in 1978 Balaban and Schleyer developed such a system [47] using graph theory.

Without delving into the terminology of graph theory, the basis of this idea comes from the ability to fuse adamantane units on four separate faces to form polymantanes. Starting with adamantane, there are four different directions in which the molecule can grow, as represented in Figure 1.8. Fusing together two adamantane units produces diamantane, which can be symbolised by a single line between the centres of the two adamantane units. Thus diamantane has the prefix *[1]* representing the orientation of the added adamantane unit with respect to the first adamantane. The prefix *[1]* is chosen above the other three directions simply because it is the lowest. The addition of another adamantane unit to form triamantane cannot happen in the 1 direction, because that is already occupied. All sites for addition are equivalent so the prefix *[12]* is produced, represented by two lines connected at 109°. The first line represents the

formation of diamantane (the [1..] in the prefix), the second line describes the fusing of another adamantane unit to this to form triamantane (the [...2] in the prefix).

So far we have only produced prefixes for unique isomers, but the addition of another adamantane unit to triamantane can happen in four different ways.

First let us look at the case that would form *anti*-tetramantane. To produce this molecule, an adamantane unit is added to triamantane in the 1 orientation, i.e. the same direction as that which produced diamantane from adamantane. This produces the prefix [121] and thus *anti*-tetramantane becomes [121] tetramantane. If instead, we fuse an adamantane unit in either of the remaining orientations on the terminal adamantane, we produce either of the enantiomers of *skew*-tetramantane, or [123] tetramantane (again 3 is chosen because it is the lowest number).

To produce the final tetramantane, an adamantane unit is fused to the central unit in triamantane. This has caused a problem, since until now, what had always been a straight line connecting adamantane units, has become branched. If we imagine walking through this molecule, we start heading in the 1 direction and then the path splits into the 2 and 3 directions. A branching in the line is represented by a number in parenthesis in the prefix, so *iso*-tetramantane becomes [1(2)3] tetramantane.

Moving up to the pentamantanes, there are now many isomers which are easily recognisable by their respective prefix. A few examples are; [1212] pentamantane, formed by addition of an adamantane unit to the end of [121] tetramantane, [1234] pentamantane, formed by the addition of an adamantane unit to [123] tetramantane, and [1(2,3)4] pentamantane, a tetrahedral polymantane.

The above rules are too concise to allow the naming of an unknown polymantane, but should be detailed enough to allow the diagnosis of the correct molecular structure from a given prefix.

1.4.3 Higher Diamondoids in oil

By the mid-nineties, several polymantane structures had been discovered in petroleum by gas chromatography/mass spectrometry (GC-MS). First to be observed was triamantane in 1992 [57], tentatively followed by a whole selection of tetramantanes, pentamantanes and hexamantanes in 1995 [58]. Although it was now suggested that these larger polymantane structures existed in petroleum, they were far too low in concentration to be isolable.

This does not mean these trace concentrations were not useful. Dahl *et al.* [59] used the concentration of specific diamondoids to measure the extent of cracking (thermal breakdown of heavy hydrocarbons to smaller ones) and hence estimate the extent of oil destruction. During this study it was also observed that at certain sites, diamondoid

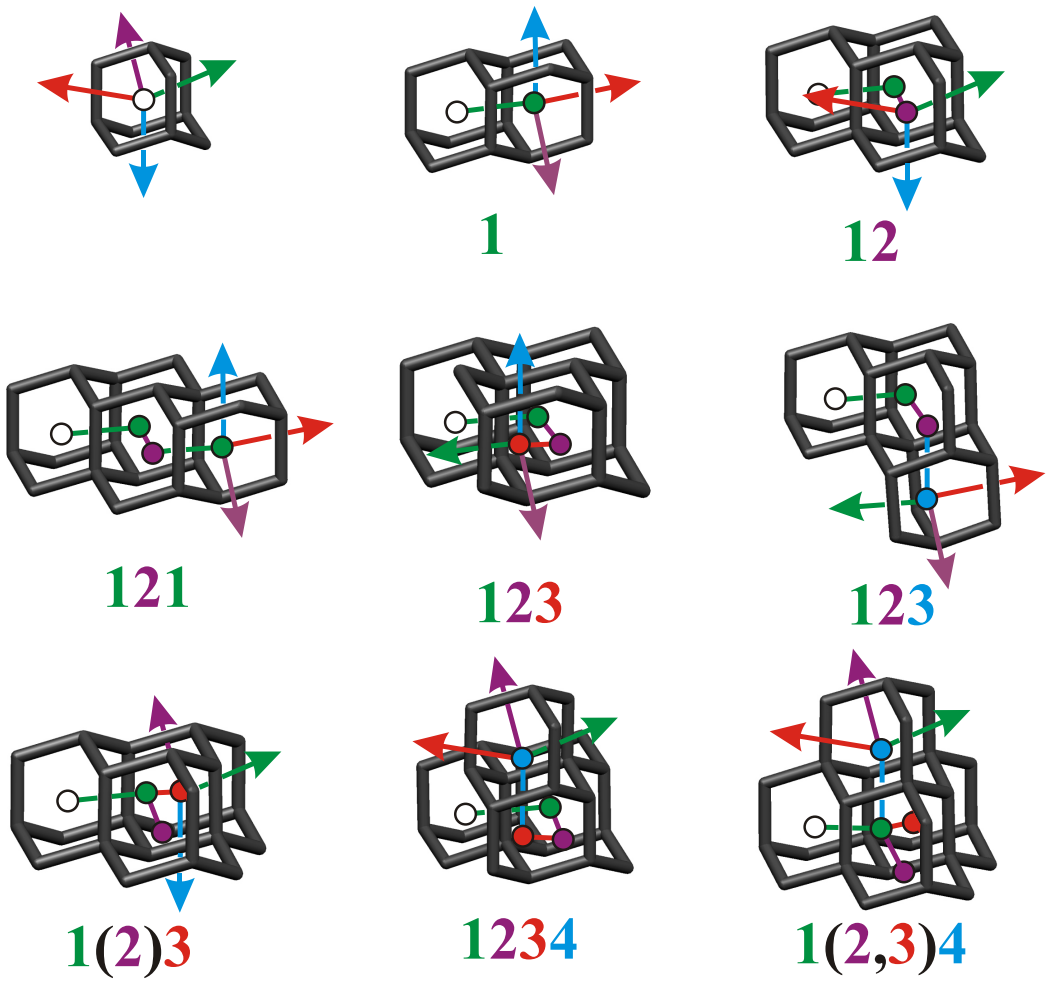

Figure 1.8: Diagram explaining the relationship between the nomenclature prefix and the structure of the diamondoid molecules.

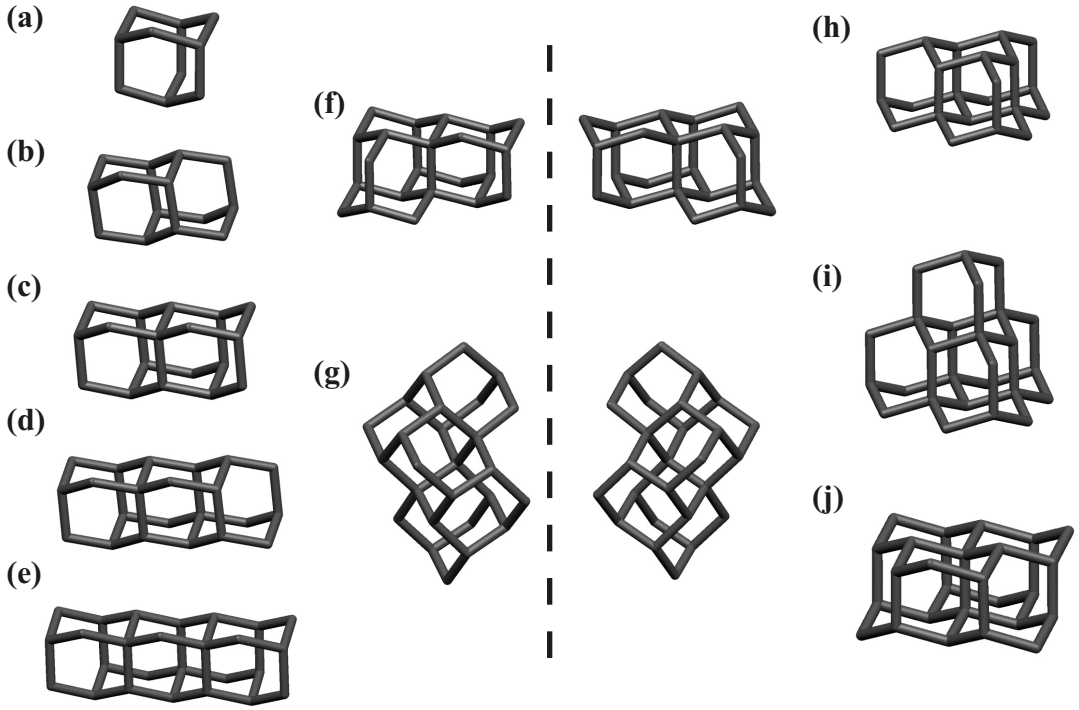

Figure 1.9: A selection of diamondoids, (a) adamantane, (b) diamantane, (c) triamantane, (d) [121] tetramantane, (e) [1212] pentamantane, (f) both enantiomers of [123] tetramantane, (g) both enantiomers of [1234] pentamantane, (h) [1(2)3] tetramantane, (i) [1(2,3)4] pentamantane and (j) [12312] hexamantane.

hydrocarbons can reach such high concentrations that they crystallize out during the production process, causing plugging problems in the wells [59].

It was eight years later that Dahl *et al.* [4] announced the isolation, from petroleum, of a selection of higher diamondoids (Figure 1.9) up to undecamantane. Using vacuum distillation and a combination of chromatographic techniques, in total they isolated and crystallized all four tetramantanes, nine pentamantanes, one hexamantane, two heptamantanes, two octamantanes, one nonamantane, one decamantane, and one undecamantane.

1.4.4 Diamondoids: Experiment and Theory

Soon after the isolation of the higher diamondoids, a small communication was produced by Dahl *et al.* [60], which contained experimental data obtained from the disc-shaped [12312] hexamantane ($C_{26}H_{30}$), shown in Figure 1.10. Various techniques were used in the analysis of this sample, including single crystal X-ray diffraction, mass spectrom-

etry, Raman spectroscopy and ^{1}H and ^{13}C NMR. The results from these experiments confirmed that the product isolated was indeed [12312] hexamantane.

So far, the only other published experimental data obtained from the higher diamondoids have been the gas-phase X-ray absorption spectra produced by Willey *et al.* [61]. These authors were interested in whether the predictions associated with quantum confinement (blue-shifting of the optical transitions with decreasing crystal size), continued to be valid down to the molecular limit. Studying diamondoid molecules as large as [12312] hexamantane, they found the X-ray absorption spectra of these structures to be closer to molecules like cyclohexane than to ideal nanodiamond crystals.

Many theoretical studies have calculated the properties of the diamondoid molecules. Eleven years before the isolation of the higher diamondoids, Shen *et al.* [62] used various methods to calculate the minimum energy geometries, total energies and heats of formation of a selection of high symmetry diamondoids. Their aim was to study the transition between small hydrocarbon molecules and nanometre-sized diamond crystal. They found that the largest cluster studied ($C_{35}H_{36}$) was still far from the infinite diamond lattice, but their results showed the merits and shortcomings of the different computational methods they used.

More recently, interest has shifted towards the properties of the molecules themselves, rather than how they relate to diamond. The possibility of using diamondoids as building blocks for nanostructures has been studied by McIntosh *et al.* [63]. They used density functional theory to calculate the equilibrium geometries and electronic densities of states for a selection of diamondoid molecules. Additionally, they considered the interaction of these molecules with themselves, functionalised molecules and carbon nanotubes. The molecules interact with each other only weakly, but the strength of the interaction could be increased by substitutionally doping the molecules with boron and nitrogen.

Since the diamondoids are effectively minute hydrogen-terminated diamonds, they are also expected to display the negative electron affinity seen for other hydrogen terminated diamond structures. The electron affinities of some higher diamondoids and nanometre-size diamond clusters were studied by Drummond *et al.* [64], using density functional and quantum Monte Carlo calculations. They predicted that the diamondoids should have a negative electron affinity and could be a simple and economical method of producing electron emitters.

The chemical, rather than physical, properties of the diamondoids have been studied by Fokin *et al.* [65]. They used density functional theory to calculate the properties of a group of diamondoid hydrocarbons and their respective radicals, cations, and radical cations. These results were then compared to the experimentally observed products of a large selection of C-H substitution reactions on diamantane. This study suggest

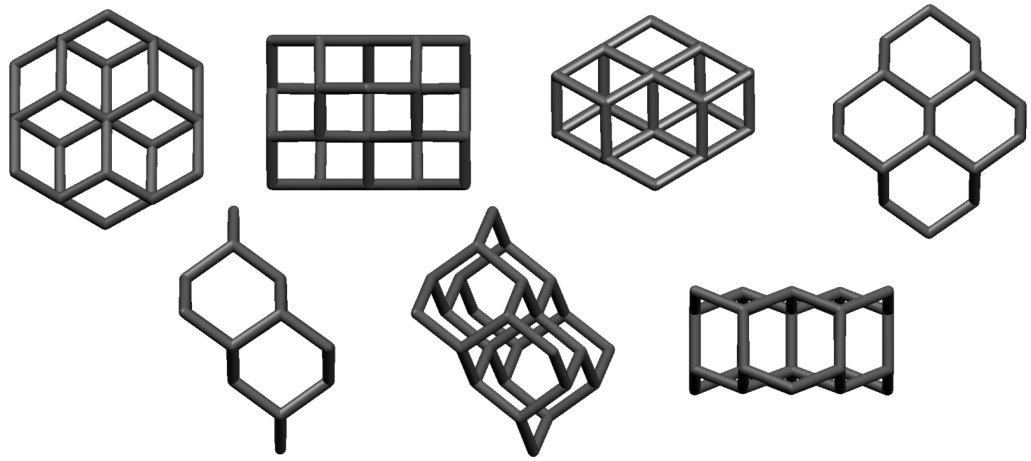

Figure 1.10: The diamondoid molecule [12312] hexamantane, shown from various different angles.

that the higher diamondoids are more reactive than adamantane and diamantane, but selective functionalisation of the higher diamondoid surfaces will be more challenging due to the large number of similarly reactive CH bonds.

1.5 Aims of this Study

As mentioned before, this thesis concentrates on three areas of carbon research; amorphous carbon, diamondoid hydrocarbons and nanocrystalline diamond. This section describes in more detail the aims of these three projects.

1.5.1 Incorporation of Sulfur into Amorphous Carbon

As described in sections 1.3.2 and 1.3.3, the incorporation of other elements into a-C films could be an important route to novel amorphous semiconductors. In the study radio-frequency PECVD was used to deposit sulfur containing a-C:H films (chapter 3).

The films were deposited from mixtures of methane and H_2S. The CH_4/H_2 ratio, DC bias (ion impact energy), and deposition pressure were varied systematically, allowing the effect these parameters had on the properties of the a-C:S:H films to be studied. Various analysis techniques were used to probe the properties of the samples. X-ray photoelectron spectroscopy and micro-combustion elemental analysis were used to determine the relative proportions of carbon, and sulfur (and hydrogen for micro-combustion). Secondary ion mass spectrometry was used to study the distribution of sulfur in the a-C:S:H films. The structure and bonding within the films were studied

by Raman spectroscopy, and the growth rate and optical properties were studied, by spectroscopic ellipsometry.

The properties of these a-C:S:H were then compared to a-C:N:H and a-C:N:S:H films, deposited with and without a background of Ar.

1.5.2 Raman Spectroscopy of Diamondoids

The new found availability of the higher diamondoid molecules has opened up the study of these structures to experimentalists as well as theorists. Before the molecules are functionalised or used in test devices, they must be characterised. One of the best techniques for characterising molecular structures, non-destructively and without the requirement of mulling agents or large amounts of material is Raman spectroscopy. A full description of the technique of Raman spectroscopy and its application to the study of diamondoids can be found in section 2.1.

The first aim of this study was to obtain Raman spectra for all the higher diamondoid molecules available (Figure 1.11). Secondly, density functional theory was used to calculate the equilibrium structures, vibrational frequencies and Raman intensities for each molecule. Finally, the variation in the Raman spectra with the size and symmetry of the diamondoids was studied, particularly focusing on any vibrations that were structurally diagnostic.

1.5.3 Raman Spectroscopy of Nano-Crystalline Diamond: An *Ab Initio* Approach

One of the problems with NCD is proving that the sample contains diamond crystallites and not just graphite/amorphous carbon. With microcrystalline diamond it is possible to see the diamond facets at the surface with an optical microscope, but the crystallites in NCD are far too small to be resolved in this manner. Common methods used to identify the presence of diamond nanocrystallites in a sample are powder X-ray diffraction and transmission electron microscopy. These techniques are time consuming and can require the destruction of the sample. What is required is a simple, fast, non-destructive method of detecting a nanocrystalline diamond phase. Raman spectroscopy (see section 2.1) is the method of choice for analysing the structure of carbon samples. It has not been shown conclusively that Raman spectroscopy can detect the nanocrystalline diamond phase. The aim of the final part of this study was to calculate the Raman spectra of small nanodiamonds, using *ab initio* theory (see section 2.1.2). These calculated spectra were then be compared to the experimental Raman spectra published in the literature (Chapter 5).

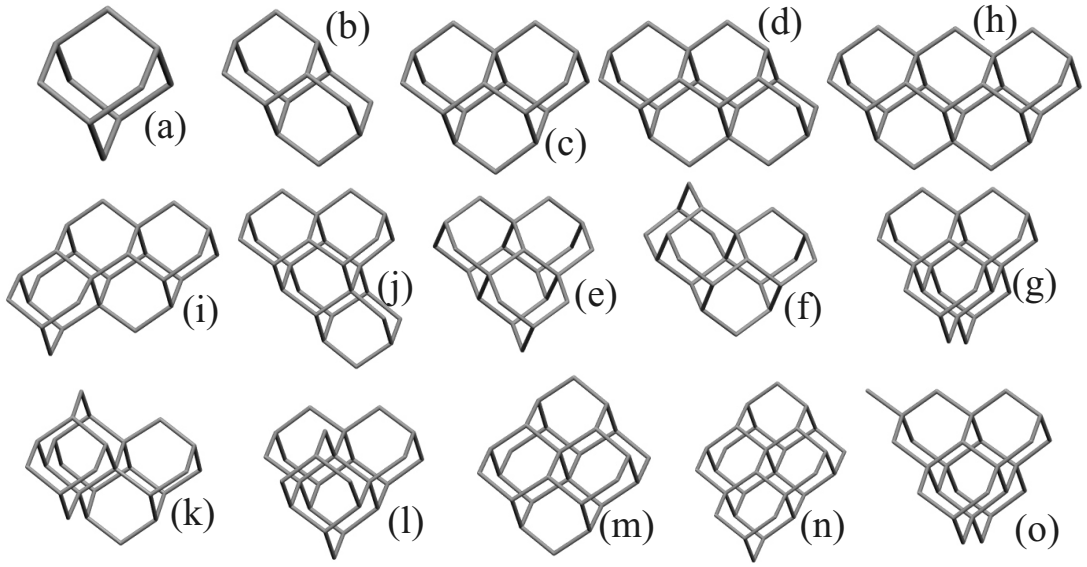

Figure 1.11: (a) adamantane $C_{10}H_{16}$, (b) diamantane $C_{14}H_{20}$, (c) Triamantane $C_{18}H_{24}$, (d) [121] tetramantane $C_{22}H_{28}$, (e) [1(2)3] tetramantane $C_{22}H_{28}$, (f) [123] tetramantane $C_{22}H_{28}$, (g) [1212] pentamantane $C_{26}H_{32}$, (h) [1(2,3)4] pentamantane $C_{26}H_{32}$, (i) [12(3)4] pentamantane $C_{26}H_{32}$, (j) [1213] pentamantane $C_{26}H_{32}$ C_1, (k) [1234] pentamantane $C_{26}H_{32}$ C_2, (l) [12(1)3] pentamantane $C_{26}H_{32}$ C_1, (m) [12312] hexamantane $C_{26}H_{30}$, (n) [121321] heptamantane $C_{30}H_{34}$, and (o) 3-methyl-[1(2,3)4] pentamantane $C_{27}H_{34}$

Bibliography

[1] F. Bundy, H. Hall, H. Strong, and R. Wentorf, *Nature*, 1955, **176**, 51.

[2] H. W. Kroto, J. R. Heath, S. C. O'Brien, R. F. Curl, and R. E. Smalley, *Nature*, 1985, **318**, 162.

[3] S. Iijima, *Nature*, 1991, **354**, 56.

[4] J. E. Dahl, S. G. Liu, and R. M. K. Carlson, *Science*, 2003, **299**, 96.

[5] S. Aisenberg and R. Chabot, *J. Appl. Phys.*, 1971, **42**, 2953.

[6] ed. S. Peters, *Handbook of Composites*, Chapman and Hall, London, 1988.

[7] ed. M. Nazare and A. Neves, *Properties, Growth and Applications of Diamond*, INSPEC, London, 2001.

[8] H. Pierson, *Handbook of Carbon, Graphite, Diamond and Fullerenes*, Noynes, New Jersey, 1993.

[9] ed. P. Walker and P. Thrower, *Chemistry and Physics of Carbon*, Marcel Dekker, New York, 1981.

[10] F. Bundy, *Physica A*, 1989, **156**, 169.

[11] J. Isberg, J. Hammersberg, E. Johansson, T. Wikstrom, D. J. Twitchen, A. J. Whitehead, S. E. Coe, and G. A. Scarsbrook, *Science*, 2002, **297**, 1670.

[12] R. Abbaschian, H. Zhu, and C. Clarke, *Diam. Relat. Mater.*, 2005, **14**, 1916.

[13] N. Greiner, D. Phillips, J. Johnson, and F. Volk, *Nature*, 1988, **333**, 440.

[14] J. B. Donnet, E. Fousson, T. K. Wang, M. Samirant, C. Baras, and M. P. Johnson, *Diam. Relat. Mater.*, 2000, **9**, 887.

[15] F. Huang, y. Tong, and S. Yun, *Phys. Solid. Stat.*, 2004, **46**, 616.

[16] J. Angus, H. Will, and W. Stanko, *J. Appl. Phys.*, 1968, **39**, 2915.

[17] P. K. Bachmann, D. Leers, and H. Lydtin, *Diam. Relat. Mater.*, 1991, **1**, 1.

[18] M. N. R. Ashfold, P. W. May, C. A. Rego, and N. M. Everitt, *Chem. Soc. Rev.*, 1994, **23**, 21.

[19] Y. Mokuno, A. Chayahara, Y. Soda, Y. Horino, and N. Fujimori, *Diam. Relat. Mater.*, 2005, **14**, 1743.

[20] D. M. Gruen, *Annu. Rev. Mater. Sci.*, 1999, **29**, 211.

[21] A. V. Gubarevich, S. Usuba, Y. Kakudate, A. Tanaka, and O. Odawara, *Jap. J. Appl. Phys.*, 2004, **43**, L920.

[22] F. J. Himpsel, J. A. Knapp, J. A. VanVechten, and D. E. Eastman, *Phys. Rev. B*, 1979, **20**, 624.

[23] M. J. Rutter and J. Robertson, *Phys. Rev. B*, 1998, **57**, 9241.

[24] D. He, L. Shao, W. Gong, E. Xie, K. Xu, and G. Chenc, *Diam. Relat. Mater.*, 2000, **9**, 1600.

[25] C. Faure, W. Hänni, C. J. Schmutz, and M. Gervanoni, *Diam. Relat. Mater.*, 1999, **8**, 830.

[26] A. Glaser, H. Jentsch, S. Rosiwal, A. Lüdtke, and R. Singer, *Mater. Sci. Eng. B*, 2006, **127**, 186.

[27] A. Kasugai, K. Sakamoto, K. Takahashi, M. Tsuneoka, T. Kariya, T. Imai, O. Braz, M. Thumm, J. R. Brandon, R. S. Sussman, A. Beale, and D. C. Ballington, *Rev. Sci. Instrum.*, 1998, **69**, 2160.

[28] T. Shibata, Y. Kitamoto, K. Unno, and E. Makino, *J. Microelectromech. Syst.*, 2000, **9**, 47.

[29] V. S. Veerasamy, H. A. Luten, R. H. Petrmichl, and S. V. Thomsen, *Thin Solid Films*, 2003, **442**, 1.

[30] J. Robertson, *Thin Solid Films*, 1999, **383**, 81.

[31] D. A. Czaplewski, J. P. Sullivan, T. A. Friedmann, D. W. Carr, B. E. N. Keeler, and J. R. Wendt, *J. Appl. Phys.*, 2005, **97**, 023517.

[32] J. Robertson, *Mater. Sci. Eng. R*, 2002, **37**, 129.

[33] J. Robertson, *Diam. Relat. Mater.*, 1994, **3**, 361.

[34] L. K. Cheah, X. Shi, E. Liu, B. K. Tay, J. R. Shi, and Z. Sun, *Philos. Mag. B*, 1999, **79**, 1647.

[35] A. Mainwood, *Phys. Stat. Sol. A*, 1999, **172**, 25.

[36] S. Koizumi, *Phys. Stat. Sol. A.*, 1999, **172**, 71.

[37] S. Sque, R. Jones, J. Goss, and P. Briddon, *Phys. Rev. Lett.*, 2004, **92**, 017402.

[38] N. Mott, *Adv. Phys.*, 1967, **16**, 49.

[39] A. Helmbold, P. Hammer, J.-U. Thiele, K. Rohwer, and D. Meissner, *Philos. Mag. B*, 1995, **72**, 335.

[40] B. Kleinsorge, A. Ilie, M. Chhowalla, W. Fukarek, W. I. Milne, and J. Robertson, *Diam. Relat. Mater.*, 1998, **7**, 472.

[41] M. AllonAlaluf and N. Croitoru, *Diam. Relat. Mater.*, 1997, **6**, 555.

[42] N. M. J. Conway, W. I. Milne, and J. Robertson, *Diam. Relat. Mater.*, 1998, **7**, 477.

[43] V. S. Veerasamy, G. A. J. Amaratunga, C. A. Davis, A. E. Timbs, W. I. Milne, and D. R. McKenzie, *J. Phys. Condens. Matter*, 1993, **5**, L169.

[44] A. Y. Liu and M. L. Cohen, *Phys. Rev. B.*, 1990, **41**, 10727.

[45] F. Claeyssens, G. M. Fuge, N. L. Allan, P. W. May, S. R. J. Pearce, and M. N. R. Ashfold, *Appl. Phys. A*, 2004, **79**, 1237.

[46] S. R. J. Pearce, P. W. May, R. K. Wild, K. R. Hallam, and P. J. Heard, *Diam. Relat. Mater.*, 2002, **11**, 1041.

[47] A. T. Balaban and P. V. R. Schleyer, *Tetrahedron*, (1978), **34**, 3599.

[48] S. Landa and V. Machacek, *Collect. Czech. Chem. Commun.*, 1933, **5**, 1.

[49] V. Prelog and R. Seiwerth, *Ber. Dtsch. Chem. Ges.*, 1941, **74**, 1644.

[50] H. Stetter, O.E.Bander, and W. Neumann, *Chem. Ber.*, 1956, **89**, 1922.

[51] P. von R. Schleyer, *J. Am. Chem. Soc.*, 1957, **79**, 3292.

[52] C. A. Cupas, P. von R. Schleyer, and D. J. Trecker, *J. Am. Chem. Soc.*, 1965, **87**, 917.

[53] S. Hala, S. Landa, and V. Hanus, *Angew. Chem. Internat. Edit.*, 1966, **5**, 1045.

[54] V. Z. Williams, P. von R. Schleyer, G. J. Gleicher, and L. B. Rodewald, *J. Am. Chem. Soc.*, 1966, **88**, 3862.

[55] W. Burns, T. Mitchell, M. McKervey, J. Rooney, G. Ferguson, and P. Roberts., *J. Chem. Soc. Chem. Commun.*, 1976, **21**, 893.

[56] P. von R. Schleyer, Wiley, New York, 1990; chapter My Thirty Years in Hydrocarbon Cages: From Adamantane to Dodecahedrane, pp. 1–38.

[57] W. Wingert, *Fuel*, 1992, **71**, 37.

[58] R. Lin and Z. A. Wilk, *Fuel*, 1995, **74**, 1512.

[59] J. E. Dahl, J. M. Moldowan, K. E. Peters, G. E. Claypool, M. A. Rooney, G. E. Michael, M. R. Mello, and M. L. Kohnen, *Nature*, 1999, **399**, 54.

[60] J. E. P. Dahl, J. M. Moldowan, T. M. Peakman, J. C. Clardy, E. Lobkovsky, M. M. Olmstead, P. W. May, T. J. Davis, J. W. Steeds, K. E. Peters, A. Pepper, A. Ekuan, and R. M. K. Carlson, *Angew. Chem. Int. Ed.*, 2003, **42**, 2040.

[61] T. M. Willey, C. Bostedt, T. van Buuren, J. E. Dahl, S. G. Liu, R. M. K. Carlson, L. J. Terminello, and T. Moller, *Phys. Rev. Lett.*, 2005, **95**, 113401.

[62] M. Z. Shen, H. F. Schaefer, C. X. Liang, J. H. Lii, N. L. Allinger, and P. V. Schleyer, *J. Am. Chem. Soc.*, 1992, **114**, 497.

[63] G. C. McIntosh, M. Yoon, S. Berber, and D. Tománek, *Phys. Rev. B*, (2004), **70**, 045401.

[64] N. D. Drummond, A. J. Williamson, R. J. Needs, and G. Galli, *Phys. Rev. Lett.*, 2005, **95**, 096801.

[65] A. A. Fokin, B. A. Tkachenko, P. A. Gunchenko, D. V. Gusev, and P. R. Schreiner, *Chem. Eur. J.*, 2005, **11**, 7091.

Chapter 2

Experimental and Theoretical Techniques

This chapter contains detailed descriptions of all the experimental techniques employed in this study.

2.1 Raman Spectroscopy

In these studies, the most widely used analysis technique is Raman spectroscopy. The Raman effect describes the inelastic scattering of photons by a substance. This effect is observed as a shift in the frequency of the scattered light relative to the excitation frequency. The magnitude of the shift is dependent on the vibrational energy levels of the substance, whereas the intensity of the shifted light is dependent on the magnitude of the change in polarisability associated with the vibration. The Raman effect was predicted by Smekal in 1923 [1], and later observed experimentally by Raman and Krishnan in 1928 [2].

Before the data produced by Raman spectroscopy can be interpreted, the theory behind the scattering processes and the vibrational energy levels must be understood. For further information on the subjects covered in this section, see references [3–5].

2.1.1 The Theory of Raman Spectroscopy

When light interacts with a molecule, the light distorts the electron cloud around the nuclei to form a short lived 'virtual state'. This virtual state has a perturbed electron arrangement but does not result in a large nuclear displacement. This system is unstable and light is immediately released as scattered radiation. The degree of distortion of the electron cloud is proportional to the energy transfered to the system. The energy E of an electromagnetic photon is described by the equation $E = h\nu$, where ν is the

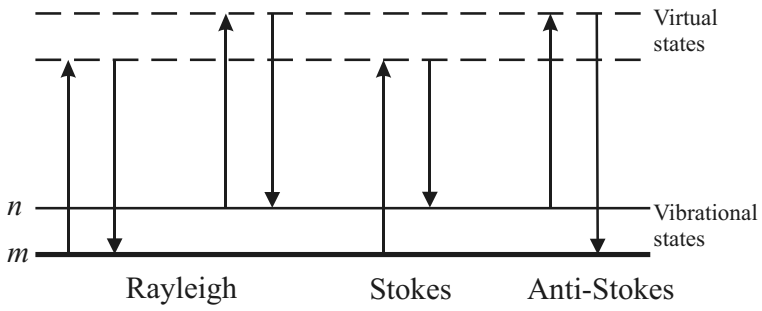

Figure 2.1: Scattering transitions: Rayleigh scattering - no difference in energy between incident and scattered radiation, Stokes scattering - scattered radiation has lower energy than the incident radiation, anti-Stokes scattering - scattered radiation has higher energy than the incident radiation.

frequency of the radiation and h is Planck's constant. This shows that the higher the frequency of the radiation, the higher the photon energy. A higher energy photon transfers more energy to the virtual state and hence has a higher scattering efficiency. An every day example of this is the sky appearing blue due to the higher scattering efficiency of blue light.

On interaction with a molecule, light may be scattered in two different ways; elastically or inelastically.

In elastic scattering, commonly called Rayleigh scattering, the interaction is purely between the light and electron cloud. No nuclear motion is involved. This is the dominant process, and the intensity of Rayleigh-scattered light is approximately 1/1000th of the excitation intensity.

In inelastic or Raman scattering, some nuclear motion is induced or lost during the scattering process. Since energy must be conserved, the energy change in the molecule during this process results in an equal and opposite energy change in the photon. If energy is lost to the molecule, the energy of the photon is decreased and is said to be 'Stokes scattered'. If the light interacts with a molecule which is already in a vibrationally excited state, energy can be lost from the molecule to the photon. This process is called 'anti-Stokes scattering'. The transitions involved in Rayleigh, Stokes and anti-Stokes scattering are shown in Figure 2.1.

Vibrations of molecules

When there is no change in the electronic energy, the energy of a molecule may be divided into different degrees of freedom. A molecule with N atoms has $3N$ degrees of freedom. Three of these degrees of freedom are used to describe the translation of

the molecule in 3-dimensional space. For non-linear molecules, three are taken up by rotation, whereas only two are used for rotation of a linear molecule. The remaining degrees of freedom describe the vibrations of a molecule and hence are equal to the number of normal modes of vibration. For a non-linear molecule the number of normal modes is $3N - 6$ and, for a linear molecule $3N - 5$.

The vibrational motion arises from the restorative force of the electronic and nuclear interaction. At small displacements, the potential energy can be approximated as being parabolic. This is called the harmonic approximation, because the parabolic potential leads to harmonic oscillations. At higher vibrational energies, the harmonic approximation breaks down; the parabolic approximation cannot be correct at large extension because it does not allow for dissociation. A better approximation is the Morse potential which allows for dissociation at large extension.

Raman spectroscopy and the complementary technique of infra-red (IR) absorption spectroscopy can be used to probe the vibrational structure of a molecule. IR absorption is not heavily used in this study, but a brief introduction is given as a useful comparison with Raman spectroscopy.

IR absorption spectroscopy is a complementary technique to Raman spectroscopy because the vibrational modes excited by Raman scattering are sometimes the same modes that absorb in the IR. Raman spectroscopy uses a single monochromatic light source and measures the change in frequency of the scattered light. IR absorption spectroscopy measures the change in intensity as IR light is scanned though a sample. A simple question arises, "why use both techniques if they both measure the same thing?". It is true that both techniques measure the vibrational frequencies of a sample but they do so by different mechanisms, each with different associated selection rules. For a molecule to absorb a photon of IR radiation, it must have a vibrational mode at the same frequency as the photon, and that vibration must induce a change in the dipole moment of the molecule. If there is no change in dipole moment with the nuclear motion of the vibration, there is no absorption. In Raman spectroscopy, to produce a change in frequency of the scattered light, the vibrational mode must induce a change in the polarisability of the molecule. Again, if there is no change in polarisability the vibration is not observed in the Raman spectrum. As well as these fundamental aspects, there are different selection rules that affect the IR absorption and Raman spectra differently. These selection rules depend on the symmetry of the molecule, therefore before these contemplating these rules, let us must briefly study group theory.

Molecular Symmetry

The arrangement of nuclei in a molecule can be described by 'symmetry elements' such as rotation axes and mirror planes. These symmetry elements describe symmetry

T_{d}	E	$8C_3$	$3C_2$	$6\sigma_d$	$6S_4$	$h = 24$
A_1	1	1	1	1	1	$x^2 + y^2 + z^2$
A_2	1	1	1	-1	-1	
E	2	-1	2	0	0	$(3z^2 - r^2, x^2 - y^2)$
T_1	3	0	-1	-1	1	(R_x, R_y, R_z)
T_2	3	0	-1	1	-1	(x, y, z), (xy, xz, yz)

Table 2.1: T_{d} character table

operations such as rotation, reflection, inversion, etc. Performance of a particular set of these symmetry operations leaves the molecule indistinguishable from the original nuclear arrangement. This set of symmetry operations is described by the point group of the molecule.

The clearest way to explain the symmetry elements, and their effect on the Raman and IR spectra, without delving too deeply into group theory, is with examples.

For example let us take methane, a tetrahedral arrangement of hydrogen atoms around a central carbon (Figure 2.2). The highest symmetry axes of the tetrahedral structure of methane are the C_3 rotational axes which lie down each CH bond (Figure 2.2 (b)). Halfway between the CH bonds, through the centre of the carbon atom, there are also C_2 rotational axes (Figure 2.2 (c)). These C_2 axes are also S_4 axes. An S operation is an improper rotation, that is, a rotation followed by a reflection in the plane perpendicular to the rotational axis. The presence of all these symmetry operations indicates that methane belongs to the T_{d} point group.

Table 2.1 is the character table for the T_{d} point group. The title row of the table contains the point group label, the type of symmetry operations and the order of the group (the total number of symmetry operations). The title column in the character table contains a label called a symmetry species. These symmetry species label the irreducible representations of the point group. The letters A and B are used for singly-degenerate symmetry species, E is used for doubly-degenerate species and T is used for triply-degenerate species.

The symmetry of each vibrational mode of a molecule can be described by a single irreducible representation. Knowledge of the symmetry of a vibration is important in determining whether it is likely to appear in the IR absorption spectrum, Raman spectrum, both, or not at all. Methane is a non-linear molecule and hence has 9 $(3 \times 5) - 6)$ vibrational modes. Let us now determine the symmetry of these modes.

To determine the symmetry of the vibrations in methane let us treat the co-ordinates as a basis and determine the irreducible representations they span by observing how they transform into one another when performing the symmetry operations of the molecular point group (Figure 2.3). If the direction of the displacement remains unchanged

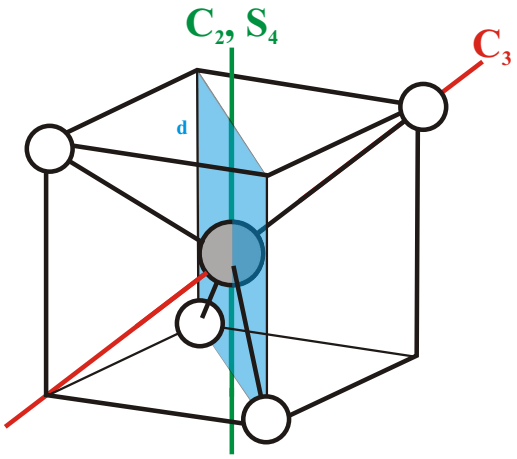

Figure 2.2: Structure of methane (grey circle - carbon, white circle - hydrogen) and its associated symmetry elements. The red line represents a C_3 rotational axis, green line represents a C_2 and S_4 rotation and improper rotation axes, respectively. The light blue plane is a dihedral mirror plane.

with the symmetry operation it is given a value of 1. If the direction of the displacement is reversed, it returns -1. If the atom being displaced is moved out of its position by the symmetry operation it returns a value of 0.

The first symmetry operation is the identity E. This is the null operation. Under this operation all 15 displacements remain unchanged, so our value for E is 15. The C_3 operation moves all the displacements so makes no contribution to the character (a value of 0). Under C_2 rotation, all the hydrogen displacements are moved so also contribute nothing. The displacements on the carbon in the x and y direction become negative with respect to their previous positions, giving us -2. The displacement of the carbon along the z axis remains unchanged, contributing 1, leaving us with -1. With improper rotation, the z displacement on the carbon atom is reversed and all others are changed, giving -1. By reflection, 3 displacements are reversed, 6 remain unchanged, and the rest are moved from their positions, producing a character of 3. The reducible representation that has been determined (15,0,1,-1,-1,3) spans the irreducible representations A_1 + E + T_1 + $3T_2$. These symmetry species represent the translational, rotational and vibrational motions of the molecule. The final column in the character table shows that translational (x, y, z) motion spans T_2, and the rotational motion (R_x, R_y, R_z) spans T_1. Subtracting these from our previous selection leaves us with A_1 + E + $2T_2$. These are the nine vibration modes of methane, two-triply degenerate sets, one-doubly degenerate and one-singly degenerate (Figure 2.4).

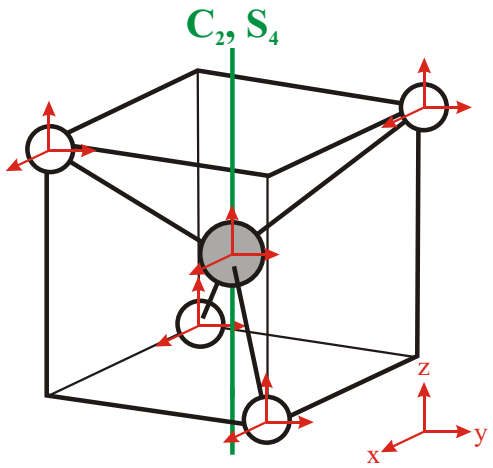

Figure 2.3: Structure of methane, the grey circle represents carbon, the white circle, hydrogen. The red axes represent the three degrees of freedom of each atom.

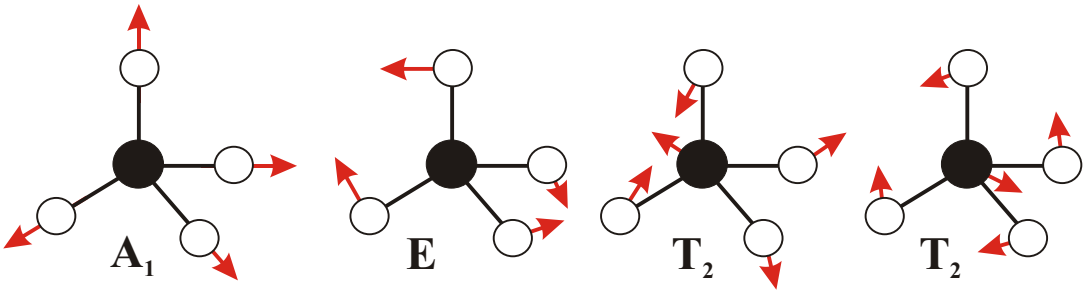

Figure 2.4: Normal modes of vibration of the methane molecule.

Selection Rules

Consider the transition between the ground state ($v = 0$) and the vibrationally excited state $v = 1$. The intensity of the Raman transition depends on the value of the following integral;

$$\int \psi_1^* \alpha \psi_0 \, \mathrm{d}Q \tag{2.1}$$

where ψ_0 and ψ_1 are vibrational wavefunctions of the ground and excited states respectively, and α, the molecular polarisability, is regarded as a function only of the nuclear vibrational co-ordinate Q. The wavefunctions ψ_0 and ψ_1, functions of Q, belong to symmetry species of the molecular point group. The ground state wavefunction ψ_0 always belongs to the totally symmetric A_1 species. The vibrationally excited wavefunction ψ_1 has the same symmetry species as the vibration itself (it is assumed the vibration is a simple harmonic). The polarisability transforms in the same way as the quadratic forms (x^2, xy etc) displayed in the final column of the character table. For the fundamental transition to be Raman active, the value of the integral must not be zero. The integral is only non-zero when the symmetry species of the vibrational mode is the same as the symmetry species of the polarisability. In our example of methane, for a fundamental vibration to be Raman active it must be of either T_2, E or A_1 symmetry.

For the IR transitions, the integral depends on the dipole moment instead of the polarisability;

$$\int \psi_1^* \mu \psi_0 \, \mathrm{d}Q \tag{2.2}$$

where μ is the permanent dipole moment. The dipole moment transforms as the translations (x, y, z), so by the same arguments as above, only the T_2 vibrations are active in the IR spectrum of methane. Notice that the T_1 symmetry modes are inactive in both spectra.

The conclusions of the above section suggest that there should be four signals in the Raman spectrum of methane, and two in the IR spectrum. However, just because the modes are allowed by symmetry does not mean they will appear in each spectrum. If the magnitude of the dipole moment or polarisability change of a mode is not large enough, the mode may not appear in either the IR or Raman spectrum.

The final rule does not apply for methane, since it is only relevant for molecules with an inversion centre. If the operation of inversion is present in a point group, all the symmetry species associated with that group are denoted either *gerade* or *ungerade*,

referred to as the *parity*. These are the German words for *even* and *odd* respectively, and are used to describe how molecular properties behave under inversion.

The components of the dipole moment have odd parity, where as the components of the polarisability have even parity. Because the final state cannot have both even and odd parity under inversion, the integral cannot be non-zero for both types of transition. This means that for a molecule with a centre of inversion, a vibrational mode cannot be both IR and Raman active. This is called the *mutual exclusion rule*.

Vibrations of Solids

If the structure under investigation is no longer a single molecule, but an infinite array of atoms, there is an additional selection rule to consider. Before this selection rule is introduced, let us first define some of the terminology used to describe vibrations in the solid state. Further reading on this topic can be found in the following references [6–10].

The fundamental quanta of lattice vibrations are called *phonons*, by analogy with the quanta of electromagnetic radiation. The are two types of phonon: *Acoustic modes*, in which all atoms in the unit cell move in phase and *Optic modes*, in which some atoms in the unit cell move out of phase with the others. The displacements of the nuclei can either be parallel (longitudinal) or perpendicular (transverse) to the direction of the propagation of the wave. Each phonon is described by a wavevector $\mathbf{k}$. All possible wavevectors describing lattice motion lie between $\mid \mathbf{k} \mid = 0$ and $\mid \mathbf{k} \mid = \pi/a$, that is, within the first Brillouin zone (the Brillouin zone is the Wigner-Seitz unit cell but for the reciprocal lattice). A phonon of wavevector $\mathbf{k}$ will interact with particles such as phonons and electrons as if it has a momentum $\hbar\mathbf{k}$.

In the Raman process, both energy and momentum are conserved;

$$\nu_i = \nu_s \pm \nu_{ph} \tag{2.3}$$

$$\mathbf{k}_i = \mathbf{k}_s \pm \mathbf{k}_{ph} \tag{2.4}$$

where subscript i, s and ph refer to the incoming photons, the scattered photons and the phonon respectively and the $\pm$ sign refers to Stokes and anti-Stokes scattering. $\mathbf{k}_i$ and $\mathbf{k}_s$ are much smaller than the wavevector at the Brillouin zone boundary, hence $\mathbf{k}_{ph}$ is also very small. This is the foundation of the final selection rule that needs to be covered. This rule states that first-order Raman scattering only excites optical phonons at the centre point of the Brillouin zone, $\mathbf{k}_{ph} \simeq 0$.

2.1.2 Calculating Vibrational Frequencies and Raman Intensities

The most fundamental, and yet difficult, aspect of Raman spectroscopy is the assignment of signals that appear in the spectrum. The importance of this aspect depends on the application, however. If Raman spectroscopy is employed as a routine means of testing for identical substances, such as in quality control or synthesis of a natural product, or to look for differences, eg. compound decomposition over time or change in molecular structure with phase change, a simple fingerprinting method may be used.

Characteristic frequency tables [11] can be used to assign vibrations of specific functional groups to peaks in the spectra, and hence to identify molecular structures, but these procedures can be time consuming and inaccurate. This method also only works if the structure of the molecule of interest is similar to that of previously characterised molecules.

If the molecule of interest is significantly different to previously studied structures, the use of frequency tables can become challenging, especially if the molecule is large and has low symmetry. For difficult cases, or circumstances that require a high level of accuracy, the vibrational frequencies can be calculated using molecular modelling software. For very large systems or cases where information about the Raman intensity is not important, molecular mechanics force fields and semiempirical electronic structure methods may be used. If the value of the Raman intensity for each vibrational mode is required, *ab initio* and density functional electronic structure methods must be used.

The following section describes some of the theory behind these methods, with particular emphasis on the calculation of the vibrational modes and Raman intensities. Further reading for the following section can be found in the references [12–16].

Wavefunctions and The Schrödinger Equation

In quantum mechanics, the wave-particle duality of matter describes how rather than travelling along a definite trajectory, a particle is distributed though space like a wave. This wave is described by a wavefunction ψ which contains all the dynamical information about the system. The wavefunction is a time and co-ordinate dependent function.

Although the wavefunction is an abstract concept, the square of the modulus of the wavefunction $|\psi|^2$ ($= \psi^*\psi$, if ψ is complex) has physical meaning. In one dimension, if the wavefunction of a particle has the value Ψ at some point x, the probability of finding the particle between x and $x + \mathrm{d}x$ is proportional to $|\Psi|^2\mathrm{d}x$. If, instead of obtaining relative probabilities, absolute values of the probability are required, the wavefunction can be scaled such that the integral of the wavefunction over all accessible space will be equal to 1;

$$\int \psi^* \psi \mathrm{d}x = 1 \tag{2.5}$$

In this case the wavefunction is said to be normalised.

The relationship between the wavefunction and energy of a system is given by the Schrödinger equation. The time-independent Schrödinger equation for a particle of mass m moving in one dimension is;

$$-\frac{\hbar}{2m}\frac{\mathrm{d}^2\psi}{\mathrm{d}x^2} + V(x)\psi = E\psi \tag{2.6}$$

where E is the energy of the system, $V(x)$ is the potential energy of the particle at the point x and $\hbar$ equals $h/2\pi$. This equation can be written in the form of an eigenvalue equation;

$$\hat{H}\psi = E\psi \tag{2.7}$$

where E is the eigenvalue, ψ is the eigenfunction, $\hat{H}$ is the Hamiltonian operator, which for a single particle travelling in one dimension equals;

$$\hat{H} = -\frac{\hbar}{2m}\frac{\mathrm{d}^2\psi}{\mathrm{d}x^2} + V(x) \tag{2.8}$$

The Hamiltonian is the operator yielding the eigenvalue E, the energy of a system with eigenfunction ψ. Any physical observable can be represented by an operator of which ψ is the eigenfunction and the eigenvalues are the allowed values of the observable.

Of course, the problems under consideration here do not deal with single particles, molecules consist of many particles interacting with each other. So what does the Schrödinger equation look like for these many body problems?

For a system containing a number of nuclei and electrons, the Hamiltonian can be described in terms of the electron kinetic energy, the nuclear kinetic energy, electron-nuclear attraction and the electron-electron and nuclear-nuclear repulsion;

$$\hat{H} = \sum_{i=1}^{n}\frac{-\nabla_i^2}{2} + \sum_{A=1}^{N}\frac{-\nabla_A^2}{2M_A} + \sum_{i,A}^{n,N}\frac{-Z_A}{r_{iA}} + \sum_{i,j>i}^{n}\frac{1}{r_{ij}} + \sum_{A,B>A}^{N}\frac{Z_A Z_B}{R_{AB}} \tag{2.9}$$

where M_A is the ratio of the mass of nucleus A to the mass of an electron, Z_A is the atomic number of nucleus A, r_{ij} is the separation between the ith and jth electron, R_{AB} is the separation between the Ath and Bth electron, r_{iA} is the separation between the ith electron and the Ath electron and the Laplacian operators ∇_i^2 and ∇_A^2 involve differentiation with respect to the co-ordinates of the ith electron and Ath nucleus, respectively.

The Born-Oppenheimer Approximation

Equation 2.9 is large and somewhat unwieldy, but fortunately some approximations can be made to simplify it. One of these is the Born-Oppenheimer approximation. The assumption this makes is that nuclei are far heavier than electrons and hence the motion of nuclei is slow relative to that of electrons. This allows a molecule to be approximated by stationary nuclei, with the electrons moving in the field of the fixed nuclei. Returning now to the Schrödinger equation, it is possible to completely neglect the nuclear kinetic energy term, and to consider the nuclear-nuclear repulsion term as a constant. This leaves us with the electronic Hamiltonian;

$$\hat{H}_{elec} = \sum_{i=1}^{n} \frac{-\nabla_i^2}{2} + \sum_{i,A}^{n,N} \frac{-Z_A}{r_{iA}} + \sum_{i,j>i}^{n} \frac{1}{r_{ij}} \tag{2.10}$$

No constant is required for the nuclear-nuclear repulsion term, as any constant added to an operator only adds to the eigenvalues and has no effect on the eigenfunctions. The solution of the Schrödinger equation involving the electronic Hamiltonian is the electronic wavefunction ψ_{elec}. The electronic wavefunction explicitly depends on the electronic co-ordinates but only parametrically on the nuclear co-ordinates. For each different set of nuclear co-ordinates ψ_{elec} is a different function of the electronic co-ordinates. To determine the total energy for a fixed set of nuclei the nuclear repulsion must also be included;

$$E_{tot}(R_A) = E_{elec} + \sum_{A,B>A}^{N} \frac{Z_A Z_B}{R_{AB}} \tag{2.11}$$

To determine the total energy of the molecule, including electronic, vibrational, rotational and translational energies, the Schrödinger equation must be solved for the energy of the nuclear motion. For this the electronic co-ordinates are replaced by their values, averaged over the electronic wavefunction. The Hamiltonian for the nuclear motion in an averaged field of electrons is;

$$\hat{H}_{nuc} = \sum_{A=1}^{N} \frac{-\nabla_A^2}{2M_A} + E_{tot}(R_A) \tag{2.12}$$

This is the operator for the nuclear Schrödinger equation;

$$\hat{H}_{nuc}\psi_{nuc} = E\psi_{nuc} \tag{2.13}$$

where ψ_{nuc} is the nuclear wavefunction and E is the Born-Oppenheimer approximation to the total energy.

Molecular Orbital Theory

Even with the Born-Oppenheimer approximation, exact solution of the electronic Schrödinger equation is impossible, except for single-electron systems like H, He^+ and H_2^+. The characteristics of hydrogenic wavefunctions can be found by solving the Schrödinger equation for a single electron moving about a nucleus. To solve the Schrödinger equation for a many electron system, a way of approximating the many electron wavefunction must be found.

The first assumption made is that the many electron wavefunction can be expressed as a product of many single electron wavefunctions, or *orbitals*. To completely describe the electron two concepts must be included; (a) electrons have a spin of $\pm$ 1/2 and (b) electrons are indistinguishable. The outcome of these two statements requires that the electronic wavefunction be antisymmetric with respect to the interchange of the co-ordinate of any two electrons;

$$\psi(x_1, x_2) = \frac{1}{\sqrt{2}}\{\chi_1(x_1) \times \chi_2(x_2) - \chi_1(x_2) \times \chi_2(x_1)\} \tag{2.14}$$

where $\psi(x_1, x_2)$ is the antisymmetrised two-electron wavefunction, χ_1 and χ_2 are spin orbitals and $1/\sqrt{2}$ is a normalisation factor. The wavefunction needs to be antisymmetrised with respect to the exchange of every pair of electrons. This leads to a larger number of terms for many-electron systems. Fortunately, the determinant of a matrix of spin orbitals and electrons is equivalent to our antisymmetric wavefunction;

$$\begin{vmatrix} \chi_1(x_1) & \chi_2(x_1) \\ \chi_1(x_2) & \chi_2(x_2) \end{vmatrix} = \{\chi_1(x_1) \times \chi_2(x_2) - \chi_1(x_2) \times \chi_2(x_1)\} \tag{2.15}$$

If two rows of the matrix are switched, the sign of the determinant changes, which satisfies the Pauli principle. If two rows are the same, two electrons occupy the same spin orbital, the wavefunction is meaningless and the determinant equals zero.

To construct the molecular wavefunction the linear combination of atomic orbitals (LCAO) approximation is used. This supposes that molecular orbitals can be constructed from linear superpositions of atomic orbitals centred on individual atoms,

$$\phi_i = \sum_a C_{ia}\chi_a \tag{2.16}$$

where ϕ_i is the molecular orbital, χ_a represents the atomic orbitals and C_{ia} is a set of coefficients weighting the contributions of the atomic orbitals to the molecular orbitals.

The atomic orbitals used in these constructions are based on hydrogen-like like atomic orbitals but with modified radial functions. These are called Slater-type orbitals (STOs). Slater-type orbitals are not easy to treat computationally and are generally replaced by orbitals based on Gaussian functions (GTOs). Unlike Slater functions the Gaussian functions do not exhibit a cusp at the origin, and they also decay toward zero more quickly. Instead of replacing a Slater-type orbital with a single Gaussian function, a linear combination of Gaussian functions is used. An assembly of orbital functions is called a *basis set*.

Basis sets exist in a variety of different sizes. Short-hand notation schemes are used to describe the number of contracted basis functions used for each orbital, and the number of primitive Gaussian functions used for each contrated basis function. A minimal basis set only contains the number of functions required to accommodate the filled orbital in each atom. The basis set STO-3G is a minimal basis set in which both core and valence orbitals are constructed from a single contracted function made from 3 primative gaussians. Better results can be obtained if more than one contracted function is used per orbital. Larger basis sets use a single contracted function to describe the core electrons and several contracted functions for the valence electrons. The basis set 6-31G uses six primitive Gaussian functions to create the contracted function for each core orbital, and four Gaussians to create two contracted function for each the valence orbitals. One contracted part of each valence orbtial is described by three Gaussians, the other by a single Gaussian function.

For an example, let us consider hydrogen and carbon, and the 6-31G basis set. Hydrogen has no core electrons, so the 1s orbital consists of two basis functions, the first made of three primitive Gaussians, the second made of a single primitive Gaussian. For carbon there is a single 1s basis function (6 primitive Gaussians), two 2s (3 and 1

primitive Gaussians) 3×2 2p functions (3 and 1 primitive Gaussians for the p_x, p_y and p_z) giving a total of 9 basis functions made from 22 primitive Gaussians.

Basis sets can be augmented by the addition of diffuse and polarisation functions. The addition of diffuse functions improves the description of the electron density far from the nucleus. This is important when considering anions or molecules with lone pairs. The presence of diffuse functions is denoted by the addition of a "+" to the basis set notation (6-31+G). Polarisation functions are used to aid the description of the distortion of the electron cloud during bonding. The addition of polarisation functions is indicated by "*" or "(d)" at the end of the basis set notation (6-31G* or 6-31(d)).

The Variation Principle

Once an approximate wavefunction is determined, it needs to be made as close as possible to the actual wavefunction. The method used to achieve this aim is the variation principle. The variation principle allows an upper limit for a system's ground state energy to be calculated. It states that if an arbitrary wavefunction is used to calculate the energy, the value calculated is never less than the true energy;

$$\int \phi^* \hat{H} \phi \, \mathrm{d}\tau \geq E \tag{2.17}$$

The variation principle allows us to determine the best values for the c_{ij} coefficients that define the molecular orbitals ψ in terms of the atomic orbitals ϕ. Doing this is the basis of the Hartree-Fock (HF) electronic structure theory.

Hartree-Fock Theory

The majority of the calculations performed in chapter 5 are performed using HF theory. In this theory, the spin-orbitals of a Slater determinant wavefunction are optimised using a self-consistent method of minimising the energy.

The electronic Hamiltonian can be written as a sum of one- and two-electron terms;

$$\hat{H}_{elec} = \sum_{i=1}^{n} h_i + \sum_{i,j>i}^{n} \frac{1}{r_{ij}} \tag{2.18}$$

where h_i is the one electron Hamiltonian containing the terms for the electron kinetic energy and nuclear-electronic Coulombic attraction.

The energy of the Slater determinant wavefunction can be calculated with the following equation;

$$E_{SD} = \int \psi_{SD} \hat{H}_{elec} \psi_{SD} \, \mathrm{d}\tau \tag{2.19}$$

The first term of the electronic hamiltonian is the sum of the one electron energies of each orbital, and is equal to the sum of the electron kinetic energy T_e and the nuclear-electron Coulombic attraction potential energy, V_{Ne}. The second term (the potential due to electron-electron repulsion V_{ee}) is the difference between two terms; the Coulomb and Exchange intergrals. The Coulomb intergrals give the energies of the Coulombic attraction between the electrons, the Exchange intergrals "correct" the Coulomb intergrals to take into account the antisymmetry of the wavefunction.

These terms give us the equation for the electronic energy of a system described by Slater determinant wavefunctions, expressed by various potential and kinetic energy terms;

$$E_{SD} = V_{NN} + T_e + V_{Ne} + V_{ee} \tag{2.20}$$

Once the energy of the Slater determinant wavefunction has been determined, the coefficients c_{ij} can be varied in a self-consistent iterative manner until the change in energy is below some threshold amount. The Slater determinant wavefunction corresponding to the lowest value of the energy is called the HF wavefunction.

Density Functional Theory

HF theory is not perfect, since each electron only sees the average field of the other electrons. In a real system, the electrons avoid each other more than predicted in HF theory, and hence the inter-electron repulsion is smaller, which yields a lower energy. The difference between the HF energy and the true energy (with the Born-Oppenheimer approximation and neglecting relativistic effects) of the system is the *correlation energy.* Correlation can be included into a HF calculation by using Moller-Plesset perturbation, configuration interaction or coupled cluster theories, but these become very computationally expensive for larger systems.

Another way of calculating molecular structures and properties is called *Density Functional Theory* (DFT). This theory is based on the idea that the electron density ρ uniquely determines the Hamiltonian, called the first Hohenberg-Kohn theorem. The nuclear positions, electronic energy and the number of electrons can be determined directly from the density, and these values are all that are required to describe the electronic Hamiltonian. This suggests that, in principle, it is possible to determine the energy from ρ, using a density functional $E[\rho]$.

Apart from the inclusion of correlation, another advantage of DFT is that the complexity of the density is independent of the number of electrons, implying that the cost of a density functional calculation should scale better than the equivalent HF calculation. The problem with DFT is that the exact functional connecting the ground-state energy to the electron density is unknown.

As with HF theory, the electronic energy functional can be split into three terms; the electron kinetic energy $T[\rho]$, the nuclear-electron attraction $V_{ne}[\rho]$, and the electron-electron repulsion $V_{ee}[\rho]$. The unknown terms in the equation are the $T[\rho]$ and the $V_{ee}[\rho]$. Again, as with HF theory the electron-electron component can be separated into Coulomb $J[\rho]$ and exchange $E'_{xc}[\rho]$ terms, of which only the explicit form of the exchange term is unknown. Unlike HF, electron correlation is included in all terms in DFT.

The first attempts to use the electron density to derive chemical information used a simple expression for the kinetic energy, based on that of a free electron gas. Classical terms were adopted for the nuclear-electron and electron-electron contributions. This approximation was relatively simple but could only be applied to atoms, due to its prediction that no molecular system was stable with respect to its fragments.

A solution to the problem of having large unknowns in the energy functional equation is the *Kohn-Sham approach*. In this approach, the kinetic energy is separated into two terms; the first term describes the exact kinetic energy of a system of non-interacting electrons, the second term is a small term which contains the effect of the interactions on the kinetic energy. The first part of the kinetic energy can be calculated in a similar way to HF theory. A Slater determinant is constructed from N spin orbitals to create an N-electron wavefunction that produces the same ground state electron density as the real system. This allows the calculation of the larger portion of the kinetic energy, leaving the more complicated remainder to be dealt with in an approximate manner. The second term for the kinetic energy is grouped with the other terms whose explicit terms are unknown (the exchange term $E'_{xc}[\rho]$) to form the exchange-correlation energy, $E_{XC}[\rho]$.

Three main methods have been developed to approximate the exchange-correlation energy; the local density approximation, the generalised gradient approximation and hybrid functionals.

The local density approximation (LDA) uses the uniform electron gas to determine the exchange and correlation energies. In this approximation, the exchange energy is equal to the Slater approximation to the HF exchange. No explicit expression exists for the correlation energy, so analytical expressions derived from Monte-Carlo simulations are used. The problem with this approach is that a uniform local density is assumed which is quite a drastic approximation for a chemical system that has an anything

but constant electron density. Despite this, well depth energies for first row dimers calculated with LDA are considerably closer to the experimental values than those calculated with HF [17].

Truly non-local functionals are very difficult to treat, so instead, a comparison between local and non-local is used. Generalised gradient methods supplement the density with information about the gradient of the charge density. The slope of the density gives a rough idea of the environment of the electron; high slope near the nucleus, low slope far from the nucleus. Again the exchange-correlation energy is split into separate exchange and correlation components. These components often (but not always) include semi-empirical parameters derived from fitting to known systems. Examples of this are Becke's B88 exchange functional, which contains a parameter fitted to produce exactly known exchange energies of rare gas atoms, and the correlation function of Lee, Yang and Parr (LYP), derived from an expression from the correlation energy of a helium atom.

Usually the energy contribution due to exchange is larger than that due to correlation. Therefore, accurate determination of the exchange energy is very important for DFT calculations. To achieve accurate values of the exchange energy, hybrid functionals are often used. These functionals are a mixture of pure density functionals for the exchange and exact HF exchange. In chapter 4 Becke's three-parameter hybrid functional for the exchange, along with the correlation functional LYP (the so called *B3LYP method*) is extensively used. The B3LYP exchange-correlation energy is given by the following expression;

$$E_{XC}^{B3LYP}[\rho] = (1-a)E_X^S[\rho] + aE_X^{HF}[\rho] + bE_X^{B88}[\rho] + cE_C^{LYP} + (1-c)E_C^{VWN}[\rho] \quad (2.21)$$

where E_X is the exchange energy, E_C is the correlation energy, S is from the Slater exchange, HF is from the HF exchange, $B88$ is from Becke's GGA exchange, LYP is from Lee, Parr and Yang's GGA correlation functional and VWN is an LDA correlation functional. The parameters a, b and c are equal to 0.20, 0.72 and 0.81 respectively. The values of these parameters were determined by fitting to the G1 molecule set [18].

Determining The Equilibrium Molecular Structure, Vibrational Frequencies and Raman Intensities

Once the wavefunction (or electron density) and the energy of a system have been calculated, the next step is to determine physical quantities. The first step in most *ab initio* calculations is to minimise the energy of the system with respect to the nuclear co-ordinates, that is, optimise the geometry of the molecule.

The optimisation of the geometry of a polyatomic molecule is a difficult task because of the large number of geometrical parameters involved. The search for the minimum in the nuclear potential energy is much more efficient if the energy gradient of the system is determined analytically. In this case, one can calculate the second derivatives of the energy with respect to a change in geometry (Hessian matrix). If the structure of a molecule is at its potential minimum the first derivatives of the energy with respect to the nuclear co-ordinates will be zero. If it is a true minimum and not a saddle point corresponding to a transition state, all the eigenvalues of the matrix of the second derivatives will be positive (one will be negative for a transition state). At a minimum, the Hessian has five or six eigenvalues with the value zero, corresponding to the translation and rotation of the molecule. The direction of the first derivative of the energy indicates where the minimum lies and the magnitude indicates the gradient of the potential energy surface. The energy of the system can be lowered by moving the nuclei in response to the force acting on them. The force is equal to the negative value of the gradient. When the nuclei have been moved, the energy and the gradient are re-calculated. This process of changing the positions of the nuclei and re-calculating the energy and gradient continues until the gradient converges to zero and the minimum energy structure is obtained.

Once the minimum energy structure is obtained (the first derivative equals zero), the eigenvalues and eigenvectors of the mass-weighted Hessian matrix correspond to the square of the harmonic vibrational frequencies and the associated nuclear displacements. There will be $3N$ eigenvalues, of which 5 or 6 will be zero valued, depending on whether the molecule is linear or non-linear. These zero-valued eigenvalues correspond to translations and rotations of the molecule.

The intensity of the Raman-scattered light depends on the frequency of the excitation source. Raman intensities can only be calculated for systems that satisfy the Placzek polarisability theorem. The conditions required for this are; the frequency of the excitation source must be larger than the vibrational frequency, and the energy of the excitation source must be less than any electronic transition of the molecule (not resonant Raman spectroscopy). If this is the case, the Raman intensities can be determined from the polarisability derivatives.

Differencing the energy E with respect to an external electric field produces the dipole moment μ. IR absorption intensities can be obtained for each vibrational mode by differentiating the dipole moment with respect to the normal mode displacements. The second differential of the energy with respect to the electric field produces the polarisability α. It is the differentiation of the polarisability with respect to the normal mode displacements that permits the calculation of the Raman intensities.

Molecular Mechanics

If the system under investigation is too large to be studied by *ab initio* methods, an alternative method is available for the determination of the vibrational frequencies, but not the Raman intensities. This method is called *molecular mechanics*.

Molecular mechanics uses an empirical method to represent the potential energy of a molecule as a function of the geometrical variables. These parameters are generally chosen by fitting to experimental data. Being a function of only the nuclear positions, molecular mechanics methods cannot provide any information on the electronic structure of a molecule. The molecular mechanics force field is built up from contributions due to processes such as bond stretching, bond angle bending, rotations about dihedral angles, as well as non-bonding interactions. These processes are generally modelled by simple functions such as Hooke's law. The simplicity of molecular mechanics permits the calculation of the vibrational frequencies of systems with several hundreds of atoms. In chapter 5 of this study the molecular mechanics force field AMBER [19] is used, as implemented in the Gaussian03 software suite [20].

2.1.3 Raman Spectroscopy of Diamondoids

The combination of Raman spectroscopy and *ab initio* electronic structure methods is a popular way to determine the vibrational energy levels of lower diamondoid molecules. In this section some of the work already published in this field is reviewed, as an introduction to this study. The history of the diamondoids and their nomenclature system has been discussed in section 1.4.

Adamantane

The Raman and IR absorption spectra of adamantane ($C_{10}H_{16}$) and perdeuterated adamantane ($C_{10}D_{16}$) were studied by Bailey [21] in 1971. The spectra produced by adamantane were assigned using the valence force field of Snyder and Schachtschneider [22], developed for use with saturated hydrocarbons. The perdeuterated adamantane spectra were assigned using the Redlich-Teller isotopic product rule [23].

Much of the later work on the Raman and IR spectra of adamantane has been used to develop force constant scaling factors. In 1995 Bistriĉić *et al.* measured the Raman and IR absorption spectra of adamantane and three partially-deuterated adamantanes. Combining these with the fully deuterated adamantane spectra of Bailey, they compared scaled empirical and scaled semi-empirical methods of assigning the spectra. Szász and Kovács [24] again studied adamantane and perdeuterated adamantane, but this time scaled the force constants produced by a density functional calculation B3LYP/6-31G*.

Jensen [25] used Hartree Fock, B3LYP and MP2 theories, with the 6-31G* basis set to assign the Raman spectrum of adamantane and perdeuterated adamantane. Instead of scaling the force constants, he produced scaling factors for the vibrational frequencies. He found that each different type of motion (CH stretch, CH_2 wag, C-C-C bend etc.) required different scaling factors, but the factor was consistent for that type of motion. This consistency of the scaling factors was seen as confirmation of the peak assignments.

Adamantane Derivatives

Similar methods are commonly used in the analysis of the Raman spectra of substituted adamantanes.

Bistriĉić *et al.* have studied the Raman and IR spectra of two adamantane derivatives, 1,1'-biadamantane [26] and 2-adamantanone [27]. The assignment of the normal modes of 1,1'-biadamantane was based on AM1 semiempirical calculations. Normal modes were assigned in terms of the normal modes of adamantane and motions of the central CC bond. For 2-adamantanone, vibrational frequencies and Raman intensities were calculated with the BLYP and B3LYP functionals with the 6-31G(d,p) basis set. The two methods produced comparable geometries, vibrational frequencies, Raman and IR intensities. The calculated intensities of the vibrations between 1200-1500 cm^{-1} were found to be poor when compared to the experimental. This poor agreement was due to an overestimation of the calculated intensity of vibrations associated with methylene hydrogen atoms. The overestimation of the calculated intensity is thought to be due to systematic shortcomings in the theory.

The Raman, IR and surface-enhanced Raman spectra of the anti-Parkinson drug amantadine (1-aminoadamantane) have been studied by Rivas *et al.* [28]. To assign the Raman spectra they used HF theory and the 6-31G* basis set. The surface-enhanced Raman spectra showed evidence for the formation of a bond between the nitrogen and the colloidal silver used to produce the surface enhancement, as well as other effects.

Kovács and Szabó [29] studied the Raman and IR spectra of perfluoroadamantane ($C_{10}F_{16}$). Spectra were interpreted with the aid of quantum chemical calculations at the B3LYP/6-31G* level. They found that fluorination results in characteristic changes of the vibrational properties of the adamantane skeleton.

Other Diamondoids

Raman spectroscopy studies of diamondoids larger than adamantane are, at best, quite rare.

The Raman spectra of adamantane, diamantane and triamantane were studied in 1980 by Jenkins and Lewis [30]. They produced and assigned the Raman spectra of

these three molecules taken at room and low temperature (∼25 K). The purpose of their study was to use the low frequency lattice modes to determine the crystal phase changes that occur with changing temperature.

May *et al.* [31] studied the Raman spectra of adamantane and diamantane for comparison with the spectra produced by chemical vapour deposition (CVD) diamond films. They assigned the spectra on the basis of HF calculations with the 3-21G* basis set. The aim of the study was to determine if peaks in the spectra of CVD diamond often assigned to "nanophase" diamond could be traced to peaks in the spectra of the diamondoids. Only a superficial correlation was found between the peak positions of the polymantanes and the nanophase diamond peaks. They concluded that the nanophase peaks must be due to other features of the crystalline material, such as surface modes.

The largest diamondoid which has been studied by Raman spectroscopy is cyclohexamantane. The experimental spectrum was published by Dahl *et al.* in 2003 [32]. The spectrum was partially assigned by comparison with the Raman spectra of adamantane and nanocrystalline diamond. A fuller assignment was made by Richardson *et al.* [33]. They used massively-parallelised code and the PerdewBurkeErnzerhof generalized-gradient approximation (GGA) for the exchange and correlation functions and a large basis set. Their calculated frequencies and intensities were found to be in excellent agreement with the experimental data of Dahl *et al.* [32].

Several other groups have calculated theoretical vibrational spectra for larger diamondoid molecules. Chang *et al.* [34] used the B3LYP/6-31* combination to calculate the Raman spectra of diamondoids up to tetramantane. Lu *et al.* [35] also used B3LYP/6-31G* to calculate the IR spectra of a selection of diamondoids. Both studies suffered from the fact that only the experimental Raman spectra of the smaller diamondoids have been produced.

This Study

This study takes advantage of the recent isolation of a large selection of higher diamondoids [36], by obtaining experimental Raman spectra for the largest selection of polymantane structures to date. The two main areas investigated are; (a) The effect of molecular size, shape and symmetry on the Raman spectra [37] (Chapter 4), and (b) The relationship to the Raman spectrum of nanocrystalline diamond (Chapter 5).

2.1.4 Raman Spectroscopy as a Characterisation Tool for Carbon Based Materials

Whether the carbon sample being studied is crystalline or amorphous, its properties are dependent on its structure. Amorphous carbon films are smoother and softer than nanocrystalline diamond films which, in-turn, are smoother and less transparent than

microcrystalline films. The requirements of the application determine which type of film is used.

Common techniques such as X-ray diffraction and transmission electron microscopy will allow the identification of diamond crystals in a sample, but these methods are time consuming and may require the destruction of the sample. What is really required is a fast, non-destructive method of characterising unambiguously, a variety of thin carbon films. The simplicity of Raman spectroscopy makes it the method of choice for carbon sample characterisation. The choice of laser wavelength can be varied depending upon the required application. Common choices are visible light (e.g. 632 nm red from a HeNe laser or 514.5 nm green from an argon ion laser), ultraviolet (e.g. 325 nm from a He:Cd laser) or IR (e.g. 785 nm from a diode laser).

Single Crystal Diamond

The identification of pure diamond by Raman spectroscopy is trivial. The characteristic fingerprint of diamond is a single sharp Raman line at 1332 cm^{-1}, see Figure 2.5. This line is produced by the triply-degenerate transverse optical mode originating from the Brillouin zone centre. The diamond structure is constructed by placing a basis of two carbons at each lattice point of a face-centred cubic arrangement (Figures 2.6 (a) and (b)). The vibrational motion associated with this Raman signal involves the stretching of this two-atom basis with all unit cells moving in phase (Figures 2.6 (c)). A thorough investigation of the first- and second-order Raman spectra of diamond was published by Solin and Ramdas in 1970 [38].

Most CVD diamond films consist of small diamond crystallites surrounded by graphitic or amorphous carbon grain boundaries. These boundaries produce extra signals in the Raman spectrum that can help diagnose the crystallite size and overall quality of the diamond sample. Before these peaks can be understood let us discuss the Raman spectra of graphite and amorphous carbon.

Crystalline Graphite

It was not until the advent of the laser that Raman spectroscopy could be used to analyse black materials like graphite. The Raman spectrum of graphite was first taken by Tuinstra and Koenig in 1970 [39]. They discovered that a single crystal of graphite produces a single peak at 1575 cm^{-1} whereas in all other graphitic materials (activated charcoal, carbon black, etc.) a second feature appears at 1355 cm^{-1}. The 1575 cm^{-1} mode was assigned as the E_g Brillouin zone centre optical mode due to symmetry arguments, although only few depolarisation measurements could be made.

The assignment of the second peak was slightly more difficult. The simplest suggestion for the origin of this peak was a diamond-like atomic arrangement, rather than

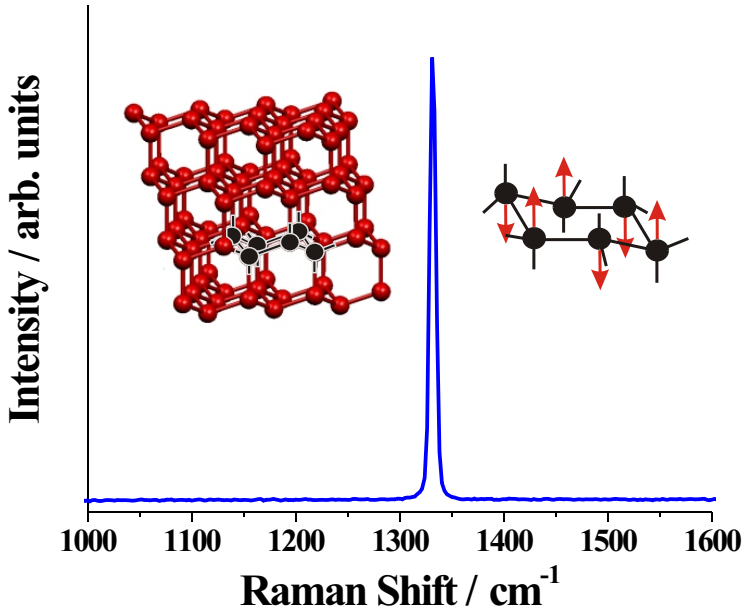

Figure 2.5: Raman spectrum of diamond. Inset shows the structure of diamond and the nuclear displacements associated with the Raman active vibration.

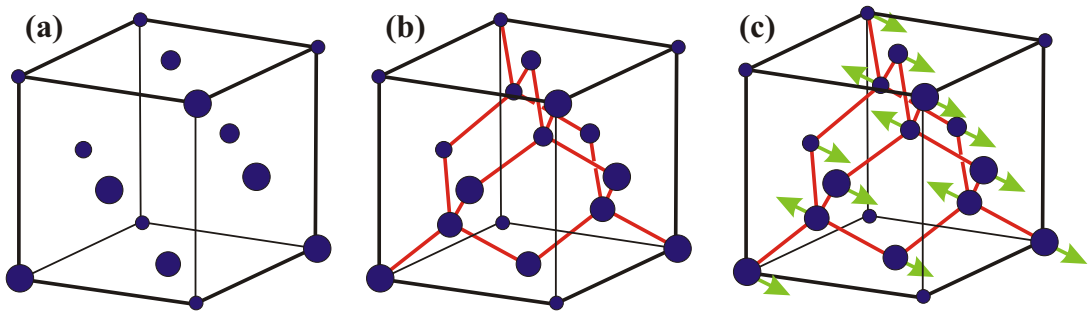

Figure 2.6: Unit cells, (a) Face-centred cubic, (b) Diamond, (c) The diamond unit cell illustrating the nuclear displacements associated with the first-order Raman signal.

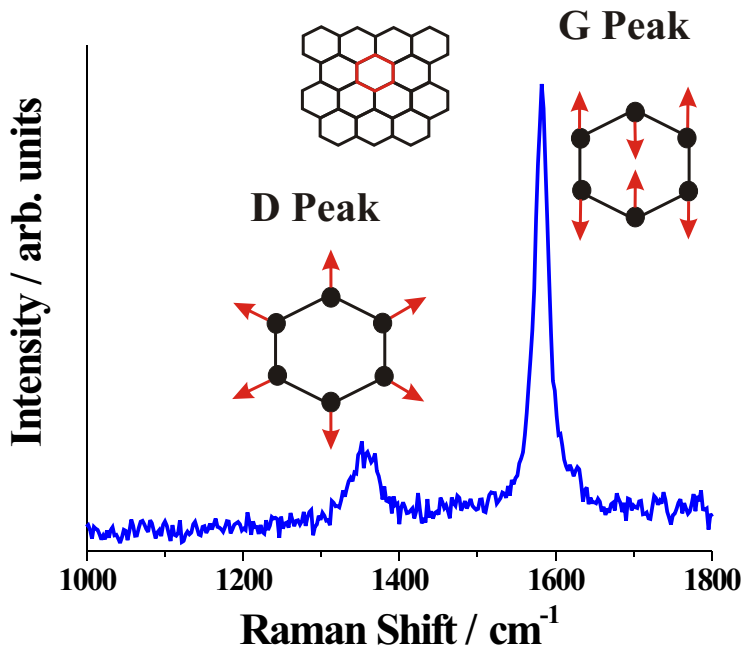

Figure 2.7: 514 nm Raman spectrum of highly orientated pyrolitic graphite, with inset cartoons of the nuclear displacements associated with each vibration.

a graphitic signal. As stated above, the diamond Raman signal appears at 1332 cm^{-1}. It is possible that any non-graphitic material in the samples that were not pure single crystals had a diamond-like structure. This assignment was discounted for several reasons, including the fact that the frequency of the diamond vibration would require a large upward shift and the narrow band width of the observed peak would not be expected for a disorganised signal. Instead, the origin of the 1355 cm^{-1} was attributed to particle size effects [39].

The intensity of this second peak increases relative to the zone-centre peak as (a) the amount of disorganised carbon increases and (b) the graphite crystal size decreases. The 1575 cm^{-1} peak (called the G peak, after crystalline Graphite) is the only Raman active mode of the infinite lattice. The other peak (the D peak from Disordered graphite) is caused by A_{1g} ring-breathing modes at the K zone boundary becoming Raman active due to a breakdown of the solid-state selection rules that prevent its appearance in the spectrum of the perfect crystal (Figure 2.7).

Amorphous Carbon

Amorphous carbon (a-C) films are mixtures of sp^3- (as in diamond) and sp^2- (as in graphite) hybridised carbon lacking in long range order. The properties of these films

are strongly dependent on the ratio of these two types of carbon. Films with high sp^3 content (called tetrahedral amorphous carbon, ta-C) are generally harder, more transparent and have a higher resistivity than those of high sp^2 content, although they are also highly stressed. It is also common for amorphous carbon films to contain hydrogen, by virtue of the way they are prepared. Hydrogenated a-C films are softer, more stable and tend to have higher transparency than the hydrogen-free films.

It has been observed for amorphous Si and Ge that the reduced Raman spectrum starts to resemble a broadened vibrational density of states of the single crystal [40]. It might then be expected that the Raman spectrum of amorphous carbon starts to resemble the vibrational density of states of diamond, but this is not the case. Instead, the visible Raman spectra produced by nearly all types of amorphous carbon are dominated by the G and D peaks of disordered graphite [41].

Unlike amorphous Si and Ge which contain purely sp^3 hybridised atoms, amorphous carbon is a mixture of sp^2 and sp^3 hybridised atoms. When taking the Raman spectrum of a multi-component system it is important to consider the relative polarisability of each component. The π bonds formed by the sp^2 hybridised carbons are more polarisable than the σ bond formed by the sp^3 hybridised carbon, and so have a larger Raman cross-section. Also, when using visible lasers for excitation, the π states are resonantly enhanced, whereas the σ states are not. As a result even the Raman spectra of high (80%) sp^3 content films are dominated by the sp^2 signal when excited with visible-wavelength lasers [41].

The G and D peaks observed in the amorphous carbon Raman spectra are generally much broader than those observed for graphite, depending on the ordering within the sample. There is also a slight difference in the assignment of the G peak in amorphous carbon. In the amorphous phase, the "G" peak does not just mean graphite - the G mode arises from stretching of any pair of sp^2 sites, whether in rings or chains. The D mode is still assigned as the breathing mode of sp^2 sites in rings not chains.

As opposed to being controlled by the proportion of sp^2 to sp^3 structures, the Raman spectrum of amorphous carbon is dependent on the configuration of the sp^2 sites bonded in clusters. Only in cases where their sp^2 clustering is controlled by the sp^3 fraction, such as very-high-sp^3-proportion tetrahedral amorphous carbon, can the Raman spectrum be used to determine the sp^2/sp^3 ratio.

The ratio of the intensity of the D peak to the intensity of the G peak [$I(\mathrm{D})/I(\mathrm{G})$] can provide a useful measure of the disorder in an a-C sample. Starting with a pure graphite single crystal, the Raman spectrum contains only a sharp G peak and no D peak, because there is no disorder. As the crystallite size is reduced and the long range periodicity is broken, the D peak appears and increases in intensity. In this regime, the $I(\mathrm{D})/I(\mathrm{G})$ ratio is found to be inversely proportional to the graphite crystallite grain

size [39]. The $I(\mathrm{D})/I(\mathrm{G})$ ratio reaches a maximum for a nanocrystalline graphite sample which contains the maximum disorder while still only containing sp^2 rings (grain size of a few nanometers). To increase the disorder further, from nanocrystalline graphite to a-C, some of the ring structure is replaced by sp^2 chains and an sp^3 network. The disorder is still high so the D peak is still present, but the relative proportion of sp^2 rings to sp^2 chains is decreasing; so too does the $I(\mathrm{D})/I(\mathrm{G})$ ratio. Now $I(\mathrm{D})/I(\mathrm{G})$ becomes proportional to the square of the grain size [42]. This continues until there is no sp^2 ring structure in the a-C film, and then only a single broad G peak remains. An in depth discussion of the G and D peak position and intensity variation can be found in the study by Ferrari and Robertson [41].

Figure 2.8 shows the Raman spectra of two a-C films grown by pulsed laser ablation under the same conditions apart from the temperature of the substrate. The spectra have been fitted with two Gaussians corresponding to the G (blue) and D (green) peaks. It is clear that the higher temperature has produced an increase in the $I(\mathrm{D})/I(\mathrm{G})$ ratio implying an increase in the ordering of the π bonds.

It is possible to observe vibrations produced by the sp^3 network in the Raman spectrum of a-C but only by using UV excitation, which excites the π states into resonance. The signal produced is broad and very weak and appears at around 1050 cm^{-1}. Referred to as the T peak (for Tetrahedral), it is only observable in samples with very high sp^3 content (such as ta-C) [43].

This study, specifically chapter 3, uses Raman spectroscopy to determine the effect of the incorporation of sulfur on the graphitic clustering in hydrogenated amorphous carbon thin films. Raman spectroscopy is routinely used to determine the structural changes associated with the introduction of a dopant atom. The doping of amorphous carbon with nitrogen generally produces an increase in the $I(\mathrm{D})/I(\mathrm{G})$ ratio, indicating an increase in the graphitic clustering within the sample [44–48]. Similar trends are observed with the addition of phosphorous [49] and high levels of boron [50]. Conversely, the addition of silicon [51] or hydrogen [52] produces a reduction in the $I(\mathrm{D})/I(\mathrm{G})$ ratio, suggesting a reduction in the graphitic nature of the samples. This is thought to be due to the stabilising effect silicon and hydrogen have on the sp^3-hybridised form of carbon.

Microcrystalline Diamond

Having discussed the non-diamond features that are likely to be seen in the Raman spectra of carbon materials, let us now use this knowledge to help us analyse the Raman spectra of CVD diamond samples. The Raman spectrum of microcrystalline CVD diamond can generally be deconvoluted into separate contributions from the 1332 cm^{-1} diamond phonon and the D and G modes of amorphous carbon. The relative

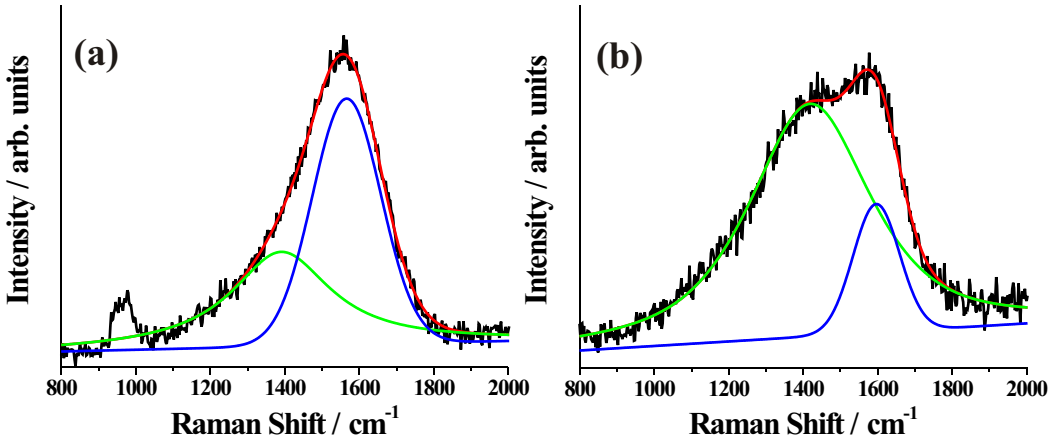

Figure 2.8: Raman spectra of two a-C films, deposited on Si substrate maintained at (a) 25°C and (b) 400°C. Red line is the sum of the two components used to fit the measured spectrum (black). The small peak around 1000 cm^{-1} in (a) is the second-order silicon signal. The spectra were taken from reference [53].

intensity of the diamond-to-non-diamond signals is strongly dependent on the excitation wavelength. Whether this is due to resonance enhancement of the sp^3 component, a decrease in the resonance enhancement of the sp^2 component, or some other process, is not yet fully understood [54].

The Raman spectra displayed in Figure 2.9 are of the same sample but taken with different laser excitation wavelengths. These spectra clearly show the increase in the $I(\text{diamond})/I(\text{G})$ ratio with decreasing excitation wavelength. This emphasises that the laser wavelength has to be chosen very carefully depending on what the experiment is trying to determine. Research into nanocrystalline diamond is becoming popular due to the smooth surface, film homogeneity and high Youngs modulus of this material, making it ideal for microelectronic mechanical devices [55]. However, analysis of a nanocrystalline sample by Raman spectroscopy using IR excitation would not produce a diamond line; the signal from the amorphous carbon grain boundaries would be far too strong. UV excitation, on the other hand, would reveal a small diamond signal indicating that the sample was, indeed, nanocrystalline diamond, rather than simply amorphous carbon. Conversely, differentiating two high quality CVD diamond samples would be much easier with IR excitation than UV, since the sp^2 impurities would be enhanced.

The relative intensity of the diamond line to the intensity of the G peak is often used as a crude measure of the phase purity of CVD diamond [56]. This can be extremely useful when empirically relating deposition conditions to sample quality (Figure 2.9).

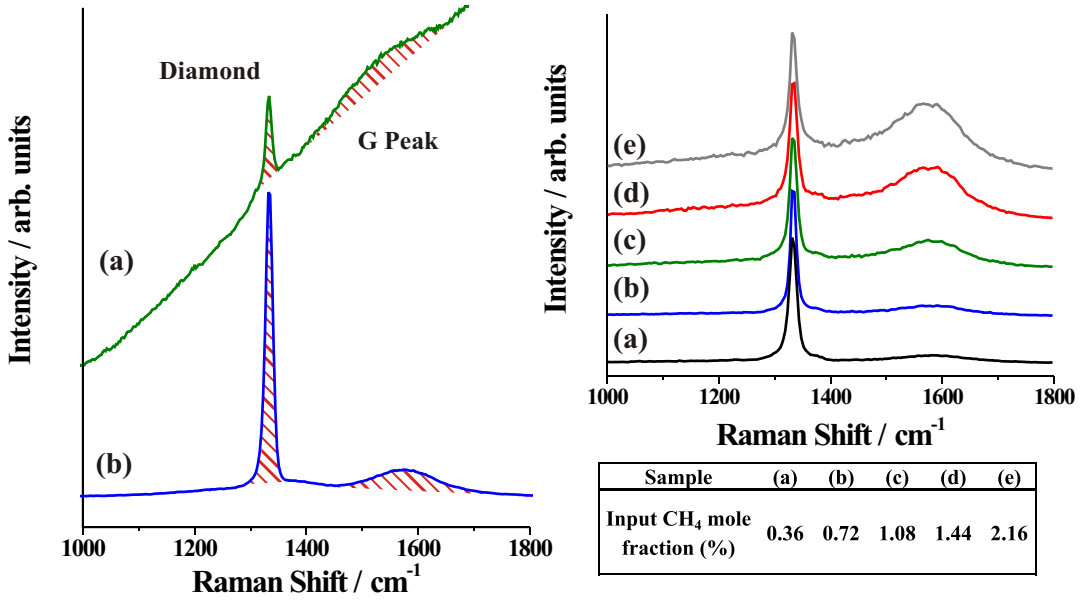

Figure 2.9: On the left: Raman spectra of microcrystalline diamond taken with (a) 514 nm [I(diamond)/I(G)=2.2] and (b) 325 nm excitation [I(diamond)/I(G)=11.7]. The rising background in the 514.5 nm spectrum is due to strong photoluminescence from nitrogen-vacancy defects. On the right: Raman spectra of microcrystalline diamond films grown by CVD using CH_4/H_2 gas mixtures , taken at 244 nm. Increasing the CH_4 mole fraction of the gas mixture during growth decreases the quality of the diamond film, as evidenced by the increasing G band around 1550 cm^{-1}. Taken from reference [56].

Nanocrystalline Diamond

As the diamond crystallites reduce in size from micrometres to nanometres, analysis of the Raman spectrum becomes considerably more complicated. When dealing with a large perfect crystal, where the lattice size is effectively infinite, only certain phonons are Raman active and the spectra are quite simple. In nanocrystalline or highly-disordered samples, the selection rules break down, allowing many more vibrational modes to become Raman active. The effects of this appear in two ways: (a) shifting and asymmetric broadening of existing peaks and (b) the appearance of new signals activated by disorder. The activation of the D peak with disorder in graphite [39] is an example of the latter. Peak shifting and asymmetric broadening has been observed in the 1332 cm^{-1} mode of shock-synthesised nanodiamond powders [57], but in diamond thin films any change in peak position is generally taken as a sign of compressive or tensile stress in the film [54].

The appearance of new signals activated by disorder in nanodiamond films is still a subject of some controversy. Figure 2.10 shows a 325 nm Raman spectrum of a film grown under typical nanodiamond conditions. The diamond line and the G and D peaks are present, but there is also a small broad signal at $\sim$1150 cm^{-1} which is not observed in the spectrum of microcrystalline diamond. The presence of this peak is often taken as direct evidence for nanosized diamond crystals, since at first it was thought that it was a disorder-activated peak [58, 59]. It is now believed that this peak arises from an sp^2 hybridised structure, such as polyacetylene-like molecules, that may be present on the surface and in grain boundaries [60–62].

The interpretation of the Raman spectra obtained from nanocrystalline diamond powders are also not without controversy. A broad, weak signal been observed at around 600 cm^{-1} in the Raman spectrum of sub-200 nm diamond particles [57, 59]. The intensity of this signal has been shown to be inversely proportional to the size of the particles investigated [57], a trend which might be expected for a peak activated by particle size effects. So far, this peak has only tentatively been assigned as longitudinal acoustic phonons near the Brillouin zone boundary. The theory behind this assignment is the close proximity of this signal to a maximum in the diamond vibrational density of states.

In Chapter 5 this problem is approached from a different angle. Instead of considering the confinement of the diamond lattice, the change in the Raman spectra of diamond hydrocarbons with increasing size is considered.

2.1.5 Description of the Raman Spectrometers

Two spectrometers were primarily used in this study; a three-wavelength Renishaw RM2000 spectrometer, and a Renishaw InVia spectrometer. The basic setup of these

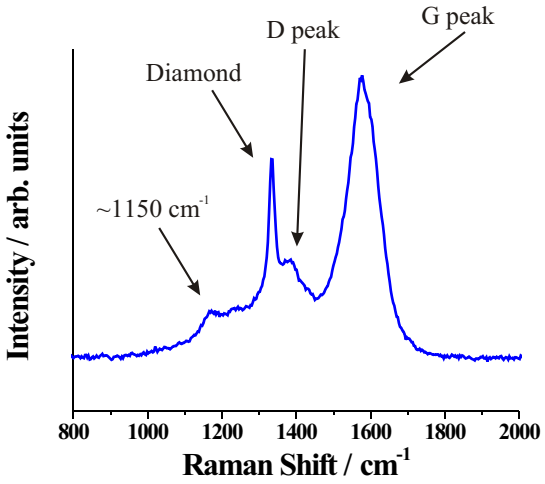

Figure 2.10: Raman spectrum of nanocrystalline diamond taken with 325 nm excitation. The sample was deposited by microwave PECVD at 0.8 kW and 100 Torr, from a gas mixture containing 97% Ar, 2% H_2 and 1% CH_4.

spectrometers is the same, and is outlined in Figure 2.11.

In all cases the excitation source is a laser which is directed into the spectrometer via an array of mirrors. On entering the spectrometer the beam is passed through a set of optics to set the profile of the beam. A set of neutral density filters controls the laser power illuminating the sample. To insure a monochromatic source, the beam is passed through a wavelength-specific filter that removes any plasma lines from the laser. The beam is reflected into a microscope, which is focused onto the sample. The scattered light is collected back up the microscope and reflected into the spectrometer. This collected light is passed though another filter to remove the intense Rayleigh-scattered radiation, leaving the weaker Raman-scattered light. The Raman-scattered light is focused by another set of optics, before the different wavelengths are separated by the diffraction grating. The different wavelengths are then detected by a charge-coupled device (CCD) connected to a personal computer running Renishaw's Wire1.0 software.

The software was also used to set the spectrum accumulation parameters, such as scanning range, exposure time and number of accumulations. Four different scanning modes were available with these spectrometers; static, step and repeat, matched step and repeat, and continuous. A static scan can only detect a limited range, typically several hundred to several thousand wavenumbers. The grating is not moved so the range of the spectrum depends on the lines per millimetre on the grating and the wavelength of the excitation laser. The advantage of this is speed; the time taken to acquire the spectrum is equivalent to the exposure time multiplied by the number of accumulations that are averaged. If a larger wavenumber range is required, the other

scanning modes offer different methods of accomplishing this. The first mode is the "step-and-repeat". This is effectively a set of static exposures taken at different centre positions, to cover a large range. The overlapping regions are "stitched together" by the software to show the data over the spectral range requested. A major disadvantage of this method is the appearance of discontinuities in the areas where the static exposures are stitched together. The "matched step-and-repeat" goes some way to fixing this problem by matching the baselines between the segments, but it is still not ideal. Fortunately, the problems of the step-and-repeat modes can be avoided by using the "continuous scanning" mode. In this mode the grating is rotated as the spectrum is accumulated, allowing a large range to be studied. All the spectra displayed in this study were taken using either the static or continuous scanning modes, depending on the range of interest.

The exposure time of the spectrum was varied from sample to sample in order to obtain a satisfactory signal-to-noise level. The maximum exposure time used was 120 seconds. The longer the exposure time, the higher the probability of a cosmic ray event passing through the CCD. When this happens a sharp peak, approximately one or two pixels wide, appears in the spectrum. This is not ideal, but if long exposures are required there is a way to prevent cosmic ray peaks ruining a spectrum. The Wire software has a "cosmic ray removal" option. When selected, three accumulations are taken before the spectrum is acquired. This allows the software to detect and disregard any anomalously large signals, leaving the spectrum free of cosmic ray signals. This option is best used with many accumulations of short exposure time, to reduce the amount of time taken for the cosmic ray removal steps.

Before the spectrum is acquired, it is important to determine whether or not the laser is damaging the sample. To change the power of the laser incident on the sample, a selection of neutral density filters in a rotating mount are built into the spectrometer. If there is a change in the widths or positions of the peaks in the spectrum with different laser power, then it is likely that the sample is being damaged. If there is evidence of sample damage, even at the lowest powers, the samples may be rotated under the laser to increase the area in which the energy from the laser is dissipated. This is often required when using UV or near-UV lasers for excitation.

The Renishaw RM2000 in the School of Chemistry is a multi-wavelength system with three different excitation sources. These sources are; a 785 nm diode laser, the 514.5 nm line of an Ar^+ laser, and the 325 nm line of a He-Cd laser. When set-up for use with the 785 nm and 514.5 nm excitation energy, glass lenses and the 1200 l/mm grating is used. Dispersing the output from a Ne lamp through the spectrometer in this set-up shows a spectral resolution of $\sim$ 2.7 cm^{-1} (FWHM) at an emission λ of $\sim$830 nm and $\sim$6.5 cm^{-1} (FWHM) at an emission λ of $\sim$540 nm. When using the

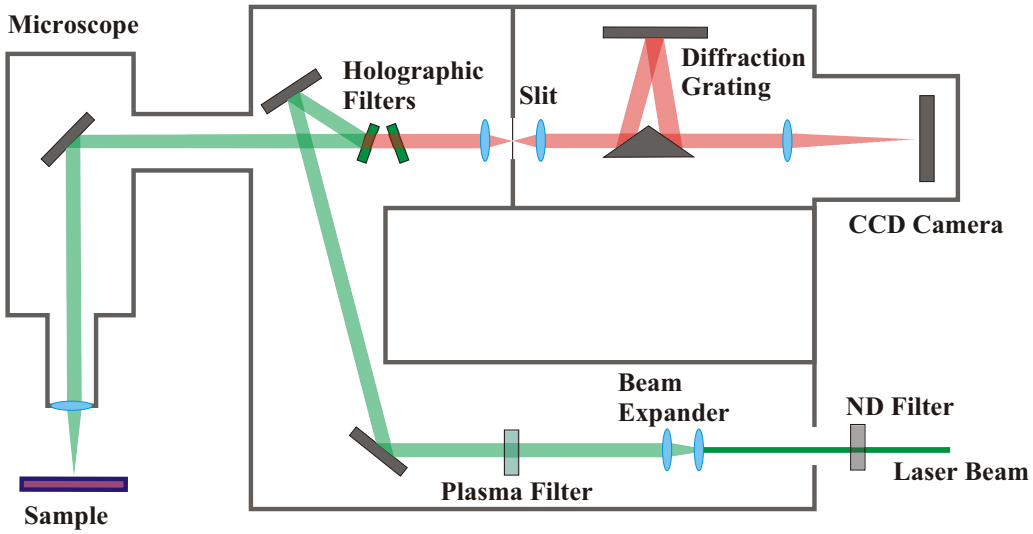

Figure 2.11: Schematic diagram of the Raman spectrometer

325 nm excitation, the glass lenses are replaced by quartz lenses, and the 1200 l/mm grating by a 2400 l/mm grating. When set up for UV the system has a relatively poor resolution, giving a Ne lamp linewidth of greater than 10 cm^{-1}.

The Renishaw InVia in the Physics Department was used with the help of James Pomeroy, Andrei Sura and Martin Kuball. The 488 nm line of an Ar^+ laser was used in combination with a 2400 l/mm grating.

The diamondoid samples studied were either powders or small crystals. The powder samples were pressed flat to produce a good surface to focus the laser beam onto. The Raman spectra of the a-C:H films were obtained from the thin film on a silicon substrate. In most cases the first-order (520 cm^{-1}), and occasionally the second-order (broad signal around $\sim 980cm^{-1}$), silicon signals were visible in the spectra.

2.2 The Deposition Method

In this study, hydrogenated amorphous carbon films were deposited using capacitively-coupled radio-frequency plasma-enhanced chemical vapour deposition (Chapter 3). Chemical vapour deposition is a method by which a solid substance is deposited onto a surface from a chemical reaction in the gas phase [63]. The term “plasma-enhanced” is used when the deposition of the sample is aided by the excitation of gas into an ionised state (a plasma). For electrical discharge plasmas (direct current or radio frequency)

the extent of ionisation is very small, with only one charged particle per 10^5-10^6 neutrals. In such plasmas, electrons are the main current carriers, being light and mobile. The acceleration of the electron in the electric field increases the electron temperature relative to the gas temperature. Collisions of the high temperature electrons with the low temperature gas molecules permits the formation of ionic and radical species that without a plasma could only exist with a very high gas temperature. The presence of (relatively) cold gas alongside high temperature active species distinguishes the plasma reactor from conventional thermal processes [64].

2.2.1 The RF Discharge Process

The discharge used for the deposition of amorphous carbon was produced by passing a current, alternating at radio-frequencies (13.56 MHz), through a low pressure of methane. The advantage of using AC over DC is that the requirement of drawing direct current through the system is removed. This permits the use of insulating substrates or electrodes without charging.

When the field is applied, the plasma does not strike instantaneously. First a free electron must be produced, either by ionisation of the gas by a cosmic ray, or by field emission from an electrode. This electron is accelerated by the electric field until it collides with a gas molecule. If the collision is inelastic, the molecule may release another electron. This process of acceleration and collision creates a cascade mechanism that initiates the plasma. To maintain the discharge, the rate of loss of electrons must not be larger than the electron generation rate. Electrons can be lost by recombination with positive ions or to the walls of the reactor. Electrons are generated by inelastic collision with gas molecules and also by secondary electron ejection from the electrodes when bombarded with high energy particles (this is the primary electron generation mechanism in DC discharges [65]). Both the electron loss and generation mechanisms depend on the pressure of the gas in the reaction chamber. If the pressure is too low, the electrons do not collide with enough molecules to produce a cascade. If the pressure is too high, the electrons suffer too many low energy collisions, and do not gain enough energy to ionise the gas.

When an RF discharge is initiated, a *sheath* forms over the electrode surfaces. The large difference in velocity between the electrons and ions means many more electrons will hit the electrode area per unit time. This causes the surface to charge negatively with respect to the plasma, until the repulsion of the negative electric field balances the electron and ion flux to the surface. This region of excess negative charge around a surface is called the sheath. Since fewer electrons are found in the sheath, less electron impact excitation reactions occur, resulting in lower luminescence originating from this area. It is often possible to observe the sheath as a dark space surrounding a surface

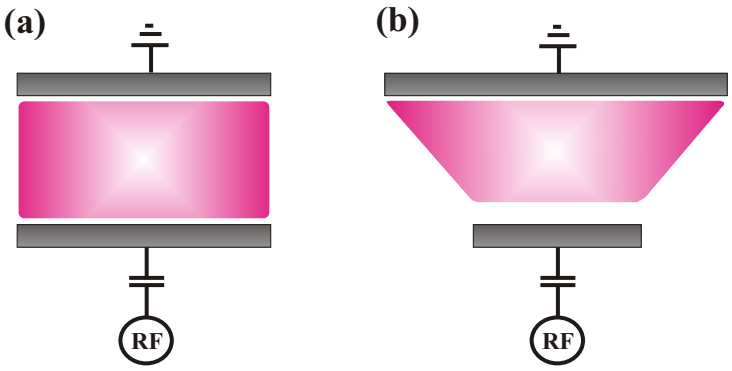

Figure 2.12: Illustration of the different sheath widths obtained with (a) electrodes of equal area, (b) a small powered electrode and a large earthed electrode.

in a plasma [66].

The sheaths act as diodes, so the electrodes develop DC-self bias voltages equivalent to their peak RF voltages. The RF voltage is divided between the sheaths of the two electrodes according to their inverse capacitance. Thus, the DC-self bias varies inversely with the electrode areas. Generally, the powered electrode holds the substrate and is smaller than the earthed electrode. This gives the powered electrode a lower capacitance and thus it acquires a large bias voltage, becoming negative with respect to the larger, earthed electrode (figure 2.12. The large negative sheath voltage accelerates the positive ions toward the substrate giving the bombardment required for the deposition of amorphous carbon films [43].

2.2.2 Experimental Set-up

Figure 2.13 shows the set-up of the deposition reactor. The RF power is produced by an ENI ACG500 500 W RF generator (a). The RF signal is passed into a ENI Matchwork 5 matching network (c) which is connected to the powered electrode (d). The matching network controller (b) automatically adjusts the two air capacitors in the matching network to minimise the power reflected back to the generator. The DC bias is monitored by the digital display box (f), which is connected to the network controller. The plasma is generated between the powered electrode (10 cm diameter) and the larger earthed electrode (e). The earthed electrode is made up of the entire aluminium vacuum chamber 26.5 cm diameter cylinder, 35 cm long) apart from the central powered electrode. The two electrodes are kept insulated from one another by a PTFE barrier. Process gases were: methane (CH_4), hydrogen sulfide (H_2S), nitrogen (N_2), argon (Ar), ammonia (NH_3) and carbon disulfide (CS_2). Process gases were passed into the chamber via Tylan mass flow controllers, providing maximum flow-

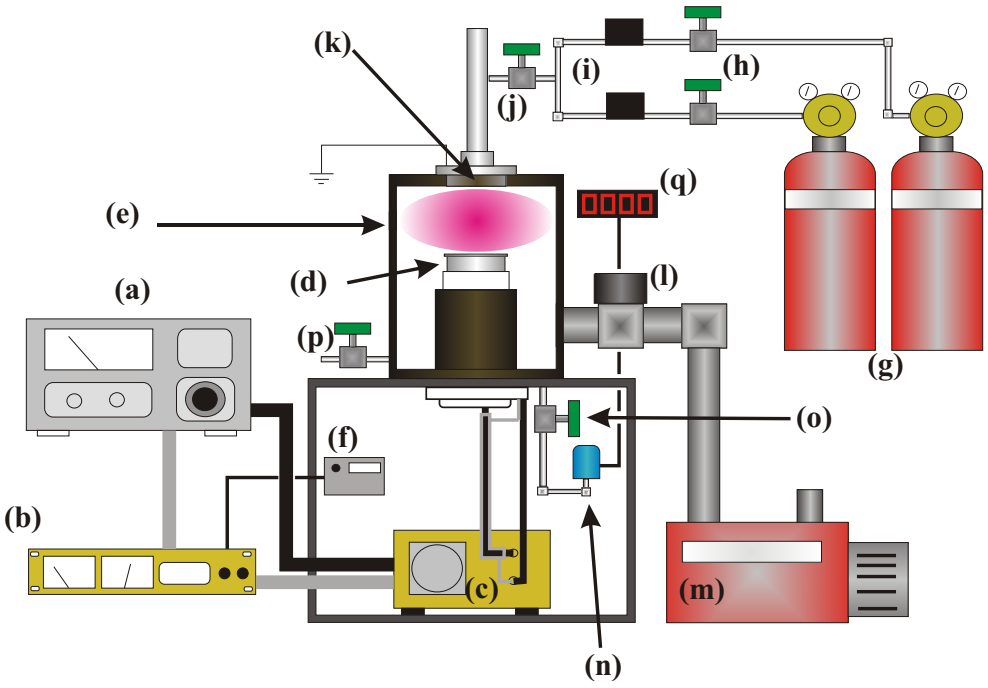

Figure 2.13: Experimental set-up: (a) RF generator, (b) Matching network controller, (c) Matching network, (d) Powered electrode, (e) Earthed electrode, (f) DC bias monitor, (g) Gas cylinders, (h) Cylinder isolation valves, (i) Mass flow controllers, (j) Gas inlet valve, (k) Gas inlet shower head, (l) Throttle valve, (m) Rotary pump, (n) Baratron pressure gauge, (o) Baratron isolation valve, (p) N_2 purge valve (q) Pressure monitor gauge.

rates of 10, 50 or 200 sccm. The carbon disulfide used was in liquid form, and was passed into the vacuum system via a needle valve, which was also used to control the flow rate. The process gases enter the deposition chamber through the earthed shower head (k). The vacuum was maintained by an Edwards two-stage rotary pump which produced a base pressure of approximately 1 mTorr. The pumping rate was controlled by a throttle valve between the vacuum pump and the deposition chamber. Pressure was monitored by a MKS Baratron capacitance manometer.

When not in use, the chamber and gas inlet up to valves (h) were left under vacuum with the Baratron isolation valve open.

The Deposition method

Substrates used in this project were either mirror-polished, boron-doped, single crystal, (100) silicon wafers, $10 \times 10 \times 3$ mm quartz blocks, aluminium foil or a steel disc. The silicon wafers were cut to size by cleaving along the crystal planes. Before deposition,

the silicon and quartz substrates were mechanically cleaned with cotton wool soaked with isopropyl alcohol (IPA), then treated in an ultrasonic bath of IPA, before being washed with acetone and blown with dry nitrogen. The aluminium foil substrates were wrapped around a 6-inch-diameter silicon wafer. The aluminium and steel substrates were cleaned in a similar manner to the silicon/quartz but without the ultrasonic treatment.

During the deposition run the DC bias and gas pressure were kept constant by adjusting the RF power and throttle valve (l) when any deviation was observed. Deposition parameters, such as length of deposition run, process gas mixture, pressure and DC bias were varied in a systematic manner to determine their affect on the properties of the samples produced (Chapter 3). After deposition the chamber was cleaned with isopropyl alcohol to remove any amorphous carbon from the electrodes.

2.3 X-Ray Photoelectron Spectroscopy

This section introduces the technique of X-ray photoelectron spectroscopy (XPS) and its use in the analysis of amorphous carbon films. All XPS measurements analysed in this study were performed by Dr Sean Pearce at the Interface Analysis Centre, Bristol.

2.3.1 Theory

The photoelectric effect is one of the finest examples of wave-particle duality, a fundamental principle of quantum mechanics [12]. The ejection of electrons from a material exposed to light features three main experimental observations that are difficult to explain using classical mechanics: (a) No electrons are ejected until a threshold frequency, characteristic to the material, is exceeded, regardless of the intensity of the radiation. (b) The kinetic energy of the ejected electrons increases linearly with the frequency of the incident radiation, and is independent of the intensity of the radiation. (c) Above the threshold frequency, electrons are ejected instantly, regardless of the radiation intensity.

To explain these observations, the light had to be treated as if it behaved like a particle instead of a wave. The energy E carried by this particle of light (or photon) is equal to the frequency ν of the light multiplied by Planck's constant h. By conservation of energy, the kinetic energy of the ejected electron is described by the following equation;

$$\frac{1}{2}m_e v^2 = h\nu - \Phi \tag{2.22}$$

where m_e and v are the mass and velocity of the electron and Φ is the workfunction. The workfunction is characteristic of the material being studied and is equal to the energy required to remove an electron from the material to infinity. Ejection of the electron cannot occur if the frequency of the light is such that $\Phi > h\nu$.

2.3.2 X-ray Photoelectron Spectroscopy in Surface Analysis

In modern surface science, XPS is used to determine the composition of the top few nanometers of a sample [67]. This section only considers the ejection of core electrons and not valence electrons. For study of the electron valence band, it is common to use ultraviolet photoelectron spectroscopy, simply because less energy is required for the photoemission of valence electrons.

A slightly modified version of equation 2.22 is used to determine the binding energy of the ejected core electrons;

$$\frac{1}{2}m_e v^2 = h\nu - E_B - \Phi \tag{2.23}$$

Here, E_B refers to the binding energy of electron in the solid and Φ, the "workfunction", depends on the sample and the spectrometer and is usually determined by calibration of the spectrometer energy scale. This equation assumes that the electron ejection process is elastic. For a monochromatic X-ray source, a discrete selection of electron kinetic energies should be produced corresponding to the binding energies of the electrons in the sample. An illustration of the photoemission process is shown in Figure 2.14.

In a typical XPS wide spectrum (Figure 2.15) a series of core electron peaks are observed on a background which generally increases with decreasing electron kinetic energy (increasing binding energy). The background signal increase occurs step-wise on the low kinetic energy side of prominent peaks. This increase is caused by a loss of kinetic energy from the photoemission electrons within the solid by various inelastic processes.

The peaks due to emission from core electron shells can vary in width and (slightly) in position, and can also appear as doublets with specific area ratios.

The position of the peak, although characteristic of the material and electron orbital can vary with the chemical environment in which the atom is located. This variation in chemical environment can be due to a difference in oxidation state, lattice site or bonding to an element with high electronegativity. It is well known that electronegative elements such as the halogens, oxygen and nitrogen, when bonded to carbon can produce a shift of 1-3 eV in the C 1s binding energy, relative to the binding energy of C bonded to C or H. These small shifts allow deconvolution of the C 1s peak in polymers

and similar materials to indicate successful surface modification or oxidation.

The width of the core peaks depends on the resolution of the spectrometer, the width of the photon source and the inherent width of the core level.

Doublet core levels arise from spin-orbit coupling which is dependent on the value of j ($= l \pm s$) of the orbital. For s orbitals $l = 0$ so $j = 1/2$, there is no spin-orbit coupling, and hence the s core electron peaks are not doublets. The relative intensities of the doublets are given by the degeneracy ($= 2j + 1$) of the levels. For a p orbital $j = 3/2$ or $1/2$ with degeneracies of 4 and 2, respectively. This means that the doublet produced by a p core electron peak will have an intensity ratio of 2/1, the weaker peak (lower j value) having the higher binding energy.

Other signals observed in the XPS spectrum are X-ray satellite peaks, Auger electron peaks and plasmon loss peaks. Throughout this study, Mg Kα radiation was used to excite the photoemission process and produce the strong, sharp, core peaks displayed in Figure 2.15. This radiation source is not monochromated, leading to the emission of electrons by lines other than the principal line. In this case, the X-ray satellite peak produced by the extra excitation line is very weak and appears at approximately 10 eV lower binding energy than the main core electron peak.

A process related to photoelectric emission is Auger electron emission. When a core electron is ejected, a vacancy is left. This vacancy is filled by the decay of an electron from the valence shell into the core. The excess energy produced by this process leads to the ejection of an electron from the valence shell, a so-called Auger electron. In Auger electron spectroscopy, the excitation is caused by bombarding the surface with electrons. When a core electron is emitted in XPS, this decay and release of an Auger electron mechanism also occurs and the Auger electrons are detected. In the spectrum shown in Figure 2.15, the features at ∼750 and ∼1000 eV are due to Auger electrons.

The final signal, the plasmon loss peak, is produced by an inelastic emission. When an electron with sufficient energy passes through a solid, it can lose energy by exciting collective oscillations of the electrons. An electron that has lost energy by the excitation of these plasmon modes is said to have suffered plasmon loss. The plasmon loss peak appears at lower kinetic or higher binding energy than a core peak. The separation between the two should be characteristic of the material being studied. A plasmon loss peak can be seen at slightly higher binding energy than the strongest core signal in Figure 2.15.

2.3.3 X-Ray Photoelectron Spectroscopy of Amorphous Carbon

XPS has two main uses in the analysis of amorphous carbon; Determination of the sp^2/sp^3 ratio of the surface carbon and evaluation of the surface composition of the sample.

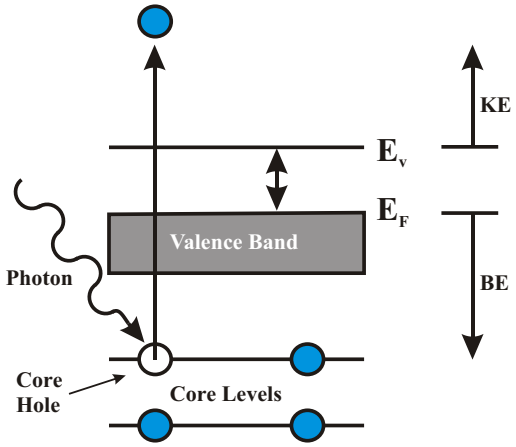

Figure 2.14: Illustration of the X-ray photoelectron emission process. E_V and E_F are the vacuum and Fermi levels respectively

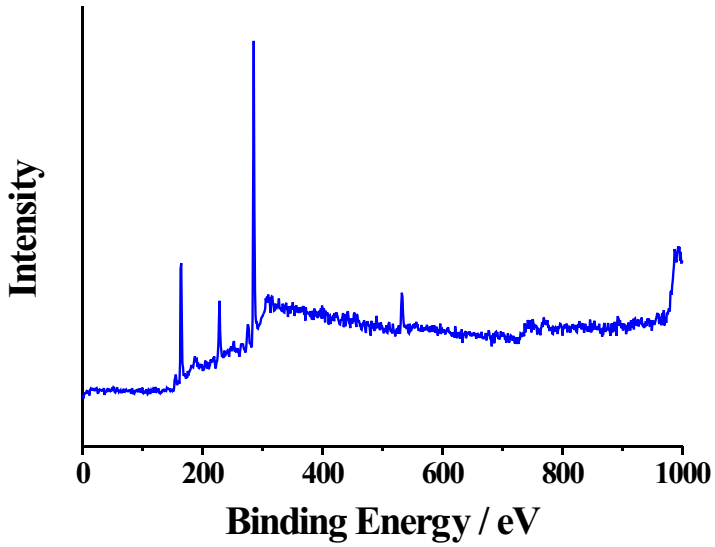

Figure 2.15: A Typical XPS spectrum of amorphous carbon.

The sp^2/sp^3 ratio is calculated by fitting of a high resolution C 1s peak profile into separate sp^2, sp^3 and C-bonded-to-O components [68–72]. The fitting process uses 3 Gaussian functions, one for each component, and a Shirley background (smooth step-shaped background). The ratio of the area of the sp^2 peak to the sp^3 peak is equal to the sp^2/sp^3 ratio of the film.

Compositional analysis has been performed by many groups on amorphous carbon films doped with various different elements [49,73–75]. Despite only analysing the very surface of the samples, clear relationships were found between the amount of dopant in the sample and in the initial conditions (gas phase proportion, target concentration, etc.). Many of these groups also deconvolute the high resolution spectra to try to determine the relative proportions of different bonding configurations of the different constituent elements.

In this study (section 3.3.1), XPS is used to determine the effect of different deposition conditions on the efficiency of the incorporation of sulfur into amorphous carbon. Deconvolution of the high resolution spectra is not attempted due to the large number of different bonding environments likely to be present (C-C sp^2 and sp^3, C-S sp^2 and sp^3, as well as those involving hydrogen).

2.4 Secondary Ion Mass Spectrometry

This section discusses the technique of Secondary Ion Mass Spectrometry (SIMS) and its use in the analysis of amorphous carbon films. All SIMS measurements analysed in this study were performed by Dr. Sean Pearce at the Interface Analysis Centre, Bristol.

In SIMS, the surface of a sample is bombarded with heavy ions (primary ions) causing electrons, atoms and clusters to be sputtered from the sample (Figure 2.16). The composition of the ejected ion plume (secondary ions) is analysed by mass spectrometry [76, 77]. The primary ion used for sputtering is generally Ar^+, Ga^+ or Cs^+. Sputtered material is ejected as neutrals, ions both positive and negative, singly and multiply charged, and as clusters of particles. The positive and negative ions are not detected at the same time, SIMS is either run in positive or negative mode. In each of these modes the sample is biased with the same polarity as the ions of interest to accelerate them away from the sample and into the mass spectrometer. SIMS is a very sensitive surface analysis method and is frequently used to detect low concentrations of dopant atoms in solids.

The probability that a particular atom or cluster is ionised depends on the stability of the ion, its ionisation energy (or electron affinity) and the properties of the solid sample. All these different factors make the quantification of a SIMS mass spectrum difficult.

By focusing the primary ion beam on the same area of a sample for a long period

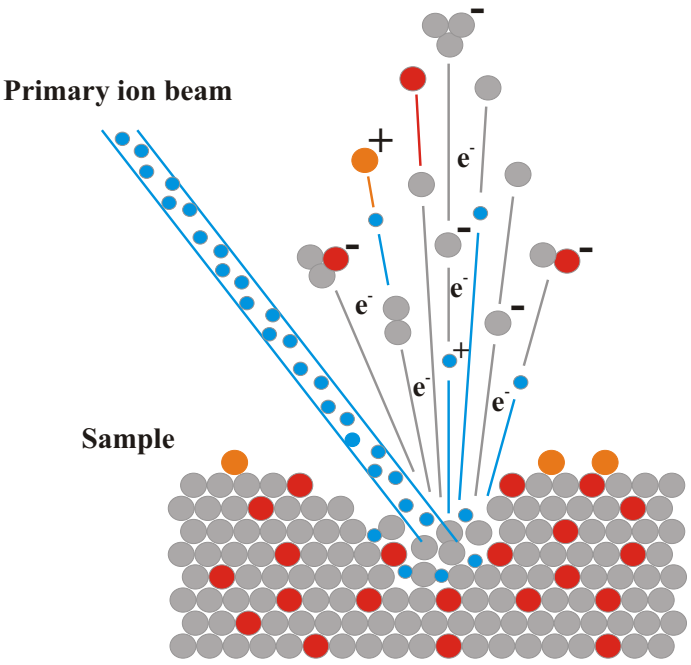

Figure 2.16: Illustration of the sputtering process involved in SIMS.

of time it is possible to sputter through the sample. A depth profile of the variation in concentration of sample constituents can be made by this method. For the depth profile of a low level dopant in a matrix of constant composition many of the problems of quantification can be ignored. A depth profile usually displays the number of counts as a function of the etch time. If the sample is etched through to the substrate and the sample thickness is known, the depth profile can be displayed as a function of sample depth instead of time. It is often not possible to do this for thick samples or for measurements taken with low primary ion beam currents, where the etch-rate is slow.

It is also possible to use SIMS to create an elemental map of the sample surface. This is very useful because it can be used to relate the composition of the sample to the morphology or to check the uniformity across the sample. To create an elemental map the signal of a specific ion is monitored as the ion beam is rastered across the surface. As well as ejecting ions, the sputtering process causes the liberation of secondary electrons. These electrons can be detected and used to produce an image of the surface in a similar manner to a scanning electron microscope. Combinations of depth profiling and elemental mapping can be used to great effect when determining the homogeneity of a sample.

2.4.1 Secondary Ion Mass Spectrometry of Amorphous Carbon

In the study of amorphous carbons, SIMS is generally used to determine the uniformity of the distribution of dopant atoms.

Vainonen-Ahlgren *et al.* [78] used SIMS to study the diffusion of Si atoms during the annealing of amorphous carbon. The samples were implanted with $^{30}Si^{+}$ ions, then depth profiled to determine the distribution of ^{30}Si throughout the sample thickness. Samples were then annealed at various temperatures, and depth profiled again to observe how the silicon distribution had changed.

Pearce *et al.* [75] studied the high-level doping of amorphous carbon films to produce amorphous "carbon-phosphide" films. They used SIMS depth profiling to determine the uniformity of the phosphorous and carbon distribution within their samples.

The previous studies only used SIMS in negative ion mode. Lampertia *et al.* [79] used SIMS in both positive and negative ion modes to study a-C:F:H films. The positive ion mass spectrum was dominated by peaks due to contaminants such as Na, Al, K and Ca, whereas the negative ion mode shows ions of small C/H/F compounds. They also produced elemental maps showing the surface distribution of fluorine. Nakamura *et al.* [80] used photolysis of perfluoroazooctane to surface fluorinate their amorphous carbon films. They used negative ion SIMS to detect the presence of F at the film surface.

In this study (section 3.3.2) SIMS is used to determine the uniformity of the distribution of sulfur in a-C:S:H films. Elemental maps are used to determine the surface composition and depth profiles are used to access the homogeneity of the sample.

2.5 UV/Visible Absorption Spectroscopy

Semiconductors have a fundamental absorption edge in the near-IR, visible or ultraviolet spectral region. The absorption edge is caused by the energy of the photons exceeding the energy required to promote an electron in the valence band across the band gap into the conduction band [81]. This section describes the determination of the optical band gap energy of amorphous carbon by UV/Vis absorption spectroscopy.

In UV/Vis spectroscopy, light is passed through a sample and the difference between the initial and final intensities are recorded. The spectrum produced is displayed as wavelength against absorbance, where absorbance is defined by the following equation;

$$\text{Absorbance} = -\log_{10}\left(\frac{I(l)}{I(0)}\right) \tag{2.24}$$

where $I(0)$ and $I(l)$ are the initial light intensity and the light intensity after a distance

l through the sample, respectively. If the thickness of the sample is known Beer's law can be used;

$$I(l) = I(0)e^{-\alpha l} \tag{2.25}$$

to calculate the absorption coefficient from the absorbance.

$$\text{Absorbance} = \frac{\alpha l}{\ln(10)} \tag{2.26}$$

In a crystal, the band gap is defined as the minimum energy between the occupied valence band and empty conduction band states. For an amorphous semiconductor, the situation is slightly more complicated because there is no true gap. Instead an arbitrary definition must be used for the optical gap. The two most common definitions are the E_{04} and the Tauc band gaps. The E_{04} band gap takes the value of the photon energy for which the absorption coefficient equals 10^4. The Tauc gap is found by extrapolating the linear part of a plot of $(\alpha E)^{(1/2)}$ against the photon energy. The intercept of this line with the energy axis gives the value of the Tauc optical gap.

2.5.1 UV/Vis Absorption Spectroscopy of Amorphous Carbon

The optical band gap energy is directly related to the structure within the amorphous carbon sample. Diamond has a large indirect band gap of 5.5 eV whereas graphite has effectively no band gap. Clearly then, the more diamond-like a sample the larger its optical band gap will be. The largest published value for the optical band gap of a non-hydrogenated amorphous carbon film is 3.5 eV (E_{04}) [82]. The film was deposited using a filtered cathodic arc system and had an sp^3 fraction of approximately 88%. The situation is complicated by the addition of hydrogen. Polymeric hydrogenated amorphous carbon films have been deposited with optical gaps as high as 4 eV (E_{04}) [83]. The hydrogen stabilises the sp^3-hybridised carbon producing a film with a wide band gap. While stabilising the sp^3-hybridised carbon, the presence of hydrogen also makes the films more polymer-like than diamond-like, so they tend to be very soft.

The optical band gap of an amorphous carbon film is strongly dependent on the conditions from which the film is deposited. Lacerda *et al.* [84] studied the variation in the Tauc band gap as a function of the deposition bias of a methane discharge. They found that as the bias was increased the films became more graphitic in nature, the hydrogen content increased and the optical band gap decreased. Chhowalla *et al.* [85] studied the optical band gap as a function of the ion energy of their filtered cathodic

vacuum arc and the substrate temperature. They found that the maximum value of the optical gap was produced with an ion impact energy of 100 eV and temperature below 100°C. These observations are consistent with the subplantation growth mechanism (section 1.3.1).

In this study UV/Vis and spectroscopic ellipsometry are used to determine how the optical band gaps of our samples vary with deposition conditions, specifically the concentration of sulfur incorporated (section 3.5.2). Several groups [51, 86, 87] have studied the variation in the optical band gap with the addition of a dopant element. Since the optical gap is related to the graphitisation of the sample, the results of these studies are similar to those discussed in the section dealing with Raman spectroscopy of amorphous carbon (section 2.1.4).

2.6 Ellipsometry

2.6.1 Theory of Ellipsometry

Ellipsometry is a sensitive and non-destructive technique used to measure the thickness and optical constants of thin films [88]. The technique works by measuring the change in polarisation of a light wave with reflection off a surface. To understand the theory behind this effect let us first define the optical constants n and k and also the three types of polarisation; linear, circular and elliptical, and describe how they interact with surfaces.

Optical Constants of Materials

The optical properties of materials are described by the complex refractive index $\tilde{n}$;

$$\tilde{n} = n + ik \tag{2.27}$$

where the real part of the equation, n is the refractive index and the imaginary part, k is the extinction coefficient.

The refractive index is defined as the ratio of the velocity of light in free space c to the velocity of light in the material v, $n = c/v$. The value of the refractive index is dependent on the frequency of the light (an effect called dispersion), although over the visible region the dispersion of a transparent material is small.

The extinction coefficient describes the absorption of light by the material. Its value is directly proportional to the absorption coefficient α;

$$k = \frac{\alpha\lambda}{4\pi} \tag{2.28}$$

where λ is the wavelength of light.

Polarisation

Consider the linearly polarised light wave shown in Figure 2.17(a). The blue line represents the electric field, which is oscillating in the x-direction as the wave propagates in the z-direction. The red arrow shows the nett electric field viewed down the z-axis. To make the step from linear polarisation to circular polarisation let us first consider an off-axis linearly-polarised wave. In this case, it is possible to express the wave as two components, E_x and E_y, the projection of the wave onto the x- and y- axes, respectively. Figure 2.17(b) shows the two components of a linearly polarised light wave where the nett electric field oscillates at 45° to the x-axis. The two components are orthogonal, equal in amplitude, and in-phase.

To produce circularly-polarised light, the phase of one of the components needs to be shifted by 90° in the z direction, as in Figure 2.17 . This makes the components perfectly out of phase, when one is at maximum amplitude the other is at zero amplitude, and vice versa. The net electric field of these two components, viewed down the z-axis, now traces a circle, hence the light is circularly polarised.

If the amplitudes of the two components are not equal and/or the components are not perfectly in or out of phase, elliptically-polarised light results. Linearly- and circularly-polarised light are actually just subsets of elliptically-polarised light.

Reflection and Brewster's Angle

To explain fully how ellipsometry works, let us include a surface in the scenario. If a light wave is reflected off a surface, a plane of incidence perpendicular to the surface is created (Figure 2.18). The components of the light wave can now be re-defined with respect to the surface. The x-component becomes the p-component ("P" for parallel to the plane of incidence) and the y-component becomes the s-component ("S" for senkrecht, German for perpendicular). Ellipsometry works because these two components reflect differently from a sample depending on the angle of incidence. The angle of incidence at which the difference between the reflected intensity of the s- and p- components is maximised, is known as the Brewster angle. The Brewster angle for light reflected from the interface of two transparent media is described by the equation;

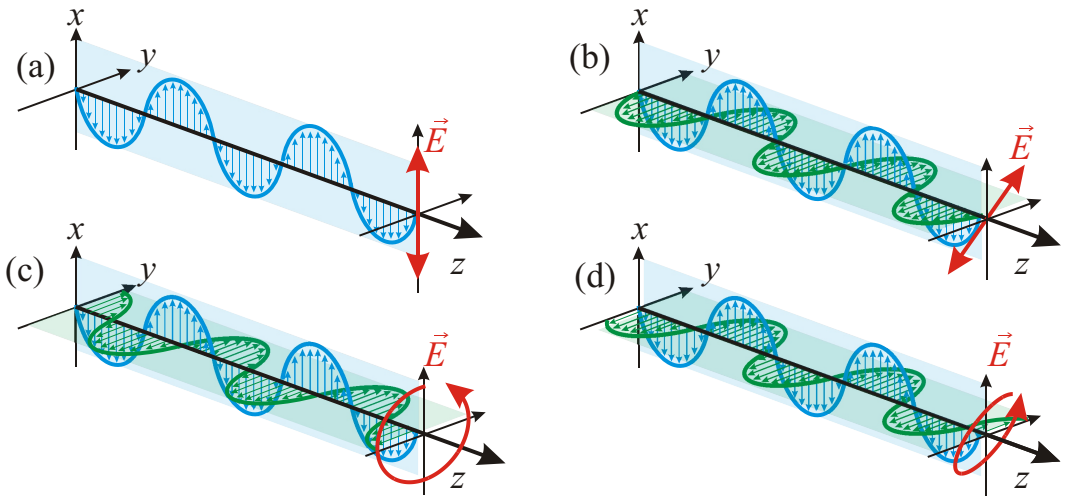

Figure 2.17: Electric field components for, (a) linearly-polarised light, (b) off-axis linearly-polarised light, (c) circularly-polarised light, and (d) elliptically-polarised light.

$$\phi_B = \arctan(n_2/n_1) \tag{2.29}$$

where n_x is the refractive index of each material. At this angle, p-polarised radiation is totally refracted into the second medium, there is no reflected p-component. A consequence of this is that any elliptically-polarised light incident on the surface of a non-absorbing material at the Brewster angle (except for linear p-polarised) is reflected linearly s-polarised.

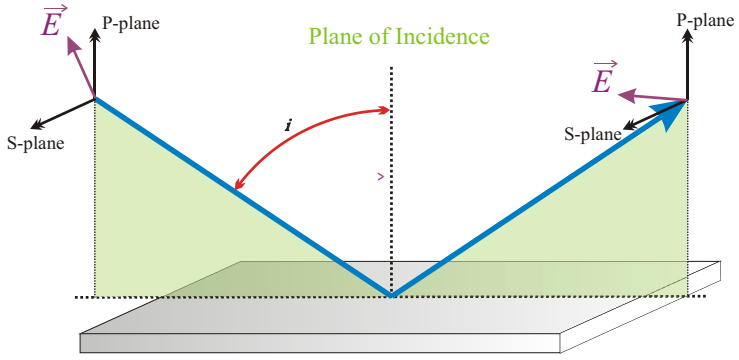

Figure 2.18: Reflection of light from a surface showing the angle and plane of incidence.

Fresnel Reflection Coefficients

To improve the description even further let us add a thin film to the surface. To not overly complicate the situation, it is assumed that the film is thin and transparent, the substrate is optically thick (no back reflections) and that both media are isotropic (Figure 2.19). When the incident light strikes the sample it, in principle, forms an infinite series of multiple reflections within the thin film. However the splitting of the light beam into reflected and transmitted components means the intensity eventually dies out.

For the reflection off a bulk sample, the change in the magnitude of the electric field in each direction (E_p and E_s) is described by the Fresnel reflection coefficients r_p and r_s;

$$r_p \equiv \frac{E_p^{\text{reflected}}}{E_p^{\text{incident}}} = \frac{n_1 \cos\phi_0 - n_0 \cos\phi_1}{n_1 \cos\phi_0 + n_0 \cos\phi_1} \tag{2.30}$$

$$r_s \equiv \frac{E_s^{\text{reflected}}}{E_s^{\text{incident}}} = \frac{n_0 \cos\phi_0 - n_1 \cos\phi_1}{n_0 \cos\phi 0 + n_1 \cos\phi_1} \tag{2.31}$$

where n_0 and n_1 are the ambient and bulk refractive indices and ϕ_0 and ϕ_1 are the angles of reflectance and transmittance, respectively.

Returning to the thin film example, the pseudo-Fresnel reflection coefficients (R_p and R_s), for the p-polarised component, are described by;

$$R_p = \frac{r_{01}^p + r_{01}^p e^{-i2\beta}}{1 + r_{01}^p r_{12}^p e^{-i2\beta}} \tag{2.32}$$

where r_{ij}^p is the reflection coefficient of the interface between the i and j layers and β is the film phase thickness (optical thickness) given by;

$$\beta = 2\pi \frac{d}{\lambda} \sqrt{n_1^2 - n_0^2 \sin^2\phi_0} \tag{2.33}$$

where d is the film thickness and λ is the wavelength of the light. The same formulae are used for the s-component but subscript p is replaced by subscript s.

Ellipsometry Measurements

The values actually measured by ellipsometry are the amplitude ratio Ψ and phase difference Δ between the incident and reflected components. These values are a func-

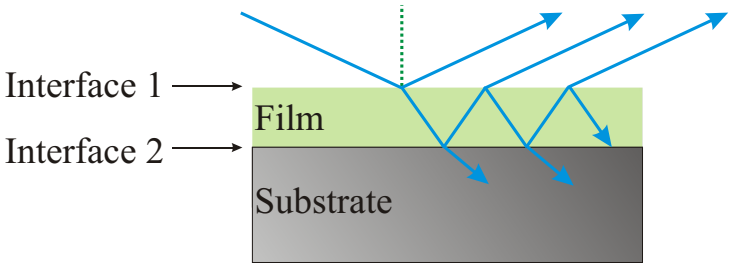

Figure 2.19: Multiple reflections from a thin film at an interface.

tion of the ratio of the pseudo-Fresnel reflection coefficients as given by the following equation;

$$\rho = R_p/R_s = tan(\Psi)e^{i\Delta} \tag{2.34}$$

where the pseudo-Fresnel reflection coefficients R_p and R_s are related to the incident and reflected beams for each polarisation by (for p-polarisation);

$$R_p \equiv \frac{E^r_{\text{total}}}{E^{\text{incident}}} \tag{2.35}$$

and similarly for R_s.

Data Analysis

By itself, the data obtained from ellipsometry is of little use. The measured values (Ψ and Δ) are functions of the optical constants, thicknesses, interfacial roughnesses, etc., of the entire sample being analysed. The only way to extract the thickness and optical constants of a specific layer of the sample is by model-based analysis. Generally, the sample modelling is performed on specifically-written software and involves an iterative fitting process to minimise some error function describing the difference between the experimental and the generated data.

Let us use measurement of the native oxide layer thickness on a silicon wafer as a simple example. Both silicon and SiO_2 have well know optical constants so the only variable in the equation is the thickness of the oxide layer. Figure 2.20 (a) shows the experimentally obtained values of Ψ and Δ at 70 and 75° between 300 and 1000 nm. To start the fitting procedure a model of the sample must be made. In this case the model is quite simple; x nm of SiO_2 on bulk (optically thick, no back face reflections)

silicon. The wafer in this example is mirror polished so there is no requirement for a roughness layer at the SiO_2/air interface. The back of the silicon is rough, so there should be no backside reflections to complicate the fitting. After creating the rough model an educated guess at any unknown parameters must be made, in this case the thickness of the oxide layer. If the starting guess is far from the actual value, the iterative fitting might converge to a local minimum and not produce a sensible fit with a low mean squared error (MSE). Figure 2.20 shows the data generated from the model for (b) a 200 nm oxide layer and (c) a 5 nm oxide layer. It is clear that the 5 nm is a much better starting approximation than the 200 nm oxide, although as the analysed sample gets more complicated and there are more unknown parameters, the initial guess becomes more difficult. Allowing the software to iterate the 5 nm initial thickness, it quickly arrives at a minimum MSE corresponding to an oxide thickness of 2.7 nm (Figure 2.20(d)), a reasonably standard thickness for a native SiO_2 layer.

2.6.2 Spectroscopic Ellipsometry of Amorphous Carbon

The above example of finding film thickness when optical constants of all components are known is relatively trivial. In practice, it is not always possible to know either the film thickness or the dispersion of the optical constants, in which case, model-based analysis becomes considerably more difficult. In cases such as these, it is necessary to enforce some type of dispersion on the optical constants using a suitable parameterised model.

The two models most commonly used to model the optical properties of amorphous semiconductors, such as amorphous carbon, were developed by Forouhi and Bloomer [89] and Jellison and Modine [90, 91]. The model produced by Jellison and Modine is based on similar approximations to the earlier Forouhi and Bloomer model, but corrects some of the problems associated with this model. The Jellison and Modine model is also called the Tauc-Lorentz model, because it uses the Tauc expression for the imaginary part of the complex dielectric function (which is related to the complex refractive index) near the band edge and the Lorentz expression for the imaginary part of the complex dielectric function of a Lorentz oscillator [92].

The parameterised models are used to determine the sample thickness and the values of the refractive index n and extinction co-efficient k. For amorphous carbon films, the sample thickness can be used to determine the growth rate, n relates to the hardness and resistance to laser damage [93] of the sample, and k can be used to calculate the absorption co-efficient which (as in UV/Vis) allows the determination of the optical bandgap [94–96].

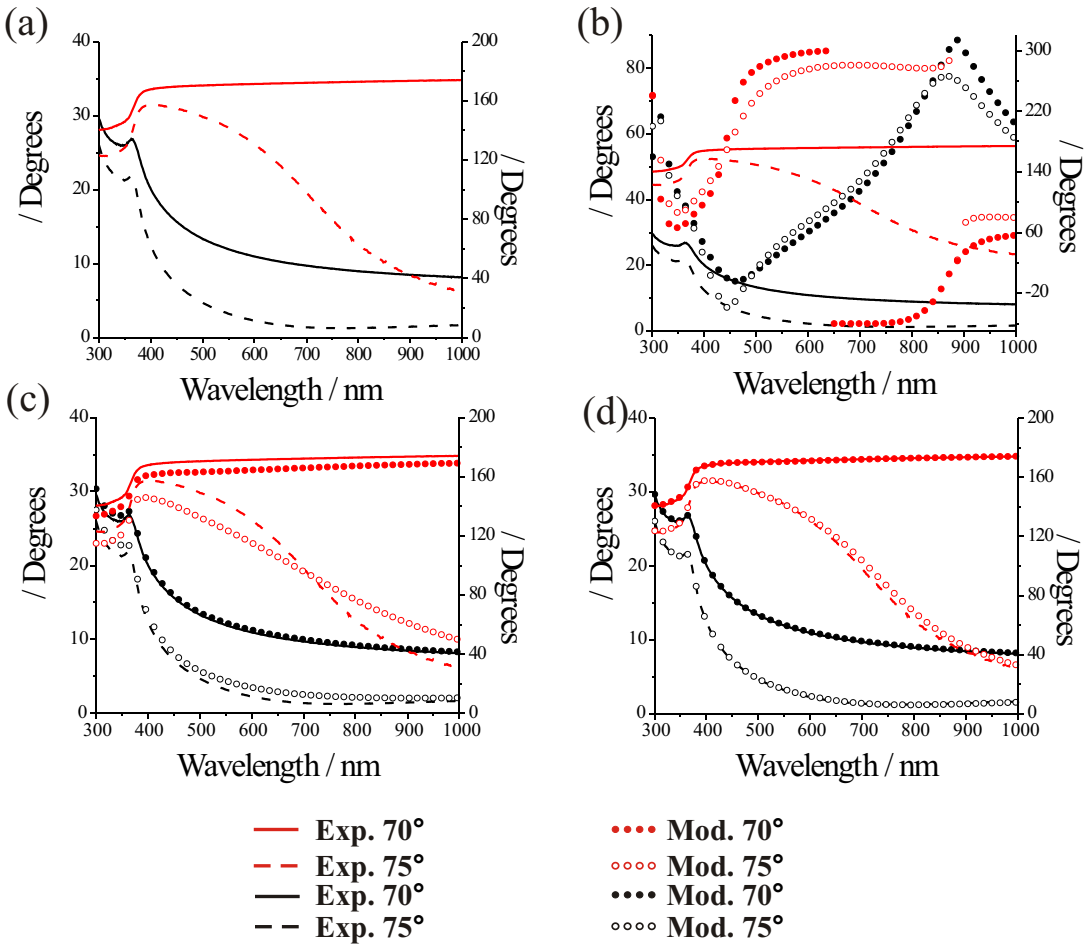

Figure 2.20: Ellipsometry data for the native oxide layer on a silicon wafer, (a) Experimental data, (b) Experimental data and model data for a 200 nm oxide layer, (c) Experimental data and model data for a 5 nm oxide layer, (d) Experimental data and fitted model data giving 2.7 nm as the oxide layer thickness.

2.6.3 Ellipsometry method

In this study, ellipsometry measurements were performed using a JA Woollam Co., Inc. M2000U variable angle spectroscopic ellipsometer. Figure 2.21 is diagram showing the arrangement of the main optical components of this system. The light source is a lamp which projects a beam of white light toward the sample. The beam passes through a polariser and a rotating compensator creating linearly and then circularly polarised light. The circularly-polarised beam reflects off the sample and passes through an analyser which converts it to linearly-polarised light before it is detected by dispersal onto a CCD detector array.

Spectra were acquired over the range 200-1000 nm at angles of 55, 60, 65, 70 and 75°. The sample thickness and optical properties were determined by fitting the plots of Ψ and Δ against wavelength at different angles with modelled data. The model used was a layer of amorphous semiconductor on optically thick silicon. The optical properties of the amorphous semiconductor layer were described by the Tauc-Lorentz model, the optical properties of the bulk silicon were taken from standard tables. The film thickness and 5 parameters of the Tauc-Lorentz model were used for fitting. Quality of fit was determined by the value of the mean squared error. Once this value is minimised with respect to the fitting parameters the optical properties of the sample can be obtained. To determine the optical band gap of the amorphous carbon films the value of the absorption coefficient α was calculated from the extinction coefficient using the following equation;

$$\alpha = \frac{4\pi k}{\lambda} \tag{2.36}$$

where λ is the wavelength specific to the value of k. The optical band gap energy is then calculated using the same methods as for UV/Vis absorption spectroscopy described in section 2.5.

2.7 Micro-Combustion Elemental Analysis

In this study, micro-combustion elemental analysis was performed by Des Davis in the Macromolecular Lab at the School of Chemistry, University of Bristol.

Micro-combustion elemental analysis is a relatively simple method of determining the composition of organic materials. Elements detectable by these methods include carbon, hydrogen, nitrogen, the halogens, sulfur and oxygen [97].

Samples are packed into an oxidisable container and then dropped into a heated quartz tube, through which a constant flow of helium is passed. As the sample is

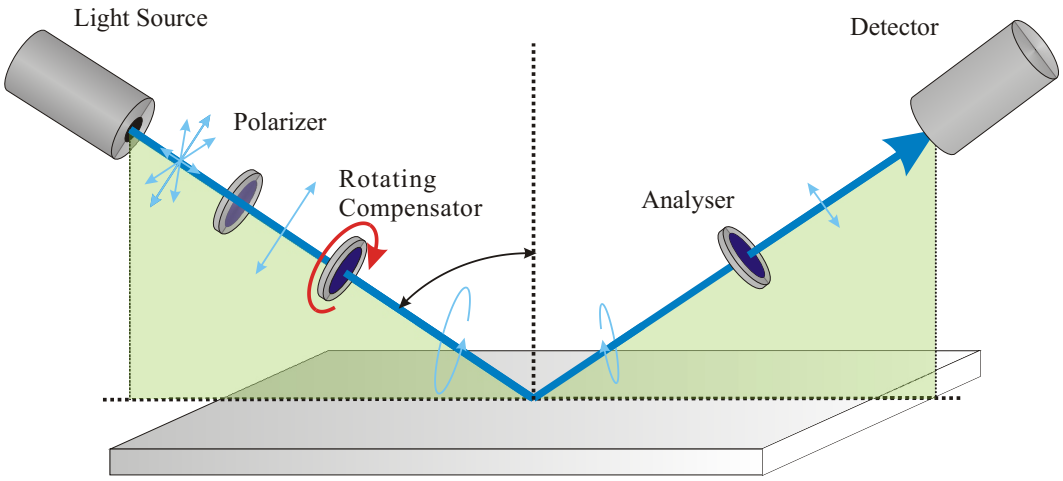

Figure 2.21: Schematic diagram of the ellipsometer.

introduced, oxygen is added to the helium stream causing combustion of the sample. All carbon, hydrogen and nitrogen in the sample are converted to CO_2, H_2O and NO_x during the flash combustion. The inert flow of helium carries these compounds over heated copper, reducing the NO_x to N_2. The gases are then separated by a gas chromatograph and detected by thermal conductivity measurements.

2.8 Micro-Combustion Elemental Analysis of Amorphous Carbon

The use of micro-combustion to determine the elemental composition of amorphous carbons is fairly uncommon. This is possibly due to the relatively large amount of material required and the difficulty in removing the sample from the substrate. Preferred techniques include X-ray photoelectron spectroscopy and Rutherford back scattering spectrometry which permit the analysis of a thin film on a substrate. The advantage micro-combustion has over XPS is the detection of hydrogen which exists in large quantities in a-C:H films.

Previous studies by our group have used micro-combustion elemental analysis to determine the hydrogen content of a-C:H films. The a-C:H films were either deposited by RF PECVD of methane [72] or pulsed laser ablation of poly methyl-methacrylate [98]. In this study, various methods were used to produce the ∼10 mg of amorphous carbon required for micro-combustion elemental analysis. Details of these experiments can be found in section 3.11.1.

Bibliography

[1] A. Smekal, *Die Naturwissenschaften*, 1923, **43**, 873.

[2] C. V. Raman and K. S. Krishnan, *Nature*, 1928, **121**, 501.

[3] P. Atkins and F. RS, *Molecular Quantum Mechanics*, Oxford University Press, Oxford, 1997.

[4] E. Smith and G. Dent, *Modern Raman Spectroscopy: A Practical Approach*, Wiley, Chichester, 2005.

[5] ed. H. Szymanski, *Raman Spectroscopy: Theory and Practice*, Plenum Press, New York, 1967.

[6] M. Dove, *Structure and Dynamics: An Atomic View of Materials*, Oxford University Press, Oxford, 2003.

[7] P. Ossi, *Disordered Materials: An Introduction*, Springer, Berlin, 2003.

[8] S. Reich, C. Thomsen, and J. Maultzsch, *Carbon Nanotubes*, Wiley-VCH, Weinheim, 2004.

[9] C. Kittel, *Introduction to Solid State Physics*, Wiley, Hoboken, NJ, 1996.

[10] A. Putnis, *Introduction to Mineral Sciences*, Cambridge University Press, Cambridge, 1992.

[11] H. Barańska and A. labudzińska J. Terpiński, *Laser Raman Spectroscopy - analytical applications*, Ellis Horwood Limited, Chichester, 1987.

[12] P. Atkins, *Physical Chemistry*, Oxford University Press, Oxford, 1998.

[13] A. Szabo and N. S. Ostlund, *Modern quantum chemistry :introduction to advanced electronic structure theory*, Macmillan Publishing Co., Inc., New York, 1989.

[14] D. M. Hirst, *A computational approach to chemistry*, Blackwell Scientific, Oxford, 1990.

[15] W. Koch and M. C. Holthausen, *A chemist's guide to density functional theory*, Wiley-VCH, Weinheim, 2001.

[16] A. R. Leach, *Molecular modelling: principles and applications*, Prentice Hall, Harlow, 2001.

[17] R. O. Jones and O. Gunnarsson, *Rev. Mod. Phys.*, 1989, **61**, 689.

[18] A. D. Becke, *J. Chem. Phys.*, 1993, **98**, 5648.

[19] W. Cornell, P. Cieplak, C. Bayly, I. Gould, K. Mertz, D. Ferguson, D. Spellmeyer, T. Fox, J. Caldwell, and P. Kollman, *J. Am. Chem. Soc.*, 1995, **117**, 5179.

[20] M. J. Frisch, G. W. Trucks, H. B. Schlegel, G. E. Scuseria, M. A. Robb, J. R. Cheeseman, J. A. Montgomery, Jr., T. Vreven, K. N. Kudin, J. C. Burant, J. M. Millam, S. S. Iyengar, J. Tomasi, V. Barone, B. Mennucci, M. Cossi, G. S. N. Rega, G. A. Petersson, H. Nakatsuji, M. Hada, M. Ehara, K. Toyota, R. Fukuda, J. Hasegawa, M. Ishida, T. Nakajima, Y. Honda, O. Kitao, H. Nakai, M. K. X. Li, J. E. Knox, H. P. Hratchian, J. B. Cross, C. Adamo, J. Jaramillo, R. Gomperts, R. E. Stratmann, O. Yazyev, A. J. Austin, R. Cammi, C. Pomelli, J. W. Ochterski, P. Y. Ayala, K. Morokuma, G. A. Voth, P. Salvador, J. J. Dannenberg, V. G. Zakrzewski, S. Dapprich, A. D. Daniels, M. C. Strain, O. Farkas, D. K. Malick, A. D. Rabuck, K. Raghavachari, J. B. Foresman, J. V. Ortiz, Q. Cui, A. G. Baboul, S. Clifford, J. Cioslowski, B. B. Stefanov, G. Liu, A. Liashenko, P. Piskorz, I. Komaromi, R. L. Martin, D. J. Fox, T. Keith, M. A. Al-Laham, C. Y. Peng, A. Nanayakkara, M. Challacombe, P. M. W. Gill, B. Johnson, W. Chen, M. W. Wong, C. Gonzalez, and J. A. Pople, Gaussian 03, revision b.04, 2003.

[21] R. Bailey, *Spectrochim. Acta Part A*, 1971, **27**, 1447.

[22] R. G. Snyder and J. H. Schachtschneider, *Spectrochim. Acta*, 1965, **21**, 169.

[23] P. C. E.B. Wilson Jr., J.C. Decius, *Molecular vibrations :the theory of infrared and Raman vibrational spectra*, McGraw-Hill Book Company, Inc. New York, 1955.

[24] S. G. and K. A., *Molecular Physics*, 1999, **96**, 161–167.

[25] J. O. Jensen, *Spectrochim. Acta Part A*, 2004, **60**, 1895.

[26] L. Bistriĉić, G. Baranović, and K. Mlinarić-Majerski, *J. Mol. Struct.*, 1999, **508**(1-3), 207–215.

[27] L. Bistriĉić, L. Pejov, and G. Baranović, *J. Mol. Struct. Theochem.*, 2002, **594**, 79.

[28] L. Rivas, S. Sanchez-Cortes, J. Stanicova, J. V. Garcia-Ramos, and P. Miskovsky, *Vibrational Spectroscopy*, 1999, **20**(2), 179.

[29] A. Kovacs and A. Szabo, *J. Mol. Struct.*, 2000, **519**, 13.

[30] T. E. Jenkins and J. Lewis, *Spectrochim. Acta Part A*, 1980, **36**, 259.

[31] P. W. May, S. H. Ashworth, C. D. O. Pickard, M. N. R. Ashfold, T. Peakman, and J. W. Steeds, *Phys. Chem. Comm.*, 1998, **4**.

[32] J. E. P. Dahl, J. M. Moldowan, T. M. Peakman, J. C. Clardy, E. Lobkovsky, M. M. Olmstead, P. W. May, T. J. Davis, J. W. Steeds, K. E. Peters, A. Pepper, A. Ekuan, and R. M. K. Carlson, *Angew. Chem. Int. Ed.*, 2003, **42**, 2040.

[33] S. L. Richardson, T. Baruah, M. J. Mehl, and M. R. Pederson, *Chem. Phys. Lett*, 2005, **403**, 83.

[34] Y. F. Chang, Y. L. Zhao, M. Zhao, P. J. Liu, and R. S. Wang, *Acta Chimica Sinica*, 2004, **62**, 1867.

[35] A. J. Lu, B. C. Pan, and J. G. Han, *Phys. Rev. B.*, 2005, **72**, 035447.

[36] J. E. Dahl, S. G. Liu, and R. M. K. Carlson, *Science*, 2003, **299**, 96.

[37] J. Filik, J. Harvey, N. Allan, P. May, J. Dahl, S. Liu, and R. Carlson, *Spectrochim. Acta A. Mol. Biomol. Spect.*, 2006, **64**, 681.

[38] S. A. Solin and A. K. Ramdas, *Phys. Rev. B.*, 1970, **1**, 1687.

[39] F. Tuinstra and J. L. Koenig, *J. Chem. Phys.*, 1970, **53**, 1126.

[40] R. Alben, D. Weaire, J. E. S. Jr., and M. H. Brodsky, *Phys. Rev. B.*, 1975, **11**, 2271.

[41] A. C. Ferrari and J. Robertson, *Phys. Rev. B.*, 2000, **61**, 14095.

[42] M. Chhowalla, A. C. Ferrari, J. Robertson, and G. A. J. Amaratunga, *Appl. Phys. Lett.*, 2000, **76**, 1419.

[43] J. Robertson, *Mater. Sci. Eng. R*, 2002, **37**, 129.

[44] D. P. Magill, A. A. Ogwu, J. A. McLaughlin, P. D. Maguire, R. W. McCullough, D. Voulot, and D. Gillen, *J. Vac. Sci. Technol. A*, 2001, **19**, 2456.

[45] J. Schwan, V. Batori, S. Ulrich, H. Ehrhardt, and S. R. P. Silva, *J. Appl. Phys.*, 1998, **84**, 2071.

[46] M. Guerino, M. Massi, H. S. Maciel, C. Otani, and R. D. Mansano, *Microelectronics Journal*, 2003, **34**, 639.

[47] E. Braca, G. Saraceni, J. M. Kenny, L. Lozzi, and S. Santucci, *Thin Solid Films*, 2002, **415**, 195.

[48] G. Q. Yu, S. H. Lee, D. G. Lee, H. D. Na, H. S. Park, and J. J. Lee, *Surf. Coat. Technol.*, 2002, **154**, 68.

[49] G. M. Fuge, P. W. May, K. N. Rosser, S. R. J. Pearce, and M. N. R. Ashfold, *Diam. Relat. Maters.*, 2004, **13**, 1442.

[50] M. Rusop, X. Tian, T. Kinugawa, T. Soga, T. Jimbo, and M. Umeno, *Appl. Surf. Sci.*, 2005, **252**, 1693.

[51] G. Abbas, P. Papakonstantinou, T. Okpalugo, J. McLaughlin, J. Filik, and E. Harkin-Jones, *Thin Solid Films*, 2005, **482**, 201.

[52] T. Mikami, H. Nakazawa, M. Kudo, and M. Mashita, *Thin Solid Films*, 2005, **488**, 87.

[53] G. Fuge, C. Rennick, S. Pearce, P. May, and M. Ashfold, *Diam. Relat. Maters.*, 2003, **12**, 1049.

[54] S. Prawer and R. J. Nemanich, *Phil. Trans. R. Soc. Lond. A*, 2004, **362**, 2537.

[55] O. Auciello, J. Birrell, J. A. Carlisle, J. E. Gerbi, X. Xiao, B. Peng, and H. D. Espinosa, *J. Phys.: Condens. Matter*, 2004, **16**, R539.

[56] S. Leeds, T. Davis, P. May, C. Pickard, and M. Ashfold, *Diam. Relat. Mater.*, 1998, **7**, 233.

[57] M. Yoshikawa, Y. Mori, M. Maegawa, G. Katagiri, H. Ishida, and A. Ishitani, *Appl. Phys. Lett.*, 1993, **62**, 3114.

[58] R. J. Nemanich, J. T. Glass, G. Lucovsky, and R. E. Shroder, *J. Vac. Sci. Tech. A.*, 1988, **6**, 1783.

[59] S. Prawer, K. W. Nugent, D. N. Jamieson, J. O. Orwa, L. A. Bursill, and J. L. Peng, *Chem. Phys. Lett.*, 2000, **332**, 93.

[60] R. Pfeiffer, H. Kuzmany, N. Salk, and B. Gunther, *Appl. Phys. Lett.*, 2003, **82**, 4149.

[61] A. C. Ferrari and J. Robertson, *Phys. Rev. B*, 2001, **63**, 121405.

[62] A. C. Ferrari and J. Robertson, *Phil. Trans. R. Soc. Lond. A*, 2004, **362**, 2477.

[63] H. O. Pierson, *Handbook of Chemical Vapor Deposition*, Noytes Publications, Norwich, NY, 1999.

[64] ed. D. M. Manos and D. L. Flamm, *Plasma Etching An Introduction*, Academic Press, Inc., Boston, 1989.

[65] H. R. Koenig and L. I. Maissel, *IBM J. Res. Devel.*, 1970, **14**, 168.

[66] A. van Roosmalen, J. Baggerman, and S. Brader, *Dry Etching for VLSI*, Plenum Press, New York, 1991.

[67] ed. D. Briggs and M. Seah, *Practical Surface Analysis Volume 1*, John Wiley and Sons, Chichester, 1990.

[68] S. T. Jackson and R. G. Nuzzo, *Appl. Surf. Sci.*, 1995, **90**, 195.

[69] J. Diaz, G. Paolicelli, S. Ferrer, and F. Comin, *Phys. Rev. B.*, 1996, **54**, 8064.

[70] P. Merel, M. Tabbal, M. Chaker, S. Moisa, and J. Margot, *Appl. Surf. Sci.*, 1998, **136**, 105.

[71] T. Y. Leung, W. F. Man, P. K. Lim, W. C. Chan, F. Gaspari, and S. Zukotynski, *J. Non-Cryst. Solids*, 1999, **254**, 156.

[72] J. Filik, P. W. May, S. R. J. Pearce, R. K. Wild, and K. R. Hallam, *Diam. Relat. Mater.*, 2003, **12**, 974.

[73] Y. Inoue, T. Komoguchi, H. Nakata, and O. Takai, *Thin Solid Films*, 1998, **322**, 41.

[74] Y. Hayashi, K. Krishna, H. Ebisu, T. Soga, M. Umeno, and T. Jimbo, *Diam. Relat. Mater.*, 2001, **10**, 1002.

[75] S. R. J. Pearce, P. W. May, R. K. Wild, K. R. Hallam, and P. J. Heard, *Diam. Relat. Mater.*, 2002, **11**, 1041.

[76] ed. D. Briggs and M. Seah, *Practical Surface Analysis Volume 2*, John Wiley and Sons, Chichester, 1992.

[77] L. C. Feldman and J. W. Mayer, *Fundamentals of Surface and Thin Film Analysis*, Elsevier Science Publishing Co., Inc., New York, 1986.

[78] E. Vainonen-Ahlgren, T. Ahlgren, L. Khriachtchev, J. Likonen, S. Lehto, J. Keinonen, , and C. H. Wu, *J. Nucl. Mater.*, 2001, **290-293**, 216.

[79] A. Lampertia, C. Bottania, and P. Ossia, *J. Am. Soc. Mass. Spectrom.*, 2005, **16**, 126.

[80] T. Nakamura, T. Ohana, M. Suzuki, M. Ishihara, A. Tanaka, and Y. Koga, *Diam. Relat. Mater.*, 2005, **14**, 1019.

[81] M. Fox, *Optical properties of solids*, Oxford University Press, Oxford, 2001.

[82] K. B. K. Teo, A. C. Ferrari, G. Fanchini, S. E. Rodil, J. Yuan, J. T. H. Tsai, E. Laurenti, A. Tagliaferro, J. Robertson, and W. I. Milne, *Diam. Relat. Mater.*, 2002, **11**, 1086.

[83] Rusli, J. Robertson, and G. A. J. Amaratunga, *J. Appl. Phys.*, 1996, **80**, 2998.

[84] R. Lacerda and F. Marques, *Appl. Phys. Lett.*, 1998, **73**, 617.

[85] M. Chhowalla, J. Robertson, C. Chen, S. Silva, C. Davis, G. Amaratunga, and W. Milne, *J. Appl. Phys.*, 1997, **81**, 139.

[86] S. R. P. Silva and G. A. J. Amaratunga, *Thin Solid Films*, 1995, **270**, 194.

[87] N. M. J. Conway, W. I. Milne, and J. Robertson, *Diam. Relat. Mater.*, 1998, **7**, 477.

[88] Guide to using wvase32. J.A. Woollam Co., Inc.

[89] A. R. Forouhi and I. Bloomer, *Phys. Rev. B.*, 1986, **34**, 7018.

[90] G. E. Jellison and F. A. Modine, *Appl. Phys. Lett.*, 1996, **69**, 371.

[91] G. E. Jellison and F. A. Modine, *Appl. Phys. Lett.*, 1996, **69**, 2137.

[92] G. E. Jellison, V. I. Merkulov, A. A. Puretzky, D. B. Geohegan, G. Eres, D. H. Lowndes, and J. B. Caughman, *Thin Solid Films*, 2000, **377**, 68.

[93] D. P. Dowling, K. Donnelly, M. Monclus, and M. McGuinness, *Diam. Relat. Mater.*, 1998, **7**, 432.

[94] J. Hong, A. Goullet, and G. Turban, *Thin Solid Films*, 1999, **352**, 41.

[95] Y. Hayashi, G. Yu, M. M. Rahman, K. M. Krishna, T. Soga, T. Jimbo, and M. Umeno, *Appl. Phys. Lett.*, 2001, **78**, 3962.

[96] G. Adamopoulos, J. Robertson, N. A. Morrison, and C. Godet, *J. Appl. Phys.*, 2004, **96**, 6348.

[97] D. A. Skoog, D. M. West, F. J. Hollar, and S. R. Crouch, *Fundamentals of Analytical Chemistry*, Thomson Brooks/Cole, USA, 2004.

[98] R. J. Lade, D. J. Munns, S. E. Johnson, P. W. M. K. N. Rosser, and M. N. R. Ashfold, *Diam. Relat. Mater.*, 1998, **7**, 699.

Chapter 3

Incorporation of Sulfur into Hydrogenated Amorphous Carbon

3.1 Introduction

As shown in the section 1.3, thin amorphous carbon films have a varied and exciting range of applications. Many of these require the fine tuning of a film's tribological, optical, and electronic properties, all of which are highly correlated. It has been demonstrated on many occasions that these properties can be altered by varying the standard deposition conditions, for example by addition of hydrogen or by changing the ion impact energy.

Another way of tuning a film's properties is by the addition of a dopant element. Traditionally dopants are used in very low concentration (typically 1 atom in 10^6), but since the doping efficiency of amorphous carbon is very low somewhat higher concentrations are used. Sometimes the concentration of dopant reaches an almost stoichiometric amount, by which point it is no longer valid to refer to it as doped amorphous carbon. Instead, a name that describes the binary nature of the material should be used, such as carbon nitride in the case of heavy nitrogen doping. The doping of amorphous carbon with high levels of nitrogen, boron and phosphorus has been studied on many occasions in the search for novel materials with new and extreme properties.

In this project a capacitively-coupled radio frequency discharge of methane and hydrogen sulfide was used to study the incorporation of sulfur into hydrogenated amorphous carbon, from sulfur doped a-C:H to a-C:S:H alloys.

Appendix A contains a reference to a concise version of the material displayed in this chapter which has been published in the journal *Diamond and Related Materials*.

3.2 Deposition Conditions

As described in chapter 2, the main deposition conditions that can be altered to affect the film properties are; the process gas mixture, the DC bias, the total gas flow rate, the deposition pressure and the deposition time. For the first data set, only the deposition time and total gas flow rate were kept constant throughout. The deposition time was set to 30 minutes which was sufficient to produce a film thick enough for analysis under most conditions. The total gas flow rate was decided by the range of the mass flow controllers (MFCs).

All other conditions were varied over a selected range. Considering first the gas mixture, methane was passed though a 50 sccm N_2 MFC, which, when corrected for methane, produced a maximum flow rate of 36 sccm. For hydrogen sulfide, a 10 sccm diborane/H_2 MFC was used, producing a maximum flow rate of 8.44 sccm. Taking these maximum flow rates into account a total flow rate of 30 sccm was employed, which gave a minimum deposition pressure of 10 mTorr. Considering the ranges of the MFCs and the total flow rate this enabled us to use 5 different process gas mixtures (Figure 3.1).

To avoid producing polymeric amorphous carbon films it was important to maintain a reasonably high ion impact energy. Previous work in our deposition reactor [1] has shown that the maximum sp^3/sp^2 ratio is achieved at 10 mTorr with a DC bias of -100 to -200 V. To stay close to this diamond-like region the DC bias was varied between -100 to -400 V for pressures of 10 - 50 mTorr (Figure 3.1).

This combination of 5 different process gas mixtures, 4 values for the DC bias and 3 process pressures gave 60 different deposition conditions.

Films were deposited onto mirror polished, 1×1 cm, boron-doped, single crystal, (100) silicon substrates, by placing them on the powered electrode.

Over the range of deposition conditions used there was a large variation in film thickness. Out of the 60 different sets of deposition conditions used, 9 had a growth rate that was too low to produce a film in the 30 minutes deposition time. These 9 sets of conditions tended to be at 10 mTorr and have a higher proportion of sulfur in the gas mixture.

The sulfur containing films appeared to be slightly softer than a similar a-C:H film, shown by the tendency of the films to get scratched in handling and storage. The a-C:S:H films were also more stable, being less likely to delaminate after deposition.

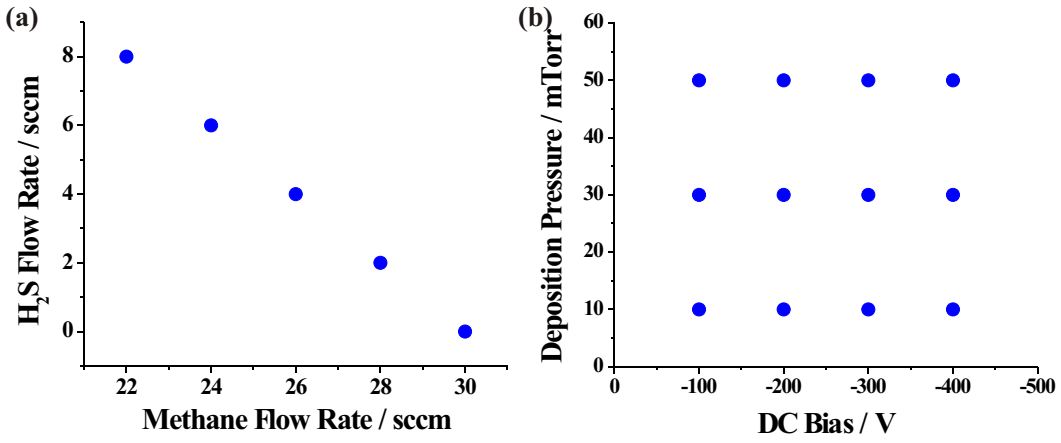

Figure 3.1: Deposition conditions (a) flow rates of H_2S and methane used to produce the total flow rate of 30 sccm, (b) the values of the deposition pressure and DC bias used to deposit the first sample set.

3.3 Compositional Analysis

Once the set of samples had been produced the next step was to try to quantify how much sulfur had been incorporated and to determine whether the distribution of sulfur was uniform throughout the sample. Two techniques were employed for this analysis, XPS and SIMS. These two techniques were performed by Sean Pearce in the University of Bristol interface analysis centre. Both these techniques require ultra high vacuum and are very expensive to use and the apparatus is difficult to maintain. These factors limited the number of samples that could be analysed, so compositional analysis was only performed on a selection of the 60 samples.

3.3.1 X-Ray Photoelectron Spectroscopy

Figure 3.2(a) shows a typical wide XPS spectrum of an a-C:H:S film. The sharp peaks are due to electrons ejected from the carbon 1s, sulfur 2s, sulfur 2p and oxygen 1s orbitals. The surface oxygen content was due to atmospheric oxidation and was seen to increase slightly with the time between deposition and analysis.

There are several other signals that appear in an XPS spectrum apart from the peaks mentioned above. Next to these peaks, at slightly lower binding energy (BE), there is a weak satellite peak produced by ejection of photoelectrons by different energy x-rays, caused by having a non-monochromated X-ray source. At slightly higher BE, each peak has a neighbouring weak broad peak. This is the plasmon loss signal and is produced by the interaction of ejected photoelectrons with free electrons in the solid. After each photoelectron peak, at the higher BE side, there is an increase in the level of the background signal. This increase in baseline signal is due to inelastic collisions of

the photoelectrons before ejection from the surface. Finally there are two broad signals, one at 750 eV, the other at 1000 eV. These are produced by Auger KVV (ejection from K-shell, electron falls from valence shell, another electron is ejected from the valence shell) electron emission from oxygen and carbon respectively.

From the intensities of the core electron peaks and the correct sensitivity factors, XPS can be used to determine the chemical composition of the sample. This composition is produced as an atomic concentration. This provides us with a problem, XPS cannot detected hydrogen or helium because they have no core electrons. The films analysed in this project are expected to be ∼35 atomic % hydrogen and therefore absolute atomic concentrations cannot be determined. Since the oxygen content was similar for all samples, the variation in sulfur content shall be quoted as the ratio of sulfur atoms to carbon atoms.

Process Gas Mixture

The first condition to be varied was the composition of the process gas mixture. Using the CH_4 and H_2S flow rates shown in Figure 3.1 the amount of H_2S in the gas phase could be varied between 0 and 26.67% of the total gas pressure. The variation of the surface sulfur/carbon ratio with the percentage of H_2S in the gas phase is shown in Figure 3.2(b).

The amount of sulfur incorporated into the sample surface is directly proportional to the H_2S in the gas mixture from which the film was deposited. Under the conditions shown here there is almost a 1:1 relationship between the gas phase sulfur/carbon ratio and sulfur/carbon ratio that is measured in the sample surface.

Process Pressure

In the original data set only three different deposition pressures were used. To improve the reliability of the pressure variation data a further sample was deposited at 40 mTorr.

The effect of the deposition pressure on the surface sulfur content can be seen in Figure 3.2(c). The sulfur/carbon ratio decreased slightly as the chamber pressure was raised. Over the range studied, the deposition pressure had much less of an effect on the sulfur content than the process gas mixture (variation over total range of 0.05 compared to 0.4) but there was still a noticeable effect.

In an RF plasma reactor such as this, a change in deposition pressure has many effects. First of all the mean free path is reduced, making ions more likely to collide with neutrals in the sheath region, producing a lower and less well defined ion impact energy. Secondly a higher power is required to produce the same DC bias when the

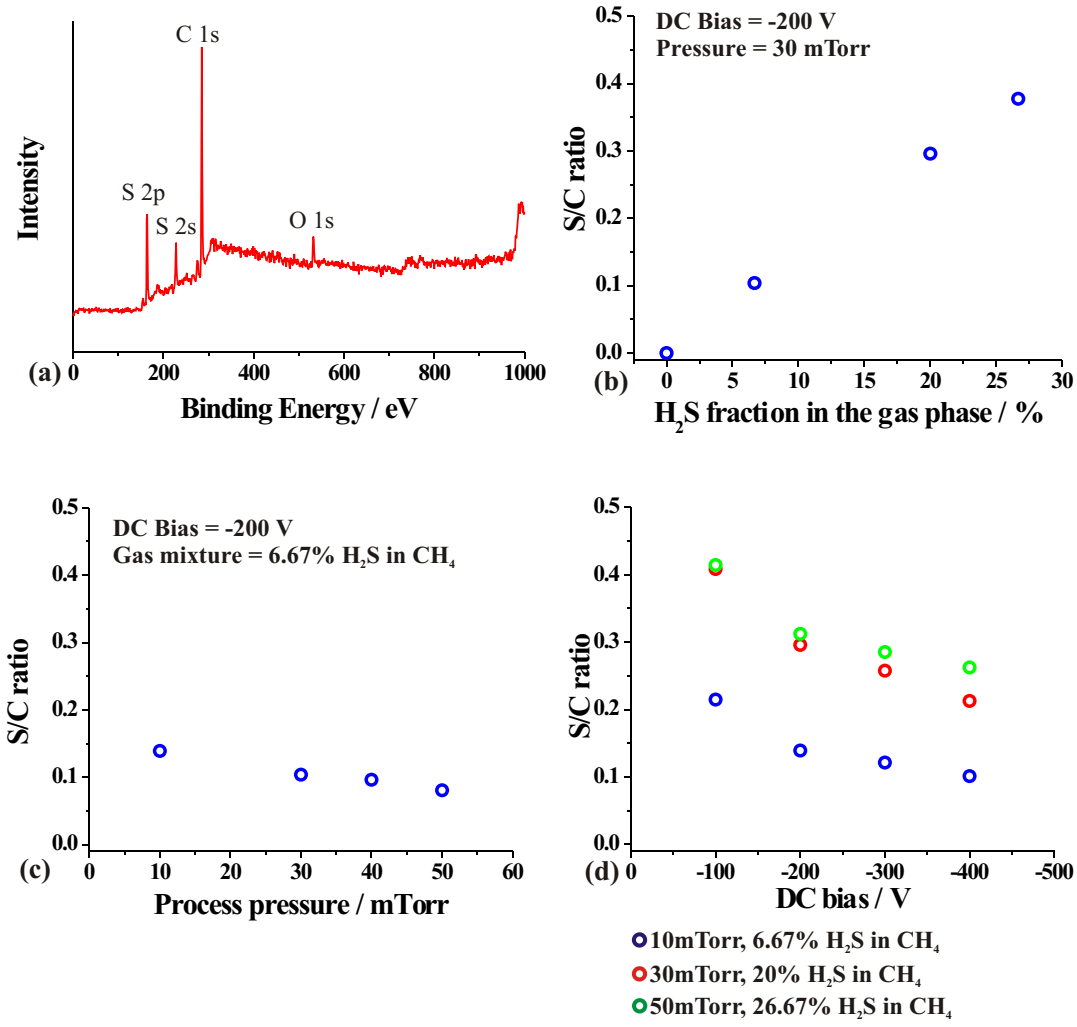

Figure 3.2: XPS results, (a) Typical wide XPS spectrum of an a-C:S:H films, (b) Variation of the surface sulfur content with the proportion of H_2S in the process gas mixture, (c) Variation of the surface sulfur content with the proportion of H_2S in the process gas pressure. (d) Variation of the surface sulfur content with the DC bias under three different process gas mixtures and pressures.

chamber pressure is increased. This high power increases the degree of dissociation in the plasma which, inturn, affects the chemistry of the plasma.

This leads us to suggest that the slight reduction in the sample sulfur content with increasing chamber pressure is due to either: (a) ion energy effects, which studying the variation in sulfur concentration with DC bias (see next section) will show, (b) an increase in plasma chemistry which could encourage polymerisation of sulfur species, or (c) a combination of both these effects.

As the chamber pressure was increased, especially at high H_2S/CH_4 ratios, a yellowy-white powdery deposit was noticed in the "colder" parts of the chamber, for example on the quartz window and near the pump inlet where no plasma forms. These deposits could be the result of polymerisation reactions mentioned above, which could act as a sink for the sulfur species reducing the availability of sulfur for film growth.

DC Bias

The affect of changing the DC bias on the surface sulfur content for three different process gas mixture and pressure combinations is shown in Figure 3.2(d). In all cases the sulfur content reduces as the DC bias increases. The magnitude of this effect is only slightly higher than that of varying the deposition pressure (change of 0.1 compared to 0.05).

It has been observed that the hydrogen content in a-C:H films also decreases with increasing DC bias. In the case of hydrogen the increase in ion impact energy causes increased displacement of hydrogen atoms in the film which can either be trapped or form H_2 by recombination with other H atoms or by H abstraction from the a-C:H film. These hydrogen molecules either become trapped in voids or diffuse out of the film. Also, to increase the DC bias a higher RF power is needed which also increases the degree of dissociation in the plasma. This could increase the concentration of H ions and radicals at the film surface leading to chemical etching of any surface bound species.

Similar arguments may be applicable to sulfur as well as hydrogen. Al-Dallal *et al.* [2] who deposited similar a-C:S:H films have observed low temperature ($\sim 200\,^{\circ}C$) evolution of H_2S gas. At this temperature H_2S could not be produced by the rupture of C-S bonds so must have been produced by the release of H_2S trapped in voids.

High Resolution Spectra

High resolution XPS spectra of the C 1s and S 2p peaks are shown in Figure 3.3. The S 2p peak has a shoulder, which is most likely due to splitting of the binding energy by spin-orbit coupling. Spin-orbit coupling is observed when an electron is removed from an orbital with non-zero angular momentum ($l > 0$). The magnitude of the spin orbit

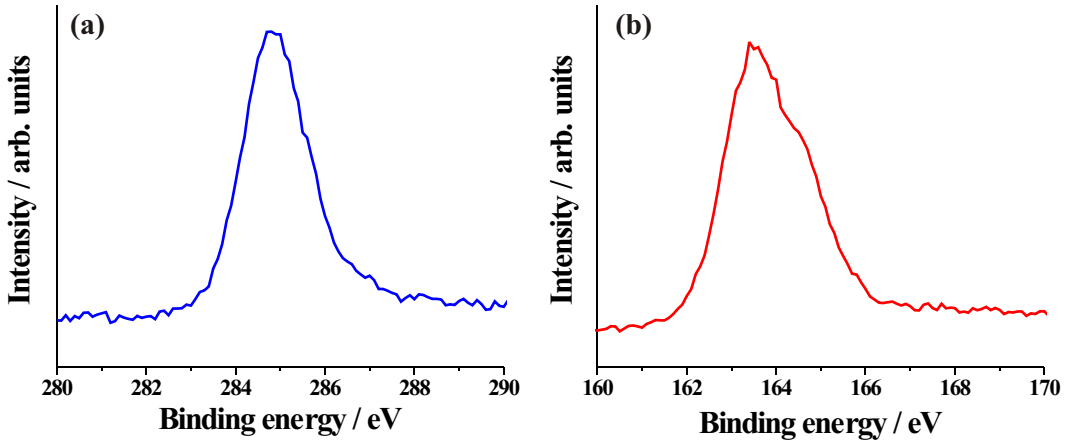

Figure 3.3: High resolution XPS spectra of (a) the C 1s peak and (b) the S 2p peak.

splitting increases with increasing atomic number, decreases with increasing principal quantum number (4p levels are split more than 5p levels), and with increasing angular momentum quantum number (4p levels are split more than 4f levels). The intensity ratio of two peaks should be 2:1 when accounting for the degeneracy of the states. The lower j value has a higher binging energy, but is half as intense. Fitting the high resolution S 2p peak produced a spin orbit splitting value of ∼1.3 eV, similar to that observed by XPS for other sulfur compounds [3].

In previous work by our group [1] and others [4,5] the high resolution C 1s signal has been used to determine the sp^2/sp^3 ratio of amorphous carbon samples. The binding energy of a core electron is dependent on the hybridisation and the chemical environment of the atom. To calculate the sp^2/sp^3 ratio, the C 1s peak was methodically deconvoluted into three separate components; sp^3 hybridised C-C, sp^2 hybridised C-C, and C-O. The ratio of the areas of the sp^2 and sp^3 components was then taken to be equal to the sp^2/sp^3 ratio. In this study it was not possible to derive this information from the deconvolution of the C 1s peak. With the inclusion of carbon bonded to sulfur the C 1s peaks can be split into many more components (sp^3 C-C, sp^3 C-S, sp^2 C-C, sp^2 C-S, as well as the C-O combinations), making the fitting far less accurate. Also, because so few films were analysed in this section, and they were deposited under a wide range of different biases, pressures and process gases (which all affect sample structure, and hence the XPS peak shape) no qualitative trends were seen in the C 1s peak shape or position that could be attributed to anything except a change in the C/S ratio.

3.3.2 Secondary Ion Mass Spectrometry

Figure 3.4(a) shows a SIMS negative ion mass spectrum of an a-C:H:S film deposited at -100 V, 10 mTorr and with 6.67% H_2S in the process gas mixture. The XPS results for this film showed it to have a surface sulfur/carbon ratio of 0.21. The peaks at 32 and 33 m/z are produced by S^- and SH^-, which is further evidence that sulfur has been successfully incorporated into the a-C:H films. The natural isotope ratio of sulfur is aproximately 20:1 S^{32}:S^{34}, so it is likely that the peak at 34m/z is due to both H_2S^{32} and S^{34}. The relative sensitivity of SIMS to different species can vary over several orders of magnitude, so no quantitative information can be gained about the relative proportions of carbon and sulfur.

Care must also be taken when studying the species that appear in the mass spectrum. In Figure 3.4(a) there is a peak at 56 m/z which could be due to C_2S. This is not evidence for direct bonding between carbon and sulfur in the film. When the sample is being sputtered into the detector it is possible there are gas-phase reactions between the sputtered ions above the surface of the film producing bonding configurations that do not exist in the sample.

Figure 3.4(b) shows the SIMS depth profile for the same film. The y-axis is an arbitrary scale and does not correspond to absolute or even relative concentrations but for any one species gives insight into its relative abundance with depth. At the start of the depth profile (0-500 s) the etch rate of the ions has not reached equilibrium, so this section is not an accurate description of the film composition.

The profiles for all the species are reasonably linear (above 500 s) suggesting the composition of the sample is homogeneous. The oxygen signal has a small peak at 2000 s which corresponds to the native oxide layer on the silicon.

As well as depth profiling a sample, SIMS can also be used produce elemental maps of the species distributions. In these maps, the light areas correspond to regions where a certain element was detected. The maps in Figures 3.5(a), (b), (c) and (d) are maps of carbon, sulfur, oxygen and a coloured overlay of all three, respectively. The mapped region contains a selection of areas etched to different depths, which appear as a set of concentric rectangles. The black rectangle in the centre of the image corresponds to where the sample has been etched through to the silicon wafer, so there is no C, S or O in that region. The next rectangle out has been etched down into the bulk of the film. The final rectangle has had only a quick exposure to remove the surface layer. The remainder of the map depicts the surface composition. The structure to the bottom right of the depth profiled area is a region of damage produced by sample handling and storage.

The carbon and sulfur maps (Figure 3.5 (a) and (b)) show reasonably homogeneous distributions throughout bulk and surface of the sample, with no obvious areas of

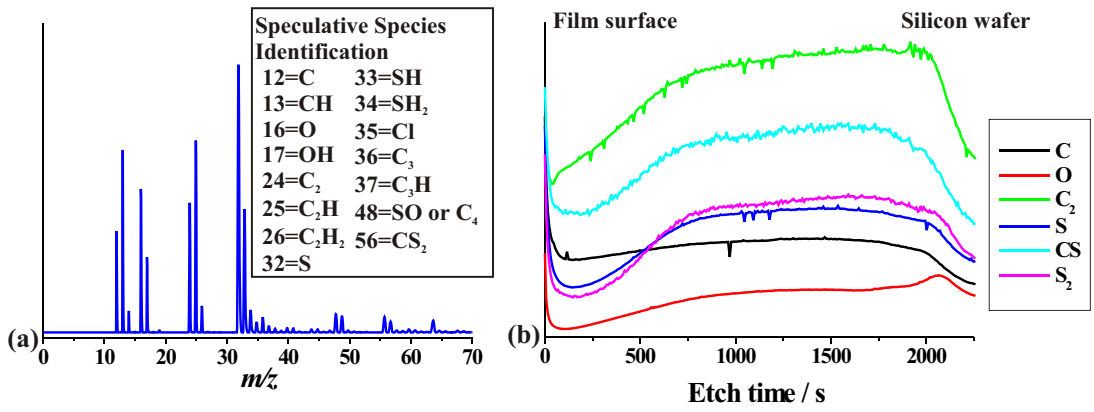

Figure 3.4: Results produced by SIMS (a) SIMS wide spectrum, (b) SIMS depth profile.

clustering. The oxygen map (Figure 3.5 (c)) shows slight oxidation of the surface layer, but the brightest regions are around the area of damage.

3.4 Structural Analysis

Since the high resolution XPS spectra cannot be fitted to produce the sp^2/sp^3 ratio, and too much material is required for solid state ^{13}C NMR (Appendix B), the only method of structural analysis available is Raman spectroscopy.

3.4.1 Raman Spectroscopy

The Raman spectra of a-C:S:H films, deposited under similar conditions to those deposited here, have been studied by Al-Dallal *et al.* [2]. They observed a peak at 670 cm^{-1} which grew in intensity as the sulfur content in their carbon matrix increased. They attributed this peak to C-S bond stretching. This peak was not observed in the Raman spectrum of any of the samples in this data set, suggesting our samples have a lower proportion of C-S bonds than those of Al-Dallal *et al.* (although the article by l-Dallal *et al.* did not state the wavelength of laser used in their Raman study, or if the spectra were smoothed proir to analysis). Generally there was very little difference between the Raman spectra produced by an a-C:S:H film and a similar a-C:H film.

The Raman spectra of a series of a-C:S:H films are shown in Figure 3.6(a). There is a visible increase in the intensity of the D peak shoulder with an increasing proportion of H_2S in the gas phase, suggesting that the presence of sulfur in the film, or its effect

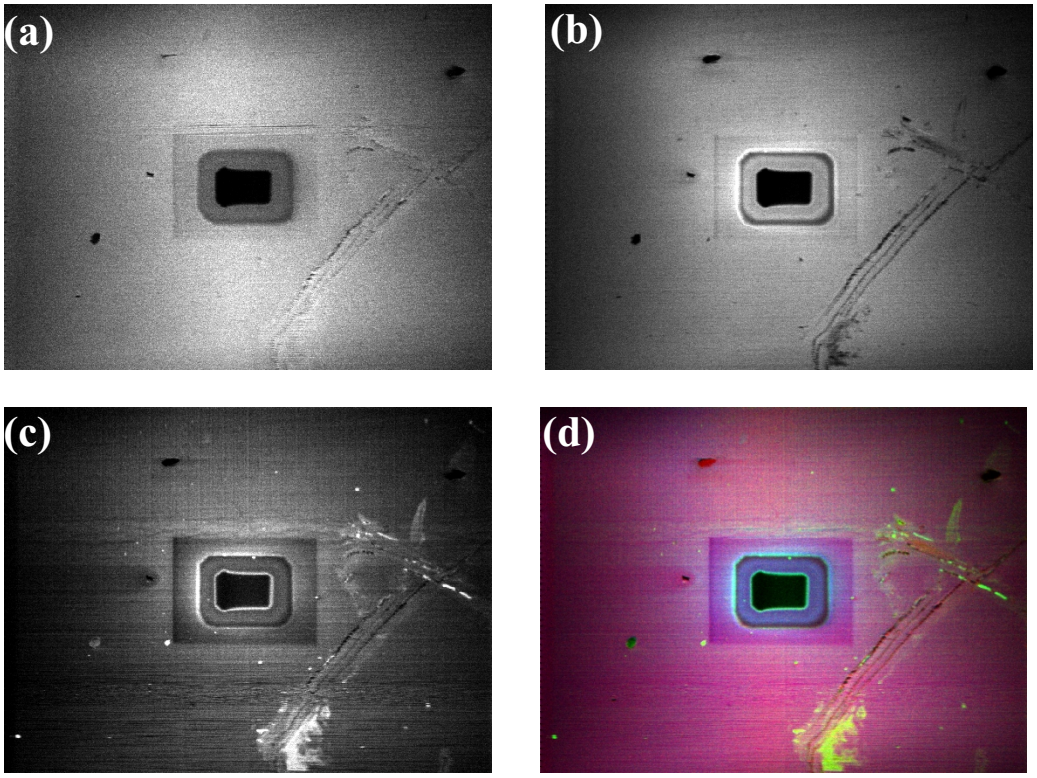

Figure 3.5: SIMS elemental maps of a depth profiled area; (a) carbon, (b) sulfur, (c) oxygen, and (d) an overlay of the carbon (red), sulfur (blue) and oxygen (green) maps with the secondary electron image.

on the plasma chemistry, increases the aromatic six-membered ring clustering in the film. To gain a better insight into the variation of the carbon ordering with changing deposition conditions, the Raman spectra of all the films in the data set were fitted with two Gaussians, corresponding to the D and G peaks (Figure 3.6(b)).

All the films produced in this study display a relatively low $I(\mathrm{D})/I(\mathrm{G})$ ratio and large G peak width, indicating that there is very little ordering of the sp^2 carbon in the samples produced. For small aromatic clusters there is a linear relationship between the $I(\mathrm{D})/I(\mathrm{G})$ ratio and the G peak width [6] so plotting a graph of these two values should yield a reasonably straight line. This plot is shown in Figure 3.7(a) and there is indeed a clear correlation between the $I(\mathrm{D})/I(\mathrm{G})$ ratio and the G peak width. The next step is to separate the data in Figure 3.7(a) to see how the magnitude of the aromatic clustering produced by the addition of sulfur compares to that produced by the other deposition conditions.

In Figure 3.7(b) the data are separated by the percentage of H_2S in the process gas mixture. The different conditions are distinguished by the colour of the data points. There is a clear clustering of the points suggesting that the proportion of H_2S in the gas phase has the dominant effect on the aromatic clustering in the a-C:S:H films. This is also shown by the lowest values of the $I(\mathrm{D})/I(\mathrm{G})$ ratio and the highest values of G peak width being found for the films deposited without the addition of sulfur.

To check this theory, the same plots were produced, but this time the deposition pressure (Figure 3.7(c)) and DC bias (Figure 3.7(d)) are colour coded. In both plots the different coloured points are found spread throughout the entire plot, there is no clustering as seen in the process gas mixture plot. In the pressure plot there is a visibly lower number of points for 10 mTorr, especially at high $I(\mathrm{D})/I(\mathrm{G})$ ratio and low G peak width. This is because at low pressures and high H_2S proportions (which would be expected to produce the more ordered films) no film was produced after the 30 minutes deposition run.

Finally, averages of the $I(\mathrm{D})/I(\mathrm{G})$ ratio and G peak width were calculated with respect to the separate deposition conditions. The plot of these averages are shown in Figure 3.7(e). The points relating to data grouped by the H_2S proportion in the gas phase have formed a line with a similar gradient to the plot of the full data shown in Figure 3.7(a). Moreover, these points are in order, with the highest H_2 proportion having the highest $I(\mathrm{D})/I(\mathrm{G})$ ratio, and the sulfur-free films having the lowest $I(\mathrm{D})/I(\mathrm{G})$ ratio. The averages grouped by bias and pressure, on the other hand, are grouped around the centre of the plot, again showing that the H_2S proportion in the gas phase has the largest effect on the graphitic clustering of the a-C:S:H films.

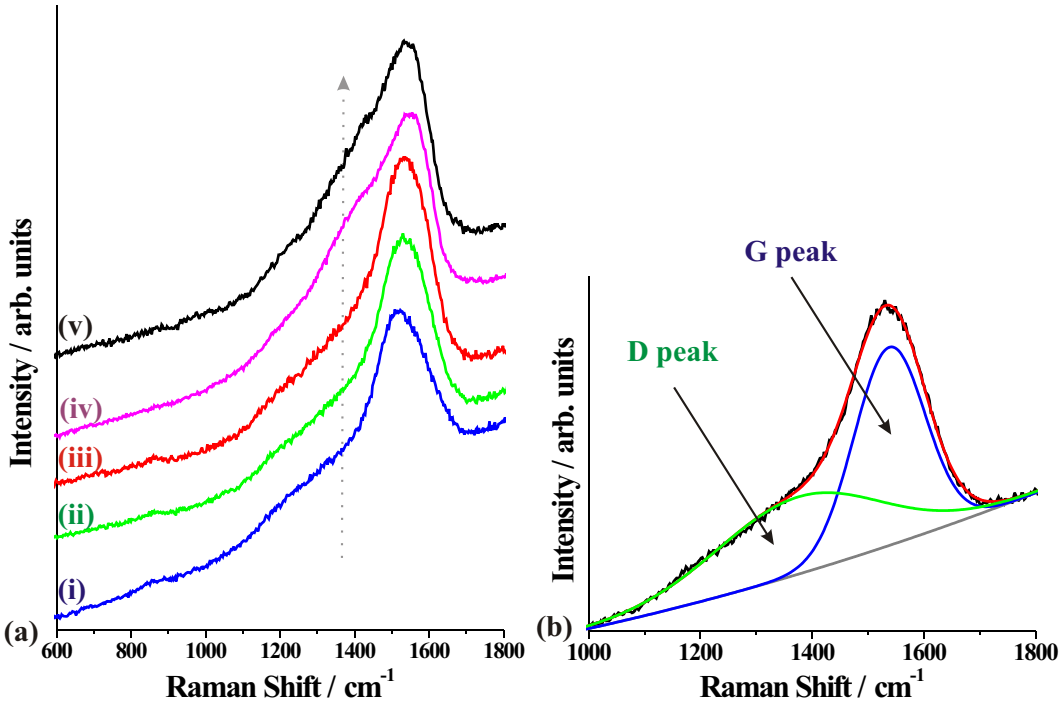

Figure 3.6: (a) Raman spectra of a-C:S:H films grown with different CH_4/H_2S ratios, spectra offset for display purposes; (i) 0% H_2S, (ii) 6.7% H_2S, (iii) 13.3% H_2S, (iv) 20% H_2S and (v) 26.7% H_2S. The arrow highlights the increase in the intensity of the D peak with an increasing H_2S proportion, (b) A typical Raman spectrum of an a-C:S:H film fitted with a linear background and two gaussians. Gaussian profiles have been skewed by addition of the linear background.

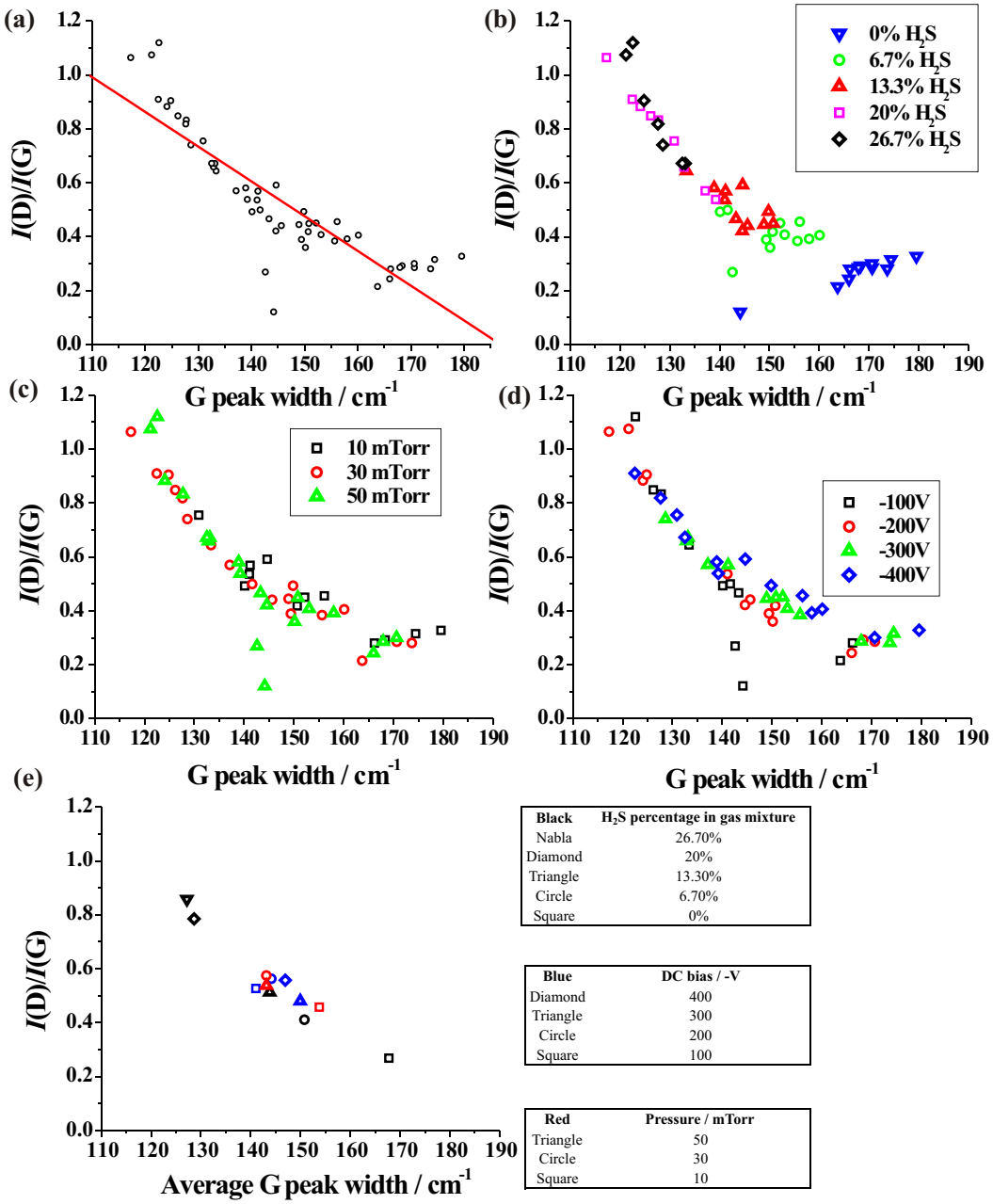

Figure 3.7: (a) A plot of the $I(\mathrm{D})/I(\mathrm{G})$ ratio against the G peak width for all films deposited, (b) as in (a) but with different coloured points representing different percentages of H_2S in the process gas mixture, (c) as in (a) but with different coloured points representing different process gas pressures, (d) as in (a) but with different coloured points representing different values of the DC bias, (e) A plot of the average $I(\mathrm{D})/I(\mathrm{G})$ ratio against the average G peak width for all films deposited, different colours represent averages for different deposition variables.

3.5 Growth Rate and Optical Properties

The thickness and optical properties of the deposited a-C:S:H films were simultaneously determined by spectroscopic ellipsometry. A second set of samples was deposited to ensure all films were a suitable thickness to aid the fitting of the ellipsometry data. As well as varying the deposition conditions mentioned above, the total flow rate was also included in this data set. The growth rate was calculated by dividing the thickness by the deposition time (assuming a constant growth rate over the entire deposition run).

3.5.1 Growth Rate

Figure 3.8(a) shows the variation of growth rate with the percentage of H_2S in the gas phase. The data can be fitted approximately with a quadratic curve, showing that the decrease in growth rate is not simply caused by the linear decrease in carbon containing species in the feedstock gas. If the H_2S/CH_4 ratio gets too high, no film is deposited (growth rate is zero). There are still carbon species in the plasma, so a-C:H deposition should still be occurring, but no film is produced. To account for this let us assume that sulfur-based plasma species, in a high enough concentration, chemically etch the growing a-C:S:H film by producing neutral volatile molecules such as CS_2, CH_3SH, etc. At low sulfur concentration there is a lower probability that these molecules are formed, the sulfur implants into the predominantly carbon film and is trapped. As the sulfur concentration is increased, more sulfur species are present in the growing film. The probability that an impacting sulfur atom collides with a carbon bound to a sulfur increases, so the etch rate increases. At high sulfur concentration, any carbon deposited is quickly etched, but no a-S is produced due to the presence of hydrogen atoms or ions reacting with sulfur to form H_2S.

The change in growth rate with deposition gas pressure is shown in Figure 3.8(b). Raising the deposition pressure produces a linear increase in the growth rate. At higher pressure, more power is required to produce the same DC bias. The larger power and gas density results in a greater number of ions striking the substrate and hence increase the growth rate.

Figure 3.8(c) shows the change in growth rate with the DC bias. The growth rate shows a linear increase up to -350 V, but the growth rate at -400 V is slightly lower than expected. This slight deviation could be due to an enhanced sputtering rate caused by the higher energy ion impacts.

The total gas flow rate (Figure 3.8(d)) has only a small effect on the growth rate (over the range of the mass flow controllers) compared to other conditions. Reducing the flow rate into the reaction chamber means using a lower pumping efficiency to maintain the same deposition pressure. This lower pump rate leads to a larger gas

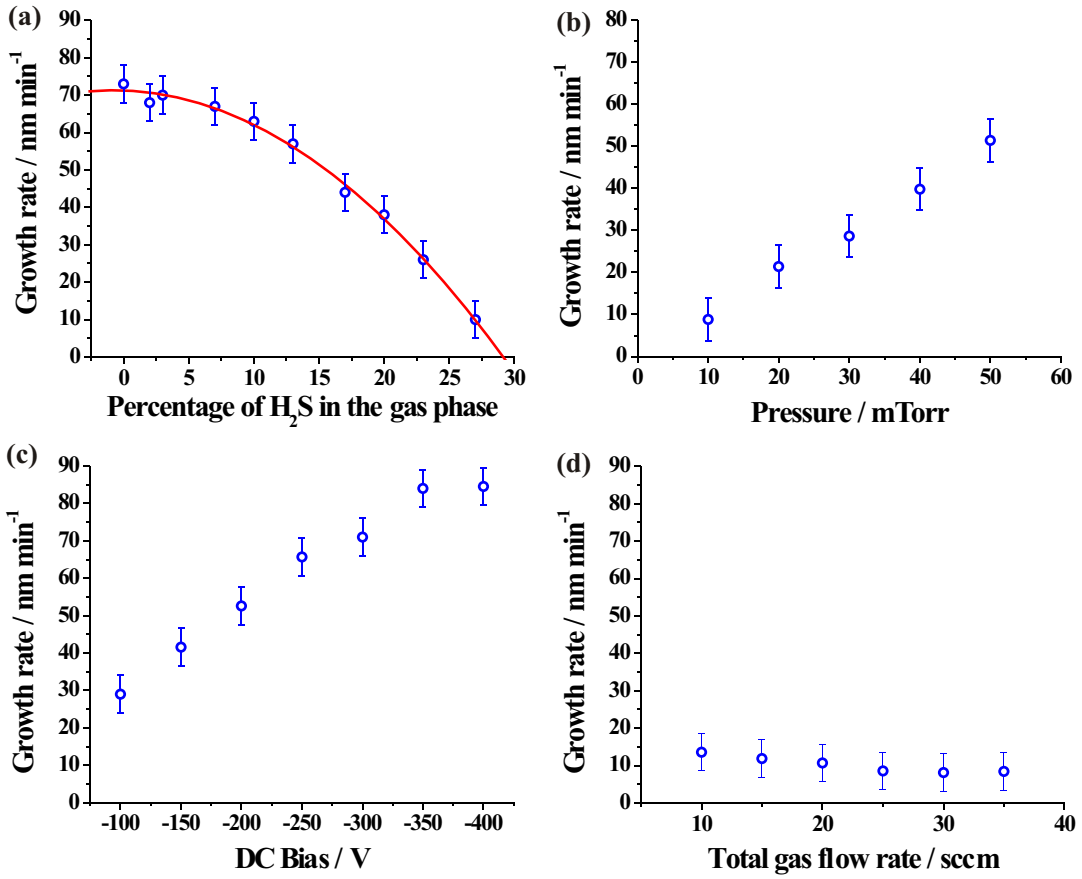

Figure 3.8: Variation of growth rate with different deposition conditions: (a) the percentage of H_2S in the gas phase, with: DC bias = -200 V, pressure = 30 mTorr, 30 sccm total flow rate; (b) the deposition pressure, with: DC bias = -100 V, H_2S:CH_4 = 2:28, 30 sccm total flow rate; (c) DC bias, with: H_2S:CH_4 = 2:28, pressure = 30 mTorr, 30 sccm total flow rate, (d) The total gas flow rate, with: DC bias = -100 V, H_2S:CH_4 = 2:28, pressure = 10 mTorr.

residence time in the plasma, which could have an effect on the plasma chemistry. The growth rate appears to increase proportionally with residency time, possibly due to sink reactions of sulfur in the gas phase becoming more important. These reactions could lower the number of sulfur ions impacting into the growing film and hence reduce the etch rate of carbon by sulfur species. A study of the film composition would have helped confirm this theory but sadly, due to the expense of XPS, was not possible.

3.5.2 Optical Properties

The two properties studied in this section are the optical band gap and the refractive index. The optical band gap energy is strongly dependent on the structure of the film, the more diamond-like a sample is, the wider its band gap. The refractive index has been shown to correlate strongly with the hardness and resistance to laser damage of amorphous carbon films [7].

Optical band gap

Three different values of the band gap energy are quoted in this section; Tauc-Lorentz, E04 and Tauc. The different names relate to the different methods used to calculate the band gap energy. Tauc-Lorentz is the energy gap value produced by the ellipsometry fitting process and is generally accepted to be ∼0.5 eV too low. The E04 and Tauc gap energies are calculated from the absorption coefficient α, which can be determined by either spectroscopic ellipsometry or UV/Vis absorption spectroscopy. The E04 band gap value is the energy E at which α equals 10^4 cm^{-1}. The Tauc gap energy is determined by the extrapolation of the linear part of a graph of $(\alpha \times E)^{1/2}$ against E. Out of all these values, the E04 energy is the most reliable because of the difficulty in the extrapolation used in the Tauc method.

The traditional method of determining α is by UV/Vis absorption spectroscopy. For comparison with the value of α from ellipsometry, UV/Vis absorption spectra were obtained from a-C:S:H films deposited on quartz substrates. To calculate the absorption coefficient it was assumed that the reflected component was negligible. The sample thickness was assumed to be the same as a film deposited on silicon under the same conditions. The absorption coefficient was calculated using the following equation;

$$\text{Absorbance} = \frac{\alpha l}{\ln(10)} = 0.434\alpha l \tag{3.1}$$

where α is the absorption coefficient and l is the sample length. The value of the absorbance is determined by the UV/Vis absorption spectrum and is equal to;

$$\text{Absorbance} = -\log_{10}\frac{I(l)}{I_0} \tag{3.2}$$

where I_0 is the initial light intensity and $I(l)$ is the intensity of the light after passing through a film thickness l.

Figure 3.9 shows a comparison of the value of the E04 band gap determined by ellipsometry and UV/Vis. Both techniques produced similar values, but there is more scatter and larger errors in the UV/Vis results. The larger errors in the UV/Vis data are most likely to be produced by the difficulty in determining the exact energy for

which $\alpha = 10^4$ and the poor bonding of the amorphous carbon to the quartz substrates. Since both methods produce similar results, with the ellipsometry data appearing more consistent, only ellipsometry is used for further data sets.

Figure 3.10(a) shows the variation of the band gap energy with increase in the percentage of H_2S in the gas phase. As the amount of sulfur in the gas phase (and hence the deposited film) increases there is a slight decrease in the band gap energy. This fits well with the Raman data which showed an increase in the graphitic clustering with increasing sulfur incorporation (Figure 3.6(b)).

As the deposition pressure is increased (Figure 3.10(b)) there is also an increase in the band gap. The bias used in this series was -100 V. As the pressure increases, the accelerating ions are more likely to be scattered by collisions with neutral molecules in the sheath. This scattering lowers the average value of the impact energy, leading to deposition of more polymeric films with higher hydrogen content. Hydrogen in a film stabilises the sp^3 hybridised carbon, increasing the band gap.

Figure 3.10(c) shows the change in band gap with DC bias. There is a clear decrease in band gap energy with increasing DC bias. The DC bias controls the energy with which ions impact into the growing film. The mechanism of amorphous carbon growth is known as "subplantation". At a specific impact energy, ions penetrate into the film increasing the local density which favours the formation of sp^3 hybridised carbon. At too low an impact energy, the ions don't penetrate the film's surface. This produces a polymeric film with a high sp^3 proportion, high hydrogen content and hence a wide band gap. At too high an impact energy, the ions penetrate through the surface, sputtering off hydrogen and suppling energy to the surrounding film, allowing it to relax to the more thermodynamically stable sp^2 hybridisation. These factors produce a sample with a low band gap energy.

At constant deposition pressure, changing the total flow rate changes the residence time of the process gas. A larger residence time increases the probability of chemical reactions in the process gas before it is pumped away. Figure 3.10(d) shows that increasing the total flow rate reduces the value of the band gap energy. It is possible that at lower flow rate (high residence time) the methane reacts to form larger hydrocarbons. When ionised, these larger molecules would impact with a lower energy than smaller hydrocarbons, producing a more polymeric film with a larger band gap. Ideally, a diagnostic technique such as residual gas analysis could be used to look for changes in gas composition which would provide evidence for this theory.

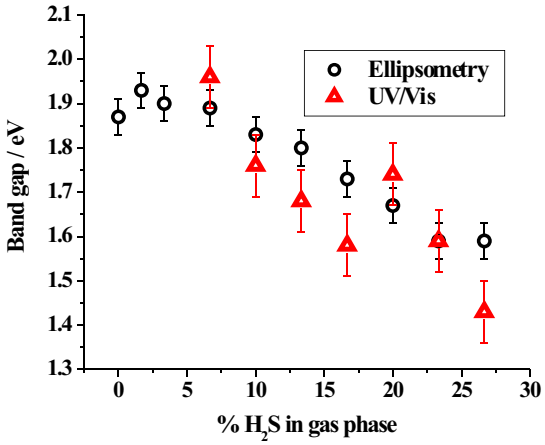

Figure 3.9: Comparison of the value of the E04 band gap determined from UV/Vis and ellipsometry. The errors are determined from different samples deposited under the same conditions.

Refractive Index

The value of the refractive index n of a substance is dependent on the wavelength of the interacting light. Spectroscopic ellipsometry produces values of n from 200 - 1000 nm. In this section the value of the refractive index at 675.8 nm is studied to allow comparison with literature values. The refractive index has been shown to correlate with hardness and resistance to laser damage [7]. Diamond-like a-C:H films tend to have refractive indices between 1.6 and 2.3, if n is below 1.6 the films are designated more polymer-like than diamond-like (for comparison the refractive indices of diamond and polyethylene are 2.4 [8] and 1.5 respectively [9]). All the films produced in this study have a value of n greater than 1.8, implying the films can still be classed as diamond-like.

Figure 3.11 (a) shows that there is a slight increase in the refractive index with an increase in the proportion of H_2S in the gas phase. The usual explanation for an observed increase in refractive index is a reduction in the hydrogen content of the film. Whether this is true in this case, or the observed increase is due to the presence of sulfur in the gas phase or film, is unclear.

Figure 3.11(b) shows the relationship between the refractive index and the deposition pressure. As the pressure is increased, there is a lowering of the refractive index of the deposited film. This lowering of the refractive index probably relates to softening of the sample caused by an increase in the hydrogen content. The hydrogen content is dependent on the ion impact energy, which is reduced as the pressure increases.

The relationship between the ion impact energy and hydrogen content is also shown by the change in refractive index with DC bias (Figure 3.11(c)). Out of all of the

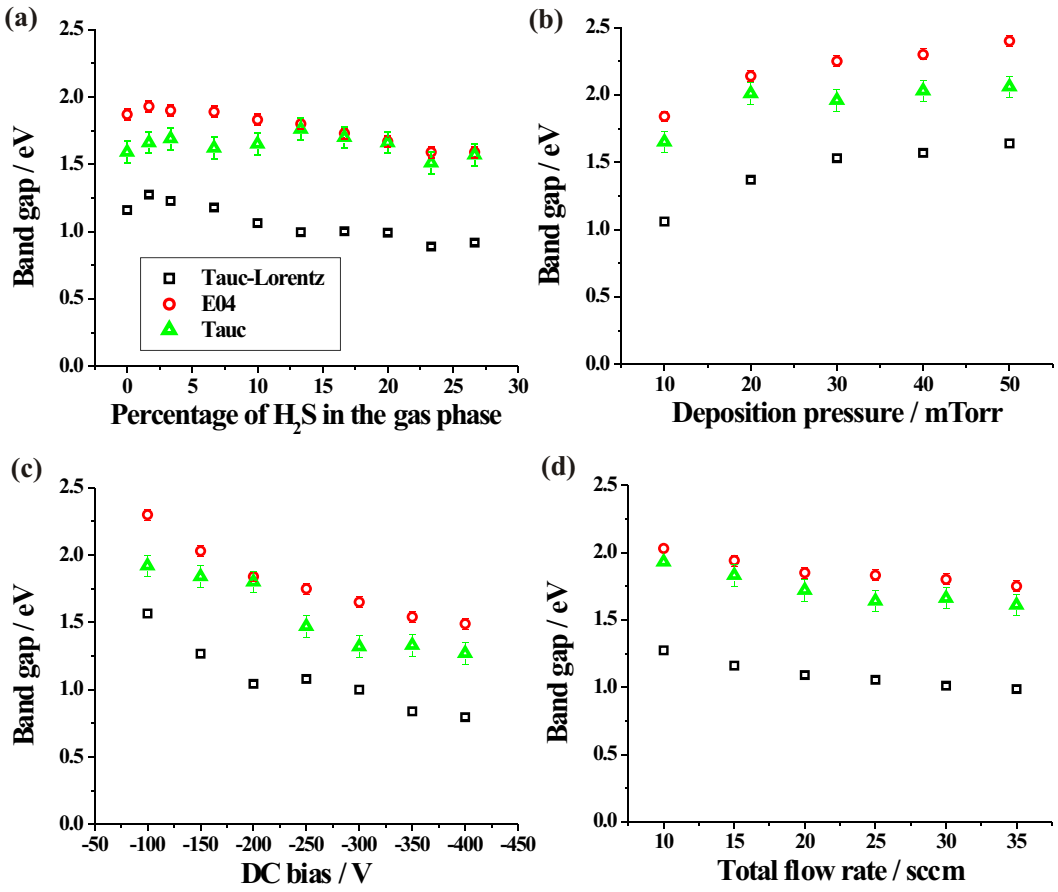

Figure 3.10: Plot of the band gap energy against deposition conditions: (a) the percentage of H_2S in the gas phase, with: DC bias = -200 V, pressure = 30 mTorr, 30 sccm total flow rate; (b) deposition pressure, with: DC bias = -100 V, H_2S:CH_4 = 2:28, 30 sccm total flow rate; (c) DC bias, with: H_2S:CH_4 = 2:28, pressure = 30 mTorr, 30 sccm total flow rate; (d) total gas flow rate. with: DC bias = -100 V, H_2S:CH_4 = 2:28, pressure = 10 mTorr.

conditions studied, the DC bias has the largest effect on the refractive index. As the DC bias increases, the ion impact energy increases, this increases the sputtering of hydrogen from the surface of the growing film, producing a harder film with a higher refractive index.

In order to explain the observed change in band gap with changing flow rate it is proposed that the decrease in flow rate results in chemical reactions in the plasma which produce larger hydrocarbons. Hydrocarbon ions with larger mass impact with lower energy per carbon atom, producing a similar effect to lowering the DC bias. This also fits the trend seen for the change in refractive index with total flow rate (Figure 3.11(d)). As the flow rate is decreased, the refractive index decreases, suggesting a softer film and hence a higher hydrogen content.

3.6 Deposition of a-C:S films from CS_2

To aid analysis of the data from the previous section, further experiments were carried out using pure CS_2 (so the films will be H-free) as the process gas instead of a mixture of CH_4 and H_2S. No films could be deposited from CH_4/H_2S gas mixtures with a C:S ratio of 1:2 in the plasma under the conditions used in the last section and the same was found for CS_2 plasmas. It was possible to produce polymeric CS_2 films using a very low DC bias, however. These films were analysed using Raman spectroscopy to probe the C-S bonding.

3.6.1 Raman Spectroscopy

The Raman spectrum of a typical polymeric CS_2 film is shown compared to that of an a-C:S:H film in Figure 3.12.

The spectrum produced by the polymerised CS_2 film is similar to that of the a-C:S:H film in that both show a strong signal around 1500 cm^{-1} (the D and G peaks in amorphous carbon) but the profile of this signal from the CS_2 film is not as smooth as for the a-C:S:H film. The two-Gaussian fitting procedure shown in Figure 3.6(b) could not be used on the peak in the spectrum of the CS_2 film, suggesting that the vibrational modes producing this signal are somewhat more complex than just being the D and G modes of amorphous carbon.

There are two broad peaks in the polymerised CS_2 spectrum that do not appear in the spectrum of the a-C:S:H film. The first is at $\sim$450 cm^{-1}, just below the sharp first-order silicon signal. The second peak is the second-order silicon signal ($\sim$1000 cm^{-1}), not observed in the a-C:S:H film due to the higher thickness and lower transparency of the sample.

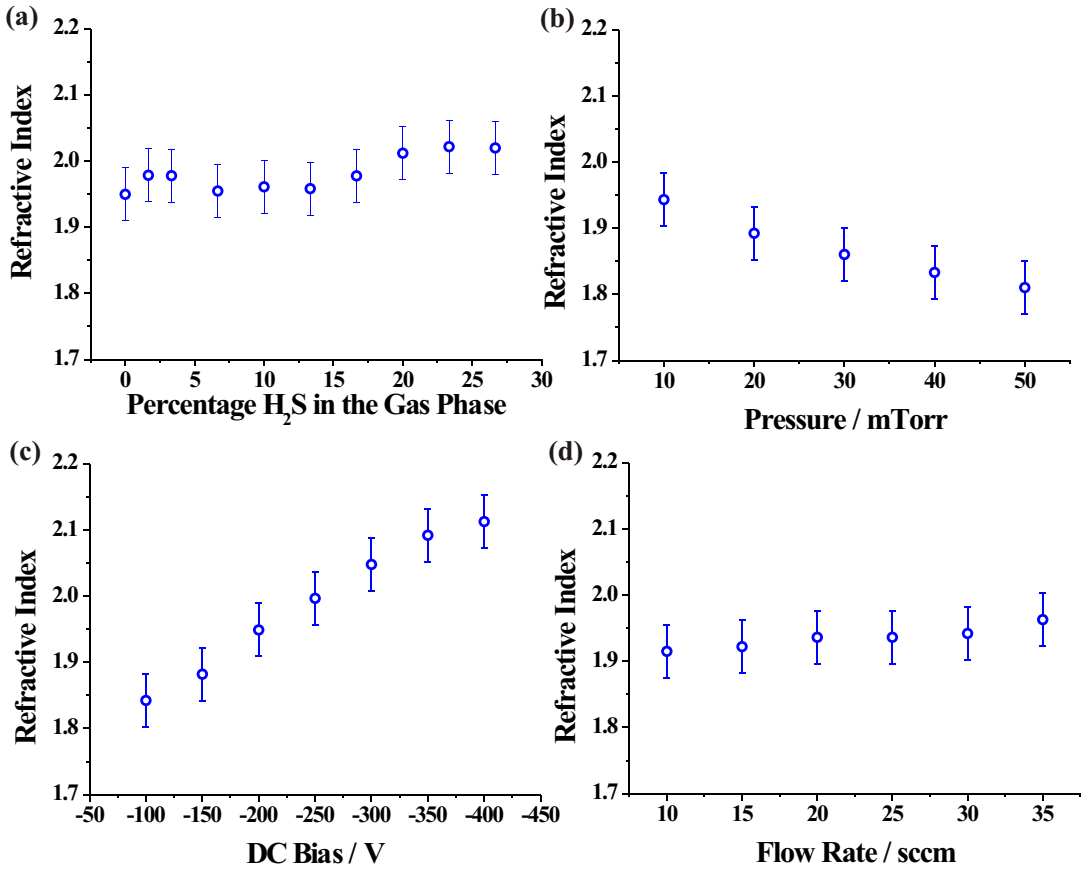

Figure 3.11: Plot of the refractive index against deposition conditions: (a) the percentage of H_2S in the gas phase, with: DC bias = -200 V, pressure = 30 mTorr, 30 sccm total flow rate; (b) the deposition pressure, with: DC bias = -100 V, H_2S:CH_4 = 2:28, 30 sccm total flow rate; (c) DC bias, with: H_2S:CH_4 = 2:28, pressure = 30 mTorr, 30 sccm total flow rate; (d) total gas flow rate, with: DC bias = -100 V, H_2S:CH_4 = 2:28, pressure = 10 mTorr.

Al-Dallal *et al.* [2] observed a weak signal at 670 cm^{-1} in the spectrum of their a-C:S:H films which they attributed to C-S bond stretching modes (typically found between 620 and 740 cm^{-1} [10]). No such peak is apparent in the spectrum of the polymerised CS_2 films shown here suggesting that either there is no signal from the C-S bonds in this spectrum or there is an alternative assignment for the observation of Al-Dallal *et al.*

To assist assignment, the position of these peaks were compared with those produced in the Raman spectrum of known sulfur or carbon-sulfur compounds. These frequencies were taken from a "Handbook of Infrared and Raman characteristic frequencies of organic molecules" [10].

The peak observed in our polymerised CS_2 films at $\sim$450 cm^{-1} is most likely to be due to S-S bond stretches. This is interesting as there are no S-S bonds in CS_2, so these bonds must have formed during the polymerisation process. Carbon-sulfur bond stretches are found between 620 and 740 cm^{-1}, which agrees with the assignment of Al-Dallal *et al.* [2]. This suggests that even though the films deposited in this section are very different to those in the previous section, there is still no direct evidence of carbon-sulfur bonding in the Raman spectra.

Further measurements were performed on the polymerised CS_2 films (optical properties and growth rate measurements), but no consistent results could be obtained. The poor reproducibility of these results is likely to be due to the difficulty in maintaining a low DC bias discharge in an RF system with highly asymmetric electrodes.

3.7 Comparison of a-C:S:H, a-C:N:H and a-C:S:N:H films

The incorporation of nitrogen into amorphous carbon films is the most widely studied of all dopant additions [11]. This has not just been driven by attempts to produce n-type amorphous carbon but also to create β-carbon nitride; a crystal form predicted to be bulk modulus comparable to that of diamond [12].

The next section compares the effects of incorporating nitrogen, sulfur, or a combination of both, on the structural and optical properties of a-C:H films.

3.8 Deposition Conditions

The change in the efficiency of dopant incorporation with changing deposition pressure and DC bias was studied in section 3.3.1. This study found that changing these two conditions had a much smaller effect on the overall film composition than changing the proportion of dopant in the gas phase. In this section a constant value for the gas pressure and DC bias was used and only the process gas mixture was varied. The chamber pressure and DC bias were set at 30 mTorr and -200 V, respectively. These

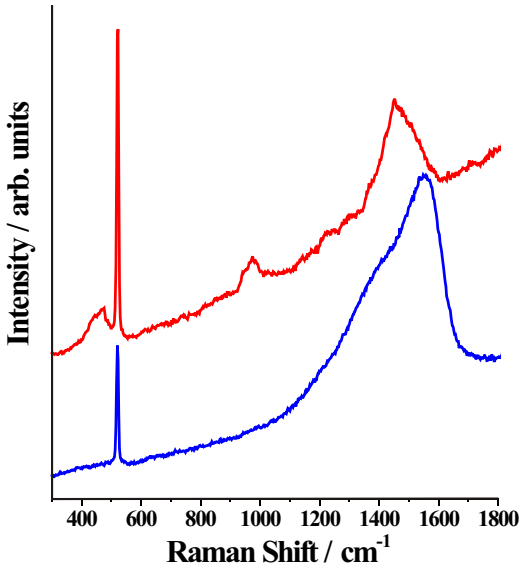

Figure 3.12: Raman spectra of a CS_2 polymer film (red) and an a-C:S:H film (blue). The a-C:S:H film contains 18.4% sulfur by XPS.

values were chosen as a compromise between high dopant incorporation efficiency (low bias, low pressure) and high growth rate (high bias, high pressure).

Methane and H_2S were introduced into the chamber as described in section 3.2. For nitrogen doping, N_2 was used as the source of nitrogen. This was introduced into the chamber via a 10 sccm N_2 mass flow controller. To be useful as a dopant it is important that N_2 breaks up into nitrogen atoms in the plasma. If this does not happen, nitrogen could just be incorporated as void-trapped N_2 molecules. To test how well N_2 dopes an a-C:H film, films were also deposited using methane/ammonia mixtures (CH_4/NH_3) and compared to the equivalent films deposited from CH_4/N_2 gas mixtures.

No mass flow controller was available for ammonia, so instead a needle valve was used to control the flow into the chamber. The flow rate was determined by introducing a set flow rate of N_2 into the chamber and allowing the system to equilibrate. When a stable pressure reading was obtained, the flow of N_2 was switched off and the chamber was evacuated to base pressure. The needle valve was then opened and adjusted until the flow of ammonia produced the same equilibrium pressure that was produced for the N_2 flow. At this point the flow rate of NH_3 was assumed to be equal to that of N_2 introduced previously.

Films were deposited from six different proportions of dopants; N_2 only, H_2S only, 1:1 H_2S:N_2, 2:1 H_2S:N_2, 2:1 N_2:H_2S and NH_3 only. Flow rates for all dopants were between 1 and 8 sccm, the total flow was kept constant by the addition of methane up

to a total flow rate of 30 sccm.

Also in this section, the effect of adding an inert buffer gas was studied. The buffer gas used was argon, which was introduced into the chamber via a 200 sccm mass flow controller. In these experiments, 50 sccm of Ar was added to the 30 sccm methane/dopant gas mixture giving a total flow rate of 80 sccm.

3.9 Structural Analysis

The only method of structural analysis available was Raman spectroscopy.

3.9.1 Raman Spectroscopy

There was little difference between the Raman spectra produced by a-C:H, a-C:N:H, a-C:S:H and a-C:S:N:H films. The only observable differences are subtle changes in the shape and intensity of the broad D and G signals.

A plot of the $I(\mathrm{D})/I(\mathrm{G})$ ratio against the G peak width shows a linear relationship (Figure 3.13(a)). Comparing this plot to the one shown in Figure 3.7, a slight difference between the spread of the points becomes apparent. The points in the new data set do not extend as far into the graphitic region of the plot (lower G width, higher $I(\mathrm{D})/I(\mathrm{G})$ ratio) as the points in the previous data set. This is unexpected because some of the most graphitic films in the previous data set were grown under the exact same conditions as this set.

The only explanation for the differences between these samples, which were deposited under the same conditions but at different times, is that the powered electrode was redesigned between the deposition of these two data sets. The aim of this redesign was to introduce the ability to deposit films at an increased temperature. It appears that some changes made during this redesign have altered the plasma in some way, changing the deposition conditions compared to the earlier electrode design (for example, changing the ratio of the earthed to powered electrode areas would change the power required to develop a certain DC bias). This difference between the new and previous data set means that the two can not be directly compared.

Returning to the new data set, Figure 3.13(b) shows the variation in the $I(\mathrm{D})/I(\mathrm{G})$ ratio as a function of the proportion of dopant in the gas phase for the N_2 only, H_2S only, 1:1 H_2S:N_2, 2:1 H_2S:N_2 and 2:1 N_2:H_2S conditions. For all conditions there is a reasonably linear increase in the $I(\mathrm{D})/I(\mathrm{G})$ ratio with increasing gas phase dopant proportion. This was also noticed in the previous data set, suggesting that the trends may still qualitatively be the same, but not quantitatively. Again this increase indicates an increase in the clustering of sp^2 sites with higher gas phase dopant concentration. There appears to be a slight difference in the magnitude of this increase depending on

which dopant gas is used. On observing the linear increase with dopant concentration it might be expected that N_2 would cause clustering at a higher rate than H_2S. Each nitrogen molecule can produce two N atoms, so for the same proportion of N_2 and H_2S in the gas phase, twice as many N atoms might be deposited in the sample as S atoms. Of course this argument assumes an equal dissociation efficiency for H_2S and N_2 when the NN triple bond is far stronger than an SH bond. Possibly because of this, H_2S appears to have a slightly greater effect on the sp^2 clustering than N_2. Whether this is down to a higher incorporation efficiency of S into the film compared to N, or whether the same concentration of S atoms in a sample induces a larger amount of clustering is not clear at the moment.

Figure 3.13(c) compares the change in sp^2 hybridised carbon atom clustering with gas phase dopant concentration for films deposited with and without an inert background of Ar. Again, in both cases, there is a reasonably linear increase in $I(\mathrm{D})/I(\mathrm{G})$ ratio with increasing dopant concentration. The films deposited with the Ar buffer appear consistently to have a slightly higher $I(\mathrm{D})/I(\mathrm{G})$ ratio than those deposited without Ar. To understand this, let us first think about the role the inert gas takes in the deposition process.

Amorphous carbon is thought to grow by the subplantation mechanism described in section 1.3.1. According to this theory, the properties of the deposited film are dependent on the energy with which the ionic carbon species implant into the growing film. At too low an impact energy there is no implantation, and ions polymerise on the substrate forming soft polymer (for a-C:H) or graphitic glassy carbon (a-C). At around 100 eV impact energy, the ions implant through the surface of the growing film, increasing the local density which favours sp^3 hybridisation. At too high an impact energy the ion implants through the surface and again increases the local density, but on its path it supplies excess energy to the surrounding film, producing a so-called "thermal spike". This allows the surrounding carbon to relax to the more thermodynamically stable sp^2 hybridisation. If argon is added to the plasma, argon ions also implant into the growing film but are not trapped. This process might increase the local density by knocking carbon atoms deeper into the film, but it may also produce a thermal spike and possibly increase the sputtering of hydrogen (which stabilises sp^3 hybridised carbon). Both effects can increase the ring clustering of sp^2 carbon atoms.

To assist our understanding of the effect of nitrogen on the sp^2 hybridised carbon atom ring clustering, a-C:N:H films were deposited from methane/ammonia mixtures. It was found that the deposition pressure was more stable with the addition of the argon buffer gas. This is probably due to the fact that on addition of Ar fluctuations in the ammonia flow rate (due to the needle valve) have a less significant effect on the total flow rate. Figure 3.13 (d) shows a comparison of the change in $I(\mathrm{D})/I(\mathrm{G})$ ratio with

gas phase dopant concentration for NH_3, N_2 and H_2S, methane and argon mixtures. Although there is slightly more scatter in the NH_3 data plot than the other two, the change in $I(D)/I(G)$ ratio with addition of NH_3 is closer to the H_2S line than the N_2 line. This might suggest that the incorporation of N atoms from N_2 molecules into the amorphous carbon network is not very efficient. To be incorporated into the film, N_2 either has to dissociate in the plasma or during impact on the film. Both H_2S and NH_3 only require the breaking of H-S (∼355 kJ/mol [13]) or H-N (∼390 kJ/mol [13]) bonds which are far weaker than the N_2 triple bond (∼940 kJ/mol [13]). Section 3.3.1 showed that it was possible to deposit a-C:S:H films where the deposited C/S ratio was almost the same as the process gas C/S ratio. It may be expected that a similar incorporation efficiency might be seen for NH_3, since both molecules would only require the breaking of a single S-H or N-H bond to incorporate the dopant atom into the amorphous carbon network. The incorporation of N from N_2 is likely to be lower as this would require the breaking of the comparatively strong N triple bond. Further comparison of the $CH_4/N_2/Ar$ and $CH_4/NH_3/Ar$ films using different analysis techniques may help us understand the change in properties produced by molecular nitrogen and ammonia as N atom sources for doping.

3.10 Growth Rate and Optical Properties

The growth rate and optical properties were determined simultaneously by spectroscopic ellipsometry.

3.10.1 Growth Rate

The variation in the growth rate with the proportion of dopant in the gas phase is shown in Figure 3.14(a). There is little variation in the growth rate between films deposited from mixtures including H_2S and N_2 or a mixture of the two. The trend in the decrease in growth rate is similar to that seen in section 3.5.1.

A considerable decrease in growth rate is observed with the addition of a background of Ar to the gas mixture. Figure 3.14(b) shows that for all gas mixtures there is a difference of about 20 nm min^{-1}, although this is reduced at high dopant concentration. The addition of 50 sccm of Ar to the 30 sccm process gas flow reduces the partial pressure of the methane/dopant mix in the chamber, so a decrease in growth rate is expected. There may also be an increase in the sputtering of species from the surface by implantation of Ar ions.

The deposition of a-C:N:H films from $CH_4/N_2/Ar$ and $CH_4/NH_3/Ar$ gas mixtures have again produced different results. Whereas there is little difference between the

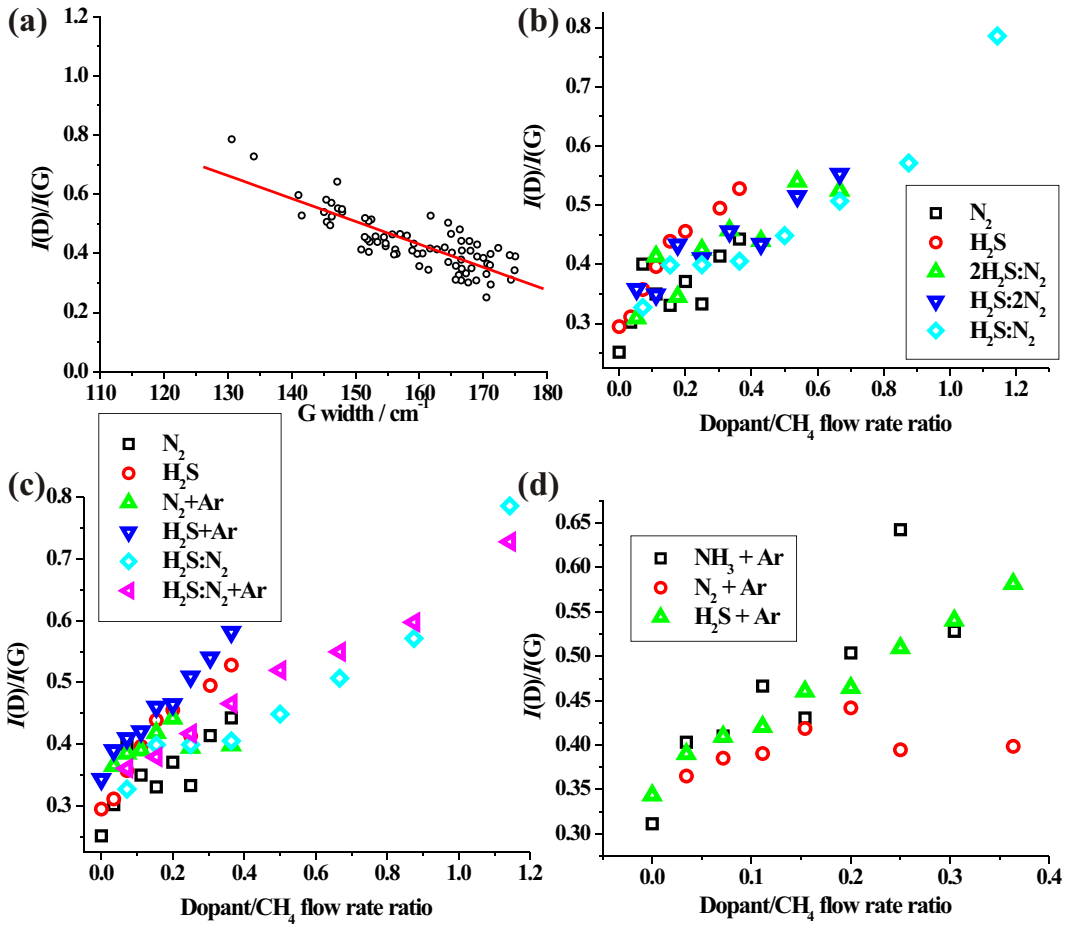

Figure 3.13: Data produced by Raman spectroscopy of the new experimental set, deposition conditions; DC bias -200 V, process pressure 30 mTorr, total flow rate 30 sccm: (a) A plot of the $I(\mathrm{D})/I(\mathrm{G})$ ratio against the G peak width for all films deposited, line displayed is a best fit to guide the eye. (b) Comparison of the variation of $I(\mathrm{D})/I(\mathrm{G})$ ratio with different dopants and dopant proportions. (c) As in (b) but including the addition of an Ar gas background. (d) Variation in $I(\mathrm{D})/I\mathrm{G}$ ratio with different proportions of N_2, H_2S and NH_3 in the process gas mixture.

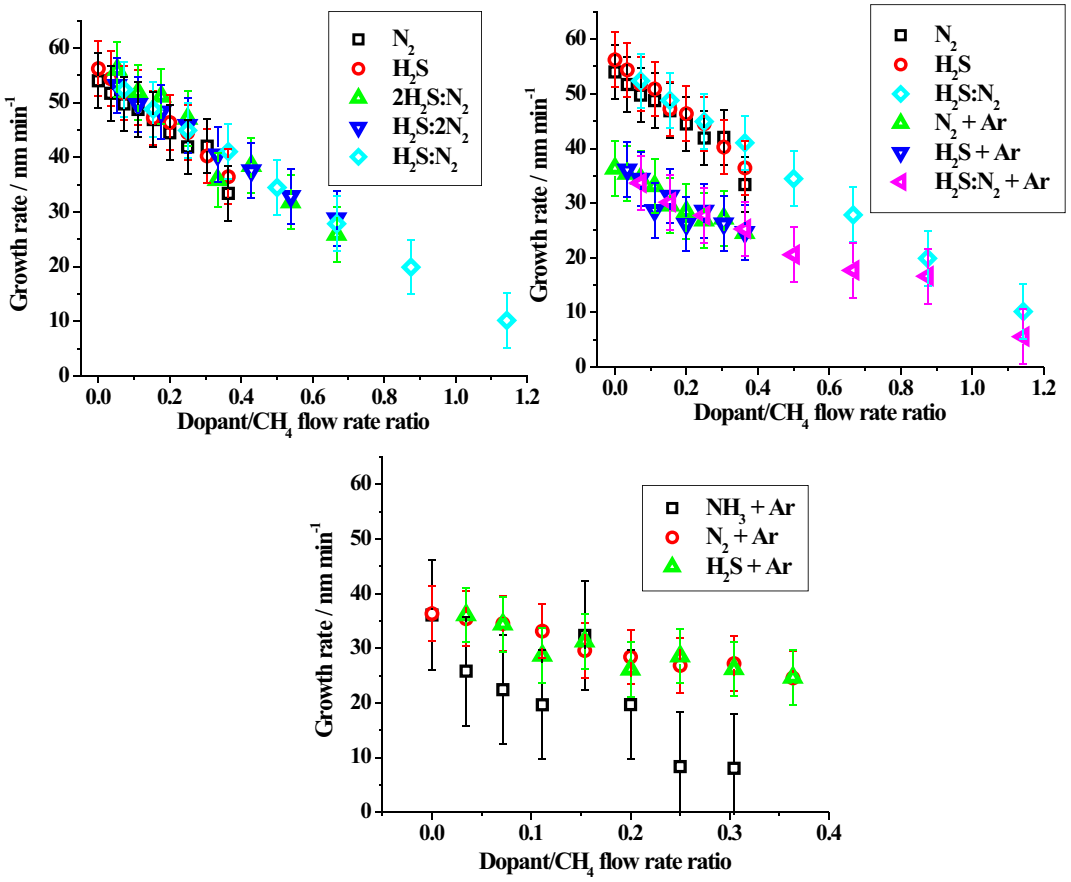

Figure 3.14: Variation of growth rate with the gas phase dopant proportion, other deposition conditions as shown in Figure 3.13 (a) N_2, H_2S and mixtures of the two, (b) with the addition of argon, (c) N_2, H_2S and NH_3 with Ar, the larger error bars for the ammonia data are due to inaccuracy of the flow through the needle valve.

growth rates of films deposited from $CH_4/N_2/Ar$ and $CH_4/H_2S/Ar$ gas mixtures, the $CH_4/NH_3/Ar$ mixture has a significantly lower growth rate. This suggests that there may not just be differences in the structures formed that contain the N atoms in the films grown from the $CH_4/N_2/Ar$ and $CH_4/NH_3/Ar$ gas mixtures (resulting in the different optical properties) but also differences in the the gas phase and surface chemistry of the plasmas (producing the different growth rates).

3.10.2 Optical Properties

Optical Band-gap

The change in E04 band gap with dopant proportion is shown in Figure 3.15(a). As with the growth rate, there is little change in the band gap between films deposited from H_2S and N_2 or a mixture of the two. Again there is a reduction in band gap energy with increasing gas phase dopant proportion.

It was shown in section 3.9.1 that there is more graphitic ring clustering within samples deposited with the addition of argon to the gas mixture compared to those deposited without. It is known that for amorphous carbon films that the band gap energy is inversely proportional to size of the graphitic clusters within the film. It might be expected then, that all the samples deposited with a background of Ar will also have a slightly lower band gap, and this is what is observed (Figure 3.15(b)).

Again the deposition of a-C:N:H films from $CH_4/N_2/Ar$ and $CH_4/NH_3/Ar$ gas mixtures has produced different results. There is little difference between the band gaps of films deposited with N_2 and H_2S but the equivalent film deposited with NH_3 has a much lower band gap. The E04 band gap energy of the films deposited with the highest proportion of NH_3 could not be determined by ellipsometry. For all values of energy (minimum value of 1.2 eV) the absorption coefficient was over 10^4 cm^{-1}. The low value of the E04 band gap deduced was not accompanied by a higher degree of graphitisation within the samples. This could be due to nitrogen producing a higher proportion of sp^2 hybridised carbon in the film without increasing the clustering of the sp^2 structures. This is further evidence for different mechanisms of incorporation of N into a-C:H depending if N_2 or NH_3 is used in the process gas mixture.

Refractive Index

As seen in section 3.5.2, there is little change in refractive index with the change in the gas phase dopant proportion. There is a noticeable difference between the refractive indices of films deposited with and without the addition of the Ar gas background (Figure 3.16). This is expected considering the films deposited with Ar also have lower band gaps and higher $I(D)/I(G)$ ratios, suggesting a lower hydrogen content and a harder film.

3.11 Compositional Analysis

It was not possible to perform XPS on this data set so an alternative form of compositional analysis had to be used. Due to the large deposition area of the RF electrode,

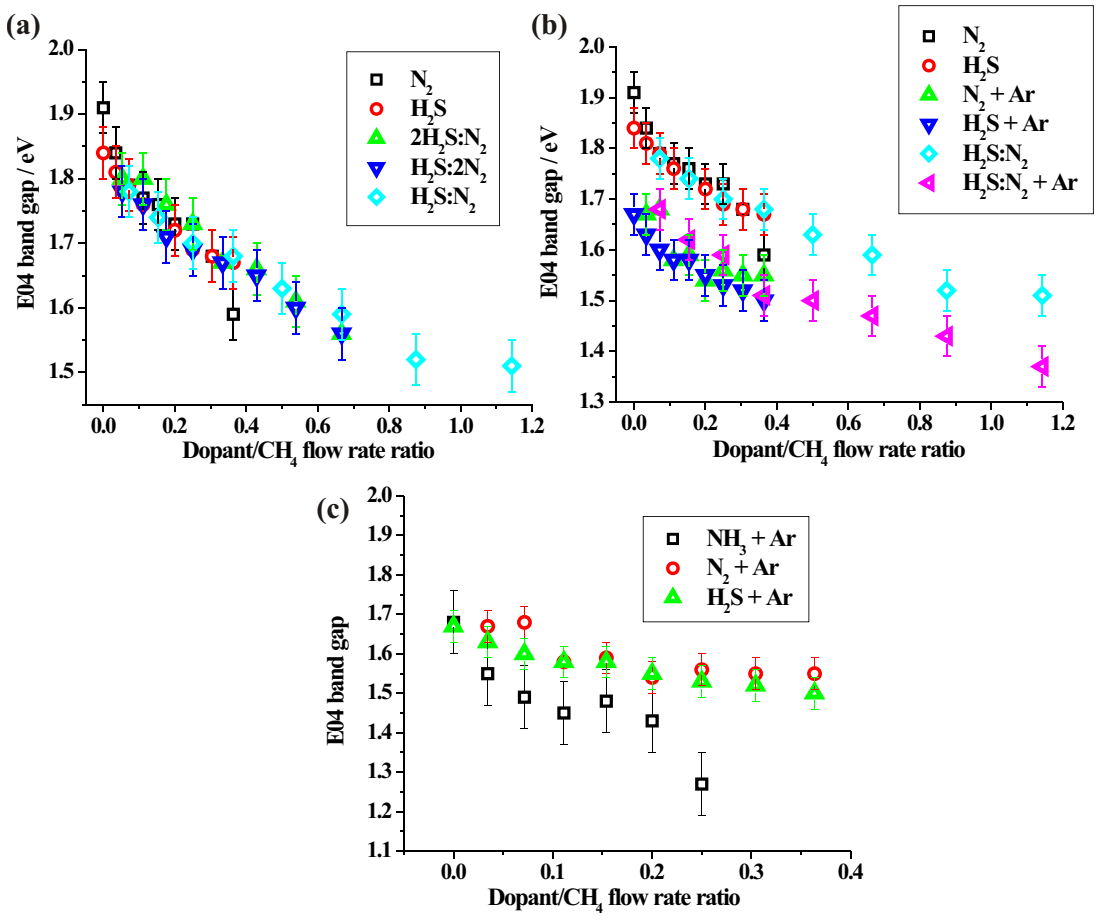

Figure 3.15: Variation of E04 band gap with the gas phase dopant proportion (a) N_2, H_2S and mixtures of the two, (b) with the addition of argon, (c) N_2, H_2S and NH_3 with Ar, the larger error bars for the ammonia data are due to inaccuracy of the flow through the needle valve.

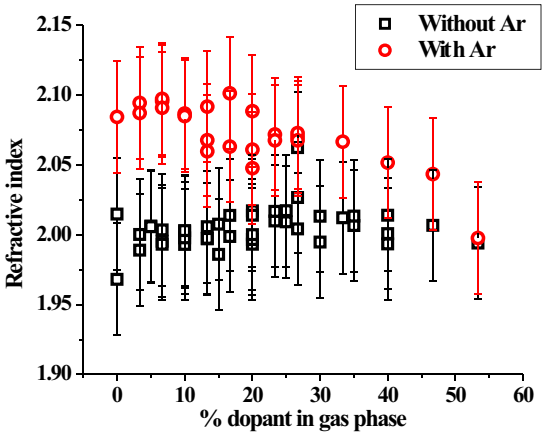

Figure 3.16: Comparison of the refractive index of films deposited with and without a background of Ar.

reasonably large amounts (10's of mg) of amorphous carbon could be produced permitting the use of micro-combustion elemental analysis.

3.11.1 Micro-Combustion Elemental Analysis

To produce the amounts of amorphous carbon powder required, the method of Donnet *et al.* [14] was used. Amorphous carbon films were deposited onto aluminium foil. The foil was then dissolved in a 1:1 mix of HCl:H_2O leaving the inert flakes of DLC floating in the solution. The mixture was diluted with purified water then the flakes were filtered off and air dried. Four 30-minute depositions produced more than 10 mg of amorphous carbon, enough for two micro-combustion runs.

In the first micro-combustion experiment, films were deposited with the same conditions as all films in this section (30 mTorr, -200 V, 30 sccm total flow rate) using methane/H_2S/N_2 gas mixtures, with a H_2S:N_2 ratio of 1:1. The data set was also repeated with a background of Ar. The results of this experiment are shown in Figure 3.17(a). Unlike XPS, micro-combustion detects C, N, S, and H, so the results can be presented in the form of atomic percentage concentrations instead of just ratios. The concentration of carbon in the samples is constant within the error bars (varies between 65-60 atomic %). There is a clear difference between the efficiency of the incorporation of sulfur and nitrogen, with almost twice as much sulfur as nitrogen in the film at high gas phase dopant proportion. This could be due to the difficulty of breaking N_2 into N atoms in the plasma, or N atom combination to form N_2 and diffusion out of the growing film.

The addition of argon has little effect on the incorporation rate of dopants in the

film. This suggests that all the changes in film properties observed with argon addition are not due to changes in dopant concentration because of the presence of Ar, but changes to the structure of the carbon network.

The micro-combustion results show that the films produced in this study have a high hydrogen content (∼35%). This means our samples may be slightly more prone to chemical degradation than other amorphous carbon films, and hence immersing them in hydrochloric acid may damage them. To test this theory micro-combustion was performed on amorphous carbon films that were deposited on a steel substrate and mechanically removed [15].

The concentration of both nitrogen and sulfur is slightly higher in the films grown on steel compared to those grown on aluminium (Figure 3.17(b)), suggesting that there maybe some degradation of the film by the HCl. A similar trend is seen for the hydrogen content (Figure 3.17(c)).

The lowest hydrogen content is seen for the films grown with a background of argon (Figure 3.17(c)). This agrees well with the refractive index data, which suggests that the films deposited with a background of Ar are slightly harder than those without.

In light of the above results, a second set of samples was deposited. Films were grown on steel from either CH_4/N_2 or CH_4/H_2S. The results from the micro-combustion of this second set are shown in Figure 3.17(d). Again, the incorporation of sulfur appears to be twice as efficient as the incorporation of nitrogen, and this is not compensating for the fact that the same flow of N_2 produces twice as many dopant atoms. This suggests that N_2 might not be the best choice of molecule for incorporating nitrogen into an amorphous carbon film. Micro-combustion could not be performed on an a-C:N:H film grown from $CH_4/NH_3/Ar$ mixtures. Only thick films can be easily removed from the steel substrate. The growth rate for $CH_4/NH_3/Ar$ films is lower than that for the equivalent $CH_4/H_2S/Ar$ or $CH_4/N_2/Ar$ film, meaning longer growth times would be required. This would not be a problem if ammonia was introduced via an MFC, but the stability of the flow from the needle value could not be guaranteed.

3.12 Summary and Conclusions

Using capacitively-coupled RFPECVD sulfur has been successfully incorporated into amorphous carbon thin films. The concentration of sulfur in a film was found to be proportional to the concentration of H_2S in the gas phase, the highest sample sulfur concentration being 27 atomic % measured by XPS. The distribution of sulfur in the carbon films was shown to be homogeneous throughout the sample by SIMS mapping and depth-profiling. Raman spectra of a-C:S:H films were similar to those of a-C:H

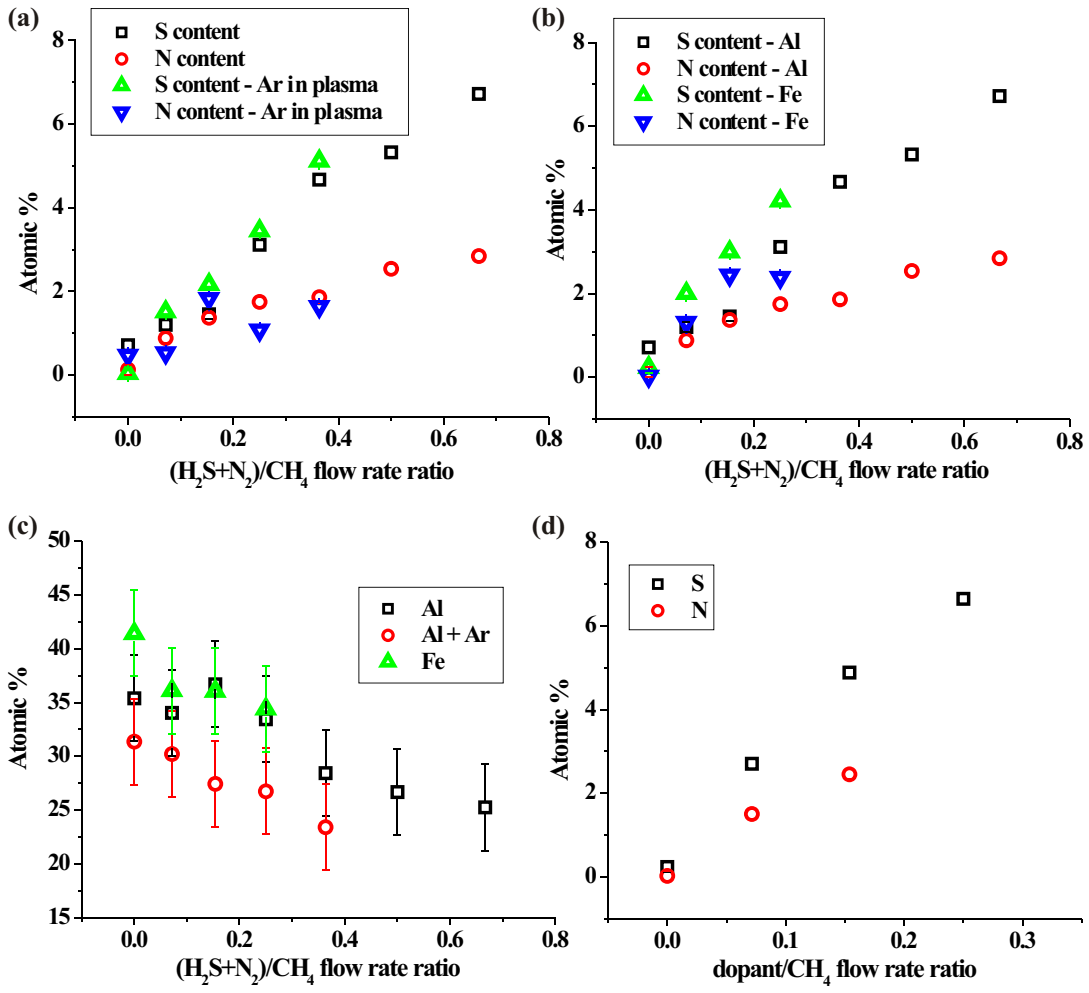

Figure 3.17: Results from micro-combustion elemental analysis, (a) Composition of films deposited with 1:1 H_2S:N_2, (b) Comparison of films grown on aluminium and steel, (c) Hydrogen content with gas phase dopant concentration for different substrates and with or without an argon background, (b) Composition of films doped with either sulfur or nitrogen.

films, showing only the D and G peaks of amorphous carbon. No peaks due to C-S bonding were observed, suggesting that the present films were different to those produced by Al-Dallal *et al.* [2]. Even plasma polymerisation of carbon disulfide only led to peaks due to S-S not C-S bonding. The Raman $I(\mathrm{D})/I(\mathrm{G})$ ratio shows that increasing the sulfur content of a sample increases the graphitic nature of the film. Over the range of experimental conditions investigated, the proportion of H_2S in the gas phase had the largest effect on the sample graphitisation. Despite the change in graphitisation with sulfur addition, there was only a slight decrease in the film's optical band gap and refractive index. The addition of H_2S to the process gas produced a large decrease in the growth rate. At high H_2S proportions the growth rate was often so low that no films were deposited.

These a-C:S:H films were compared to a-C:N:H films deposited from CH_4 and N_2 and a-C:N:S:H films deposited from CH_4, N_2 and H_2S. The effect of the addition of an inert buffer of Ar was also studied, as well as comparing a-C:N:H films deposited from CH_4/N_2 and CH_4/NH_3 gas mixtures. There was a slight difference between the properties of the a-C:S:H films grown in the first and second data sets. This is possibly due to the powered electrode being re-designed in the time between the two data sets (producing a change in the electrode geometry). Again the Raman spectra of all samples were similar to those observed for undoped a-C:H films. An increase in the graphitic nature of films with dopant concentration was observed, as in the first data set. There was little difference between the $I(\mathrm{D})/I(\mathrm{G})$ ratios of a-C:S:H, a-C:N:H and a-C:N:S:H films deposited with the same gas phase dopant concentration. There was a slight but consistent increase in the $I(\mathrm{D})/I(\mathrm{G})$ ratio on addition of a background of Ar. No difference in growth rate was observed between films deposited with the same concentration of H_2S, N_2 or a mixture of the two, although the growth rate was reduced for deposition with NH_3 and by the addition of an Ar background. There is also little difference in the band gap with different dopants, although NH_3 produces a lower band gap than N_2 or H_2S as does the addition of Ar. The refractive indices of all samples were similar, but those films deposited with the addition of Ar have consistently higher refractive indices.

Micro-combustion elemental analysis was used to determine the composition of the second data set. Thick samples were deposited on aluminium foil and then removed by dissolving the foil in HCl. The incorporation of S from H_2S was slightly more efficient than N from N_2, but less efficient than in the first experimental set. There was little difference in the dopant concentration with and without the background of Ar. Further samples were deposited on steel substrates and mechanically removed. There was a slight difference between the dopant concentration of films deposited on aluminum and steel, possibly caused by the reaction of the films with HCl. The concentration of

hydrogen in the samples decreases with dopant concentration and the addition of Ar.

The optical and mechanical properties of these a-C:S:H films do not seem to be substantially different from those of undoped a-C:H films. The incorporation of sulfur into a-C:S:H films does alter these properties, but not outside the range that tuning the deposition condition could produce in an undoped film. Whether sulfur acts as an n-type dopant in hydrogenated amorphous carbon films remains unknown.

For this project the future work would include; a full comparison of XPS and micro-combustion for elemental analysis, repeating experiments of Al-Dallal *et al.* [2] to look for signs of C-S bonding in the Raman spectra, IR spectroscopy to look for C-S bonding and different hydrogen environments, structural analysis by solid state NMR, analysis of the tribological properties such as wear and surface chemistry, and finally characterisation of the electrical properties of these materials possibly by the construction of simple devices.

Bibliography

[1] J. Filik, P. W. May, S. R. J. Pearce, R. K. Wild, and K. R. Hallam, *Diam. Relat. Mater.*, 2003, **12**, 974.

[2] S. Al-Dallal, S. M. Al-Alawi, S. Aljishi, M. Hamman, and S. Arekat, *J. Non-Cryst. Solids*, 1996, **196**, 168.

[3] O. Cavalleri, G. Gonella, S. Terreni, M. Vignolo, P. Pelori, L. Floreano, A. Morgante, M. Canepa, and R. Rolandi, *J. Phys. Condens. Matter.*, 2004, **16**(26), S2477.

[4] T. Y. Leung, W. F. Man, P. K. Lim, W. C. Chan, F. Gaspari, and S. Zukotynski, *J. Non-Cryst. Solids*, 1999, **254**, 156.

[5] P. Merel, M. Tabbal, M. Chaker, S. Moisa, and J. Margot, *Appl. Surf. Sci.*, 1998, **136**, 105.

[6] J. Schwan, S. Ulrich, V. Batori, H. Ehrhardt, and S. R. P. Silva, *J. Appl. Phys.*, 1996, **80**(1), 440.

[7] D. P. Dowling, K. Donnelly, M. Monclus, and M. McGuinness, *Diam. Relat. Mater.*, 1998, **7**, 432.

[8] ed. R. F. Davis, *Diamond Films and Coatings: Development, Properties and Applications*, Noyes Publications, New Jersey, 1993.

[9] ed. G. P. Crawford, *Flexible Flat Panel Displays*, John Wiley & Sons Ltd, Chichester, 2005.

[10] D. Lin-Vien, N. Colthup, W. Fateley, and J. Graselli, *The Handbook of Infrared and Raman Characteristic Frequencies of Organic Molecules*, Academic Press: Boston, 1991.

[11] J. Robertson, *Mater. Sci. Eng. R*, 2002, **37**, 129.

[12] A. Y. Liu and M. L. Cohen, *Phys. Rev. B.*, 1990, **41**, 10727.

[13] A. Negi and S. Anand, *A Textbook of Physical Chemistry*, New Age International Ltd., New Delhi, 1985.

[14] C. Donnet, J. Fontaine, F. Lefebvre, A. Grill, V. Patel, and C. Jahnes, *J. Appl. Phys.*, 1999, **85**, 3264.

[15] J. C. Sanchez-Lopez, C. Donnet, F. Lefebvre, C. Fernandez-Ramos, and A. Fernandez, *J. Appl. Phys.*, 2001, **90**(2), 675.

Chapter 4

Raman Spectroscopy of Diamondoids

4.1 Introduction

In this chapter, the effects of variations in structure and symmetry on the intramolecular vibrations of a selection of diamondoid molecules, from adamantane to [121321] heptamantane (Figure 4.1), are analysed by Raman spectroscopy. Assignments are made using vibrational frequencies and Raman intensities calculated at the B3LYP level of theory. Spectra are compared and contrasted with respect to the molecular geometries of the diamondoids with special attention being paid to any modes that may be structurally diagnostic.

Figure 4.1 depicts the relationships between all the diamondoids included in this study. The first three structures, adamantane (a), diamantane (b), and triamantane (c), are the only isomers possible constructed of one, two or three adamantane units. A further unit can be added in four distinct ways, producing [121] tetramantane (d), [1(2)3] tetramantane (e), and both enantiomers of the chiral [123] tetramantane (f).

All the other diamondoids in this study are built by the addition of further adamantane units to the base of these four structures with the exception of (i) which results from methyl addition to (h). The pentamantanes can be split into two groups; those whose structure can only be related to a single tetramantane, and those whose structure is based on a combination of two or all three tetramantanes. The first group contains [1212] pentamantane (g), [1(2,3)4] pentamantane (h), and chiral [1234] pentamantane (l), whose structures are uniquely based on [121] tetramantane, [1(2)3] tetramantane and [123] tetramantane, respectively. A further pentamantane, [1231] pentamantane, is predicted and would be uniquely related to [123] tetramantane, which is the base pentamantane for [12312] hexamantane (n), but this has not yet been isolated, and may not even be stable due to steric interactions between two specific neighbouring hydrogens.

The second group contains chiral [1213] pentamantane (k) (related to [121] and [123] tetramantanes), [12(3)4] pentamantane (j) (related to [123] and [1(2)3] tetramantanes) and chiral [12(1)3] pentamantane (m) (related to [121], [1(2)3] and [123] tetramantanes). This inherent ordering permits the grouping of this selection of diamondoids by their root tetramantane(s), producing five groups, adamantane to triamantane, then three groups uniquely derived from and including all tetramantanes, and finally pentamantanes that can be made by addition to either of two or all three tetramantanes. [12312] hexamantane (n) and [121321] heptamantane (o) are analysed separately due to the absence of [1231] pentamantane that would help relate [12312] hexamantane to [123] tetramantane.

All diamondoid samples were provided by MolecularDiamond Technologies, except for adamantane which was purchased from British Drug Houses Ltd. Samples were supplied as small crystals or powders (99% pure), a selection of which are shown in Figure 4.2.

Appendix A contains a reference to a concise version of the material displayed in this chapter which has been published in the journal *Spectrochimica Acta A: Molecular and Biomolecular Spectroscopy*.

4.2 Results

The Raman spectrum of a typical diamondoid, taken with 488 nm excitation, is shown in Figure 4.3. The spectrum can be separated into three regions; C-H stretch modes from 3000 - 2800 cm^{-1}, combination modes from 2800 - 2500 cm^{-1}, and all other molecular fundamental modes from 1500 - 200 cm^{-1}. Looking at the width of the bands corresponding to CH stretches compared to those associated with the lower frequency modes, the CH stretching bands are considerably broader. This broadening has been observed previously in adamantane [1] and was found to reduce considerably on cooling to below the plastic phase transition at 209 K (Figure 4.4). The cause of this broadening is unknown but is speculated to be caused by coupling of the high frequency modes to the crystal disorder.

For clarity, throughout the rest of this section all experimental and calculated spectra are separated into the two regions of interest, the high frequency CH stretch regions (2800 - 3100 cm^{-1}) and the lower frequency regions. This allows us to normalise each region to its strongest intensity peak, permitting clearer comparison of the weaker lower frequency modes. The CH stretch modes are approximately three times more intense

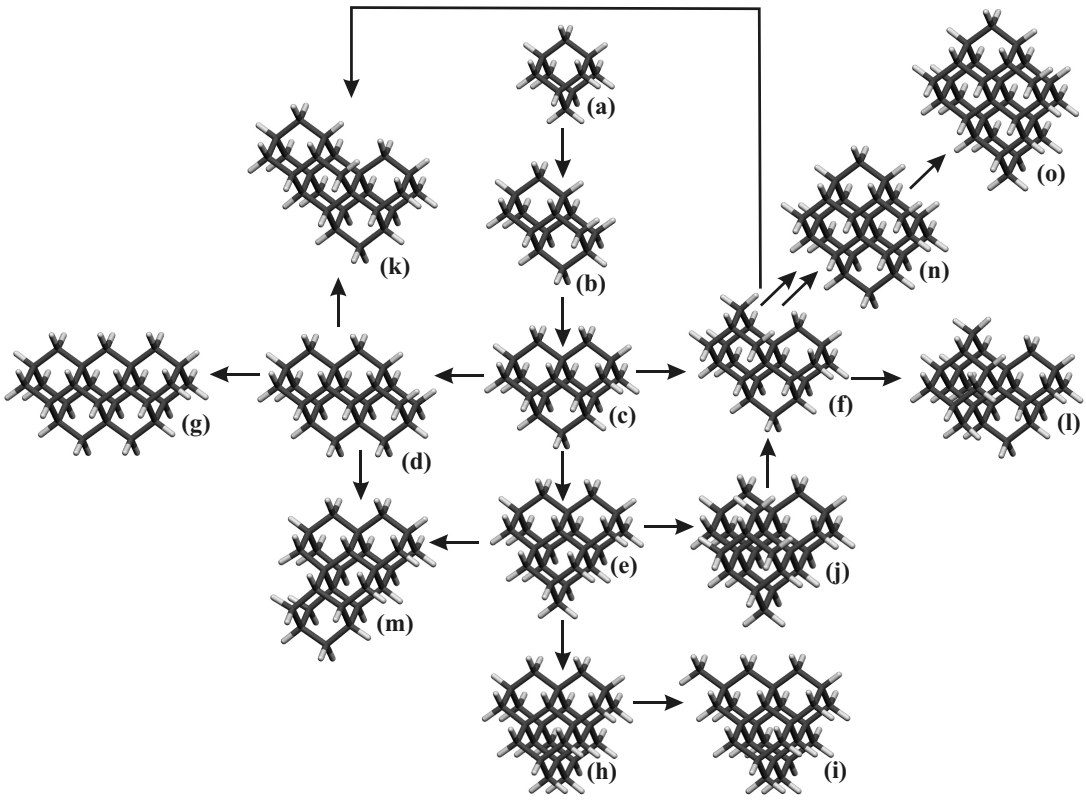

Figure 4.1: Diamondoids studied in this experiment, arrows indicate molecular growth by the face fusing of a single adamantane unit, (a) adamantane $C_{10}H_{16}$ T_d, (b) diamantane $C_{14}H_{20}$ D_{3d}, (c) Triamantane $C_{18}H_{24}$ C_{2v}, (d) [121] tetramantane $C_{22}H_{28}$ C_{2h}, (e) [1(2)3] tetramantane $C_{22}H_{28}$ C_{3v}, (f) [123] tetramantane $C_{22}H_{28}$ C_2, (g) [1212] pentamantane $C_{26}H_{32}$ C_{2v}, (h) [1(2,3)4] pentamantane $C_{26}H_{32}$ T_d, (i) 3-methyl-[1(2,3)4] pentamantane $C_{27}H_{34}$ C_{3v}, (j) [12(3)4] pentamantane $C_{26}H_{32}$ C_s, (k) [1213] pentamantane $C_{26}H_{32}$ C_1, (l) [1234] pentamantane $C_{26}H_{32}$ C_2, (m) [12(1)3] pentamantane $C_{26}H_{32}$ C_1, (n) [12312] hexamantane $C_{26}H_{30}$ D_{3d}, (o) [121321] heptamantane $C_{30}H_{34}$ C_s.

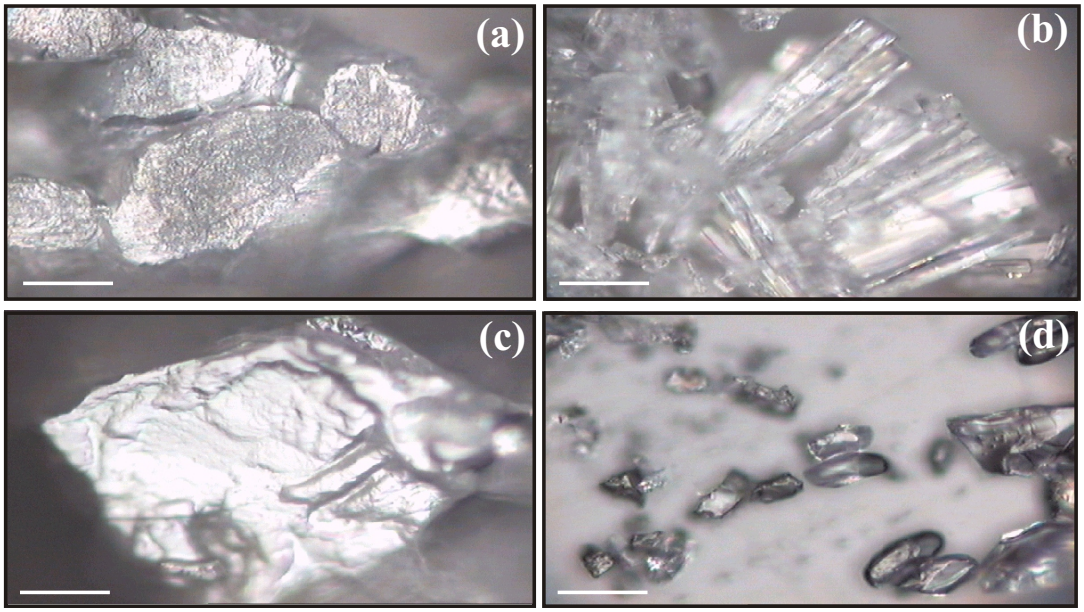

Figure 4.2: Optical microscopy pictures of crystals of (a) adamantane, (b) [1212] pentamantane (c) [1(2,3)4] pentamantane and (d) 3-methyl-[1(2,3)4] pentamantane. The scale bar on each image is 40 μm.

than the other modes, and are, in what follows, always normalised to the strongest peak. The lower frequency regions of the spectra are normalised to the strongest mode in the region 1100 - 1300 cm^{-1} not withstanding the occasional signal of high intensity at around 500 cm^{-1}.

4.2.1 Different Excitation Energies

The Raman spectra of the diamondoid crystals were taken on two separate spectrometers at four different wavelengths. The use of different excitation wavelengths is common in resonance Raman spectroscopy where a strong enhancement of signal intensity is noticed when the energy of the excitation approaches an electronic transition. In this case no resonance enhancement is expected as the HOMO-LUMO gap energy of the diamondoids is predicted [2] to be much larger than our highest excitation energy (between 6 and 8 eV, compared to 3.8 eV). The main reasons for using different wavelengths in this study was to obtain as high a resolution spectrum as possible, over a region where the response of the spectrometer was uniform and where there was no luminescent background.

Figure 4.5 shows the Raman spectrum of [1(2,3)4] pentamantane taken with the four different excitation wavelengths. The different experimental set-up for each wavelength

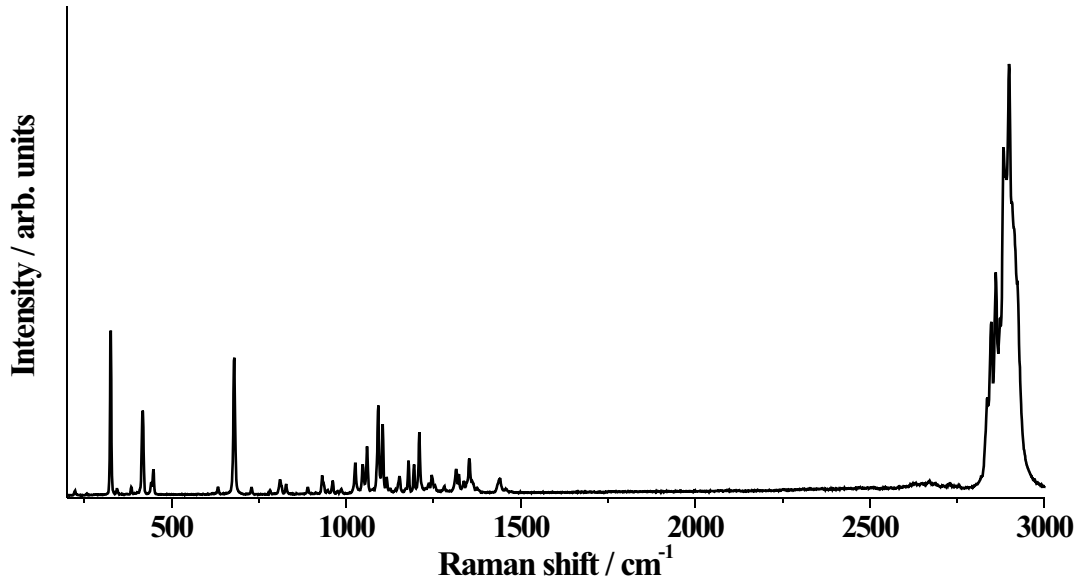

Figure 4.3: A typical diamondoid Raman spectrum, in this case [1212] pentamantane excited by 488 nm radiation.

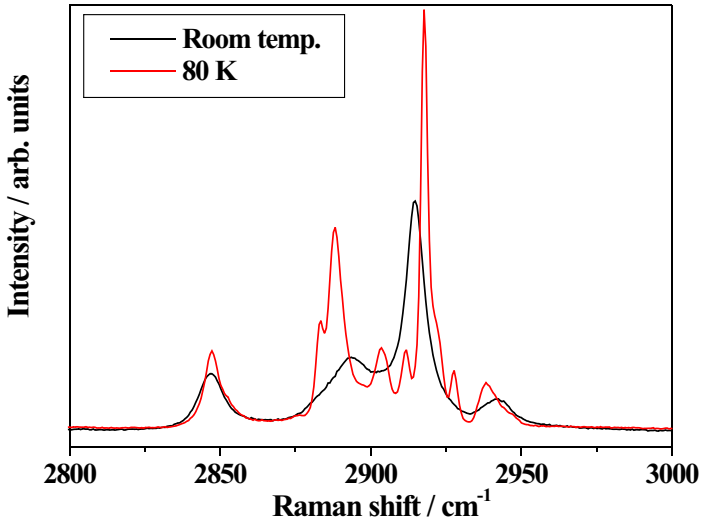

Figure 4.4: CH stretch region of the Raman spectrum of adamantane at room temperature and at 80 K

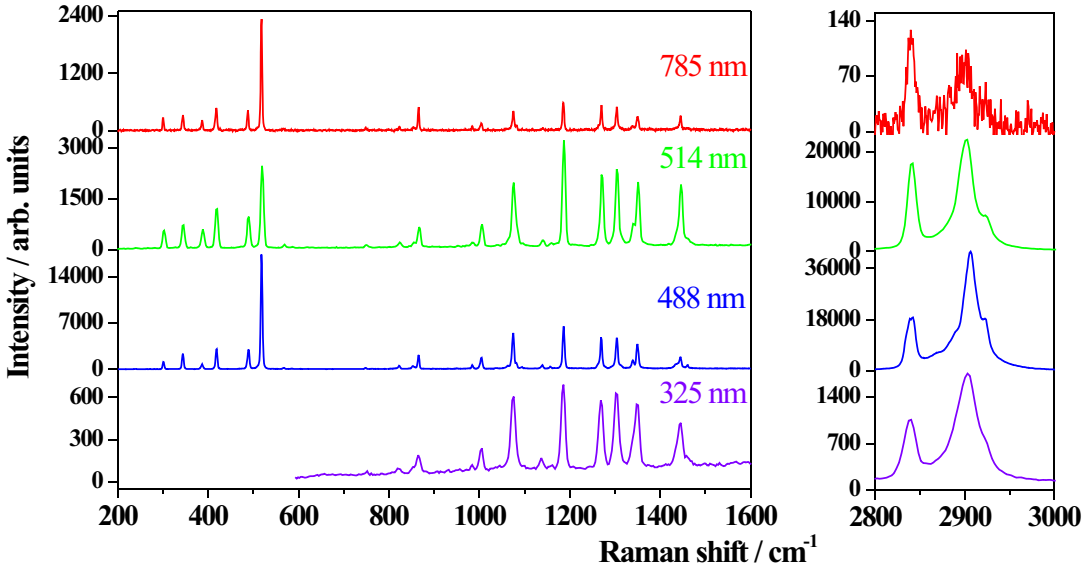

Figure 4.5: Raman spectra of [1(2,3)4] Pentamantane taken with different excitation wavelengths: Purple spectrum taken with a 325 nm He-Cd laser, blue spectrum taken with a 488 nm Ar^+ laser, green spectrum taken with a 514 nm Ar^+ laser, red spectrum taken with a 785 nm diode laser.

is described in chapter 2. The 325 nm excitation is not suitable for this study because much of the low frequency spectrum is lost with the relatively high wavenumber cut-off of the Rayleigh filter. The 785 nm excitation is also not ideal, it produces a high resolution spectrum with a filter that cuts off close to the laser line, but the sensitivity of the detector rapidly drops off in the infra-red (IR) so the CH stretch modes appear to be very weak. The detector sensitivity is reasonably uniform for the 514 nm-excited spectrum but this wavelength suffers from a poor spectral resolution due to too few lines per millimeter on the grating. This leaves only the 488 nm excitation which luckily produces a high resolution spectrum, has a flat system response and good Rayleigh filter. All spectra shown throughout this chapter were taken using the 488 nm excitation system.

4.2.2 Theory

Throughout this section all calculations were performed using the Gaussian 03 software suite [3]. Figure 4.6 shows the experimental Raman spectrum of adamantane, along with a selection of spectra calculated using different functionals and basis sets. The spectra shown in (b), (c) and (d) were all calculated with the B3LYP density functional

and the 6-311+G(2d,p), 6-31G* and the split-valence basis set of Schafer *et al.* [4] with polarisation functions on carbon, respectively. Spectra (d), (e) and (f) were all calculated with the SVP basis set but with B3LYP [5,6], the Perdew-Burke-Ernzerhof generalized-gradient approximation (PBE) for the exchange and correlation functions [7,8], and BLYP [6,9] functionals, respectively. The combination that best reproduced the experimental data was the B3LYP combination and the 6-311+G(2d,p). This is not surprising since the 6-311+G(2d,p) basis set is considerably larger than the other two used. It is not possible to calculate the Raman spectra of all the diamondoids by this method as the computational cost would be far too great. Since all the other calculations produced similar results, the most economical combination was chosen; the B3LYP density functional and the SVP basis set.

The diamondoid structures were drawn and initially cleaned-up and symmetrised using the GaussView graphical user interface. In Gaussian03, the structures were optimised and the harmonic vibrational frequencies and Raman intensities were calculated. All modes in the calculated spectra are displayed as Lorentzians, each with a full-width half-maximum of 5 cm^{-1} (similar to that seen in the experimental data).

The use of B3LYP and a split-valence basis set to calculate vibrational frequencies and Raman activities of adamantane and its derivatives has been found to successfully reproduce experimental spectra [10,11]. Differences between the calculated and experimental spectra were found to be most pronounced in CH_2/CH bending vibrations, this was also observed in our data. The causes of these deficiencies are uncertain but they are mostly likely due to use of a relatively small basis set or the effect of intermolecular interactions, or changes in symmetry, in the condensed phase that are not accounted for in our calculations on single molecules.

4.2.3 Adamantane, Diamantane, and Triamantane

Let us start with the simplest example. Adamantane has 72 vibrational modes, 11 T_2 + 7 T_1 + 6 E + 1 A_2 + 5 A_1. The T_1 and A_2 vibrations are not Raman active, leaving 22 possible Raman signals. Comparing the experimental and calculated spectra (Figure 4.7), only half of these modes have enough intensity to be observable experimentally. The CH stretch region consists of six broad vibrations, three of which are so close in energy they are unresolvable (2848 cm^{-1} (experimental), 3005 cm^{-1} (calculated), E + A_1 + T_2). The vibration with the highest Raman intensity is the fully symmetric A_1 mode (2916 cm^{-1} (exp), 3039 cm^{-1} (calc) and intensity 654 $Å^4$/amu (calc)).

The lower wavenumber region contains five strong Raman bands, the most intense being the doubly-degenerate CH_2 twist mode (1220 cm^{-1} (exp), 1238 cm^{-1} (calc) and intensity 2 × 46 $Å^4$/amu (calc)). The other visible modes are the fully symmetric

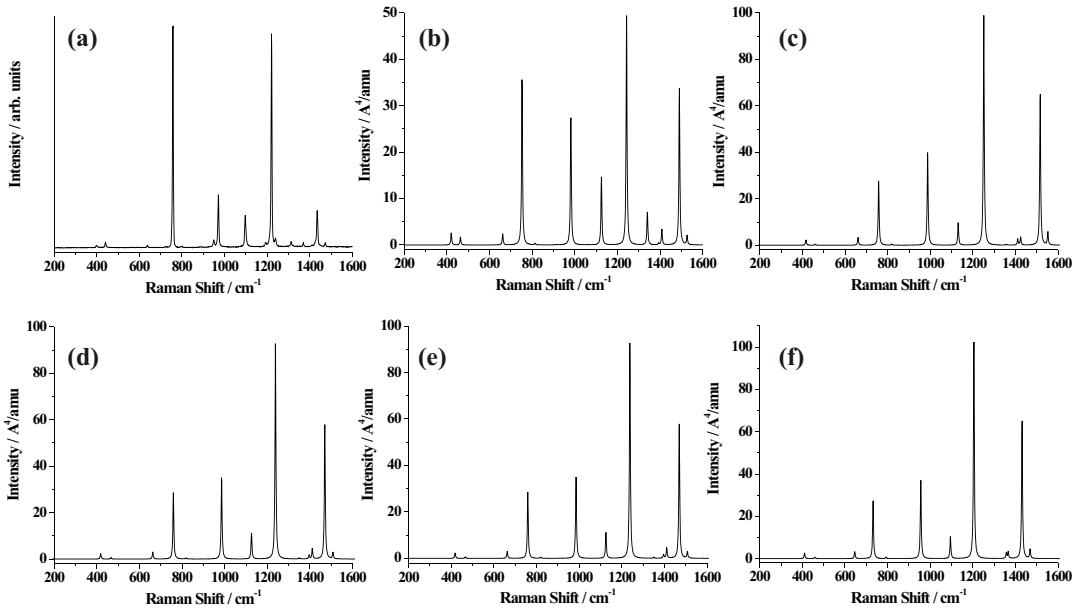

Figure 4.6: Raman spectra of adamantane (a) experimental (488 nm), (b) B3LYP/6-311+G(2d,p), (c) B3LYP/6-31G*, (d) B3LYP/SVP, (e) PBE/SVP, (f) BLYP/SVP.

A_1 CC stretch (breathing) mode (757 cm^{-1} (exp), 759 cm^{-1} (calc) and intensity 27 $Å^4$/amu (calc)), a T_2 CC stretch/CCC bend mode (971 cm^{-1} (exp), 985 cm^{-1} (calc) and intensity 3×12 $Å^4$/amu (calc)), a T_2 CH_2 rock/CH wag mode (1097 cm^{-1} (exp), 1126 cm^{-1} (calc) and intensity 3×4 $Å^4$/amu (calc)) and finally an E CH_2 scissor mode (1435 cm^{-1} (exp), 1469 cm^{-1} (calc) and intensity 2×29 $Å^4$/amu (calc).

Diamantane has 96 vibrational modes, 11 A_{1g} + 6 A_{1u} + 5 A_{2g} + 10 A_{2u} + 16 E_g + 16 E_u. Only the A_{1g} and E_g species are Raman active, leaving 27 Raman active vibrational modes. Examining the experimental and calculated spectra (Figure 4.7) there are 22 visible Raman signals. As found in the adamantane spectrum, the diamantane spectrum also contains similar broad high wavenumber CH stretch modes and the sharper lower wavenumber modes. The CH stretch regions of both these molecules have six Raman signals, produced by similar nuclear displacements, but in diamantane only two modes are close enough to be unresolvable, and hence give the extra peak in the spectrum compared to that of diamantane. In the lower wavenumber range there seems to be a reasonable correlation between the peak positions in the spectra of adamantane and diamantane, but there are more peaks present in the diamantane spectrum. For example, the single peak at 1220 cm^{-1} in the adamantane spectrum is replaced by two signals in the diamantane spectrum. Studying the nuclear displacements associated with these vibrations, all three are E_g modes consisting of CH_2 twisting motions strongly mixed with CH wagging modes. Both adamantane and diamantane have six CH_2 groups, and group theory shows that in both there should be only one E_g/E

CH_2 twist. This suggests that the appearance of more in the spectrum must be due to mixing with extra CH wag/CC stretch E_g modes produced by the larger structure of diamantane. The majority of the peaks in the diamantane spectrum can be traced back to similar peaks in the adamantane spectrum, which have been complicated by mixing induced by extra modes of the same symmetry at similar energies.

The addition of another adamantane unit produces triamantane, which has 120 vibrational modes, 35 A_1 + 25 A_2 + 29 B_1 + 31 B_2. Again, the addition of another unit has reduced the symmetry of the molecule. From adamantane to diamantane this had little effect, as in both only limited symmetries were Raman active. In triamantane, the symmetry has decreased to C_{2v}, so all modes are now Raman active, producing 120 possible signals in the Raman spectrum (Figure 4.7). This increase in molecule size and decrease in symmetry means there are now have 20 intense CH stretch vibrations in the same 100 cm^{-1} region, which produces a very poorly resolved experimental signal.

For the lower frequency region, the agreement between the experimental and calculated data appears to decrease. For adamantane and diamantane, the only major inconsistencies in the calculated intensities were the underestimation of the breathing modes (757 cm^{-1} in adamantane, 708 cm^{-1} in diamantane) and the overestimation of the CH_2 scissor modes (1435 cm^{-1}) relative to the ∼1220 cm^{-1} CH_2 twist modes. As the complexity of the Raman spectra increases the deficiencies in the calculated intensities become more prominent. The calculated spectrum for triamantane still has the same discrepancies as the adamantane and diamantane calculations but there is also disagreement in the intensity of vibrations in the region around ∼1300 cm^{-1} and ∼1100 cm^{-1}. This type of disagreement is not wholly unexpected for calculations performed on molecules of this size due to the limitations in the size of basis set [11]. The most prominent signals in the low wavenumber region are two close peaks at 1197 cm^{-1} and 1222 cm^{-1} similar to those observed in the diamantane spectrum, both of which are assigned to CH wag motions, and the 681 cm^{-1} cage deformation (CCC bend, CC stretch) which, again, also has an analogous peak in diamantane. As well as these modes there is a large abundance of weaker modes throughout the 400 - 1500 cm^{-1} region produced by the larger structure of triamantane and the absence of symmetry forbidden vibrations.

4.2.4 [1(2)3] tetramantane, [1(2,3)4] pentamantane and 3-methyl-[1(2,3)4] pentamantane

Throughout the rest of this chapter all vibrational frequencies are experimental values unless stated as otherwise.

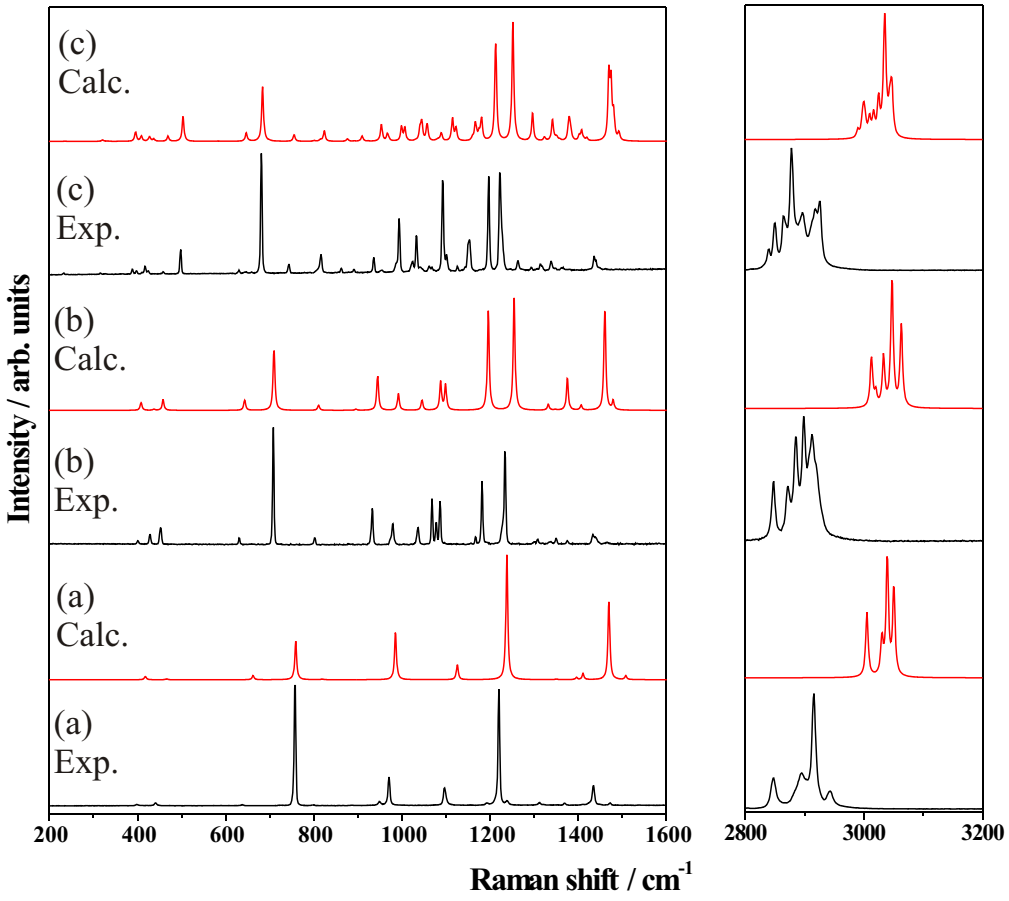

Figure 4.7: Experimental and calculated spectra for (from bottom) (a) adamantane, (b) diamantane and (c) triamantane.

As mentioned above, the attachment of an additional adamantane unit to triamantane can occur in four distinct ways, producing two distinct molecules and a pair of enantiomers. In this section, the molecules studied are made by addition to the central unit in triamantane, producing [1(2)3] tetramantane (e), and further addition to this molecule to produce several pentamantane derivatives.

The addition of an adamantane unit to the central unit in triamantane produces [1(2)3] tetramantane ($C_{22}H_{28}$), trivially referred to as "*iso*-tetramantane" . This increases the symmetry from C_{2v} to C_{3v}, meaning that of the 144 vibrational modes (29 A_1 + 19 A_2 + 48 E), only a maximum of 77 peaks would be expected in the Raman spectrum (Figure 4.8), considerably less than for triamantane due to the presence of doubly degenerate E modes and the A_2 modes being Raman inactive in C_{3v} molecules. Despite the fewer expected signals there are still 15 intense CH stretch vibrations, again making this region of the spectrum poorly resolved. The lower wavenumber region does not have notably fewer peaks than triamantane, since although triamantane has 120 Raman active vibration modes not all of them will induce a significant change in polarisability in the molecule, necessary for an experimentally observable Raman signal. Again there are two intense E CH_2 twist modes (1177 cm^{-1} and 1211 cm^{-1}) similar to those observed in the diamantane spectrum. But, as in the triamantane spectrum, the relative intensities of the neighbouring peaks are different in the calculated spectrum compared to the experimental spectrum. The most noticeable difference between the low wavenumber region of [1(2)3] tetramantane and the other diamondoid molecules studied so far is the increase in intense signals in the CCC bend/CC stretch deformation region. From adamantane to triamantane there has been only one strong signal, decreasing in wavenumber (from 757 to 681 cm^{-1}) as the molecular size increases. The same peak is still present in [1(2)3] tetramantane, but for the first time there are peaks with greater intensity at a lower wavenumber. The 659 cm^{-1} vibration involves stretching of the molecule parallel to the C_3 axis, whereas the more intense 505 cm^{-1} vibration is stretching perpendicular to this axis (Figure 4.9). The experimental intensity of this perpendicular stretch is over twice as large as any other mode in the 200 - 1500 wavenumber region but in the calculated spectrum it is only half as intense as the strongest CH_2 twist mode. This appears to be another region where only limited accuracy can be achieved because of the large size of the systems. Peak assignment is still possible but the agreement of the calculated vibrational frequencies with the experimental frequencies is considerably better than for the intensities.

As described above, [1(2)3] tetramantane is formed by adding an extra unit to one

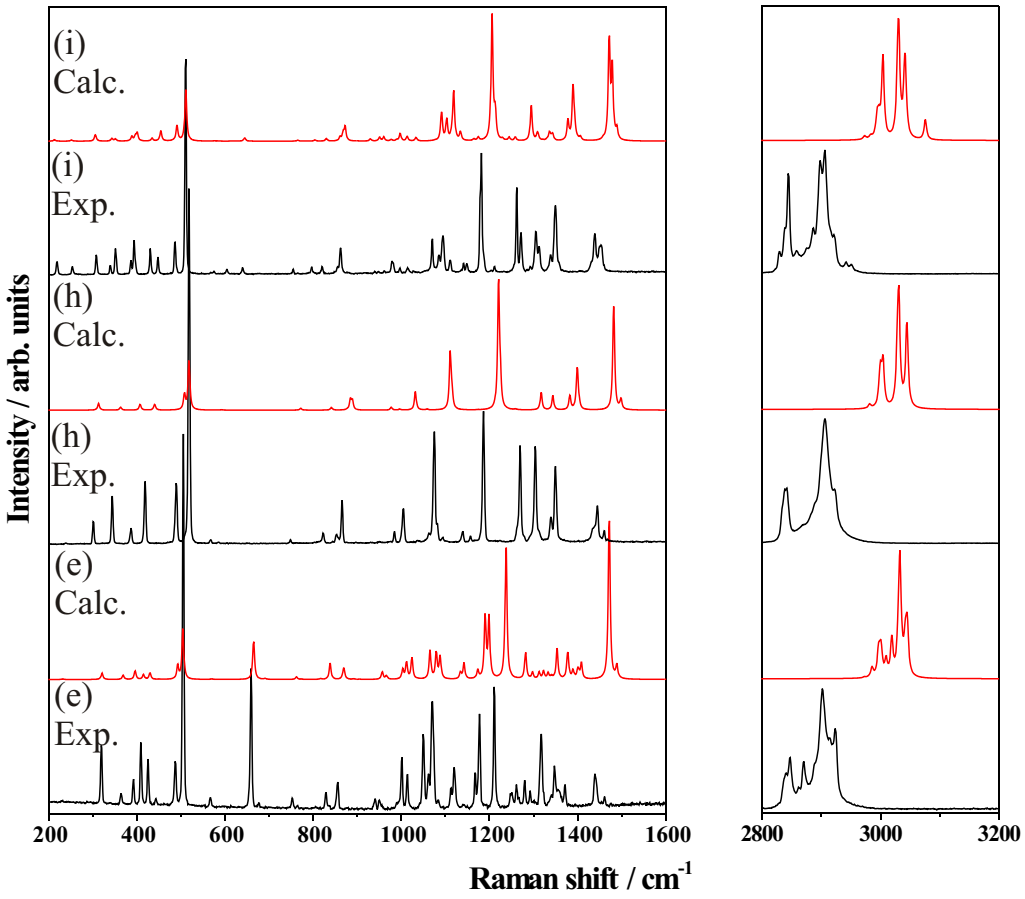

Figure 4.8: Experimental and calculated spectra for (from bottom) [1(2)3] tetramantane (e), [1(2,3)4] pentamantane (h) and 3-methyl-[1(2,3)4] pentamantane (i). Spectra have been normalised to the most intense signal at ∼1200 cm^{-1}.

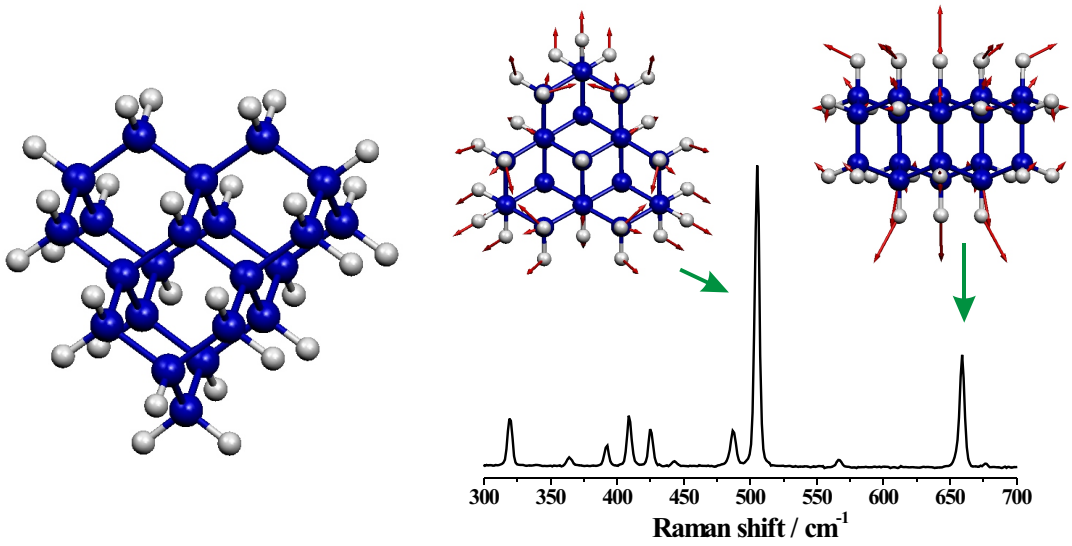

Figure 4.9: Mass weighted nuclear displacements of the 505 cm^{-1} and 659 cm^{-1} modes of [1(2)3] tetramantane.

of two equivalent sites on the central part of triamantane. Addition of a further unit to the other of these sites then leads to the smallest T_d symmetry polymantane after adamantane, [1(2,3)4] pentamantane ($C_{26}H_{32}$). [1(2,3)4] pentamantane has 168 vibrational modes, 24 T_2 + 18 T_1 + 14 E + 4 A_2 + 10 A_1, but because of the double or triple degeneracy of some of the vibrations, and the T_1 and A_2 modes being Raman inactive, there should be a maximum of 48 signals in the Raman spectrum (Figure 4.8). The high symmetry of this particular polymantane suggests that it may be rewarding to compare its Raman spectrum to those of adamantane and [1(2)3] tetramantane. The CH stretch region of the Raman spectrum of [1(2,3)4] pentamantane contains 8 vibrations which produce three broad peaks, bearing closer resemblance to the same region from adamantane than from [1(2)3] tetramantane. The CCC bend/CC stretch range, on the other hand, correlates better with that from [1(2)3] tetramantane. The only intense low wavenumber vibration in the adamantane spectrum occurs at 757 cm^{-1}, far from the 518 cm^{-1} mode in [1(2,3)4] pentamantane, whereas [1(2)3] tetramantane (as mentioned above) has both a peak at 659 cm^{-1} and at 505 cm^{-1}. Up to [1(2,3)4] pentamantane, the Raman spectra of all diamondoids (with the exception of adamantane, a special case) have displayed a peak close to ~680 cm^{-1}. So what is it about the structure of [1(2,3)4] pentamantane that removes the Raman active vibrational mode at this wavenumber?

The structures of all the diamondoid molecules in this study, can be put into one of five groups (Figure 4.10). Diamantane and triamantane are both rod-shaped diamondoids (Figure 4.10(a)) and would have the prefixes of [1] and [12] respectively,

if they were not unique isomers. Higher diamondoids of this family would involve growth in 1 dimension (the x-axis in Figure 4.10). [1(2)3] tetramantane is disc-shaped and has a comparatively isotropic structure (C_{3v} point group) which only extends in 2 dimensions (Figure 4.10(b)). [1(2,3)4] pentamantane is a tetrahedral arrangement of five adamantane units. This arrangement is also reasonably isotropic (T_d point group) but in this case the structure extends in 3 dimensions. The peak occurring at $\sim$680 cm^{-1} in all spectra, except adamantane and [1(2,3)4] pentamantane, is assigned as a breathing mode across a section which is one adamantane unit wide (Figure 4.9 shows this for [1(2)3] tetramantane). [1(2,3)4] pentamantane does not have a peak at $\sim$680 cm^{-1} because it is not 2-dimensional, there is no part of its structure that is only one-adamantane-unit across. Adamantane is a special case because all of its dimensions are one-adamantane-unit wide, and its equivalent peak is at 757 cm^{-1}, the lowest wavenumber strong Raman signal. The other two structural groups correspond to 2 and 3 dimensional diamondoids with lower symmetry than the as aforementioned molecules (Figure4.10(c), (e)). The structures of the molecules in these two final groups are described as 2D and 3D anisotropic to separate them from their higher symmetry counterparts . The hypothesis that a strong peak at $\sim$680 cm^{-1} can be used to identify a 2-dimensional diamondoid (i.e. one whose structure is one-adamantane-unit wide) will be tested further as this study progresses.

Still looking at the low wavenumber region, both [1(2)3] tetramantane and [1(2,3)4] pentamantane display reasonably intense peaks below 450 cm^{-1} which only start to appear when the polymantane structure is large, due to vibrations featuring quaternary carbon CCC bending. Yet again, the most intense vibration in the low wavenumber region (excluding the breathing mode) is an E CH_2 twist mode.

For [1(2,3)4] pentamantane there are also discrepancies between the observed and calculated spectra in the $\sim$400 cm^{-1} and $\sim$1300 cm^{-1} areas as observed for [1(2)3] tetramantane. It would be useful to see the effect of a larger basis set on the calculated spectrum but it is not feasible on a molecule this size using B3LYP, it is possible using Hartree-Fock, however. Recalculating the vibrational frequencies and Raman intensities of [1(2,3)4] pentamantane with Hartree-Fock theory and the same basis set, the frequencies are considerably worse, but there is little change in the intensities (Figure 4.11). This suggests that correlation has little effect on calculated Raman intensities. If the spectrum is recalculate using Hartree-Fock with the larger 6-311+G(2d,p) basis set, a positive effect on the calculated intensities is noticed compared to the experimental data. The most obvious deviation in the smaller basis set calculation is the gross underestimation of the intensity of the 518 cm^{-1} breathing mode. In the experimental spectrum this mode is over twice as intense as any other in the non-CH stretch region,

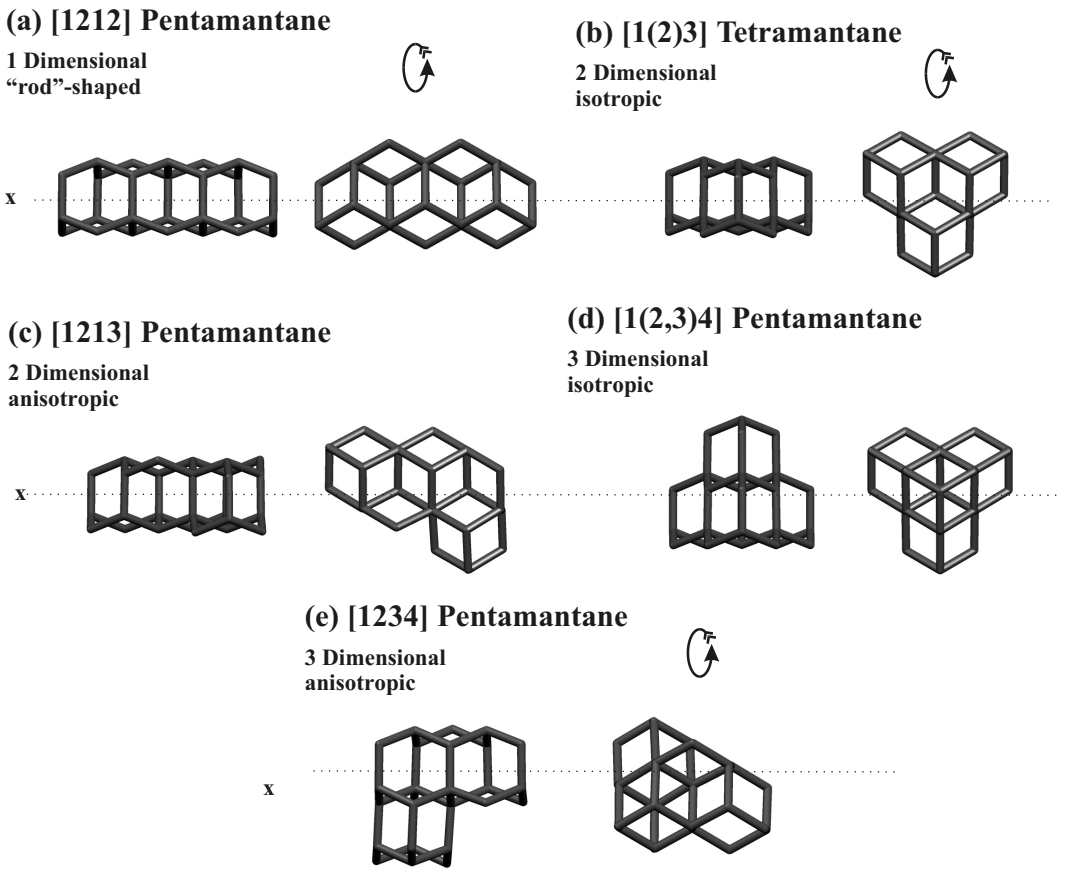

Figure 4.10: The five diamondoid structural groups. The molecules on the right in each pair are identical to those on the left but rotated 90° around the x-axis, which is shown as a dotted line.

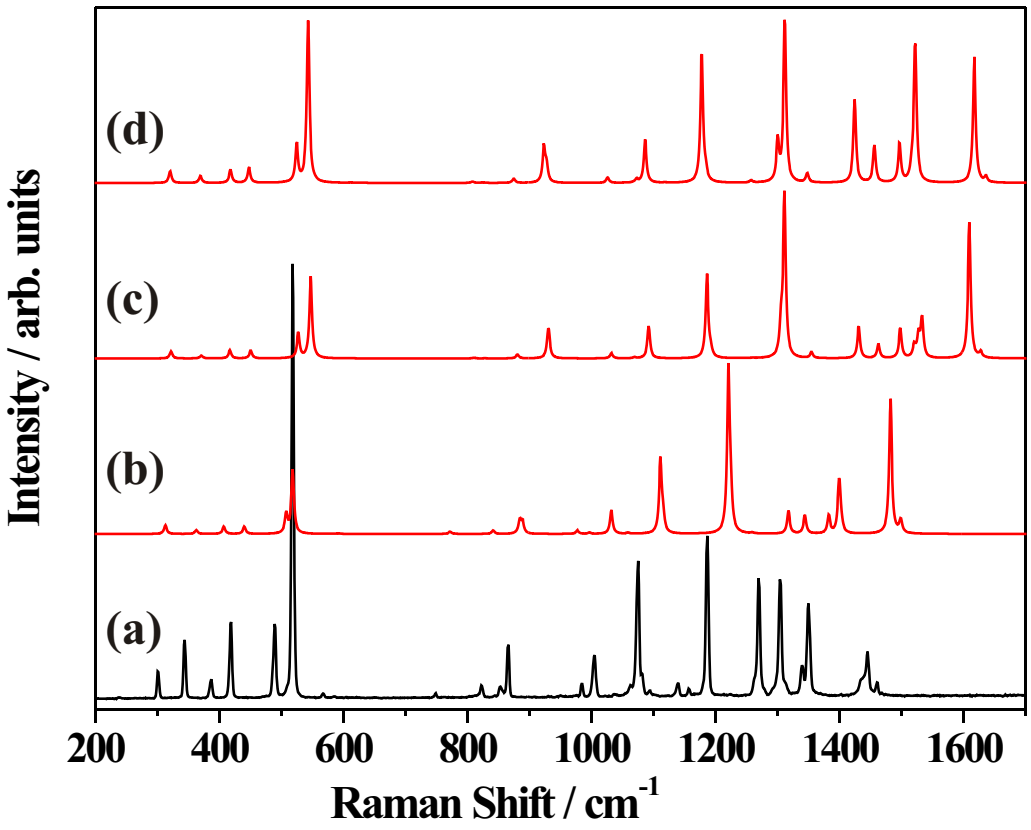

Figure 4.11: The CC stretch/CH bend region of the experimental and calculated Raman spectra of [1(2,3)4] pentamantane (a) experimental spectrum, (b) B3LYP/SVP, (c) HF/SVP, (d) HF/6-311+G(2d,p).

whereas in the smaller basis set calculation it is half as intense as the strongest mode. With the larger basis set, the calculated intensity of the breathing mode increases to be the strongest peak in the non-CH stretch region, a clear improvement over the smaller basis set calculation. In general, the overall "shape" of the larger basis set spectrum is significantly closer to the experimental than the smaller basis set, but there is still some disagreement. It would be useful to try even larger basis sets but it is not currently feasible for molecules as large as [1(2,3)4] pentamantane.

Recent work by Richardson *et al.* [12] used the Perdew-Burke-Ernzerhof generalized-gradient approximation (PBE) for the exchange and correlation functions and a very large basis set to study the Raman spectrum of [12312] hexamantane. The general shape of their calculated spectrum (intense breathing mode, weak CH_2 scissors) is considerably closer to the experimental spectrum than the one displayed here. Test

calculations using the same PBE functional but the smaller SV basis set yield similar intensities to those obtained with B3LYP. This suggests that the relative intensities produced by Richardson *et al.*, which lead to their calculated spectrum being similar to the experimental, are due to the large basis set used.

As well as [1(2,3)4] pentamantane, an an alkylated version, 3-methyl-[1(2,3)4] pentamantane ($C_{27}H_{34}$) has also been examined. Replacing the hydrogen atom at one of the apexes with a methyl group reduces the symmetry of the molecule to C_{3v} with the addition of only 3 atoms, increasing the number of vibrational modes by 9 to 177, 36 A_1 + 23 A_2 + 59 E. Because of the reduction in symmetry the number of possible Raman signals increases from 48 to 95 (A_2 not active in C_{3v}), which is far more than might be expected from just the addition of three atoms. Comparing the spectra (Figure 4.8) of these two molecules should give an insight to the effect of symmetry on a Raman spectrum. The reduction of symmetry is such that a T_2 symmetry vibration of a T_d molecule will give rise to two vibrations, of A_1 and E symmetry, in C_{3v}, while a T_1 vibration will give rise to two vibrations of A_2 and E symmetry. This shows how a near doubling of the number of Raman active vibrations results from the addition of three atoms. But do these new E symmetry modes created from T_1 modes induce a significant change in polarisability and hence produce new peaks in the spectrum? The overall shapes of the CH stretch regions of the two spectra are reasonably similar. The main differences are caused by the slight differences in frequency of the A_1 and E modes produced by the breaking of the T_2 modes by symmetry. There is also a small peak at ∼2950 cm^{-1} in the methyl-pentamantane spectrum due to the CH stretching mode of the CH_3 group. Studying the calculated frequencies and intensities in this region shows that there are Raman active modes of E symmetry in the methylated molecule that are related to inactive T_1 modes in the unmethylated, but their intensities are low compared to the other CH stretch modes (∼30 times weaker than the most intense CH stretch). The lower frequency regions of the two spectra are remarkably similar but, again, there are a few cases of peak splitting. A prime example of this is the change from a single strong T_2 vibration at 1061 cm^{-1} in the [1(2,3)4] pentamantane spectrum to three E modes in the methylated pentamantane spectrum, which cannot easily be assigned as corresponding to T_1, T_2 or E modes of the T_d parent structure due to strong mode mixing.

4.2.5 [121] tetramantane and [1212] pentamantane

The base tetramantane considered in this section is [121] tetramantane ($C_{22}H_{28}$, C_{2h}), trivially called "*anti*-tetramantane". [121] tetramantane has 144 vibrational modes, 40 A_g + 33 A_u + 32 B_g + 39 B_u, producing a maximum of 72 Raman fundamentals (Figure 4.12) due to the inactivity of the B_u and A_u modes. The majority of the

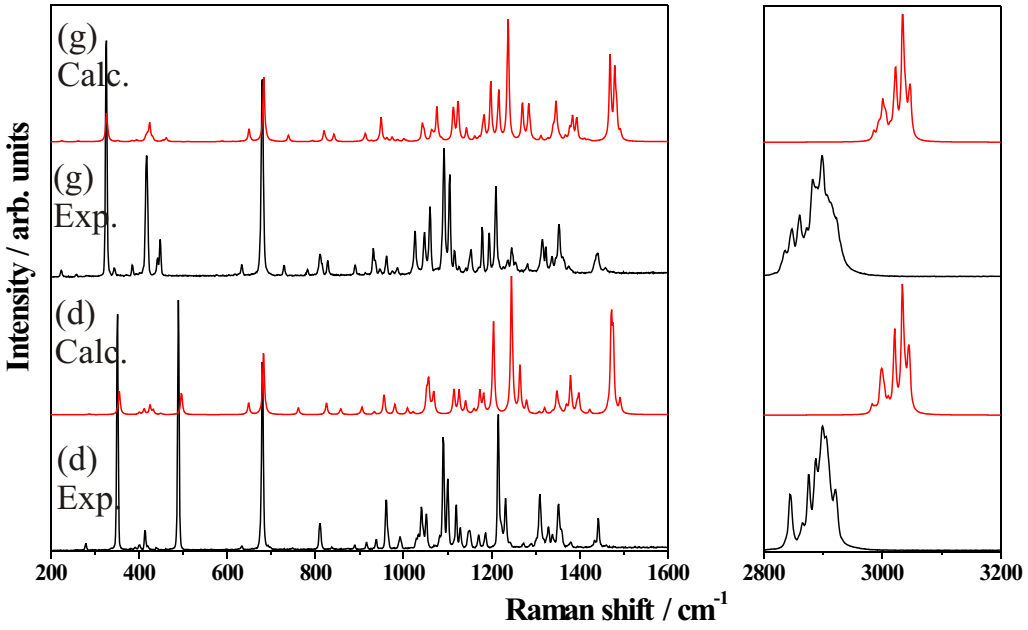

Figure 4.12: Experimental and calculated spectra for (from bottom) [121] tetramantane (d) and [1212] pentamantane (g). Spectra have been normalised to the most intense signal in the range 1000-1400 cm^{-1}.

polymantanes remaining are large ($\geq$ 50 atoms) with low symmetry ($\leq C_{2v}$). Thus the CH stretch and CH_2 twist/CH wag modes are ignored due to the growing complication in extracting information from the increasingly large number of peaks in these regions. Instead, the very low wavenumber modes (sub 800 cm^{-1}) are studied as these are still easily resolvable and should be characteristic of the unique structural features of each diamondoid. All the diamondoids examined so far can be identified by using this lower wavenumber region as a fingerprint for the molecule, with the possible exception of [1(2,3)4] pentamantane and its alkylated derivative, which can be differentiated by the highest wavenumber mode in the CH stretch region. The polymantanes adamantane through to triamantane exhibit only one very intense mode below 800 cm^{-1}, so can be distinguished by the specific wavenumber of each mode.

Returning to [121] tetramantane, as with the other 1 or 2-dimensional diamondoids studied so far, there is a very strong peak at 680 cm^{-1}, but another interesting trend is also noticeable. Comparing the area around this peak in diamantane, triamantane, and [121] tetramantane, there is always a very weak accompanying peak $\sim$50 cm^{-1} lower which is absent in the spectrum of [1(2)3] tetramantane. Looking at the series of molecules, diamantane, triamantane and [121] tetramantane, (b)-(c)-(d) in Figure 4.1, it is clear that on each occasion an adamantane unit is added to the end of the struc-

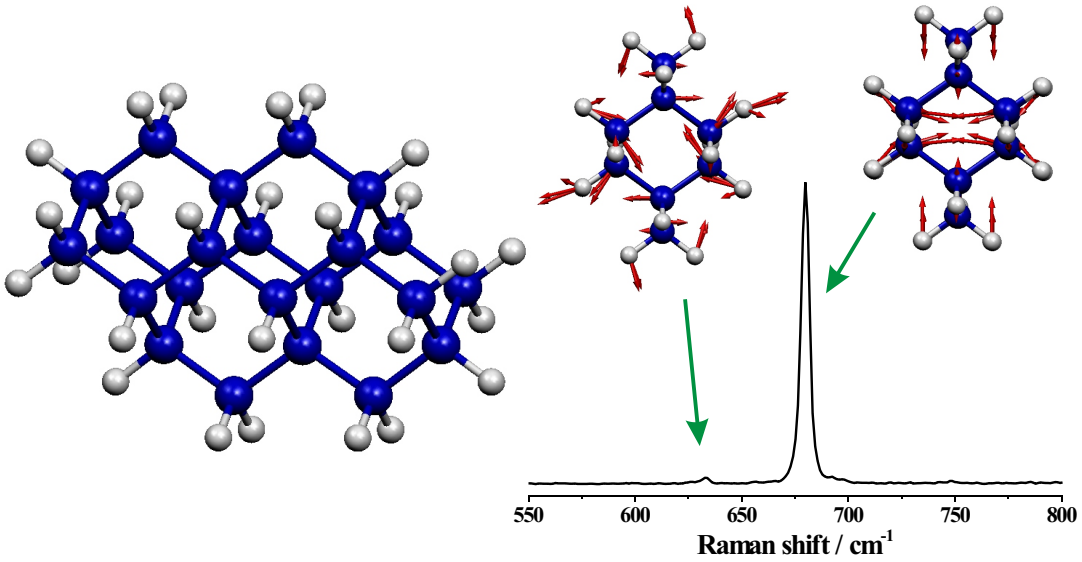

Figure 4.13: Nuclear displacements of the 680 cm^{-1} mode and its companion mode in [121] tetramantane.

ture, producing the effect of "growing" the molecule in one direction. This leads to the conclusion that the appearance of this pair of peaks is an indication that the particular diamondoid is rod-shaped (group (a) in Figure 4.10) i.e. its prefix would contain only alternating ones and twos. The nuclear displacements from the DFT calculations show that again the ∼680 cm^{-1} vibration is the same breathing mode across a single adamantane unit, and its accompanying peak is also due a CCC bend/CC stretch deformation at a different angle (Figure 4.13), so both can only occur when the molecule is in this rod-shaped group.

The only rod-shaped pentamantane is obtained by the addition of another unit onto the end of [121] tetramantane, and is called [1212] pentamantane ($C_{26}H_{32}$). This polymantane has 168 vibrational modes, 48 A_1 + 36 A_2 + 40 A_1 + 44 B_2, all 168 being Raman active due to the C_{2v} point group (Figure 4.12). Looking at the lower wavenumber regions of the two previous molecules, triamantane and [121] tetramantane, it is apparent that apart from some extra structure around the 426 cm^{-1} peak in [121] tetramantane, the only obvious difference is the relative intensity of the peaks at ∼680 cm^{-1} and ∼500 cm^{-1}, with the former being far more intense in triamantane. The spectrum of [1212] pentamantane also satisfies the rule mentioned above, as it has a peak at ∼680 cm^{-1} with a weaker companion ∼50 cm^{-1} lower, which is characteristic of a rod-like structure.

There is also the ∼426 cm^{-1} line caused by other deformations common to this

rod-like structure. An interesting observation is a down-shifting in wavenumber of the 352 cm^{-1} peak present in [121] tetramantane to 325 cm^{-1} in [1212] pentamantane. The calculations show that this mode involves stretching of the molecule in the "growth" direction, hence a reduction in frequency is expected as the molecule becomes longer. What is surprising is the absence or weakness of this mode in triamantane compared to [121] tetramantane and [1212] pentamantane. The frequency of this particular mode may be a good indication of length of these rod-shaped diamondoids.

4.2.6 [123] tetramantane and [1234] pentamantane

Addition of an adamantane unit to one of the four sites on triamantane, not considered so far, produces one enantiomer of the smallest chiral diamondoid, [123] tetramantane ($C_{22}H_{28}$, C_2), trivially called "*skew*-tetramantane". All 144 vibrational modes (73 A + 71 B) in [123] tetramantane are Raman active which explains why its spectrum (Figure 4.14) is considerably more structured than those from the other tetramantanes. Even the 500 - 800 cm^{-1} region of the spectrum, which for the previous molecules is either free of signals (as in [1(2,3)4] pentamantane) or contains the 2-dimensional or rod-shaped fingerprint peak (∼680 cm^{-1}), is starting to display more signals. As expected, there is a single peak at 655 cm^{-1}, produced by the same breathing mode across a single adamantane unit ([123] tetramantane lies in the 2-dimensional anisotropic group in Figure 4.10). There is also the 516 cm^{-1} peak that appears in the other two tetramantanes which, in all cases, is related to the mode in [1(2)3] tetramantane (an expansion perpendicular to what would be the three-fold rotational axis in diamond). But now there are other modes in this region, of a similar intensity to the 655 cm^{-1} and 516 cm^{-1} modes. These modes are at 725 cm^{-1} and 548 cm^{-1} and, again, are CCC bend/CC stretch deformations and are a feature of the more complex, less symmetrical structure of [123] tetramantane.

The chiral diamondoid [1234] pentamantane ($C_{26}H_{32}$, C_2) can only be formed by the addition of another adamantane unit to [123] tetramantane, and as the name suggests, extends the molecule in all three dimensions. This large, "screw-shaped", low symmetry molecule produces 168 vibrational modes (84 A + 84 B, all Raman active) again leading to a complicated spectrum (Figure 4.14). As with [123] tetramantane there are several peaks in the 500 - 800 cm^{-1} region and, notably, the strong signal at 529 cm^{-1}. But unlike [123] tetramantane, where the intensity of these peaks was similar to the 516 cm^{-1} peak, in this case they are only approximately half as intense. These peaks are throughout the "structural fingerprint" region, which previously contained few peaks and was very descriptive of the structure of the molecule in question.

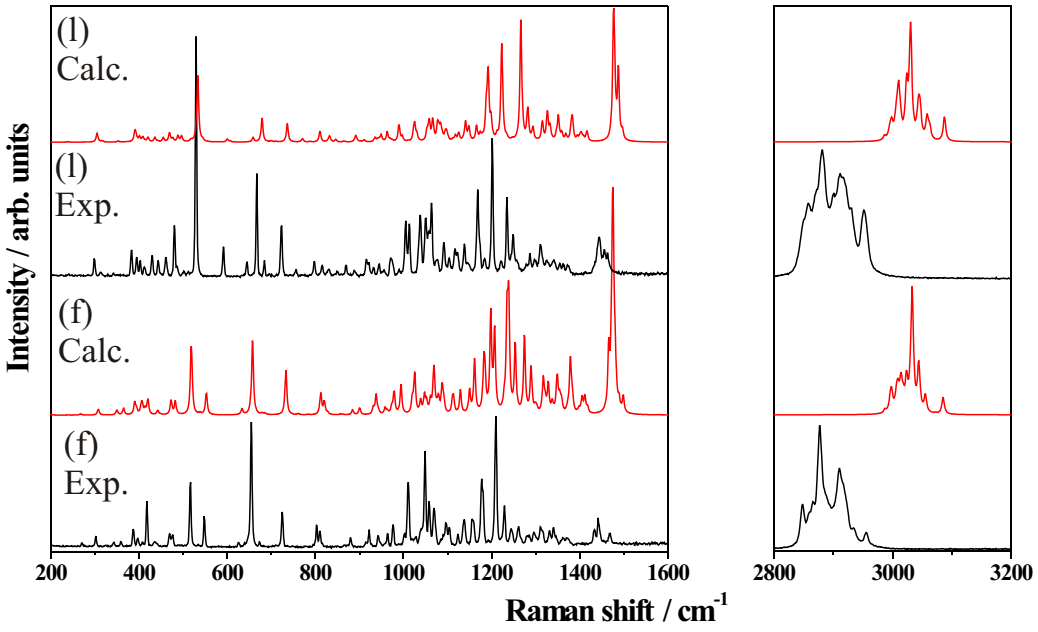

Figure 4.14: Experimental and calculated spectra for (from bottom) racemic [123] tetramantane (f) and racemic [1234] pentamantane (l). Spectra have been normalised to the most intense signal in the region 1000-1400 cm^{-1}.

The prefix to this molecule shows it extends in all 3 dimensions (like [1(2,3)4] pentamantane) but where this occurred previously there were no peaks in this region. This suggests that the fingerprint hypothesis requires some refinement, as follows:

For a 3-dimensional isotropic structure, like the tetrahedron-shaped [1(2,3)4] pentamantane, the fingerprint region will be completely devoid of intense signals as there is no significantly Raman active vibrations between those frequencies. The 1-dimensional rod-shaped ([1212...] case) still stands, but there should be no strong signals in the region 500 - 800 cm^{-1} apart from the ~680 cm^{-1} mode. An isotropic 2-dimensional structure, like the disc-shaped [1(2)3] tetramantane, can only produce the strong ~680 cm^{-1} line. Complications arise when, globally, the molecule extends in 3 dimensions but there are local areas of 2D structure. This is the 3-dimensional anisotropic case (Figure 4.10(e)), as in [1234] pentamantane. The same CCC bend/CC stretch motion that produces the single peak in the 2-dimensional structures also occurs in these local 2D structures, producing signals in the 500 - 800 cm^{-1} region of the spectrum that would not be seen for a uniform, geometric 3D structure. Using the relative intensities of the mode(s) at ~680 cm^{-1} compared to that of neighbouring modes (i.e. the ~500 cm^{-1} mode that appears in most spectra) it might be possible to tell the anisotropic 3-dimensional molecules, that have only local 2D structure, from the 2-dimensional dia-

mondoids, but the accuracy would be limited. This suggests that the fingerprint region of the spectrum is indeed diagnostic of isotropic 3-dimensional, isotropic 2-dimensional disc-shaped or 1-dimensional rod-like structures. However, more care is needed for the more complicated diamondoid molecules.

4.2.7 [12(3)4] pentamantane, [12(1)3] pentamantane and [1213] pentamantane

This section contains three diamondoids whose structures are as complicated, if not more complicated than the chiral pentamantane seen in the previous section. [12(3)4] pentamantane ($C_{26}H_{32}$, C_s, 168 vibrational modes, 90 A' + 78 A", all Raman active) can be produced by addition to either [1(2)3] or [123] tetramantane. [12(1)3] pentamantane ($C_{26}H_{32}$, C_1, 168 A vibrational modes, all Raman active), is produced by the addition of an adamantane unit to any of the three tetramantanes. [1213] pentamantane ($C_{26}H_{32}$, C_1, 168 A vibrational modes, all Raman active), is produced by the addition of an adamantane unit to either [121] or [123] tetramantane. All these molecules have several peaks in the structural fingerprint region, and clearly do not fall into the rod-shaped, isotropic 2-dimensional or isotropic 3-dimensional categories. The prefixes specific to each molecule describe whether they are anisotropic 2 or 3-dimensional, but can this also be derived from the Raman spectrum?

Including [1234] pentamantane in this analysis allows the comparison of four spectra, two anisotropic 2-dimensional molecules (Figure 4.10(c) e.g. [1213] and [12(1)3]) and two anisotropic 3-dimensional molecules (Figure 4.10(e) e.g. [1234] and [12(3)4]). The Raman spectra for all these molecules have several signals in the structural fingerprint region (Figure 4.14 and 4.15), most due to single adamantane unit breathing vibrations in local regions of the molecules. Comparing the spectra of the 2-dimensional molecules to the 3-dimensional molecules there is a clear difference, but in relative Raman intensities rather than vibrational frequencies. In the spectra of the 3-dimensional structures, the intensity of the 500 cm^{-1} mode (breathing parallel to the 111 face in diamond) is larger than any signal in the 200 - 1600 cm^{-1} region, whereas in the spectra produced by the 2-dimensional molecules the intensities are similar. This suggests that just using this region of the spectrum it is possible to derive information, even when the diamondoid structure is complex, but this analysis is definitely becoming more difficult now that the molecules are very large and have the lowest symmetries, i.e. C_1 and C_s.

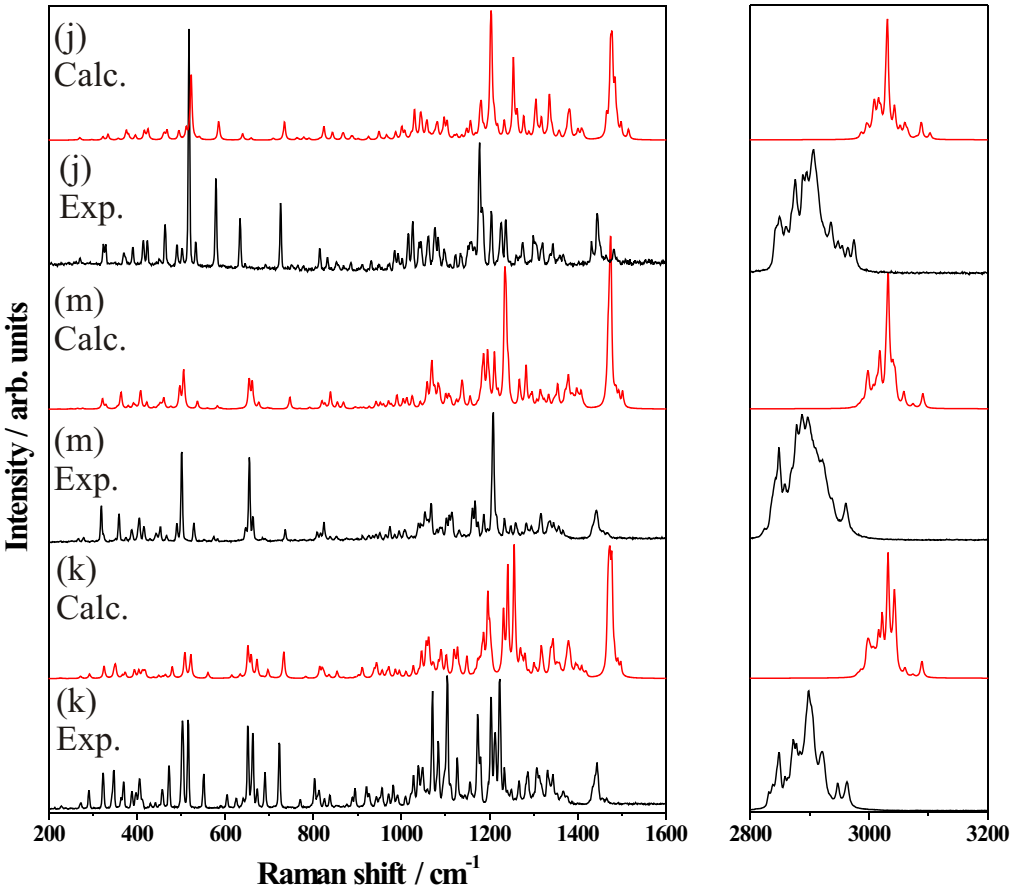

Figure 4.15: Experimental and calculated spectra for (from bottom) racemic [1213] pentamantane (k) and racemic [12(1)3] pentamantane (m) and [12(3)4] pentamantane (j). Spectra have been normalised to the most intense signal in the region 1000-1400 cm^{-1}.

4.2.8 [12312] hexamantane and [121321] heptamantane

[12312] hexamantane (trivially called cyclohexamantane) and [121321] heptamantane could have been included in the [123] tetramantane section, being derivatives of only that particular tetramantane. But, as mentioned above, the pentamantane that lies between them ([1231] pentamantane) has not been isolated, possibly because of instability caused by the steric interaction between two of its hydrogen atoms. Because of this, and due to the relatively high symmetry of [12312] hexamantane, their Raman spectra shall be compared to the spectra of other diamondoids in a more general manner.

Out of the 162 vibrational modes (17 A_{1g} + 11 A_{1u} + 10 A_{2g} + 19 A_{2u} + 27 E_g + 27 E_u), of [12312] hexamantane ($C_{26}H_{30}$ D_{3d}), only the 44 E_g and A_{1g} symmetry modes are Raman active. The highest intensity mode in the lower frequency region is again a mixed CH wag/CH_2 twist mode of E_g symmetry at 1200 cm^{-1}, which is similar those observed in the higher symmetry molecules mentioned above. The fingerprint region again shows peaks at 651 cm^{-1} and at 498 cm^{-1} due to the same CCC bend/CC stretch deformations parallel to and perpendicular to the three-fold rotational axis as observed before in [1(2)3] tetramantane. [12312] hexamantane has a 2-dimensional isotropic disc-shaped polymantane structure, and that is clearly reflected in its Raman spectrum.

Adding another adamantane unit to [12312] hexamantane produces the largest diamondoid in this study, [121321] heptamantane ($C_{30}H_{34}$, C_s). This molecule has 186 vibrational modes (100 A' + 86 A") all of them Raman active (Figure 4.16). The Raman spectra of [12312] hexamantane and [121321] heptamantane are reasonably similar. There are many more peaks in the [121321] heptamantane spectrum but it does have an extra 142 Raman active vibrational modes so this is not surprising. It might be expected that as the diamondoid molecules become larger the addition of extra adamantane units would have less of an effect on the Raman spectrum, until the only signal is the 1332 cm^{-1} phonon of the diamond crystal, but that is much greater than the size of molecules dealt with here. [121321] heptamantane has low symmetry, but it has the same strong vibrational modes in the fingerprint region as [12312] hexamantane and is also 2-dimensional.

4.2.9 Theoretical molecules

To continue testing the predictions made above, Raman spectra were calculated for a further set of molecules. There is no experimental data available for these molecules, all structures were taken from Carlson *et al.* [13]. The new molecule set is displayed in Figure 4.17 and was carefully chosen to contain molecules from all the diamondoid

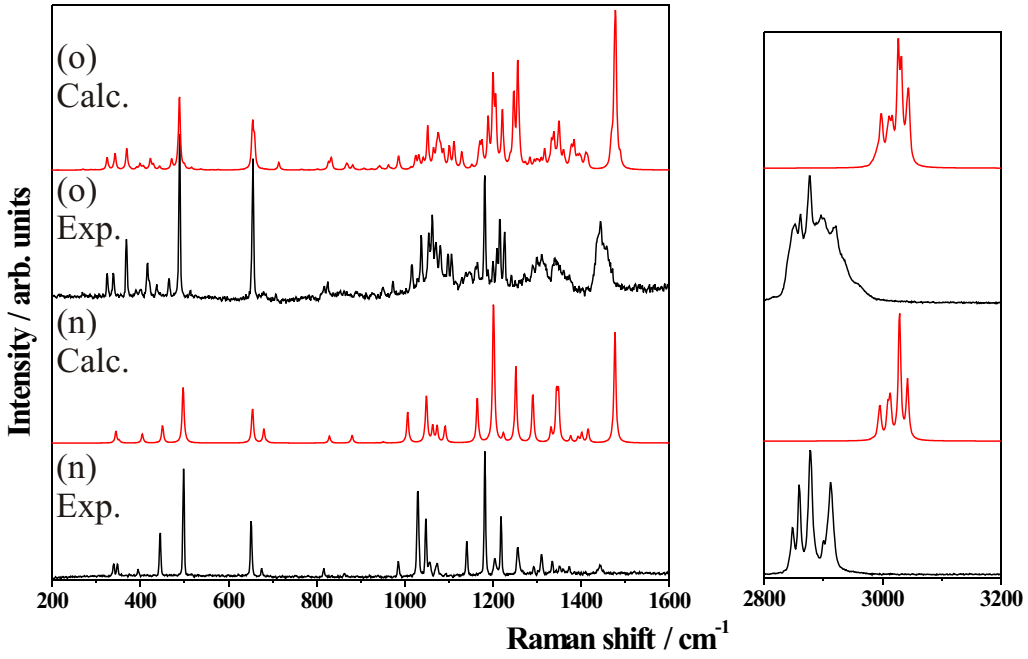

Figure 4.16: Experimental and calculated spectra for (from bottom) [12312] hexamantane (n), and [121321] heptamantane (o). Spectra have been normalised to the most intense signal in the region 1000-1400 cm^{-1}.

structural subsets outlined in Figure 4.10.

3-Dimensional isotropic diamondoids

Using the same level of theory it is only possible to study one further isotropic 3D diamondoid because of the large number of atoms required to make a solid 3D structure. The molecule studied is [1231241(2)3] decamantane, a small octahedron-shaped diamondoid with T_d symmetry. Figure 4.18 shows the calculated Raman spectrum for [1231241(2)3] decamantane (p) and [1(2,3)4] pentamantane (h). [1(2,3)4] pentamantane was the only 3D isotropic diamondoid for which experimental data was obtained. Like that of the pentamantane, the decamantane spectrum also has no strong signals in the fingerprint region, which is consistent with the foregoing hypothesis. Further analysis of these, and larger, 3D isotropic diamondoids is given in chapter 5.

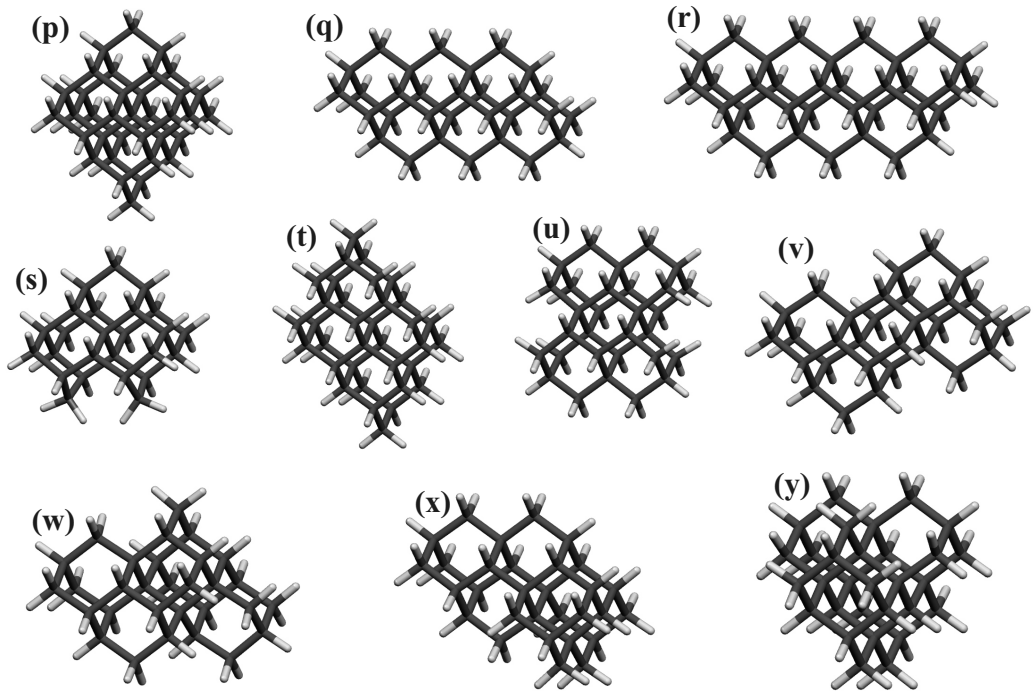

Figure 4.17: Molecules studied for which there is no experimental data, figure labels continued from Figure 4.1, (p) [1231241(2)3] decamantane, $C_{35}H_{36}$, T_d, (q) [12121] hexamantane, $C_{30}H_{36}$, C_{2h} (r) [121212] heptamantane, $C_{34}H_{40}$, C_{2v}, (s) [1231] pentamantane $C_{25}H_{30}$, C_s, (t) [1213(1)21] octamantane, $C_{34}H_{38}$, C_{2h}, (u) [1(2)3(1)2] hexamantane, $C_{30}H_{36}$, C_{2h}, (v) [12321] hexamantane, $C_{30}H_{36}$, C_i, (w) [12341] hexamantane, $C_{30}H_{36}$, C_2, (x) [121(3)4] hexamantane, $C_{30}H_{36}$, C_s, (y) [12(1,3)4] hexamantane, $C_{30}H_{36}$, C_s.

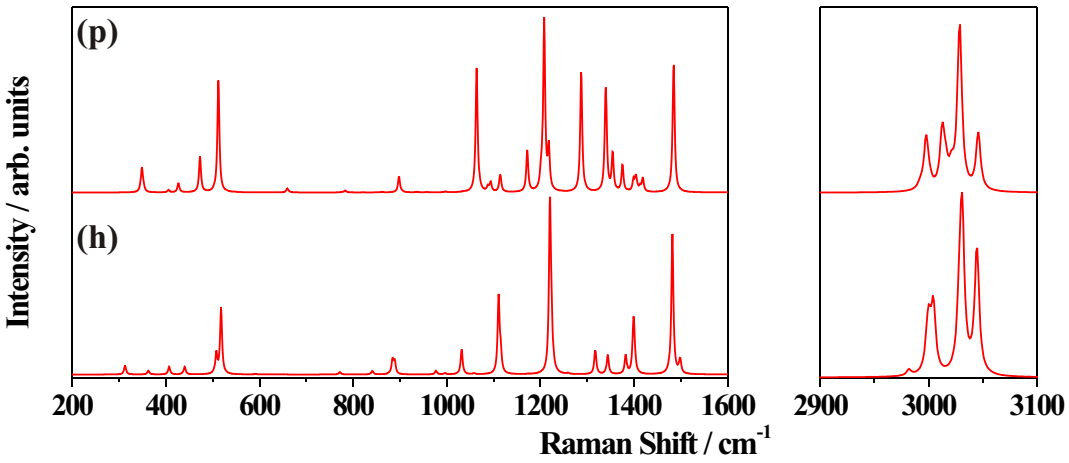

Figure 4.18: Calculated Raman spectra for (h) [1(2,3)4] pentamantane (p) [1231241(2)3] decamantane

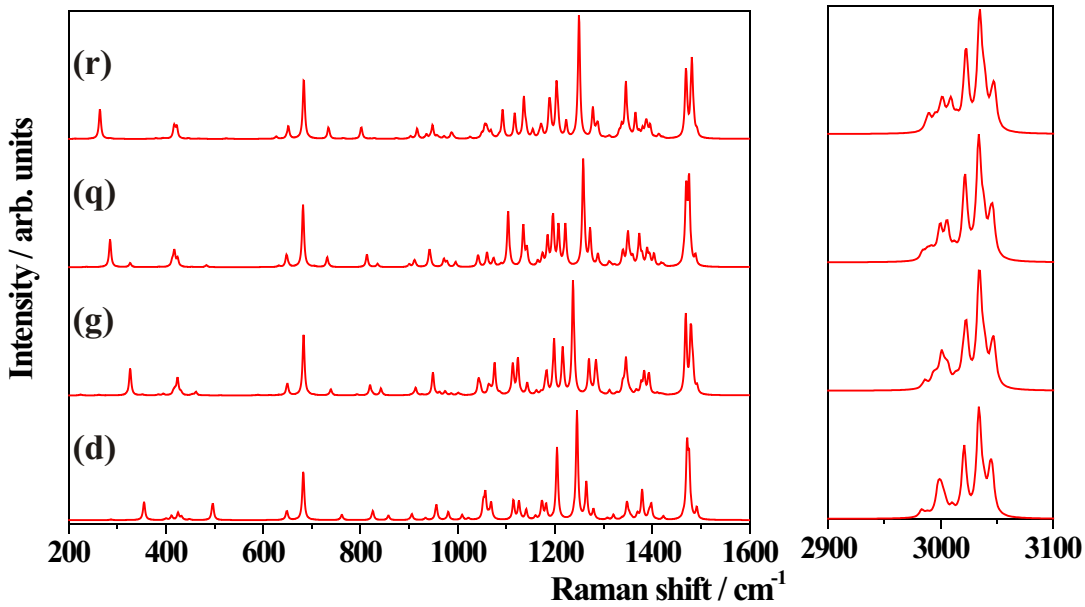

Figure 4.19: Calculated Raman spectra for, (d) [121] tetramantane, (g) [1212] pentamantane , (q) [12121] hexamantane, (r) [121212] heptamantane.

1-Dimensional "rod-shaped" diamondoids

The 1-dimensional diamondoids studied above were [121] tetramantane and [1212] pentamantane, Figure 4.1 (d) and (g) respectively. These structures are identifiable by the ∼680 cm^{-1} single adamantane unit stretch and a weak accompanying peak ∼50 cm^{-1} lower, the ∼680 cm^{-1} peak being the only strong signal in the region 500 - 800 cm^{-1}. This group of molecules has been extended by two with the calculation of [12121] hexamantane and [121212] heptamantane 4.17 (q) and (r) respectively.

The calculated Raman spectra of these new 1-dimensional diamondoids are shown in Figure 4.19. The calculated spectra of the tetramantane and pentamantane have been included to aid comparison.

The spectra of all four of these molecules are reasonably similar, especially around the fingerprint region, all showing the strong peak around 680 cm^{-1} and its weak companion peak. The down shift in the frequency of the breathing mode along the "growth" direction observed for the tetra- and pentamantanes continues for the hexa- and heptamantanes, backing up the idea that this mode may be used to determine the length of a 1D diamondoid.

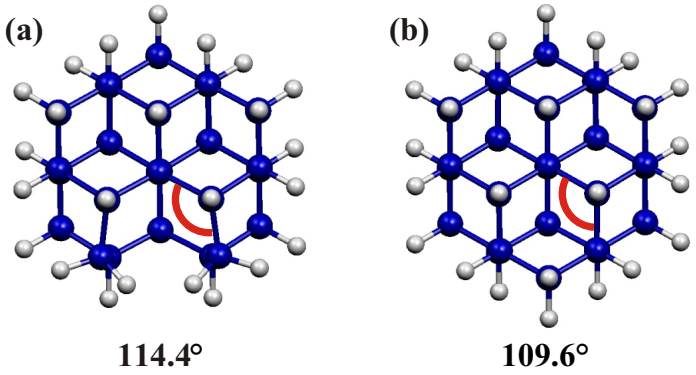

Figure 4.20: Optimised structures of (a) [1231] pentamantane and (b) [12312] hexamantane, showing the bond strain in [1231] pentamantane.

2-Dimensional diamondoids

The structures of the extra 2D diamondoids studied are shown in Figure 4.17 (s), (t), (u) and (v).

[1231] pentamantane (molecule (s) in Figure 4.17) is the smallest diamondoid that has yet to be isolated. The reasons behind the rarity of this particular structure are unknown, but it is maybe due to the instability produced by the repulsion of two close hydrogen atoms. Figure 4.20 shows the optimised structures of (a) [1231] pentamantane and (b) [12312] hexamantane. The steric repulsion of the two close hydrogens in [1231] pentamantane causes a widening in the bond angle (highlighted in Figure 4.20) to 114.4° compared to 109.6° in [12312] hexamantane. All other diamondoid structures have bond angles close to that of a perfect tetrahedral angle (109.5°) and, although the mechanism of diamondoid production in petroleum is unknown, it is possible that this intrinsic stress inhibits the formation or stability of [1231] pentamantane.

The calculated Raman spectrum of [1231] pentamantane is shown in Figure 4.21 (s). A clear difference between the spectrum of this molecule and any of the other structures studied here is the presence of very high frequency CH stretch modes (∼3170 cm^{-1}). These two vibrations are the symmetric (Figure 4.22 (a)) and asymmetric stretching modes of the two close hydrogen atoms. Throughout this chapter the CH stretch regions of the diamondoid Raman spectra have been largely ignored, mainly because of the broadening produced by taking spectra of the crystal phase. Looking back through the calculated Raman spectra there are many cases where there is a CH stretch mode at a slightly higher frequency than the main CH stretch group. The smallest diamondoid whose Raman spectrum has this slightly higher frequency CH stretch signal

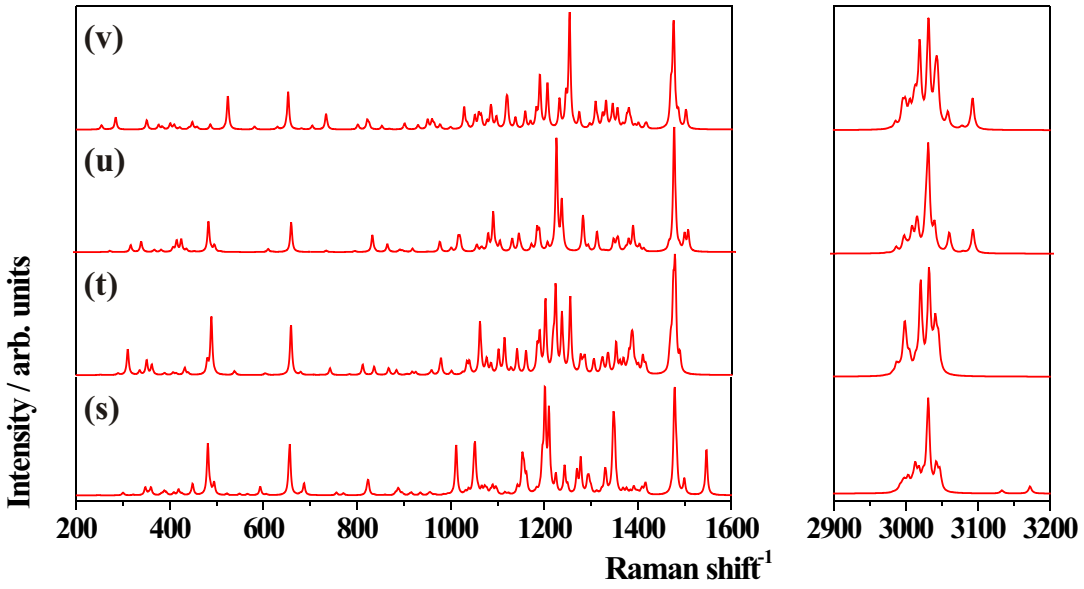

Figure 4.21: Calculated Raman spectra of, (s) [1231] pentamantane, (t) [1213(1)21] octamantane, (u) [1(2)3(2)1] hexamantane, (v) [12321] hexamantane,

is [123] tetramantane. The nuclear displacements associated with this high frequency CH stretch of [123] tetramantane are shown in Figure 4.22 (b). Again, the increase in frequency is due to close hydrogen atoms stretching towards each other. The magnitude of the CH stretch frequency shift observed in [123] tetramantane is less than that of [1231] pentamantane, but the distance between the two H atoms is larger in [123] tetramantane, so this is to be expected.

The structures corresponding to all the calculated Raman spectra with these higher frequency CH stretch signals all contain this 1-2-3 pattern in the structure. Figure 4.22 (c) shows this higher frequency CH stretch in [1213] pentamantane. Notice the similarities between the frequency and displacements of this mode and that observed in [123] tetramantane. Looking at the nomenclature prefix of [1213] pentamantane it is clear that 1-2-3 is not observed in that order and yet this 1-2-3 structure still appears in the molecule. All the 1-2-3 in the nomenclature prefix means is that three neighbouring adamantane units have been faced-fused in three different directions. This means 1-2-3, 2-1-3, 2-3-4, etc. are all equivalent, and if they are found in the prefix of a diamondoid name the Raman spectrum should display these high frequency CH modes. The only cases where this is not seen to apply is where the close hydrogen atoms in this 1-2-3 structure are replaced by adamantane units, as in [12321] hexamantane

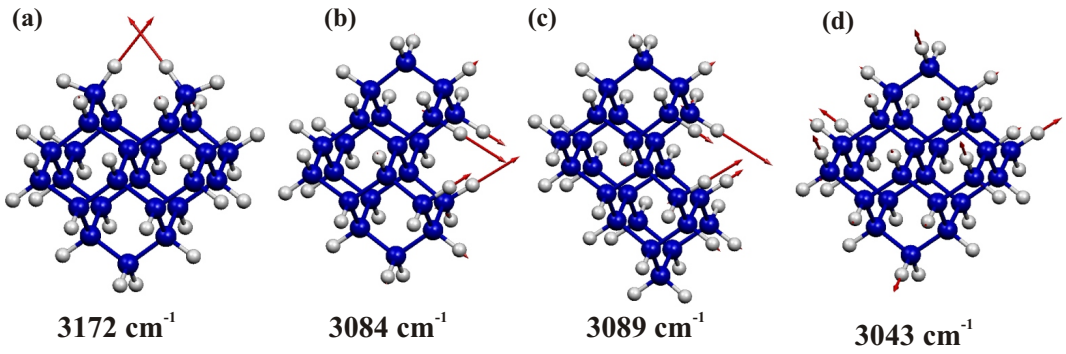

Figure 4.22: Calculated nuclear displacements associated with the highest frequency CH stretch vibration of a selection of molecules (a) [1231] pentamantane, (b) [123] tetramantane, (c) [1213] pentamantane, (d) [12321] hexamantane.

(Figure 4.22 (d)). The calculated highest frequency CH stretch of [12321] hexamantane is at 3043 cm^{-1}, similar to that of all other diamondoids that do not contain this 1-2-3 structure.

The experimental CH stretch region of the diamondoid Raman spectra are shown in Figure 4.23. The spectra of all the molecules with this 1-2-3 structure are displayed in red, the spectra of all the other diamondoids are shown in black. To the right of the vertical line at 2950 cm^{-1} nearly all the peaks are red, providing further evidence for the trend seen in the calculated data. The only discrepancy in this trend is a broad, decreasing signal in the spectrum of [121321] heptamantane, which is not predicted in the calculated data. This suggests that this particular feature may be caused by the arrangement of the molecules in the crystal (possibly by bringing two hydrogens on neighbouring molecules close to each other).

The calculated spectra of the theoretical 2D diamondoids are shown in Figure 4.21. One thing that is becoming increasingly difficult is the separation of structures into isotropic and anisotropic sub-groups. Whereas the fingerprint region of the spectrum of [121321] heptamantane in section 4.2.8 fitted into the 2D isotropic category its structure was not sufficiently symmetric to be classed as isotropic. [121321] heptamantane was formed by the addition of a single adamantane unit to the disc-shaped [12321] hexamantane, if another unit is fused onto the heptamantane, [1213(1)21] octamantane (structure - Figure 4.17 (t), spectrum - Figure 4.21 (t)) can be formed. The fingerprint region of this molecule's spectrum, and, in fact, the spectra of the other 2D molecules in this section, are close to that which would be expected for a 2D isotropic molecule, but there are a few very weak signals that should not occur for a highly symmetric structure, hence all are 2D anisotropic.

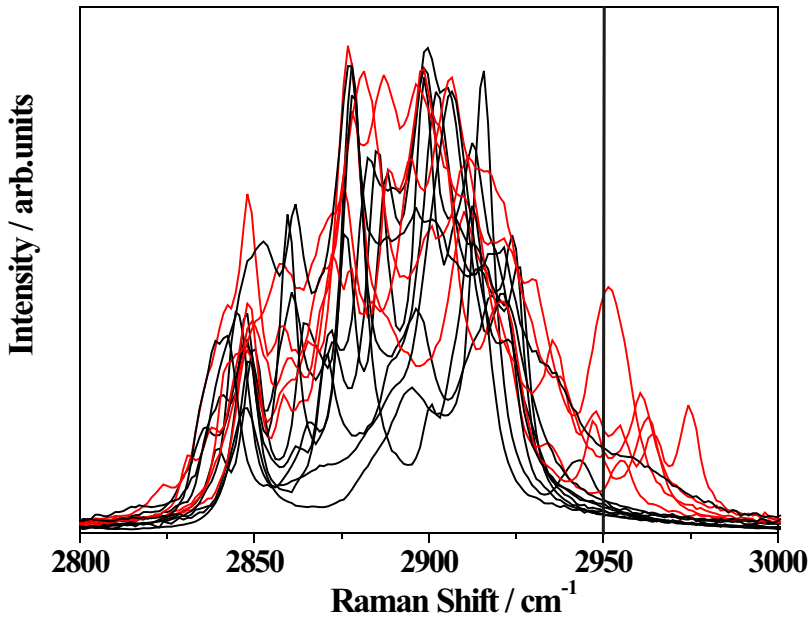

Figure 4.23: CH stretch region of the experimental spectra of all diamondoids, those with 1-2-3 structure are shown in red, all others are black.

The most important feature of the Raman spectrum of a 2D anisotropic diamondoid is that the two main strong peaks in the fingerprint region (∼680 and ∼500 cm^{-1}) are of approximately the same intensity. It can be seen from Figure 4.21 that this is the case for the spectra of all the molecules in this section. The next step is to see if the 3D anisotropic case holds up as well.

3-Dimensional anisotropic diamondoids

The structures of the extra 3D anisotropic molecules ([12341] hexamantane (w), [121(3)4] hexamantane (x), and [12(1,3)4] hexamantane (y),) studied are shown in Figure 4.17, the calculated spectra are shown in Figure 4.24. According to the theory developed throughout this chapter all these spectra should contain many peaks throughout the fingerprint region, but they should not be as intense as the peak at ∼500 cm^{-1}. This pattern is displayed in the spectra of [12341] hexamantane and [121(3)4] hexamantane, but the spectrum of [12(1,3)4] hexamantane has a very low number of intense peaks in the fingerprint region of its spectrum. Both [12341] hexamantane and [121(3)4] hexamantane were produced by face-fusing another adamantane unit on to either a 2D or 3D anisotropic diamondoid. [12(1,3)4] hexamantane, on the other hand, was formed by fusing another adamantane unit on to the 3D isotropic structure of [1(2,3)4] pentamantane (Figure 4.1 (h)). The calculated spectrum of [12(1,3)4] hexamantane appears to

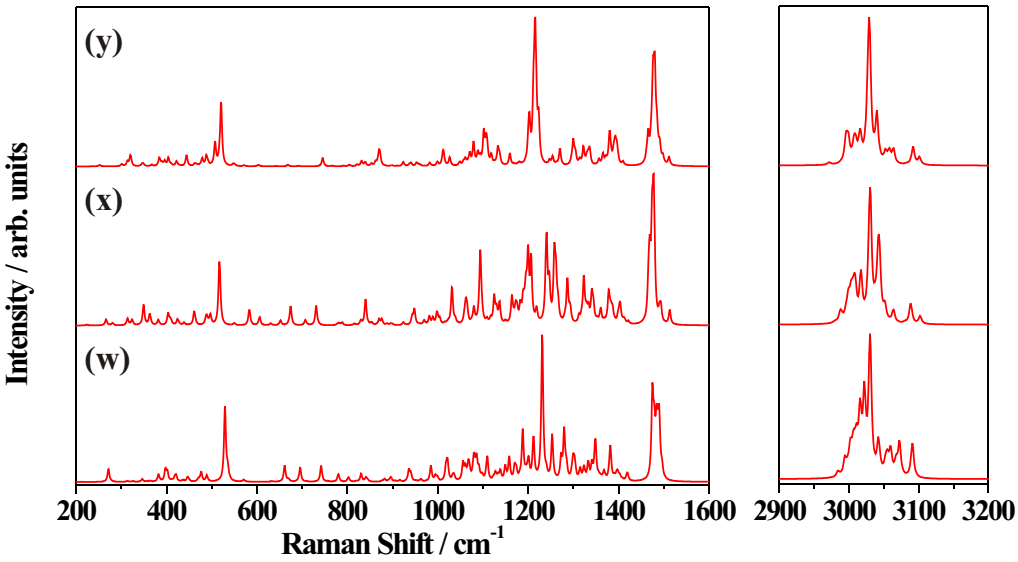

Figure 4.24: Calculated Raman spectra of, (w) [12341] hexamantane, (x) [121(3)4] hexamantane, (y) [12(1,3)4] hexamantane.

be closer to that of the isotropic [1(2,3)4] pentamantane than that of a 3D anisotropic diamondoid.

As described above, for the 2D anisotropic case, the spectrum calculated for [121321] heptamantane resembled that which would be expected for a 2D isotropic molecule, despite its anisotropic structure. Like [12(1,3)4] hexamantane, [121321] heptamantane was formed by fusing a single adamantane unit to a large highly symmetrical diamondoid, in this case disc-shaped [12321] hexamantane. From these two cases it would appear that fusing a single adamantane unit onto a large isotropic molecule is not enough to make the Raman spectrum have the fingerprint of an anisotropic molecule, despite the reduction in symmetry and perturbation of the isotropic structure.

All the molecules in this section have the 1-2-3 pattern in their structure and their nomenclature, and hence also have the associated higher frequency CH modes.

Methylated [1(2,3)4] Pentamantanes

In section 4.2.4 the effects of substituting a terminal hydrogen on [1(2,3)4] pentamantane for a methyl group were studied. The main effect this had was reducing the symmetry of the system from T_d to C_{3v}. The particular substitution position studied in section 4.2.4 is not the only way to substitute [1(2,3)4] pentamantane to produce the C_{3v} symmetry group. Figure 4.25 shows the structure of [1(2,3)4] pentamantane

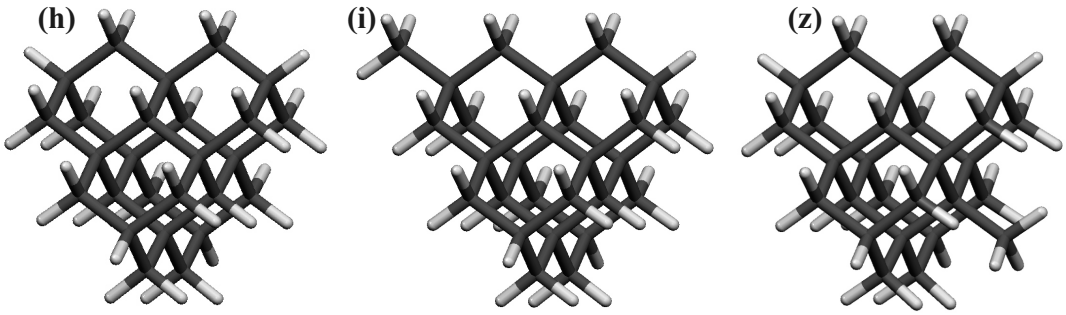

Figure 4.25: Optimised structures of (h) [1(2,3)4] pentamantane, (i) and (z) [1(2,3)4] pentamantane with a single methyl- group substituted for a surface hydrogen, producing two different molecules of C_{3v} symmetry.

and two different singly-methylated [1(2,3)4] pentamantanes of C_{3v} symmetry. The calculated spectra of these three molecules are shown in Figure 4.26.

Both of the methylated pentamantanes show splitting of peaks that were triply degenerate in [1(2,3)4] pentmantane, which is expected due to the reduction in symmetry. It appears to be very difficult to differentiate between the two substituted molecules using the lower frequency region of the Raman spectra alone, the only prominent difference is in the CH stretch region. The substitution in the molecule (z) puts the methyl-group hydrogen atoms in close proximity to the terminal hydrogen atoms on the diamondoid structure. It has been shown that when hydrogen atoms are in close proximity there is an increase in the stretching frequency of these particular CH bonds. In the calculated spectrum of the molecule (z), there is a small peak at 3141 cm^{-1}, due to stretching modes of these close hydrogens, which allows us to separate these two structures.

4.3 Conclusions

In this chapter, the experimental Raman spectra for a broad selection of diamondoid molecules ranging from adamantane to [121321] heptamantane were reported. These spectra have been interpreted in a semi-quantitative way, by comparison with computed vibrational frequencies and Raman intensities derived from density functional theory calculations. Calculated and experimental frequencies are generally in good agreement with each other, although some discrepancies arise between computed and observed intensities, mainly due to the relatively small atomic basis sets used and the fact that

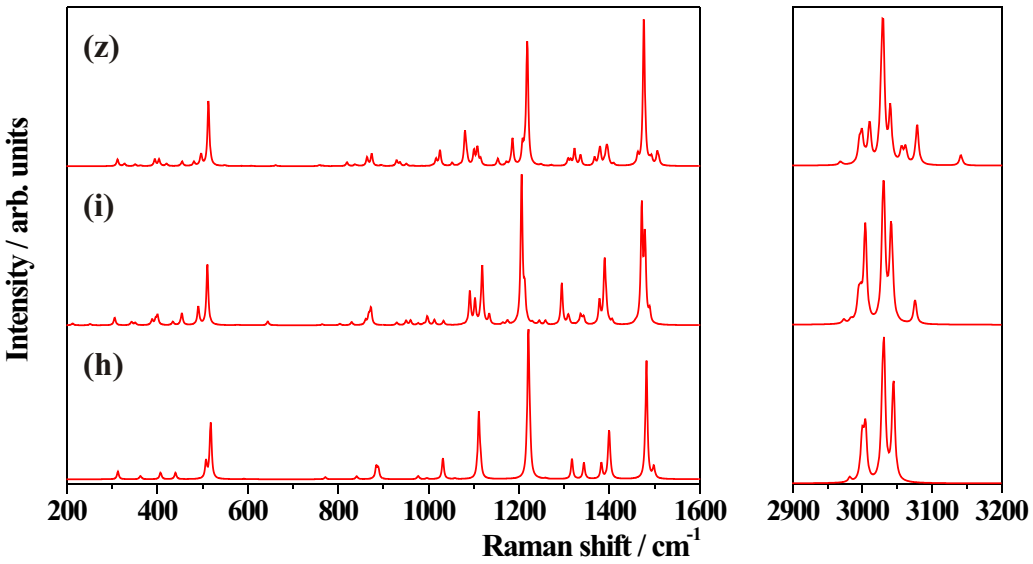

Figure 4.26: Calculated Raman spectra of molecules (h), (i) and (z) pictured in Figure 4.25.

calculations were performed on an isolated molecule whereas the experimental spectra were obtained from the solid state.

Each diamondoid in this study produced a unique Raman spectrum, enabling easy differentiation between molecules. The general features of the spectra allowed us to divide the diamondoids into five groups based on their molecular structure, with characteristic spectral properties for each group. Using only a small fingerprint region of the spectrum (550 - 700 cm^{-1}) the structural group a specific diamondoid belongs to can be identified, and hence information can be gained about its structure.

- The 1-dimensional rod-shaped diamondoids (Figure 4.27(a)) are identifiable by a single strong peak ($\sim$680 cm^{-1}) and weak companion peak ($\sim$50 cm^{-1} lower) in this fingerprint region.

- The length of the rod can be estimated from the lowest wavenumber peak.

- Isotropic (symmetrical) 2-dimensional diamondoids (Figure 4.27(b)) only have the single strong $\sim$680 cm^{-1} peak in the fingerprint region and should not have any weak signals between this peak and the strong $\sim$500 cm^{-1} signal.

- Anisotropic (low symmetry) 2-dimensional diamondoids (Figure 4.27(c)) may have several peaks in the fingerprint region but the $\sim$680 cm^{-1} peak will only be as intense as, or very slightly weaker than, the $\sim$500 cm^{-1} signal.

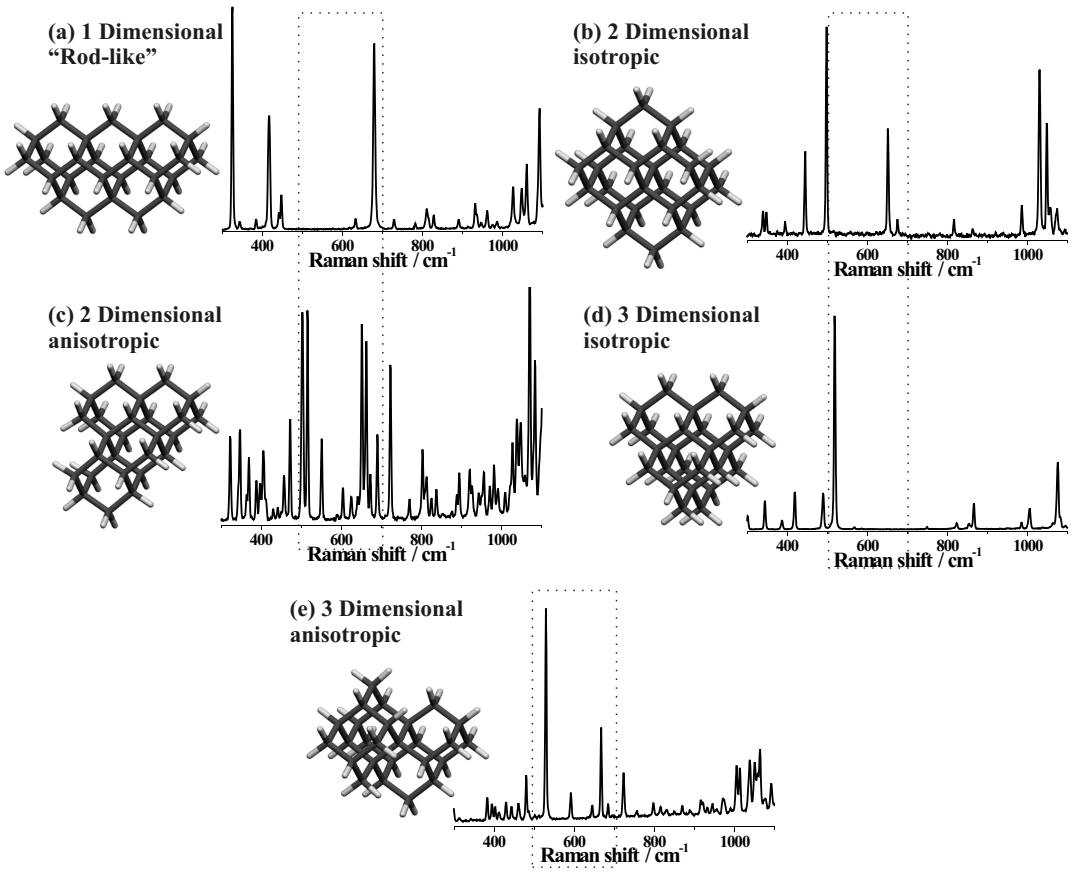

Figure 4.27: Structural fingerprint region of, (a) 1-dimensional rod-shaped [1212] pentamantane, (b) 2-dimensional isotropic disc-shaped [12312] hexamantane, (c) 2-dimensional anisotropic [1213] pentamantane, (d) 3-dimensional isotropic [1(2,3)4] pentamantane, (e) 3-dimensional anisotropic [1234] pentamantane.

- If the ∼500 cm^{-1} peak is considerably more intense than the ∼680 cm^{-1} peak the diamondoid is 3-dimensional anisotropic (Figure 4.27(e)).
- The final group, 3-dimensional isotropic, will have no peaks in the fingerprint region (Figure 4.27(d)).

This theory was tested by calculating the Raman spectra for a further set of diamondoid molecules for which no experimental spectra were available. The identification of the specific structural groups of these diamondoid molecules from only the fingerprint region of the Raman spectra was possible in all but two cases. Both of these cases arose from the creation of an anisotropic structure from addition of a single adamantane unit to a large isotropic diamondoid. The spectra of these molecules still resembled the isotropic case, suggesting the addition of a single adamantane unit to a

large isotropic structure does not perturb the diamondoid structure enough to make the Raman spectrum appear to be from an anisotropic molecule.

Theoretical analysis of the smallest diamondoid yet to be isolated, [1231] pentamantane, revealed that information about the structure of diamondoid molecules can be gained from the CH stretch region. When the diamondoid structure is such that it leads to close proximity of hydrogen atoms, there is an increase in the maximum stretching frequency observed in the CH stretch region. For diamondoids without close H proximity the maximum calculated CH stretch frequency is around 3040 cm^{-1}, raising to ∼3080 cm^{-1} for structures with close hydrogens. These close hydrogens were found to arise in structures where three neighbouring adamantane units have been face-fused in three different directions, showing that higher than normal wavenumber CH peaks were indicative of this type of structure. This trend can also be observed in the experimental data, making it a practical method of determining the presence of this type of structure.

Future work for this project would consist of IR absorption and Raman depolarisation ratio measurements on diamondoid solutions. As described in Section 2.1, the molecular point group has a large influence on the relationship between the Raman and IR absorption spectra of the molecule. Sometimes the symmetry of a vibrational mode can be determined by comparing presence or absence of peaks in the Raman and IR absorption spectra. It is often also possible to determine the symmetry of certain vibrations using Raman depolarisation ratio measurements. If a sample is illuminated with polarised light and the Raman scattered light is collected though a linearly polarising filter, the relative intensities of the Raman signals will be different depending on whether the collected light is polarised parallel or perpendicular to the excitation light. The depolarisation ratio of a signal is the intensity of the signal collected with perpendicular polarisation divided by the intensity of the signal collected with perpendicular polarisation. The depolarisation ratio of a signal caused by a totally symmetric vibrational mode is less than 0.75 and 0.75 for modes of all other symmetries [14]. Measurement of the IR absorption spectra and Raman depolarisation ratios would lead to a more complete analysis of the calculated vibrational frequencies and intensities.

Bibliography

[1] T. E. Jenkins and J. Lewis, *Spectrochim. Acta Part A*, 1980, **36**, 259.

[2] G. C. McIntosh, M. Yoon, S. Berber, and D. Tománek, *Phys. Rev. B*, (2004), **70**, 045401.

[3] M. J. Frisch, G. W. Trucks, H. B. Schlegel, G. E. Scuseria, M. A. Robb, J. R. Cheeseman, J. A. Montgomery, Jr., T. Vreven, K. N. Kudin, J. C. Burant, J. M. Millam, S. S. Iyengar, J. Tomasi, V. Barone, B. Mennucci, M. Cossi, G. S. N. Rega, G. A. Petersson, H. Nakatsuji, M. Hada, M. Ehara, K. Toyota, R. Fukuda, J. Hasegawa, M. Ishida, T. Nakajima, Y. Honda, O. Kitao, H. Nakai, M. K. X. Li, J. E. Knox, H. P. Hratchian, J. B. Cross, C. Adamo, J. Jaramillo, R. Gomperts, R. E. Stratmann, O. Yazyev, A. J. Austin, R. Cammi, C. Pomelli, J. W. Ochterski, P. Y. Ayala, K. Morokuma, G. A. Voth, P. Salvador, J. J. Dannenberg, V. G. Zakrzewski, S. Dapprich, A. D. Daniels, M. C. Strain, O. Farkas, D. K. Malick, A. D. Rabuck, K. Raghavachari, J. B. Foresman, J. V. Ortiz, Q. Cui, A. G. Baboul, S. Clifford, J. Cioslowski, B. B. Stefanov, G. Liu, A. Liashenko, P. Piskorz, I. Komaromi, R. L. Martin, D. J. Fox, T. Keith, M. A. Al-Laham, C. Y. Peng, A. Nanayakkara, M. Challacombe, P. M. W. Gill, B. Johnson, W. Chen, M. W. Wong, C. Gonzalez, and J. A. Pople, Gaussian 03, revision b.04, 2003.

[4] A. Schäfer, H. Horn, and R. Ahlrichs, *J. Chem. Phys.*, 1992, **97**, 2571.

[5] A. D. Becke, *J. Chem. Phys.*, 1993, **98**, 5648.

[6] C. Lee, W. Yang, and R. G. Parr, *Phys. Rev. B*, 1988, **37**, 785.

[7] J. P. Perdew, K. Burke, and M. Ernzerhof, *Phys. Rev. Lett.*, 1996, **77**, 3865.

[8] J. P. Perdew, K. Burke, and M. Ernzerhof, *Phys. Rev. Lett.*, 1997, **78**, 1396.

[9] A. D. Becke, *Phys. Rev. A*, 1988, **38**, 3098.

[10] J. O. Jensen, *Spectrochim. Acta Part A*, 2004, **60**, 1895.

[11] L. Bistriĉić, L. Pejov, and G. Baranović, *J. Mol. Struct. Theochem.*, 2002, **594**, 79.

[12] S. L. Richardson, T. Baruah, M. J. Mehl, and M. R. Pederson, *Chem. Phys. Lett*, 2005, **403**, 83.

[13] R. Carlson, J. Dahl, S. Liu, M. Olmstead, and R. Buerki, P.R.and Gat, Springer, 2005; chapter Diamond Molecules Found in Petroleum, pp. 63–78.

[14] ed. M. J. Pelletier, *Analytical Applications of Raman Spectroscopy*, Blackwell Sciences Ltd, Oxford, 1999.

Chapter 5

Raman Spectroscopy of Nano-Crystalline Diamond: An *Ab Initio* Approach

5.1 Introduction

Raman spectroscopy is one of the most commonly used techniques for the analysis of carbon-based materials. It is routinely used as a simple non-destructive method to analyse a wide range of carbon samples, from amorphous to crystalline. The Raman spectrum of single crystal diamond consists of a Brillouin zone-centre (Γ-point) T_{2g} mode at 1332 cm^{-1}, but various other peaks have been observed in the Raman spectra of micro- and nanocrystalline diamond thin films.

The most controversial of these is the peak observed at 1150 cm^{-1} in the Raman spectrum of chemical vapour deposited (CVD) nanocrystalline diamond films. For many years it had been proposed that this peak originates from phonon modes with $q \neq 0$, activated by the disorder induced by small grain sizes in nanocrystalline or amorphous diamond [1, 2]. This idea was reinforced by a maximum in the diamond vibrational density of states (at the L-point) at a similar wavenumber ($\sim$1240 cm^{-1}). Recently, this theory has been rejected by a number of groups [3] for many reasons, including hydrogen isotope studies [4] and peak dispersion and intensity variation in resonant Raman spectroscopy using multiple excitation wavelengths (633 - 244 nm) [5]. It has also been suggested that the diamond crystallites for which this peak were observed were not sufficiently small to allow phonons from the L-point to be active in the Raman spectrum [5]. The results from these experiments suggest the mode is more likely due to polyacetylene-type structures located at grain boundaries and interfaces [5].

This type of problem is not limited to nanodiamond thin films. The Raman spectrum of shock-synthesized nanodiamond powders also contains unassigned peaks. In this case, the mode of interest produces a broad signal around 500 cm^{-1}, tentatively assigned as originating from transverse acoustic phonons near the Brillouin zone boundary or an amorphous sp^3 phase [2, 6].

Generally, any variation in the Raman spectrum of a nanocrystalline phase is described by relaxation of the $q = 0$ selection rule, due to uncertainty in the value of the wavevector. This permits the activation of phonons that would not usually be observed in the Raman spectrum of the bulk material. Instead of taking the bulk material and studying the effects of reducing its size, it is often useful to take a molecule or small cluster reflecting the structure of the material, and study the effects of enlarging it.

The Raman spectrum of single crystal and microcrystalline graphite were first studied by Tuinstra and Koenig in 1970 [7]. They observed a single peak at 1575 cm^{-1} for single crystal graphite which they attributed to the Brillouin zone centre ($q = 0$) E_{2g} mode of the infinite crystal. The microcrystalline sample had a second accompanying peak at 1355 cm^{-1} which was ascribed to a Brillouin zone boundary A_{1g} mode, activated by particle size effects.

Recently, large polycyclic aromatic hydrocarbons (PAH - hydrogen terminated, molecularly defined, subunits of the graphite lattice) have been produced and studied as models for nanosized graphitic domains in carbon materials [8–12]. PAHs are small enough to study computationally, and have been used to show that it is possible to relate the vibrational spectra of these large molecules to the nanocrystalline phase.

In 1991 Shen [13] *et al.* used molecular mechanics, semi-empirical self-consistent field (SCF) methods and *ab-initio* SCF theory to study small hydrogen-terminated carbon clusters as an approximation to diamond. Their comparison was based on calculated carbon-carbon bond lengths, total energies and heats of formation of finite carbon clusters of T_d symmetry, up to $C_{35}H_{36}$. Their study produced useful comparisons of the levels of theory available at that time but suffered from the limitations of computing power then available and the lack of experimental data on the clusters.

The isolation of higher diamondoids [14] (hydrogen terminated, molecularly defined, subunits of the diamond lattice) permits us to compare the *ab initio* Raman spectra of these carbon clusters with experiment. After selecting an appropriate level of theory, cluster sizes up to a maximum of ∼1 nm are studied, and the calculated Raman spectra are compared with those measured experimentally for nanodiamond films and powders.

Appendix A contains a reference to a concise version of the material displayed in this chapter which has been accepted for publication in the journal *Physical Review B*.

5.2 Theoretical Methods

Calculations were performed using either Hartree-Fock theory or the three-parameter hybrid functionals of Becke and the correlation functional of Lee, Yang, and Parr (B3LYP). A range of basis sets were used, a selection found as standard in the Gaussian03 [15] software suite, and also that of Sadlej [16, 17]. Geometries were optimised using the Berny algorithm, and vibrational frequencies were then computed by determining the second derivatives of the energy with respect to the Cartesian nuclear coordinates. Finally Raman intensities were produced by numerical differentiation of dipole derivatives with respect to the electric field. For very large molecules (up to $C_{969}H_{324}$) the vibrational frequencies (but not Raman intensities) were calculated using a molecular mechanics force field. For these calculations the AMBER force field also included in the Gaussian03 software suite was used.

The diamond structure belongs to the space group $Fd3m$; its associated point group is O_{h}. It is not possible to produce a stable diamondoid molecule with this point group, since some symmetry elements of the O_{h} group, such as the inversion centre, only appear in the infinite diamond lattice. To keep the molecular approximation as close to the bulk as possible, the highest symmetry that can be achieved for stable diamond hydrocarbons, the T_{d} point group, was used. This is useful since the diamond zone-centre phonon is triply-degenerate ($T_{2\mathrm{g}}$) and this degeneracy is conserved when the symmetry is reduced to T_{d}. Restricting ourselves to T_{d} symmetry structures also reduces the computational cost, allowing the study of larger molecules. The constraint of T_{d} symmetry leaves two distinct shapes of diamond hydrocarbons; tetrahedra and octahedra. Examples of these different shapes are [1(2,3)4] pentamantane [14], a tetrahedral diamond hydrocarbon and [1231241(2)3] decamantane [14], an octahedral diamond hydrocarbon.

5.3 Selecting the Level of Theory

The first step is to compare the vibrational frequencies and Raman intensities produced by different theories and basis sets with experimentally determined values. Adamantane (C_{10} with T_{d} symmetry) is ideal for these purposes, being small enough to be computationally inexpensive but large enough to be broadly similar to diamond. To simplify the comparison, the high frequency CH stretch region was ignored and solely the lower frequency vibrational modes that involve motion of the carbon atoms were studied. Figure 5.1 shows the low frequency region of an experimental Raman spectrum of adamantane and a selection of different calculated spectra. The calculation that produces frequencies and intensities closest to those in the experimental spectrum is also the most computationally expensive, using B3LYP and the pVTZ basis set of

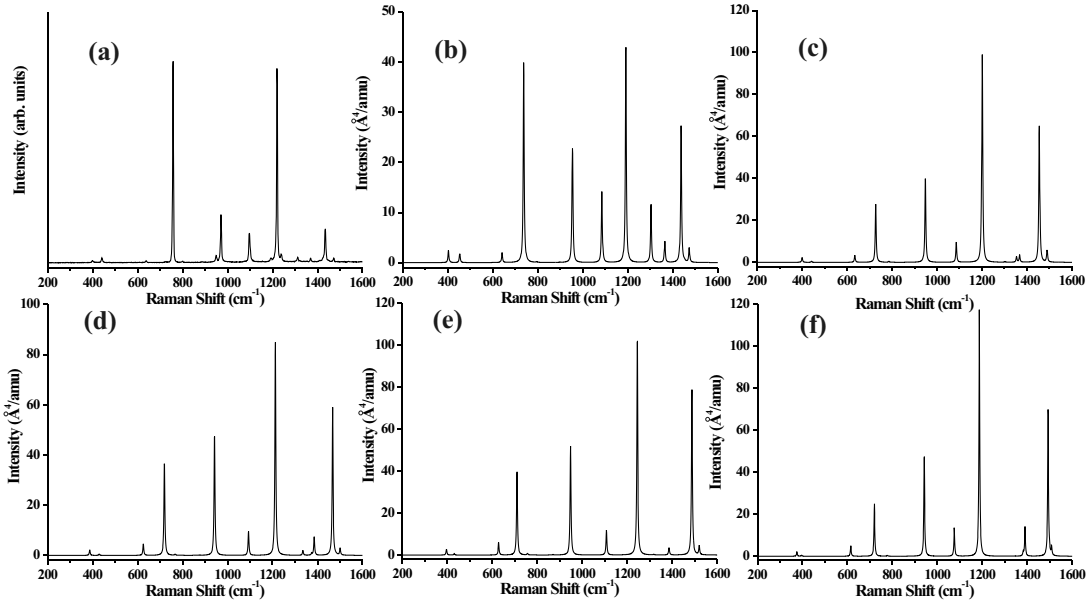

Figure 5.1: Raman spectra of adamantane, experimental [19] and calculated (with scale factors), (a) Experimental, (b) B3LYP/Sadlej (0.9726), (c) B3LYP/6-31G* (0.9603), (d) HF/6-31G*(0.8985), (e) HF/3-21G (0.9056), (f) HF/STO-3G (0.8165).

Sadlej, a combination renowned for cost-effective theoretical vibrational spectra [18]. The vibrational frequencies (excluding the CH stretch modes) produced by this method are in error by ∼1.3% when multiplied by the recommended scale factor of 0.9726. It is not possible to use this combination for any molecules larger than adamantane because the computational cost is far too great. To try to model the Raman spectrum of a nanodiamond crystal effectively it is clear that a compromise is needed. Using a lower level of theory and a smaller basis set considerably reduces the accuracy of the calculation, but allows larger molecules to be studied, thereby improving the approximation of using a diamond hydrocarbon as a model for nanodiamond.

The other spectra shown in Figure 5.1 are calculated with the following methods; (c) B3LYP/6-31G*, (d) HF/6-31G*, (e) HF/3-21G (f) HF/STO-3G. The combination used in (c) is generally seen as the best to use for larger molecules and has frequently been applied to adamantane and its derivatives [20–22]. After multiplying the calculated vibrational frequencies by the recommended scale factors [23] there appears to be little difference between the frequencies and intensities produced by the different calculations. Percentage errors vary between 2 to 3 % from B3LYP/6-31G* to HF/STO-3G (again the CH stretch modes were not included in the error calculation). Increasing the size of the molecule to the C_{26} hydrocarbon ([1(2,3)4] pentamantane, the largest molecule in this study for which experimental data is available) yields similar results. This molecule is too large for the B3LYP/Sadlej method, but all other methods produce

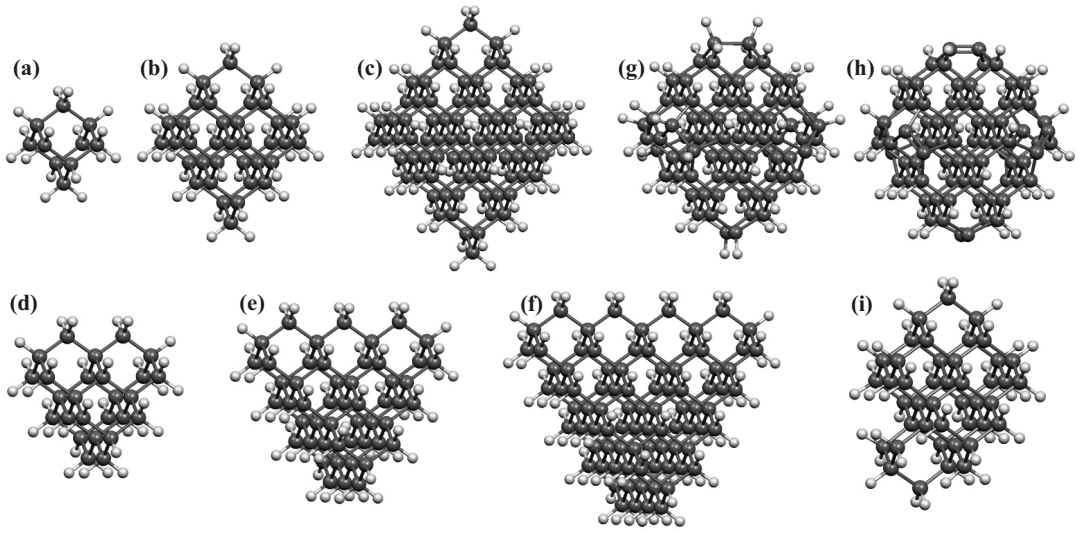

Figure 5.2: Octahedral diamond hydrocarbons, (a) $C_{10}H_{16}$, (b) $C_{35}H_{36}$, (c) $C_{84}H_{64}$; tetrahedral diamond hydrocarbons (d) $C_{26}H_{32}$, (e) $C_{51}H_{52}$, (f) $C_{87}H_{76}$; and (001) reconstructed octahedral diamond hydrocarbons (g) $C_{78}H_{52}$ (h) $C_{78}H_{40}$ and (i) the C_1 symmetry diamond hydrocarbon $C_{43}H_{44}$.

similar results, although the HF/STO-3G calculation is slightly poorer. The above investigation suggests that HF/3-21G is the optimum method to use, permitting the calculation of vibrational frequencies and Raman intensities of very large molecules of this type with acceptable accuracy.

Using this level of theory, and working within the T_d symmetry constraint, permits the study of a reasonable selection of molecules, shown in Figure 5.2. The smallest molecule (a) $C_{10}H_{16}$ is adamantane, the molecule used to select the level of theory. The top row are the tetrahedral molecules, for which an experimental Raman spectrum only exists for (b) $C_{26}H_{32}$ ([1(2,3)4] pentamantane). The bottom row are the octahedral molecules, for which there are no experimental spectra. All of the carbons in the octahedral group are tertiary or quaternary except for the apexes of the octahedra which are secondary. It is possible to remove these secondary carbon atoms, effectively truncating the molecule, producing a cuboctahedral structure. Removal of these atoms effectively performs a (100) surface reconstruction on the molecule, removing the CH_2 groups and joining the remaining dangling bonds together. Two possible molecules can be produced in this way. The first (Figure 5.2 (g)), leaves a single hydrogen atom on each carbon in the bond (C(100) 2×1:H), while the second (Figure 5.2 (h)), leaves the carbons π-bonded (C(100) 2×1). To check for any side-effects from using only T_d symmetry molecules, the vibrational frequencies and Raman intensities were calculated for a low symmetry (C_1) diamond hydrocarbon $C_{43}H_{44}$ (Figure 5.2 (i)).

5.4 Results

To study the Raman active vibrational modes in molecules of this type first the Raman active vibration in diamond must be understood. The diamond structure has $Fd3m$ symmetry and consists of two interpenetrating face-centred cubic Bravais lattices, displaced along the body diagonal of the cubic cell by one quarter-length of the diagonal. Alternatively, the structure can be considered as a face-centred cubic lattice with a two atom basis. Due to the small wave-vector of the optical photons, the phonons involved in the Raman scattering of crystalline solids have a very small momentum and only the zone-centre phonons participate in the first-order Raman scattering. In diamond, the Raman active triply-degenerate zone-centre optic mode gives rise to the single first-order Raman signal at 1332 cm^{-1}. Using periodic Hartree-Fock theory, Causá *et al.* [24] obtained a vibrational frequency of 1484 cm^{-1} (44.5 THz). When scaled using the same factors as used for molecular HF theory [23] this reduces to 1342 cm^{-1}, close to the experimental value. The nuclear displacements associated with this phonon mode consist of the two carbon atoms in the basis moving in opposite directions, with all unit cells moving in phase. As the size of the crystal is reduced, the Raman peak produced by the optical phonon is observed to shift to lower wavenumber and broaden due to particle size effects.

The calculated Raman spectra of all the molecules studied here are shown in Figure 5.3. The peaks have been given a peak width of 5 cm^{-1}, similar to the peak widths observed in our experimental data (chapter 4). None of the spectra consist of a single peak at 1332 cm^{-1} so the clusters are clearly some distance away from an infinite diamond lattice. All the spectra (except for that of $C_{10}H_{16}$) can be separated into three parts (excluding the high frequency CH stretch modes); low frequency modes below 500 cm^{-1}, modes between 1000-1400 cm^{-1}, and a collection of modes at $\sim$1500 cm^{-1}. The signals at $\sim$1500 cm^{-1} are all due to CH_2 scissor modes and, as shown in Figure 5.1, are considerably weaker in the experimental spectrum than the calculated spectrum.

5.4.1 The first-order diamond Raman peak - the crystal-molecule transition

Before considering how the results of our calculations relate to the controversial peaks observed in the Raman spectra of nano-phase diamond particles, let us first discuss how these results relate to the bulk diamond 1332 cm^{-1} Raman signal.

Let us briefly consider the experimental Raman spectra produced by diamond in various forms, from infinite crystal through micro/nanocrystalline and finally to amorphous. The bulk crystal produces a single sharp peak at 1332 cm^{-1}, due to the zone-centre optical mode. As the crystallite size is reduced to a few hundred nanometres,

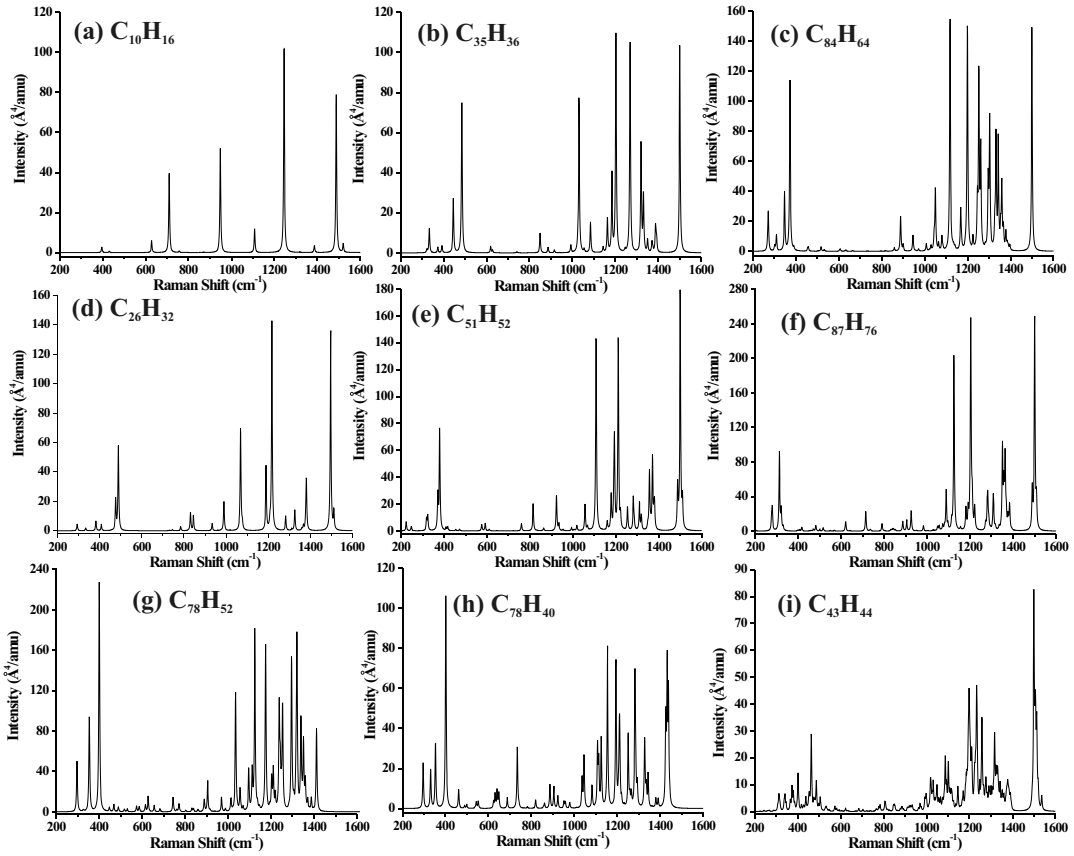

Figure 5.3: Calculated Raman spectra for (a) $C_{10}H_{16}$, (b) $C_{35}H_{36}$, (c) $C_{84}H_{64}$, (d) $C_{26}H_{32}$, (e) $C_{51}H_{52}$, (f) $C_{87}H_{76}$, (g) $C_{78}H_{52}$, (h) $C_{78}H_{40}$, and (i) $C_{43}H_{44}$.

this peak starts to broaden and shift to a lower frequency due to the relaxation of selection rules. At some point, the sample loses all long-range order and becomes amorphous. The Raman spectrum of amorphous diamond should resemble a broadened phonon density-of-states of bulk diamond, as seen for silicon and germanium [25]. This is rarely observed for diamond due to the tendency of carbon to form sp^2 hybridised structures, and hence the Raman spectrum of amorphous carbon is similar to that of disordered graphite. The diamond phonon density-of-states contains several peaks [26], most notably at $\sim$1260 cm^{-1} and $\sim$500 cm^{-1}. It is not too difficult to see how the appearance of peaks at similar frequencies to these in the Raman spectrum of nanocrystalline diamond are assigned as vibrational modes specific to nano-sized diamond crystals.

The final step in the reduction of crystallite size is towards single, isolated molecules. Unlike an amorphous network, which produces a broad Raman spectrum, molecules possess Raman spectra containing sharp, discrete signals. It would be expected then, that at a certain point, the reduction of the diamond crystallite size would start to produce sharp, molecular-like signals in the Raman spectrum.

The smallest nanodiamond powders that have been studied by Raman spectroscopy contain particles that vary in size between 2-10 nm with an average grain size of 5 nm. For these particles, the bulk diamond 1332 cm^{-1} mode is downshifted by 7 cm^{-1} and broadened to a full width half maximum (FWHM) of 10 cm^{-1}. These values are slightly lower than predicted by phonon confinement models. For a 5 nm diamond crystallite, Yoshikawa *et al.* [6] have predicted a downshift of 13 cm^{-1} and a FWHM of 38 cm^{-1}.

Returning to the spectra calculated in this study, let us consider the variation in the spectra of the octahedral diamond hydrocarbons with increasing cluster size. The structures and calculated spectra of the octahedral diamond hydrocarbons are shown in Figures 5.2 and 5.3 (a), (b) and (c) respectively. The spectrum of the smallest molecule ($C_{10}H_{16}$) contains several intense peaks that are reasonably evenly distributed in the range 600-1600 cm^{-1}. In the spectrum calculated for the next largest octahedral molecule ($C_{35}H_{36}$), the intense signals have separated into two groups; the breathing mode/cage deformations below 500 cm^{-1} and the CC stretch/CH bend modes in the region 1000-1500 cm^{-1}. Only a few weak signals are present between 500 and 1000 cm^{-1}. For the largest octahedral molecule studied here ($C_{84}H_{64}$), the frequencies of the breathing mode/cage deformations have reduced to below 400 cm^{-1}, increasing the separation between these two groups of intense signals. This separation of these two intense groups of signals is also observed in the spectra of the tetrahedral diamond hydrocarbons. From this let us assume that as a cluster becomes larger, towards the grain size found in nanodiamond powders, the frequency of these breathing mode/cage deformations reduces further still and hence would appear far from the broadened bulk

diamond mode.

The frequencies of the intense CC stretch/CH bend modes remain within a reasonably constant range (1000-1500 cm^{-1}) as the cluster size increases. The frequency of the zone-centre optic diamond mode also lies within this range. The largest molecule studied here is approximately 1 nm in diameter, while nanodiamond particles have a diameter of ∼5 nm. Yet the calculated spectrum of the ∼1 nm diamond hydrocarbon contains sharp discrete lines over a 400 cm^{-1} range and the experimental Raman spectrum of nanodiamond particles contains a single broadened peak. At some grain size the Raman spectrum of a nanodiamond must change from a single broad peak to the discrete lines calculated for these large diamond hydrocarbons, but when does this change from nano-crystal to molecule occur?

First, there are limitations to the experimental measurements. Experimental spectra are obtained from powdered samples, not isolated particles. The area of the sample analysed contains a large number of particles, of various different sizes and structures. This large distribution of particles leads to increased broadening of the bulk diamond peak, which is already broadened by phonon confinement.

Now consider the calculated data. For the ∼1 nm molecule, there are so many peaks due to CC stretching/CH bending modes in the 1000-1500 cm^{-1} region that the previously well-defined peaks are starting to coalesce. From our results on smaller molecules, in larger systems one would expect this region to become a broad unresolvable peak centred around 1250 cm^{-1}, 80 cm^{-1} lower than the bulk diamond Raman signal. This does not fit well with the experimental downshift of 10 cm^{-1} observed for the 5 nm diamond particles. The problem with considering the coalescence of this group of peaks is that the position and width of the broad feature produced is dependent on the relative intensities of the peaks in this 1000-1500 cm^{-1} region. Previous work has shown (section 4.2.4) that the accuracy of the calculated relative intensities of peaks over this region is poor when using a small basis set.

Figure 5.4(a) shows the experimental Raman spectrum of the largest isolated diamond hydrocarbon, the tetrahedral $C_{26}H_{32}$. It is clear that the intensities of the peaks in the 1300-1400 cm^{-1} region relative to neighbouring peaks are severely underestimated using the HF/3-21G combination (Figure 5.4b). Increasing the size of the basis set and adding diffuse and polarisation functions greatly improves the agreement between the experiment and theoretical spectra in this region (Figure 5.4(c),(d)). Comparing all the different basis set calculations, it appears that the intensity of the CH_2 scissor (∼1500 cm^{-1}) and CH wagging (∼1200 cm^{-1}) modes are strongly overestimated, relative to the 1300-1400 cm^{-1} region, without the use of both diffuse and polarisation functions on carbon atoms. Using HF/6-31+G*, the largest diamond hydrocarbon for which the Raman spectrum can currently be calculated is the octahedral

structure $C_{35}H_{36}$.

The HF/3-21G and HF/6-31+G* spectra of $C_{35}H_{36}$ are shown in Figures 5.4 (e) and (f), respectively. The same trend observed in the $C_{26}H_{32}$ calculated spectra are also observed here. The ∼1200 cm^{-1} CH wagging modes have decreased in intensity and the 1300-1400 cm^{-1} range now contains many peaks which are beginning to coalesce.

So, if a larger basis set calculation on $C_{35}H_{36}$ shows the beginning of a broadened structure centred around ∼1330 cm^{-1}, and a reduction in prominence of the intense CH_2 scissors and CH wagging modes, how might this extrapolate to the ∼1 nm cluster, $C_{84}H_{64}$? The HF/3-21G calculation on $C_{84}H_{64}$ also showed a cluster of peaks in the range 1300-1400 cm^{-1} becoming more intense relative to the strong CH wagging and CH_2 scissors modes. The 3-21G basis set has been shown to underestimate the intensity of the cluster relative to the wagging/scissors modes. If the 6-31+G* basis set could be used for this larger molecule it might be expected that the cluster centred around ∼1330 cm^{-1} would become even more prominent, eventually producing a broad signal, like that observed in the Raman spectra of nanocrystalline diamond powders.

Complete blurring of the cluster of peaks at ∼1330 cm^{-1} into a broad signal has not occurred in any of the spectra of the large T_d molecules here. However, the spectrum calculated using HF/3-21G for the C_1 symmetry molecule $C_{43}H_{44}$ (Figure 5.2(i)) shows a very broad signal over the range 1000-1400 cm^{-1}. The reduction in symmetry splits the degeneracy of the T_2 and E symmetry modes. If, using the HF/6-31+G* combination (or better), the Raman spectrum of a large, low symmetry diamond hydrocarbon were calculated, it should start to resemble the broadened optical mode peak seen in the Raman spectrum of nanodiamond particles.

Alternatively, if a sample of identical, perfect, T_d symmetry nanodiamond particles were produced, the broadened optical mode should start to split into well-defined peaks due to different surface/bulk mixed vibrations.

5.4.2 The ∼500 cm^{-1} mode in the Raman spectrum of nanodiamond powders

The most intense peak in the low frequency region of all clusters is produced by the fully symmetric A_1 breathing mode. In the $C_{10}H_{16}$ hydrocarbon this mode appears at 710 cm^{-1} and is calculated to be relatively weaker than observed in the experimental spectrum. From a comparison with experimental data and theory in previous work [19] it is known that this underestimation continues for $C_{26}H_{32}$, and is therefore likely to be present in all the calculated spectra. The frequency of this breathing mode is strongly dependent on the dimensions of the molecule, since it involves a simultaneous stretch of all carbon-carbon bonds in the molecule. This size dependence of the breathing mode frequency is observed in the calculated data. The frequency of the breathing mode

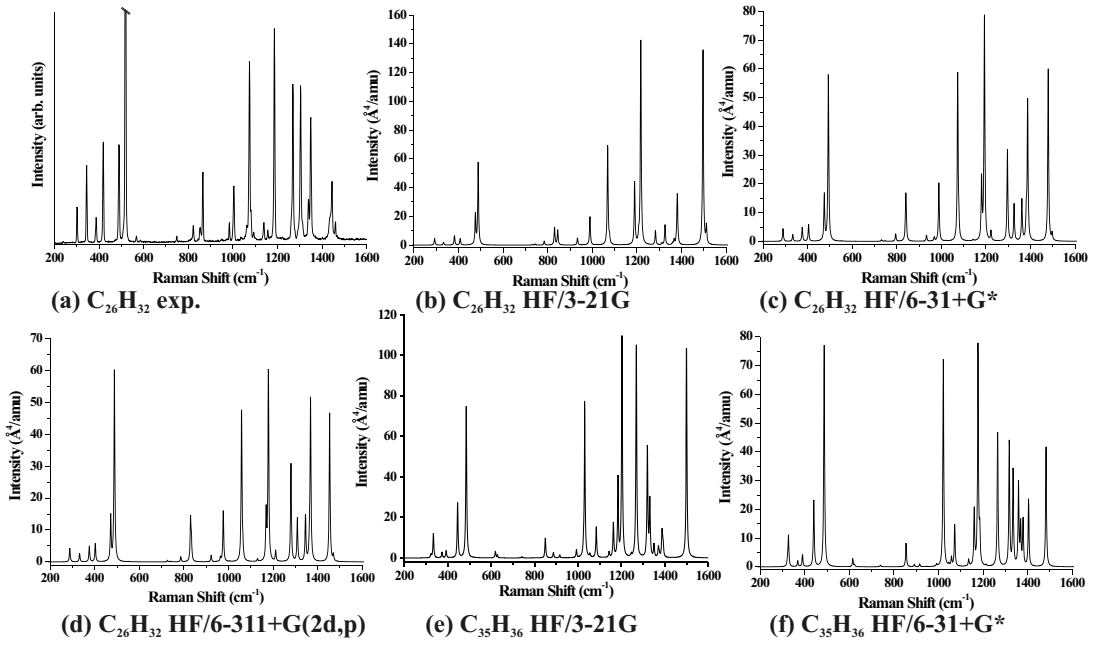

Figure 5.4: Raman spectra of diamond hydrocarbons (a) experimental Raman spectrum of $C_{26}H_{32}$ (peak at 518 cm^{-1} cropped for clarity) [19], (b), (c) and (d) spectra of $C_{26}H_{32}$, calculated using HF theory and increasingly large basis sets, (e) and (f) spectra of $C_{26}H_{32}$, calculated using HF theory with the 3-21G and 6-31+G* basis set, respectively.

is approximately the same for octahedral and tetrahedral molecules with the same number of carbon-carbon bonds in their edge. For example, $C_{26}H_{32}$ and $C_{35}H_{36}$ both have equal edge lengths of 5 carbon-carbon bonds and a breathing mode frequency of approximately 485 cm^{-1}, $C_{51}H_{52}$ and $C_{84}H_{64}$ have edges composed of 7 carbon-carbon bonds and a breathing mode frequency of approximately 375 cm^{-1}. The largest molecule studied here, the tetrahedral $C_{87}H_{76}$, has an edge length of 9 carbon-carbon bonds and a corresponding breathing mode frequency of 311 cm^{-1}.

Zhang *et al.* [27] have suggested that modes similar to these might be the cause of the broad signal at around 500 cm^{-1} seen in the Raman spectrum of shock synthesised nanodiamond. Their study used density functional theory (B3LYP) and the 6-31G(d) basis set to calculate the vibrational frequencies and Raman intensities of a selection of diamond hydrocarbons, polyaromatic hydrocarbons and transpolyacetylene chains. To reveal the "characteristic signals" from each of these three types of structure they averaged the calculated Raman spectra of molecules of various sizes. They concluded that only the diamond hydrocarbon average had an intense peak at $\sim$480 cm^{-1}, and that this could be used to identify nanocrystalline diamond using Raman spectroscopy.

The results of this study disagree with their assignment. For the diamond hydrocarbons in their study, the modes around 480 cm^{-1} are breathing modes and the frequency

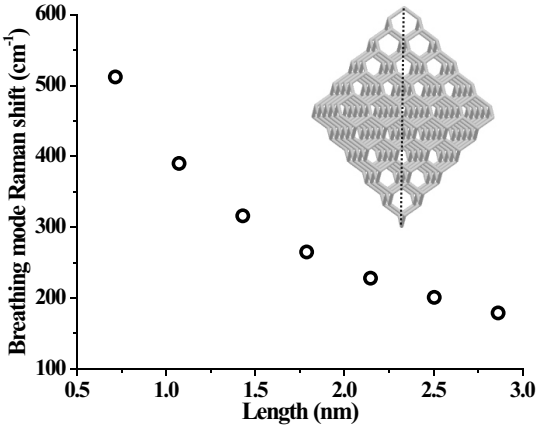

Figure 5.5: Variation in the calculated (AMBER) Raman shift of the breathing mode with molecule size. The length plotted was determined from the distance between opposite points of the octahedral structure (see inset).

of these modes is strongly dependent on the size of the molecule. The molecules studied here are much larger than those studied by Zhang *et al.* but considerably smaller than nanodiamond powders ($\leq$ 1 nm compared to $\geq$ 5 nm). Even when the size is that of $C_{87}H_{76}$, the frequency of this mode is already far below 500 cm^{-1}.

It is possible to calculate the normal vibrational frequencies (but not Raman intensities) for considerably larger molecules using a molecular mechanics force field instead of an *ab initio* method. Using the AMBER molecular mechanics method included in the Gaussian suite of software, the vibrational frequencies for octahedral clusters up to $C_{969}H_{324}$ ($\sim$2.8 nm diameter) have been calculated. Again, as the cluster size increases the wavenumber of the breathing mode decreases (Figure 5.5), to below 200 cm^{-1} for $\sim$2.8 nm. It therefore seems unlikely that this type of mode might be responsible for the broad signal at $\sim$500 cm^{-1}. It is possible that the breathing mode could be observed in the Raman spectrum of nanodiamond but it would be very close to the Rayleigh line (less than 100 cm^{-1} shift). If this line could be observed, its vibrational frequency should show a strong dependence on the size of the crystallite, producing a fast, non-destructive method of sizing nanodiamond crystals.

Low frequency Raman spectroscopy has been used successfully to determine the size of nano-scale quantum dot structures of various materials [28–31] by using the size dependent frequency of certain acoustic modes. Assignment of the observed modes is generally considered in terms of free vibrations of a homogeneous elastic sphere under stress-free boundary conditions, a theory due to Lamb [32] in 1882 which has recently been adopted and modified by many groups [33–35]. Lamb's theory produced two types of vibrational mode, spheroidal and torsional, each with its own set of angular

momentum numbers. For example the $l = 0$ spheroidal fundamental is similar (but not exactly equivalent to) the breathing mode observed in our calculations. A full study of this theory is beyond the scope of this work, but it would seem that the observation of Lamb modes in the low frequency Raman spectrum would be the easiest way to prove a sample was truly nanocrystalline.

To conclude this section, it appears that there is no simple explanation for the broad $\sim$500 cm^{-1} wavenumber vibration seen in nanodiamond, but it is unlikely to be due to the full-molecule breathing modes as suggested by Zhang *et al.* [27] because of the sharp reduction in the vibrational frequency of this type of mode as the dimensions of the molecules increase. In addition to this, in the previous section it was predicted that the other intense peaks observed in the calculated spectra (the 1000-1400 cm^{-1} region) should coalesce into the broadened optical mode seen in the nanodiamond Raman spectrum. Thus no evidence for any strongly Raman active vibrations of nanodiamond, apart from the broadened optical mode and the low frequency breathing/Lamb-type modes is apparent. Since its occurrence is absent in our perfect diamond molecule model, this peak must be due to imperfections in the nanocrystals or at their surfaces. As part of this work the (100) defect/surface reconstruction have been studied. The (100) 2×1 reconstruction does produce extra signals in the Raman spectra, due to the sp^2 out-of-plane bending modes, but these are at $\sim$750 cm^{-1}, far from the $\sim$500 cm^{-1} of the experimental peak. Calculation of the Raman spectra of a selection of common defects/surface reconstructions might yield a possible assignment of this signal, but it is beyond the scope of this study.

5.4.3 Decoupling the hydrogen motion - nanodiamond thin films

The conclusions from the section above can be applied to the Raman spectrum of isolated nanodiamond single crystals (as in nanodiamond powders), but not to thin films of nanodiamonds connected by grain boundaries. The approximation of a hydrogenated surface is fair for an isolated crystal, but in a thin film the diamond crystals are covalently bonded to an amorphous carbon matrix.

Previously, Negri *et al.* [8] have approximated the Raman spectrum of a matrix-confined graphite crystal by taking a hydrogen-terminated PAH molecule and changing the edge-terminating hydrogen mass to 100 amu. This artificial increase in the hydrogen mass separates the frequencies of the bulk stretching modes and surface atom bending modes, removing the strong mode mixing which occurred in the region 1000 - 1400 cm^{-1} when the mass of H is 1 amu.

In the Raman spectra produced by nanodiamond films the peak assigned as nanophase diamond occurs at $\sim$1150 cm^{-1}, although the evidence for this being due to polyacetylene structures at surfaces and grain boundaries is very strong [3]. Using this method

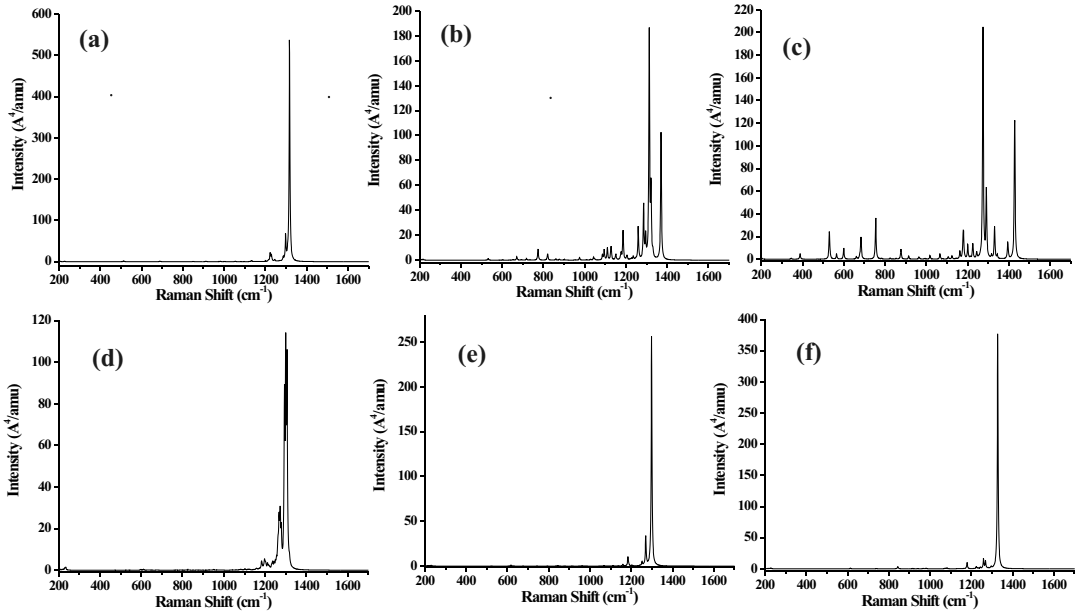

Figure 5.6: Calculated Raman spectra for (a) $C_{84}H_{64}$ (b) $C_{78}H_{52}$ (c) $C_{78}H_{40}$ and (d) $C_{43}H_{44}$ (C_1 symmetry), (e) $C_{35}H_{36}$ (f) $C_{35}H_{36}$ using the 6-31+G* basis set, all calculated with H_{mass}=100 amu

(H_{mass}=100 amu) of approximating an amorphous carbon network surrounding the diamond crystal, the Raman spectra of confined versions of the diamondoid hydrocarbons studied above have been calculated.

Figure 5.6 shows the constrained spectra for the octahedral $C_{84}H_{64}$, the 2×1:H reconstructed $C_{78}H_{52}$ and the 2×1 reconstructed $C_{78}H_{40}$. The number of signals in the spectra have reduced considerably, especially in the unreconstructed case where there is effectively only one strong signal (1317 cm^{-1}). The nuclear displacements of this mode are very similar to the 1332 cm^{-1} zone-centre mode seen in the Raman spectrum of single crystal diamond (Figure 5.7). It is triply-degenerate and is produced by the same carbon-carbon bond stretching motions as described above. This mode is produced by all the diamond hydrocarbons studied here when constrained, even the small C_{10} structure of adamantane. This suggests that if an adamantane derivative could be synthesised with a full surface termination of a heavy subsistuent, such as bromine instead of hydrogen, it should have a Raman spectrum very similar to that of diamond. This is confirmed by a HF/3-21G* calculation, although there is a shift in the vibrational frequency of this stretching mode (to 1000 cm^{-1}) caused by strain in the carbon bonds due to the steric repulsion of the large bromine atoms.

The only other peaks in the $C_{84}H_{64}$ spectrum are (i) another stretching mode at 1298 cm^{-1} similar to the diamond zone-centre mode but the direction of the stretching

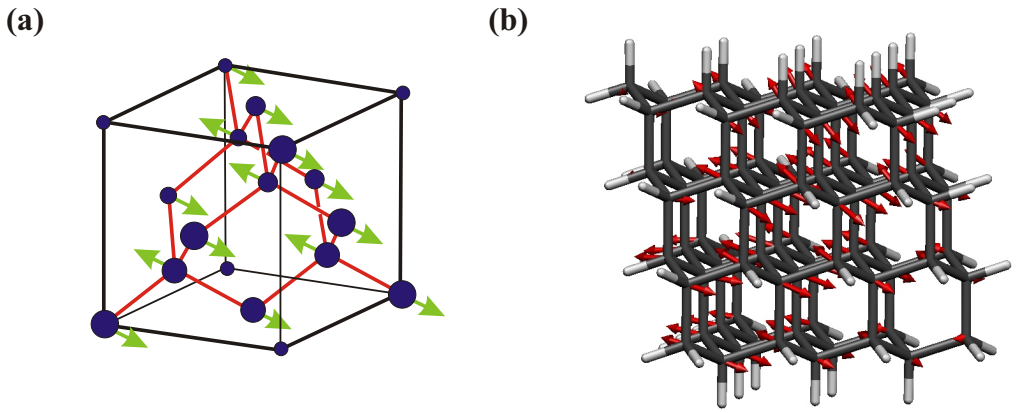

Figure 5.7: Nuclear displacement vectors (a) schematic of the diamond optical phonon and (b) calculated displacements of the vibration which produces the single strong Raman peak in the spectrum of $C_{84}H_{64}$ (H_{mass}=100 amu).

motion is opposite on each side of the molecule, and (ii) another weak cluster of CC stretch modes around 1225 cm^{-1}, which is very close to the maximum in the diamond vibrational density-of-states. These other modes are relatively weak compared to the intense main peak.

The constraining of the two reconstructed diamond hydrocarbons gives us an insight into the effect of imperfections in the grain boundaries of nanodiamond films upon their Raman spectra. The 2×1:H reconstruction introduces strain in the molecule and results in significant changes in geometry from that adopted in the diamond structure. This produces a more complex spectrum compared with the unreconstructed molecule, although all the very strong signals still feature vibrations similar to the diamond zone-centre mode, just perturbed by the reconstruction.

The 2×1 reconstruction introduces some sp^2 bonds into the structure and hence some new signals into the spectrum. The spectrum of this reconstruction features similar smearing of the diamond zone-centre-like vibration as the 2×1:H, but there are also signals similar to those seen in the unconfined molecule. The carbon-carbon sp^2 bond stretch is again at ∼1420 cm^{-1} and there are also the sp^2 out-of-plane bending modes around 750 cm^{-1}.

The calculated spectrum of confined C_1 symmetry diamond hydrocarbon (Figure 5.6(d)) is similar to that of the unreconstructed $C_{84}H_{64}$ (Figure 5.6(a)). The only large difference between these two spectra is the broadening of the single sharp peak because of the splitting of the degeneracy of the T_2 mode.

So far, all the H_{mass}=100 amu calculations have been performed using the small 3-21G basis set. This basis set did not produce accurate intensities for the vibrations between 1300-1400 cm^{-1} for the H_{mass}=1 amu case. To study how a larger basis set

(with diffuse and polarisation functions on carbon atoms) effects the H_{mass}=100 case, the Raman spectrum of the octahedral molecule $C_{35}H_{36}$ has been calculated using the 3-21G and 6-31+G* basis sets. The spectra calculated for this molecule are shown in Figures 5.6 (e) and (f). Both calculated Raman spectra display the single intense peak close to 1300 cm^{-1}, but in the spectrum calculated with the larger basis set, the peak is almost twice as intense in the smaller basis set spectrum. Again the 3-21G basis set has underestimated the intensity of the C-C stretching modes between 1300-1400 cm^{-1}. This suggests that when calculating Raman spectra for structures of this type, basis sets augmented with both diffuse and polarisation functions should be used to obtain accurate intensities.

The breathing mode is still present in the spectra for all these constrained structures but there is a considerable decrease in the vibrational frequencies (the breathing mode frequency of $C_{84}H_{64}$ is reduced to 109 cm^{-1}) and intensities. This does not rule out the use of these breathing modes for sizing nanocrystalline diamond thin films. Much of the low-frequency Raman work mentioned above is performed on quantum dot structures confined in a matrix of of glass (SiO_2). The theory produced by Lamb has also been modified to include the effects of a confining material, and also predicts a reduction in frequency, that depends upon the sound velocities in the matrix material [29].

Again, apart from the optical mode and the breathing/Lamb modes, there is no evidence for other modes produced by the diamond nanocrystal. This suggests that any extra peaks seen in the Raman spectra of nanocrystalline diamond films are due to defects, or structures at grain boundaries and surfaces.

Halogenated Surfaces

Of course it is very unlikely to find a diamondoid molecule having hydrogen atoms with a mass of 100 amu. Therefore, it is almost impossible to compare the results of section 5.4.3 to any experimental data. To create a simple model for a confined diamond crystal that might be producible for experimental measurement, the heavy hydrogen termination must be changed for one that could be created synthetically. An example of such a molecule would be adamantane with terminating halogen atoms instead of hydrogens.

The experimental Fourier-transform Raman and infra-red absorption spectra of fully fluorinated adamantane have been studied by Kovacs and Szabo [22]. They used B3LYP/6-31G* to calculate the vibrational frequencies, but not the Raman intensities, of this molecule.

A trace of the experimental Raman spectrum of perfluoroadamantane is shown in Figure 5.8. It features a broad peak around 1300 cm^{-1} and a group of sharper peaks between 300 - 600 cm^{-1}. The removal of the peaks associated with CH bending modes

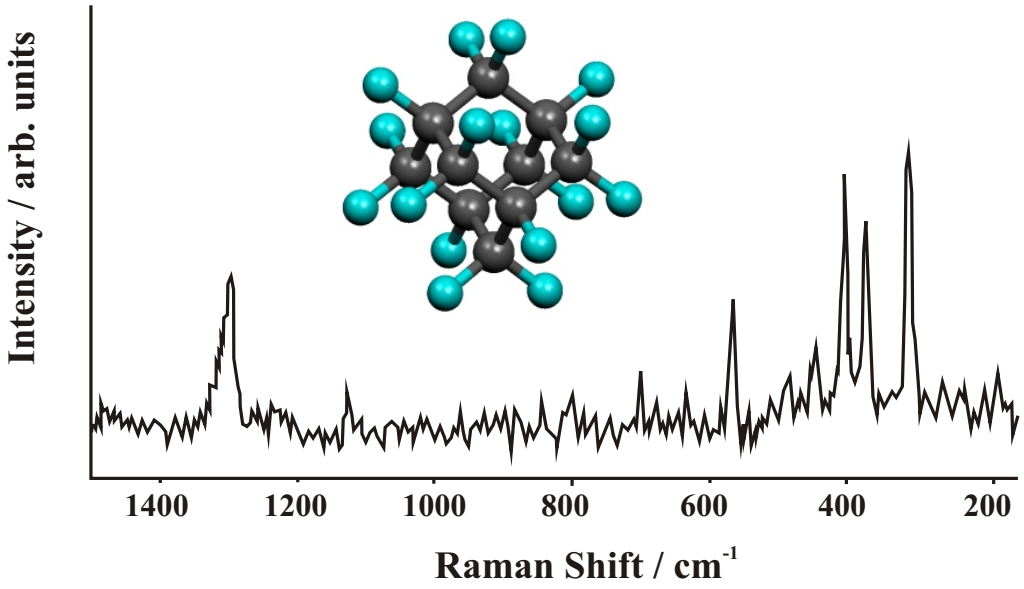

Figure 5.8: FT-Raman spectrum of perfluoroadamantane traced from reference [22].

between 1000-1500 cm^{-1} is similar to that observed in the H_{mass}= 100 amu calculations of the larger diamond hydrocarbons (Figure 5.6), but the experimental intensity of the ∼1300 cm^{-1} peak relative to the other peaks is much lower.

Figure 5.9 shows a selection of spectra calculated for perfluoroadamantane, at various different levels of theory. The different theories and basis sets appear to have a much larger effect on the calculated Raman spectrum of fluorinated adamantane compared with the hydrogen-terminated molecule (Figure 5.1). There are considerable differences between the relative intensities of the peaks around 1300 cm^{-1}. The experimental spectrum has quite a poor signal-to-noise ratio, and the ∼1300 cm^{-1} peak shows no resolvable structure, making it difficult to see which calculation best reproduces the experimental data. In all cases the calculated spectrum significantly overestimates the intensity of the ∼1300 cm^{-1} peak compared to the peaks in the 300 - 600 cm^{-1} region, although the intensity response of the experimental system is not known.

5.5 Conclusions

In this study *ab initio* methods have been used to calculate the Raman spectra of a selection of T_d diamond hydrocarbons up to 1 nm in size. All (H_{mass}=1 amu) spectra consist of three regions, the high wavenumber CH stretch region, a broad region of strongly mixed CC stretch/CH bend modes between 1000-1400 cm^{-1} and the low wavenumber breathing mode/cage deformation region ≤500 cm^{-1}.

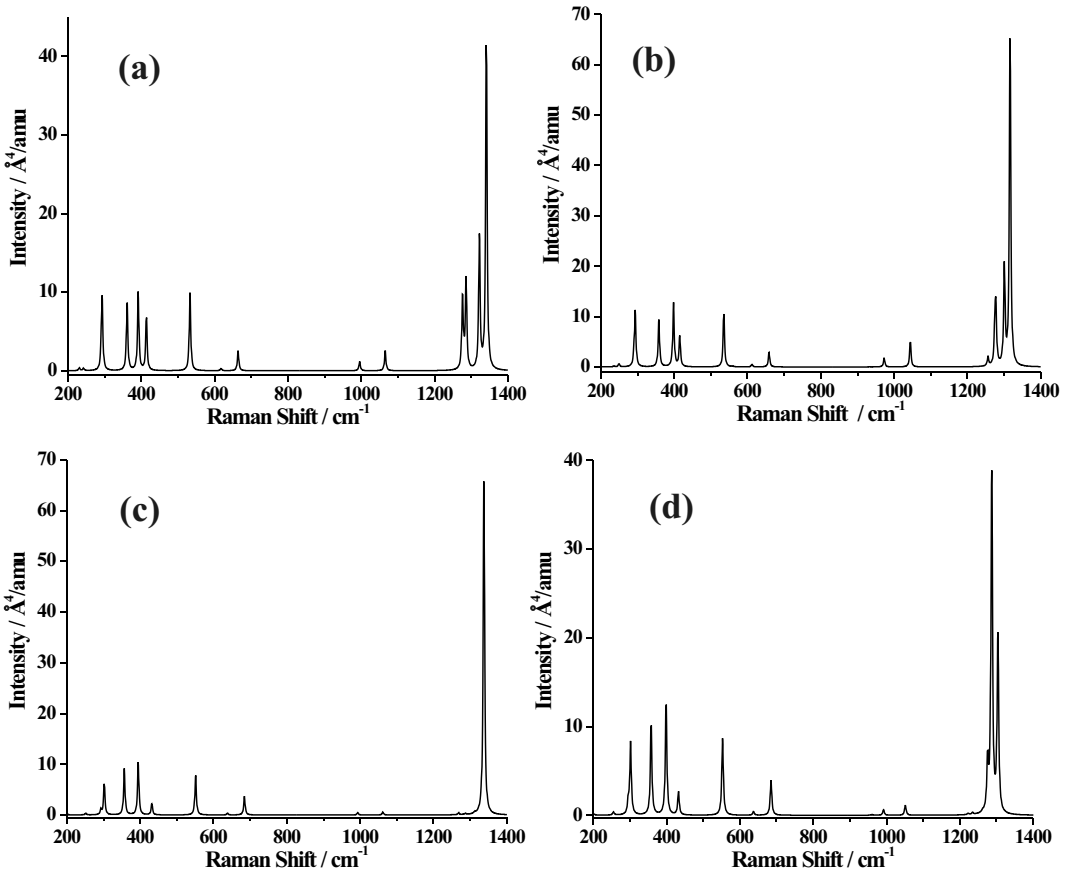

Figure 5.9: Calculated Raman spectra of perfluoroadamantane (a) HF/3-21G, (b) HF/6-31G, (c) HF/6-31+G* and (d) B3LYP/6-31+G*.

The HF/3-21G level of theory was found to produce (scaled) vibrational frequencies and intensities comparable to higher levels/larger basis sets, although the relative intensities showed marked improvement with the addition of diffuse and polarisation functions (6-31+G*).

The model of perfect T_d symmetry clusters is able to explain the changes in the Raman-active optical-phonon frequencies with particle size. Experimental data are generally obtained from a wide distribution of particle sizes and morphologies. If calculations could be performed on a larger data set featuring lower symmetries, a summation of all the spectra would approach the experimental data. Alternatively, if a powder of nanometre-sized, perfect, identical diamond crystals could be produced, its Raman spectrum must resemble those calculated here.

From the strong size dependence of the breathing mode frequency it has been shown that these vibrations cannot be the origin of the broad ~500 cm^{-1} signal seen in the Raman spectrum of nanodiamond powders. For a ~1 nm diamond crystallite the breathing mode frequency has already dropped below 400 cm^{-1}. It is possible that this signal may be due to defects or surface reconstructions, not featured in this study, becoming more prominent as the surface-to-bulk carbon ratio increases. Future work will calculate the Raman spectra of a set of defective diamond particulates to try and determine a likely candidate for the cause of the ~500 cm^{-1} signal. These defects will break the high symmetry of these molecules making these calculations too expensive with the current computational resources. The observed change in the breathing mode/cage deformation vibrational frequency might be very useful for sizing nanodiamond particles, but the signals would appear closer to the Rayleigh line (<100 cm^{-1} shift) than suggested by Zhang *et al.*

By changing the mass of the terminating hydrogen atoms, it has been shown that the Raman spectrum of a confined diamond crystal will be strongly dependent on the crystal surface termination. This leads us to believe that nanodiamond particles with a hydrogen-terminated or reconstructed surface will have a very different Raman spectrum to that of a nanodiamond film, where the crystallites are confined within a matrix of amorphous carbon and other crystallites. The Raman spectrum of even small clusters is dominated by a carbon-carbon stretch, very similar to that observed in the Raman spectrum of diamond. This suggests that even a section of the diamond lattice as small as a single unit cell, trapped in a matrix, should produce a signal close to 1332 cm^{-1}. The problem is whether or not the signal from the diamond crystal is masked by the signal from the matrix. This is probably the case for all CVD nanodiamond films, where the sp^2 grain boundaries have a much higher Raman cross-section and are resonantly enhanced.

To conclude, the analysis of the calculated spectra of these diamond hydrocarbons,

both confined and unconfined, shows little evidence to suggest any diamond phonon density-of-states-like features in the Raman spectrum of nanocrystalline diamond films and powders. It is proposed that any such peaks observed are due to defects, surface structures, amorphous material or any other non-diamond material in the sample, and are not definitive evidence for nanocrystalline diamond within a sample.

Future work for this study could involve calculating the vibrational frequencies and Raman intensities for a selection of common diamond defects in an attempt to assign the $\sim$500 cm^{-1} wavenumber peak. With more powerful computing facilities, the Raman spectra of larger, asymmetric diamond hydrocarbons could be calculated with larger basis sets augmented with diffuse and polarisation functions. This would give a more complete understanding of the Raman spectra of molecular and nano-size diamond.

Bibliography

[1] R. J. Nemanich, J. T. Glass, G. Lucovsky, and R. E. Shroder, *J. Vac. Sci. Tech. A.*, 1988, **6**, 1783.

[2] S. Prawer, K. W. Nugent, D. N. Jamieson, J. O. Orwa, L. A. Bursill, and J. L. Peng, *Chem. Phys. Lett.*, 2000, **332**, 93.

[3] A.C.Ferrari and J.Robertson, *Phil. Trans. R. Soc. Lond. A*, 2004, **362**, 2477.

[4] R. Pfeiffer, H. Kuzmany, N. Salk, and B. Gunther, *Appl. Phys. Lett.*, 2003, **82**, 4149.

[5] A. C. Ferrari and J. Robertson, *Phys. Rev. B*, 2001, **63**, 121405(R).

[6] M. Yoshikawa, Y. Mori, M. Maegawa, G. Katagiri, H. Ishida, and A. Ishitani, *Appl. Phys. Lett.*, 1993, **62**, 3114.

[7] F. Tuinstra and J. L. Koenig, *J. Chem. Phys.*, 1970, **53**, 1126.

[8] F. Negri, C. Castiglioni, M. Tommasini, and G. Zerbi, *J. Phys. Chem. A*, 2002, **106**, 3306.

[9] M. Rigolio, C. Castiglioni, G. Zerbi, and F. Negri, *J. Mol. Struct.*, 2001, **563**, 79.

[10] C. Mapelli, C. Castiglioni, E. Meroni, and G. Zerbi, *J. Mol. Struct.*, 1999, **480**, 615.

[11] C. Castiglioni, F. Negri, M. Rigolio, and G. Zerbi, *J. Chem. Phys.*, 2001, **115**, 3769.

[12] C. Castiglioni, C. Mapelli, F. Negri, and G. Zerbi, *J. Chem. Phys.*, 2001, **114**, 963.

[13] M. Z. Shen, H. F. Schaefer, C. X. Liang, J. H. Lii, N. L. Allinger, and P. V. Schleyer, *J. Am. Chem. Soc.*, 1992, **114**, 497.

[14] J. E. Dahl, S. G. Liu, and R. M. K. Carlson, *Science*, 2003, **299**, 96.

[15] M. J. Frisch, G. W. Trucks, H. B. Schlegel, G. E. Scuseria, M. A. Robb, J. R. Cheeseman, J. A. Montgomery, Jr., T. Vreven, K. N. Kudin, J. C. Burant, J. M. Millam, S. S. Iyengar, J. Tomasi, V. Barone, B. Mennucci, M. Cossi, G. S. N. Rega, G. A. Petersson, H. Nakatsuji, M. Hada, M. Ehara, K. Toyota, R. Fukuda, J. Hasegawa, M. Ishida, T. Nakajima, Y. Honda, O. Kitao, H. Nakai, M. K. X. Li, J. E. Knox, H. P. Hratchian, J. B. Cross, C. Adamo, J. Jaramillo, R. Gomperts, R. E. Stratmann, O. Yazyev, A. J. Austin, R. Cammi, C. Pomelli, J. W. Ochterski, P. Y. Ayala, K. Morokuma, G. A. Voth, P. Salvador, J. J. Dannenberg, V. G. Zakrzewski, S. Dapprich, A. D. Daniels, M. C. Strain, O. Farkas, D. K. Malick, A. D. Rabuck, K. Raghavachari, J. B. Foresman, J. V. Ortiz, Q. Cui, A. G. Baboul, S. Clifford, J. Cioslowski, B. B. Stefanov, G. Liu, A. Liashenko, P. Piskorz, I. Komaromi, R. L. Martin, D. J. Fox, T. Keith, M. A. Al-Laham, C. Y. Peng, A. Nanayakkara, M. Challacombe, P. M. W. Gill, B. Johnson, W. Chen, M. W. Wong, C. Gonzalez, and J. A. Pople, Gaussian 03, revision b.04, 2003.

[16] A. Sadlej, *Collect. Czech. Chem. Commun.*, 1988, **53**, 1995.

[17] A. Sadlej, *Theor. Chim. Acta.*, 1991, **79**, 123.

[18] M. D. Halls, J. Velkovski, and H. B. Schlegel, *Theoretical Chemistry Accounts: Theory, Computation, and Modeling (Theoretica Chimica Acta)*, 2001, **105**, 413.

[19] J. Filik, J. Harvey, N. Allan, P. May, J. Dahl, S. Liu, and R. Carlson, *Spectrochim. Acta A. Mol. Biomol. Spect.*, 2006, **64**, 681.

[20] J. O. Jensen, *Spectrochim. Acta Part A*, 2004, **60**, 1895.

[21] L. Bistriĉić, L. Pejov, and G. Baranović, *J. Mol. Struct. Theochem.*, 2002, **594**, 79.

[22] A. Kovacs and A. Szabo, *J. Mol. Struct.*, 2000, **519**, 13.

[23] A. Scott and L. Radom, *J. Phys. Chem.*, 1996, **100**, 16502.

[24] M. Caus, R. Dovesi, and C. Roetti, *Phys. Rev. B.*, 1991, **43**, 11937.

[25] R. Alben, D. Weaire, J. E. S. Jr., and M. H. Brodsky, *Phys. Rev. B.*, 1975, **11**, 2271.

[26] W. Windl, P. Pavone, K. Karch, O. Schtt, D. Strauch, P. Giannozzi, and S. Baroni, *Phys. Rev. B.*, 1993, **48**, 3164.

[27] D. J. Zhang and R. Q. Zhang, *J. Phys. Chem. B*, 2005, **109**, 9006.

[28] L. Saviot, B. Champagnon, E. Duval, I. A. Kudriavtsev, and A. I. Ekimov, *J. Non-Cryst. Solid.*, 1996, **197**, 238.

[29] L. Saviot, D. B. Murray, and M. D. M. de Lucas, *Phys. Rev. B*, 2004, **69**, 113402.

[30] M. Fujii, Y. Kanzawa, S. Hayashi, and K. Yamamoto, *Phys. Rev. B*, 1996, **54**, R8373.

[31] A. Tanaka, S. Onari, and T. Arai, *Phys. Rev. B*, 1993, **47**, 1237.

[32] H. Lamb, *Proc. London Math. Soc.*, 1882, **13**, 187.

[33] W. Cheng, S. F. Ren, and P. Y. Yu, *Phys. Rev. B*, 2003, **68**, 193309.

[34] W. Cheng, S. F. Ren, and P. Y. Yu, *Phys. Rev. B*, 2005, **71**, 174305.

[35] D. B. Murray and L. Saviot, *Physica E*, 2005, **26**, 417.

Appendix A

Publication List

Chapter 3
J. Filik, I.M. Lane, P.W. May, S.R.J. Pearce, and K.R. Hallam, Incorporation of sulfur into hydrogenated amorphous carbon films, *Diamond and Related Materials*, **13** (2004) 1377.

Chapter 4
J. Filik, J.N. Harvey, N.L. Allan, P.W. May, J.E.P. Dahl, S. Liu and R.M.K. Carlson, Raman spectroscopy of diamondoids, *Spectrochimica Acta A: Molecular and Biomolecular Spectroscopy*, **64**, (2006), 681.

Chapter 5
J. Filik, J.N. Harvey, N.L. Allan, P.W. May, J.E.P. Dahl, S. Liu and R.M.K. Carlson, Raman Spectroscopy of Nano-Crystalline Diamond: An *Ab Initio* Approach, *Physical Review B*, in press.

Appendix B

Solid-State Nuclear Magnetic Resonance

B.1 Introduction

Solid-state nuclear magnetic resonance (NMR) is the most accurate method of determining the sp^2/sp^3 ratio of amorphous carbon (a-C) materials. The method used in this study is similar to that described by Donnet *et al.* [1].

It has been found previously that the simple proton decoupling pulse sequence is the best for obtaining a quantitative value for the sp^2/sp^3 ratio [1]. This method detects all carbon atoms except those bonded to paramagnetic centres, whereas other methods (such as cross polarisation) can be more sensitive to carbon atoms bonded to hydrogen.

B.2 Experimental

Hydrogenated amorphous carbon (a-C:H) films were deposited using the apparatus described in chapter 3. For the NMR experiment, samples were deposited onto aluminium foil wrapped around a glass slide. The substrates were cleaned with isopropyl alcohol and then dried by blowing with nitrogen. Samples were grown from methane (30 sccm flow rate), at a DC bias of -100 V and pressure of 20 mTorr for 30 minutes. The soft a-C:H films were mechanically removed from the substrates with a latex-covered glass slide. A total of 60 identical deposition runs were performed, yielding 34 mg of a-C:H powder.

^{13}C NMR were carried out by Kevin Jack and Youssef Espidel at the School of Chemistry, University of Bristol. A 100 MHz HPDEC pulse sequence, with a pulse length of 3.5 μs and a recycle delay of 30 s was used. The sample was spun with a frequency of 8 kHz at 54.7° (magic angle). 3720 scans were accumulated to produce the spectrum.

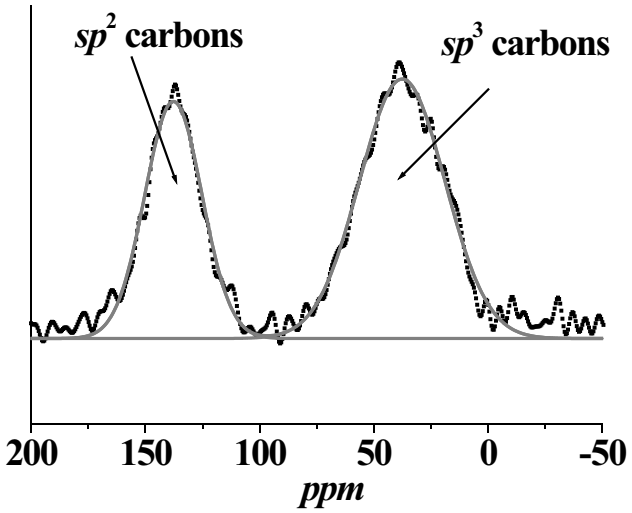

Figure B.1: ^{13}C HPDEC NMR spectrum of the a-C:H powder.

B.3 Results

The ^{13}C HPDEC NMR spectrum of the a-C:H powder is shown in figure B.1. The peaks centred at 40 and 130 ppm correspond to sp^3 and sp^2 hybridised carbon atoms, respectively. The ratio of the areas of these peaks is equivalent to the sp^2/sp^3 ratio of the sample. In this case, the sample contains $\sim$62% sp^3 hybridised carbon. From fitting the XPS C 1s peak, as described in reference [2], a sample deposited under the same conditions, but onto silicon insead of aluminum, contained $\sim$59% sp^3 hybridised carbon. This shows an excellent agreement between the results obtained from these two techniques.

B.4 Conclusions

The agreement between the NMR and XPS results for this single sample are very promising. To test the agreement further, more samples should be grown and analysed by both techniques. Unfortunately, to produce enough a-C:H powder for a single NMR measurement can take from a few weeks to a month, and also the data acquisition is very slow requiring use of the spectrometer for as long as 48 hours. These time constraints meant no further NMR experiments could be carried out in this project.

Bibliography

[1] C. Donnet, J. Fontaine, F. Lefebvre, A. Grill, V. Patel, and C. Jahnes, *J. Appl. Phys.*, 1999, **85**, 3264.

[2] J. Filik, P. W. May, S. R. J. Pearce, R. K. Wild, and K. R. Hallam, *Diam. Relat. Mater.*, 2003, **12**, 974.

Appendix C

Vibrational Frequencies and Raman Intensities of Adamantane

Symmetry	Normal Mode	Calculated Frequency [cm^{-1}]	Raman Activity [$Å^4$/amu]	Experimental Frequency [cm^{-1}]
A_1				
	ν_1	3039.42	654.3	2915
	ν_2	3005.08	100.5	2846
	ν_3	1507.92	2.8	1472
	ν_4	1060.64	0.0	-
	ν_5	759.01	28.6	757
A_2				
	ν_6	1134.53	Inactive	-
E				
	ν_7	3004.81	68.1	2846
	ν_8	1469.71	58.6	1434
	ν_9	1411.03	4.6	1368
	ν_{10}	1238.13	93.0	1220
	ν_{11}	922.92	0.0	-
	ν_{12}	417.83	2.4	399
T_1				
	ν_{13}	3046.10	Inactive	-
	ν_{14}	1356.90		-
	ν_{15}	1324.02		-
	ν_{16}	1136.71		-
	ν_{17}	1060.87		-
	ν_{18}	909.66		-
	ν_{19}	344.20		-
T_2				
	ν_{20}	3050.48	487.1	2943
	ν_{21}	3030.38	198.5	2893
	ν_{22}	3005.24	192.7	2846
	ν_{23}	1484.84	0.0	-
	ν_{24}	1396.13	1.7	1369
	ν_{25}	1350.37	0.5	1312
	ν_{26}	1125.69	11.3	1097
	ν_{27}	985.41	35.9	971
	ν_{28}	819.15	0.5	800
	ν_{29}	662.34	3.1	637
	ν_{30}	466.32	0.7	441

Table C.1: Vibrational frequencies and Raman intensities of adamantane. The experimental and calculated data for all the other diamondoid molecules in this thesis can be found on the compact disc in the back cover.